



University of Crete

Department of Materials Science and Technology

“Development of a multi-analyte acoustic biosensing
platform for clinical diagnostics”

by
Konstantinos Mitsakakis

*A dissertation submitted to the University of Crete
in fulfillment of the requirements for the degree of
Doctor of Philosophy
in Materials Science & Technology*

Heraklion 2009



Πανεπιστήμιο Κρήτης
Τμήμα Επιστήμης και Τεχνολογίας Υλικών

“ Ανάπτυξη ακουστικού βιοαισθητήρα πολλαπλής ανάλυσης για
κλινική διαγνωστική ”

Κωνσταντίνος Μητσακάκης

Ηράκλειο 2009

This work is dedicated...

to my parents

&

to all people who are in need of biomedical microsystems for their health

Αυτή η εργασία είναι αφιερωμένη...

στους γονείς μου

&

*σε όλους τους ανθρώπους που έχουν ανάγκη ιατρικά μικροσυστήματα
για την υγεία τους*

Abstract

This work focuses on the development of a multi-analyte biosensor, based on a Surface Acoustic Wave (SAW) device. The novelty of the concept lies in the way of achieving multiplicity: instead of the “traditional” way of a sensor element array, multiplicity is induced by compartmentalization of a single sensor, achieved via microfluidics (“microfluidics-on-SAW”, or “ μ F-on-SAW” setup).

Initially, the appropriate SAW device for the microsystem was selected among twelve device configurations (varying in substrate, operating frequency and waveguide thickness) upon loading with different classes of materials (mass, viscous, viscoelastic). In particular, a dual quartz-based SAW biochip was used, operating at 155 MHz with 0.70 μ m thick PMMA waveguide. Subsequently, the microfluidic module was designed targeting flexibility and simplicity. Considering functional and geometrical limitations imposed by the SAW biochip, the two components were successfully assembled. The fabrication process for the microfluidic module was soft lithography of PDMS (rapid prototyping and replica molding); 3-, 4-, and 5-channel modules were made, all successfully tested, and the 4-channel one used in the project.

Reproducibility and sensitivity tests were carried out using aqueous glycerol solutions, and standard protein biomolecules (neutravidin and biotinylated BSA, as well as protein G and IgG). The standard deviation in the signal values among the sub-areas was less than 10%, in all cases.

The proof-of-principle of multi-sample detection was achieved via four biotinylated molecules. Each one was injected in one μ F-on-SAW compartment and interacted with pre-adsorbed neutravidin; separate detection of the analytes, kinetics and equilibrium analysis were successfully demonstrated. Maximum multiplexity was achieved when the two devices of the biochip were pre-functionalized with different receptors, and four different samples were injected in each microchannel (altogether 8 probed interactions).

The final step was the application of μ F-on-SAW in multi-sample detection of clinical significance. In particular, cardiac markers were used, the detection of which was realized via antibody-antigen interactions. The four cardiac markers (CK-MB, CRP, D-dimer, and PAPP-A) were successfully detected individually and in various concentrations; analytical curves were created for each biomarker and correlation to the known physiological and pathological values was made. Eventually, by using the μ F-on-SAW it was feasible to selectively capture each marker out of a mixture or all four, a proof that the system can potentially be used in body fluids (were many “unwanted” species are present).

Finally, from the different groups of biomolecules detected throughout the project, interesting results emerged concerning the interaction of acoustic waves with biomolecules and the correlation of the acoustic signal with inherent properties of biomolecules such as their molecular weight and viscoelastic nature.

Περίληψη

Η παρούσα εργασία εστιάζεται στην ανάπτυξη ενός βιοαισθητήρα ανίχνευσης πολλαπλών δειγμάτων, βασισμένου σε μικροδιατάξεις επιφανειακών ακουστικών κυμάτων (SAW). Η καινοτομία της ιδέας βρίσκεται στον τρόπο επίτευξης της πολλαπλότητας ανάλυσης: αντί του «παραδοσιακού» τρόπου της χρήσης μιας συστοιχίας από αισθητήρες, εδώ η πολλαπλότητα επιτυγχάνεται μέσω της διαμερισματοποίησης της επιφάνειας ενός μόνο αισθητήρα σε υποπεριοχές, γεγονός που επάγεται από τη χρήση μικρορευστομηχανικών διατάξεων.

Αρχικά επιλέχθηκε η κατάλληλη μικροδιάταξη αισθητήρα SAW ανάμεσα σε δώδεκα διαφορετικές διαμορφώσεις (οι οποίες διέφεραν ως προς το υπόστρωμα, τη συχνότητα λειτουργίας και το πάχος του κυματοδηγού) χρησιμοποιώντας διαφορετικής φύσεως υλικά (με ελαστικό, ιξώδη και ιξωδοελαστικό χαρακτήρα) για το χαρακτηρισμό. Τελικά χρησιμοποιήθηκε μια διάταξη διπλού αισθητήρα με υπόστρωμα χαλαζία στα 155 MHz και με πάχος κυματοδηγού 0.70 μm . Ακολούθως, σχεδιάστηκε η μικρορευστομηχανική διάταξη/κυψελίδα, με γνώμονα την ευελιξία και απλότητα στη χρήση του συστήματος και λαμβάνοντας υπόψη λειτουργικούς και γεωμετρικούς περιορισμούς που επιβάλλονταν από τη μικροδιάταξη του διπλού αισθητήρα. Η μέθοδος κατασκευής της κυψελίδας ήταν η λιθογραφία μαλακής ύλης του υλικού PDMS (τα βασικά βήματα της οποίας ήταν η ταχεία δημιουργία πρωτοτύπου και η αντιγραφή του εκμαγείου) με την οποία κατασκευάστηκαν και δοκιμάστηκαν επιτυχώς κυψελίδες με 3, 4, και 5 κανάλια.

Η επαναληψιμότητα και η ευαισθησία ελέγχθηκαν χρησιμοποιώντας υδατικά διαλύματα γλυκερόλης και κάποιες συνήθειες πρωτεΐνες (νιουτραβιδίνη και βιοτινυλιωμένη BSA, protein G και IgG). Η απόκλιση του σήματος μεταξύ των σχηματισμένων υποπεριοχών ήταν μικρότερη από 10% σε όλες τις περιπτώσεις.

Η απόδειξη της λειτουργίας του μικροσυστήματος ως πολυ-δειγματικού αναλυτή, έγινε με χρήση τεσσάρων διαφορετικών βιοτινυλιωμένων πρωτεϊνών. Κάθε πρωτεΐνη εισήλθε σε έναν υποχώρο του μικροσυστήματος και ανιχνεύθηκε η αλληλεπίδρασή της με την ήδη προσροφημένη νιουτραβιδίνη. Η ανεξάρτητη ανίχνευση των βιομορίων στους υποχώρους καθώς και η ανάλυση της κινητικής τους έγιναν με επιτυχία. Η αξιοποίηση του μικροσυστήματος στο μέγιστο βαθμό του πραγματοποιήθηκε όταν δύο διαφορετικοί υποδοχείς προ-ακίνητοποιήθηκαν στους δύο αισθητήρες και τέσσερα διαφορετικά δείγματα εισήχθησαν στα μικροκανάλια. Έτσι ανιχνεύθηκαν συνολικά 8 διαφορετικές αλληλεπιδράσεις.

Η εφαρμογή του μικροσυστήματος σε δείγματα κλινικού ενδιαφέροντος πραγματοποιήθηκε με χρήση καρδιακών δεικτών, όπου η ανίχνευση έγινε μέσω της αλληλεπίδρασης αντιγόνου-αντισώματος. Οι τέσσερις δείκτες (CK-MB, CRP, D-dimer, και PAPP-A) αναλύθηκαν σε διάφορες συγκεντρώσεις, διερευνήθηκαν τα όρια λειτουργίας του μικροσυστήματος, και έγινε συσχετισμός με πραγματικές κλινικές τιμές. Επίσης, επιτεύχθηκε επιλεκτική ανίχνευση των πρωτεϊνών μέσα από ένα μίγμα όλων των διαθέσιμων δεικτών.

Τέλος, από τα πειράματα που έγιναν με όλα τα βιομόρια, προέκυψαν συμπεράσματα και ενδιαφέροντα δεδομένα σχετικά με το συσχετισμό του ακουστικού κύματος με ιδιότητες των βιομορίων (το μοριακό τους βάρος και την ιξωδοελαστική τους φύση).

Acknowledgements

The work for this PhD thesis was realized at Biosensors' Technology Lab, Institute of Molecular Biology and Biotechnology, Foundation for Research & Technology-Hellas (I.M.B.B. - FO.R.T.H.), where I worked as a PhD student of Materials Science & Technology Department, University of Crete. All the experiments and data analysis reported in this thesis have been carried out by me (upon training at some equipment, whenever necessary).

During the almost four-year work, I realized that the PhD is not just doing experiments, analyzing results and writing publications, but it's a whole adventure: meeting people, building your character especially at hard moments, and learning to be hard working, patient but also persistent; and all these are beyond experiments, they are life lessons. And if time went back, I would choose the same people to cooperate with, the same work place and work field and yes...I would do it again!

The enthusiasm of the previous words is obviously due to some people that I interacted with and I want to give them my thanks. First of all, of course, to my supervisor, Mrs. Electra Gizeli, Associate Professor at Biology Department, for our impeccable cooperation, her trust and positive attitude towards me and my work. Her advice as expert on the field and her guidance and support especially at moments of dead-ends in the progress of my work were very important to me. Her openness to new ideas and the "freedom" I had from her side to carry out some of my initiatives without criticism but with encouragement are greatly appreciated, as well as the opportunities she gave me for attending conferences, seminars and extra-lab activities.

At this point, I would like to thank also the members of my committee for their contribution, through the conversations we had and their advice: Mr. George Fytas, Professor at Materials Science & Technology Department, Mrs. Aggeliki Tserepi, Senior Researcher at IMEL, NCSR "Demokritos", Mrs. Maria Vamvakaki, Assistant Professor at Materials Science & Technology Department, Mrs. Kelly Velonia, Assistant Professor at Materials Science & Technology Department, Mr. George Kiriakidis, Associate Professor at Physics Department, and Mrs. Anna Mitraki, Associate Professor at Materials Science & Technology Department.

From my workplace and colleagues, I would like to express my acknowledgements first of all to Dr. Achileas Tsortos, acknowledgements which exceed the mere professional cooperation. His strong background on Biophysics, the exchange of ideas we had, his suggestions and experience, and his way of thinking were very important for me; but also our discussions about various issues, his support and the evening talks during the long-lasting experiments were very helpful to me and are greatly acknowledged. During my work, people came and people left from the lab. Among these people I feel like thanking Dr. Florian Bender for sharing his "world-wide" experience with me and his scientific expertise, and Dr. Kathryn Melzak who assisted me in getting used to a new for myself, biology-oriented, environment. To this direction, Dr. Giorgos Papadakis and Michalis Saitakis, the biologists of our lab were very helpful to me regarding the biology-related procedures and instructions. Stalo Hadjiharalambous and Dr. Maria Chatzinikolaïdou have been very supportive to me with their positive attitude in the lab, and of course, Ariadne and Alexandros, my

other PhD co-adventurers. Finally, the renowned group-dinners and tavern gatherings with my colleagues will always be greatly remembered!

Part of my work, related to microfluidics fabrication, was done at the Institute of Microelectronics in N.C.S.R. “Demokritos”, in Athens, Greece. Dr. Aggeliki Tserepi from IMEL was co-supervisor in my work and I want to acknowledge her great assistance to me, her optimistic view of things, and her valuable expertise on the field, and also for the communication we had even after the end of my stay in Athens. I also need to thank Antonia Malainou and Marilena Vlahopoulou for their time and assistance during my training in the clean room facilities and the fabrication procedures, as well as all the members of the plasma group for their eagerness to help and advice me, and for the nice moments we spent in Athens, and Dr. Evangelos Goggolidis as the head of the group.

At the sponsoring part, I would like to acknowledge the Public Welfare Foundation “Propondis” for its financial support during the academic years 2006-2008, and the Public Benefit Foundation “Alexander S. Onassis” for its financial support during the academic year 2008-2009.

Finally, and I mention it at the end as an overall, I owe very big thanks to my parents: for being very good “roommates” (!) for their understanding, their support, advice and patience, for all the happy moments we had together due to various occasions and for our memorable excursions...mum and dad, I really thank you a lot for being there!

Ευχαριστίες

Η παρούσα εργασία πραγματοποιήθηκε στο εργαστήριο Τεχνολογίας Βιοαισθητήρων, Ινστιτούτο Μοριακής Βιολογίας & Βιοτεχνολογίας του Ιδρύματος Τεχνολογίας και Έρευνας (Ι.Μ.Β.Β. – Ι.Τ.Ε.), όπου εργάστηκα ως διδακτορικός φοιτητής του Τμήματος Επιστήμης & Τεχνολογίας Υλικών του Πανεπιστημίου Κρήτης. Όλα τα πειράματα και οι αναλύσεις που περιγράφονται στην παρούσα διατριβή πραγματοποιήθηκαν από εμένα (κατόπιν εκπαίδευσης σε κάποια μηχανήματα/εγκαταστάσεις, όπου ήταν αναγκαίο).

Κατά τη διάρκεια της σχεδόν τετραετούς εργασίας μου συνειδητοποίησα ότι το διδακτορικό δεν σημαίνει μόνο πραγματοποίηση πειραμάτων, ανάλυση δεδομένων, και συγγραφή αναφορών και δημοσιεύσεων. Αντιθέτως, είναι μια ολόκληρη περιπέτεια: γνωρίζεις ανθρώπους, διαμορφώνεις χαρακτήρα ιδιαίτερα σε δύσκολες στιγμές, μαθαίνεις να εργάζεσαι με υπομονή αλλά και επιμονή. Όλα αυτά είναι πέρα από τα πειράματα...είναι μαθήματα ζωής. Και αν ο χρόνος γύριζε πίσω, θα επέλεγα τα ίδια άτομα για να συνεργαστώ μαζί τους, τον ίδιο χώρο εργασίας και το ίδιο αντικείμενο και τελικά ναι...θα το έκανα ξανά!

Ο ενθουσιασμός των παραπάνω λόγων προέρχεται προφανώς από τη αλληλεπίδραση που είχα με κάποια πρόσωπα τα οποία γνώρισα και συνεργάστηκα και θέλω να τους εκφράσω τις ευχαριστίες μου. Πρώτα φυσικά, στην υπεύθυνη καθηγήτριά μου, κ. Ηλέκτρα Γκιζελή, Αναπληρώτρια Καθηγήτρια Τμήματος Βιολογίας, για την άψογη συνεργασία μας, για την εμπιστοσύνη και τη θετική της διάθεση απέναντι στη δουλειά μου και τις πρωτοβουλίες μου. Οι συμβουλές της ως ειδικού στο ερευνητικό πεδίο και η καθοδήγησή της ιδιαίτερα σε στιγμές αδιεξόδων ήταν πολύ σημαντικές για εμένα και την εξέλιξη της εργασίας μου. Εκτιμώ ιδιαίτερα την «ελευθερία» και τη στήριξη που είχα από μέρους της για υλοποίηση πρωτοβουλιών και ιδεών μου κατά τη διάρκεια της εργασίας μου, καθώς επίσης και τις δυνατότητες και ευκαιρίες που μου έδωσε για παρακολούθηση συνεδρίων, σεμιναρίων και εξω-εργαστηριακών δραστηριοτήτων. Για όλα αυτά την ευχαριστώ θερμά.

Σε αυτό τη σημείο θα ήθελα επίσης να ευχαριστήσω για τη συμβολή τους, μέσω των συζητήσεων και των συμβουλών τους, όλα τα μέλη της επιτροπής μου: τον κ. Γεώργιο Φυτά, Καθηγητή Τμήματος Επιστήμης & Τεχνολογίας Υλικών, την κ. Αγγελική Τσερέπη, Ερευνήτρια Β', Ε.Κ.Ε.Φ.Ε. «Δημόκριτος», την κ. Μαρία Βαμβακάκη, Επίκουρο Καθηγήτρια Τμήματος Επιστήμης & Τεχνολογίας Υλικών, την κ. Κέλλυ Βελώνια, Επίκουρο Καθηγήτρια Τμήματος Επιστήμης & Τεχνολογίας Υλικών, τον κ. Γεώργιο Κυριακίδη, Αναπληρωτή Καθηγητή Τμήματος Φυσικής, και την κ. Άννα Μητράκη, Αναπληρώτρια Καθηγήτρια Τμήματος Επιστήμης & Τεχνολογίας Υλικών.

Από το χώρο εργασίας μου και τους συνεργάτες μου, θα ήθελα πρώτα από όλους να εκφράσω τις ευχαριστίες μου στον Δρ. Αχιλλέα Τσορτό, ευχαριστίες οι οποίες είναι πέρα από απλά συναδελφικής φύσεως. Το ισχυρό υπόβαθρό του στη Βιοφυσική, η ανταλλαγή ιδεών που είχαμε, οι συμβουλές και η εμπειρία του και ο τρόπος σκέψης του ήταν πολύ σημαντικά για εμένα. Οι συζητήσεις μας πάνω σε πολλά θέματα, εντός και εκτός εργασίας, η στήριξή του και οι βραδινές μας κουβέντες κατά τη διάρκεια των χρονοβόρων πειραμάτων μου, είναι μόνο μερικοί

λόγοι για τους οποίους τον ευχαριστώ θερμά. Κατά τη διάρκεια της παραμονής μου στο εργαστήριο άνθρωποι ήρθαν, άνθρωποι έφυγαν. Ανάμεσα σε αυτούς θα ήθελα να ευχαριστήσω τον Δρ. Florian Bender, για τις εμπειρίες του που μοιράστηκε μαζί μου από την πορεία του ανά τον κόσμο, αλλά και για τις επιστημονικές του γνώσεις που μου μετέδωσε. Επίσης, την Δρ. Kathryn Melzak η οποία με βοήθησε στο να συνηθίσω σε ένα πρωτόγνωρο για μένα, περιβάλλον σχετιζόμενο με βιολογικές εφαρμογές. Προς αυτήν την κατεύθυνση, ο Δρ. Γιώργος Παπαδάκης και ο Μιχάλης Σαϊτάκης, οι βιολόγοι συνεργάτες μου, με βοήθησαν σημαντικά, και τους ευχαριστώ για αυτό. Επίσης τη Στάλο Χατζηχαραλάμπους και τη Δρ. Μαρία Χατζηνικολαΐδου για την ευχάριστη διάθεσή τους στο εργαστήριο και τη στήριξή τους και θετική τους διάθεση, καθώς και τους «συνοδοιπόρους» μου στο μακρύ δρόμο του διδακτορικού, την Αριάδνη Πριγκιπάκη και τον Αλέξανδρο Πανταζή. Τέλος, οι περιβόητες συναθροίσεις και γεύματα που κατά καιρούς είχαμε με τους συνεργάτες μου θα μείνουν αξέχαστα στη μνήμη μου!

Το μέρος της εργασίας μου σχετικά με την κατασκευή της μικρορευστομηχανικής κυψελίδας πραγματοποιήθηκε στο Ινστιτούτο Μικροηλεκτρονικής (IMEL) του Ε.Κ.Ε.Φ.Ε. «Δημόκριτος» στην Αθήνα. Η Δρ. Αγγελική Τσερέπη ήταν η επιβλέπουσα ερευνήτρια της εργασίας μου στις εγκαταστάσεις καθαρού χώρου του ινστιτούτου. Θα ήθελα να την ευχαριστήσω θερμά για την πολύτιμη βοήθειά της, την αισιοδοξία την οποία διέθετε και μου μετέδιδε καθώς και την βαθιά γνώση του αντικειμένου της, αλλά και για όλη τη μετέπειτα άποψη συνεργασία και αλληλεπίδραση που είχαμε. Επίσης θέλω να ευχαριστήσω την Αντωνία Μαλαίνου και τη Μαριλένα Βλαχοπούλου για το χρόνο και την ενέργεια που διέθεσαν για την εκπαίδευσή μου στις εγκαταστάσεις και τεχνικές καθαρού χώρου, καθώς επίσης και όλα τα μέλη της ομάδας πλάσματος του IMEL για την ευχάριστη διάθεσή τους, και την προθυμία τους να με συμβουλευσουν και να με βοηθήσουν σε οποιοδήποτε πρόβλημα, και για τις ευχάριστες στιγμές στην Αθήνα, και τέλος τον επικεφαλής της ομάδας, Δρ. Ευάγγελο Γογγολίδη.

Για την οικονομική μου στήριξη, θα ήθελα να ευχαριστήσω θερμά το Κοινωφελές Ίδρυμα «Προποντίς» για την οικονομική ενίσχυση που μου παρείχε κατά τα ακαδημαϊκά έτη 2006-2008, και το Κοινωφελές Ίδρυμα «Αλέξανδρος Σ. Ωνάσης» για την οικονομική στήριξη κατά το ακαδημαϊκό έτος 2008-2009.

Τέλος, και αναφέρομαι σε αυτούς στο τέλος λόγω της συνολικής τους συμβολής, οφείλω ένα μεγάλο ευχαριστώ στους γονείς μου: για την «συμβίωσή» (!) μας στην ίδια στέγη, για την κατανόησή τους, τη στήριξή τους ιδιαίτερα σε δύσκολες στιγμές, την υπομονή και τις συμβολές τους, και τις πολύ ευχάριστες στιγμές που είχαμε με αφορμή πολλά γεγονότα που ζήσαμε μαζί, και για τις πάμπολλες και χαλαρωτικές εκδρομές που διοργανώναμε κατά καιρούς...μαμά, μπαμπά, πραγματικά σας ευχαριστώ πολύ που ήσαστε και είσαστε εδώ!

Preface - novelties of the work

“seeing is believing but measuring is knowing”

Biosensors’ technology and development is inherently an interdisciplinary research and technology area. Thus, diverse fields converge in this thesis: **physics** to describe the interaction of acoustic waves with matter; **materials science** for the characterization of various classes of materials’ properties with the acoustic devices; **engineering** for the fabrication of the microfluidic module; **biology**, as the final application objective. The outline of the thesis follows the sequence of the milestones achieved during the experimental work; the chapters are divided according to the sequential steps followed towards the development of the suggested setup.

More specifically, **Chapter 1** is an introduction in micro Total Analysis Systems (μ TAS), describes the state-of-the-art in multi-sample biosensors and sets the objectives of the work. **Chapter 2** introduces the reader with the two basic components of the developed microsystem: the acoustic sensors, and the microfluidics, while **Chapter 3** describes the experimental infrastructure. **Chapter 4** summarizes the systematic study of a variety of device configurations under various kinds of sample loading, with the objective to select the optimum device configuration to continue with. **Chapter 5** focuses on the design considerations and fabrication procedure of the microfluidic module. **Chapters 6 and 7** report the evaluation tests performed in order to test the functionality, signal response, reproducibility and sensitivity of the microsystem under various sample conditions, proving the suitability and robustness of the developed microsystem as a multi-sensor. **Chapter 8** is the “highlight” of the work, as it involves the implementation of the microsystem for an application of clinical significance: the detection of multiple cardiac biomarkers. **Chapter 9** reports on some overall observations that were done throughout the experimental work using various biomolecules; the acoustic signal is qualitatively and quantitatively correlated to biomolecules properties such as molecular weight, qualitative viscoelastic properties, etc. Finally, **Chapter 10** summarizes the main conclusions of the thesis, in terms of fabrication issues, applications and interaction of acoustic waves with materials. In addition, further development issues of μ F-on-SAW are suggested, towards an even more robust and sensitive platform.

Since a PhD is intended, by itself, to be a unique and novel work to the research and technology community, the following lines briefly summarize the novelties of the present work, which lie on both, device and application level.

- Even though the acoustic devices and microfluidics are, by themselves, well-known fields that have been developed for years, their particular combination as applied in this work has never been tried before. For the first time, multi-sensing was achieved on a single acoustic biosensor via microfluidic-induced compartmentalization of the sensor surface. Thus, the very basis of the project lies on a novel concept.

- The molecules initially used to test the functionality of the system were standard, biotinylated proteins, so it could be argued that there was nothing novel in this. However, for the first time there was a correlation between the acoustic signal and the molecular weight of proteins.
- At the clinical application level, none of the examined biomarkers (except for CRP) has ever been detected with an acoustic device. Moreover, even though other cardiac marker combinations have been implemented with other detection methods, the particular combination used in this work has not been detected with any method and in any on-chip multi-analysis format.

*Konstantinos Mitsakakis, Physicist
M.Sc. in Nanosciences & Nanotechnologies*

Λέξεις κλειδιά:

- ακουστικός βιοαισθητήρας
- μικρορευστομηχανικές διατάξεις
- πολυαναλυτική ανίχνευση
- διαγνωστικά μικροσυστήματα
- καρδιακοί δείκτες
- ιξωδοελαστικές ιδιότητες

Keywords:

- acoustic biosensor
- microfluidics
- multi-analyte detection
- diagnostic microsystems
- cardiac markers
- viscoelastic properties

Table of contents

Chapter 1. Microtechnology for Life Sciences	1
1.1. μ TAS, lab-on-chip, bioMEMS, and microarrays.....	3
1.2. Investing on microsystems for diagnostics	6
1.3. Going “multi”	7
1.4. What is a biosensor?	8
1.5. Multi-sensing in established label-free biosensors	10
1.5.1. <i>Electrochemical biosensors</i>	10
1.5.2. <i>Surface Plasmon Resonance (optical) biosensors</i>	11
1.5.3. <i>Micromechanical biosensors</i>	12
1.5.4. <i>Piezoelectric biosensors</i>	14
1.6. Existing technology in acoustic multi-sensing platforms	16
1.7. Novelty of this work: concept and realization	18
Chapter 2. Description of the microsystem components: acoustic devices and microfluidics	24
2.1. Classification of acoustic waves and devices	26
2.1.1. <i>Bulk Acoustic Waves and devices - Quartz Crystal Microbalance</i>	26
2.1.2. <i>Rayleigh Waves and SAW devices</i>	27
2.1.3. <i>Shear-Horizontal Surface Acoustic Waves and devices</i>	28
2.1.4. <i>Love waves and devices</i>	29
2.1.5. <i>Building blocks of a typical Love wave device</i>	30
2.2. Operating principle	33
2.3. Introduction to microfluidics	33
2.4. Materials for microfluidics fabrication	34
2.4.1. <i>Silicon</i>	34
2.4.2. <i>Glass</i>	35
2.4.3. <i>Polymers</i>	35
2.5. Polymer microfabrication processes for microfluidics production.....	36
2.5.1. <i>Replica molding - Soft lithography</i>	36
2.5.2. <i>Injection molding</i>	36
2.5.3. <i>Hot embossing</i>	36
2.5.4. <i>Stereolithography</i>	37
2.5.5. <i>Plasma etching</i>	37
2.6. Examples of microfluidic devices.....	37
2.6.1. <i>On-chip chromatography</i>	37
2.6.2. <i>Micromosaic Immunoassays</i>	38
2.6.3. <i>Microfluidics on a CD</i>	39
Chapter 3. Experimental instrumentation	43
3.1. Network Analyzer	45
3.2. Surface Plasmon Resonance	48
3.3. Pumping systems	49
3.4. Spin coating	50
3.5. Gold sputtering and plasma etching.....	51
3.6. Biomolecules used in the work.....	52
Chapter 4. Selection of the optimum device configuration for μF-on-SAW	53
4.1. Introduction.....	55
4.2. Analysis of SH-SAW perturbations.....	56

4.2.1. Case 1: Mass loading.....	57
4.2.2. Case 2: Viscous loading (Newtonian liquid)	58
4.2.3. Case 3: Viscous loading (Maxwell liquid).....	59
4.2.4. Case 4: Viscoelastic layers in air and liquid	60
4.3. Experimental procedure	63
4.3.1. SAW devices used.....	63
4.3.2. Materials for sensor characterization	63
4.4. Results and Discussion	64
4.4.1. Mass loading.....	64
4.4.2. Viscous loading – Low viscosity regime	66
4.4.3. High viscosity regime - Maxwell behavior	68
4.4.4. Protein adsorption	72
4.4.5. Viscoelastic properties of waveguide films	74
4.5. Conclusions.....	76
Chapter 5. Design and fabrication of the microfluidic module	79
5.1. Introduction.....	81
5.2. Design considerations	81
5.2.1. Material selection	81
5.2.2. Geometrical features.....	82
5.3. Fabrication process: Soft Lithography.....	85
5.3.1. Mask design and fabrication.....	85
5.3.2. SU8 mold fabrication.....	86
5.3.3. PDMS processing and replica molding	88
5.4. Post fabrication processing - fluidic interconnects	89
5.5. Verification of suitability	91
5.5.1. Hermeticity of the microfluidic module	91
5.5.2. Flow regime; Reynolds number	91
5.6. Conclusions.....	92
Chapter 6. Evaluation of the μF-on-SAW performance	94
6.1. Introduction.....	96
6.2. Evaluation of μ F-on-SAW upon viscous loading.....	97
6.2.1. Sequence of sample loading.....	97
6.2.2. Signal response and sensitivity of μ F-on-SAW; comparison with the standard configuration.....	98
6.3. Evaluation of μ F-on-SAW upon protein adsorption and specific protein binding	102
6.3.1. Necessity to use biomolecules for evaluation	102
6.3.2. Reproducibility of μ F-on-SAW upon biomolecular interactions	103
6.3.3. Signal-to-surface proportionality	105
6.4. Conclusions.....	106
Chapter 7. Multi-sample detection using μF-on-SAW	108
7.1. Introduction - biomolecules used for multi-analysis	110
7.2. Multiple detection with μ F-on-SAW	111
7.3. Full exploitation of 4 \times 2 sub-areas: multiplexing with μ F-on-SAW.....	113
7.4. Binding affinities and kinetics analysis	116
7.4.1. Theory on equilibrium analysis	116
7.4.2. Theory on kinetic analysis	118
7.4.3. Experimental results on equilibrium analysis.....	119
7.4.4. Experimental results on kinetic analysis.....	121
7.4.5. Comments on the results	124

7.5. Conclusions.....	125
Chapter 8. Clinical application: cardiac markers	127
8.1. Introduction - what are biomarkers?	129
8.2. Why cardiac biomarkers with μ F-on-SAW	130
8.3. Cardiac markers examined in this work.....	130
8.3.1. <i>Creatine Kinase - MB (CK-MB)</i>	131
8.3.2. <i>Cardiac Reactive Protein (CRP)</i>	132
8.3.3. <i>D-dimer</i>	132
8.3.4. <i>Pregnancy-Associated Plasma Protein-A (PAPP-A)</i>	133
8.4. Immunoassays.....	134
8.4.1. <i>Antibodies</i>	134
8.4.2. <i>Polyclonal and monoclonal antibodies</i>	135
8.5. Experimental procedure	135
8.6. Binding and kinetic analysis	139
8.7. Relation between detected values and clinical values	141
8.8. Biomarker detection from a multi-marker mixture.....	143
8.9. Conclusions.....	146
Chapter 9. Correlation of acoustic signal to biomolecules' properties	149
9.1. Introduction.....	151
9.2. SPR and SAW for the quantification of the bound mass.....	151
9.3. Correlation of acoustic signal to biomolecules' molecular weight.....	152
9.4. Acoustic signal and viscoelastic nature of probed samples	155
9.5. Viscoelastic properties of protein films	156
9.6. Conclusions.....	160
Chapter 10. Epilogue	162
10.1. Conclusions.....	164
10.2. Suggestions for future work.....	167



Chapter 1. Microtechnology for Life Sciences



In-Check™ platform for rapid bacterial diagnosis
<http://micros.st.com/stonline/products/promlit/pdf/flcheckin1205.pdf>





Chapter 1. Microtechnology for Life Sciences

1.1. μ TAS, lab-on-chip, bioMEMS, and microarrays

With rapid developments and growing interest in medicine, drug discovery, biotechnology and environmental monitoring, we have become more and more dependent on (bio)chemical analysis. Traditionally, this task has been performed in central laboratories because it requires skilled personnel and specialized equipment. However, there are many cases like pregnancy tests, blood glucose concentration tests for diabetes patients, analysis of soil and water samples, etc, where the (bio)chemical analysis must be brought closer to the “customer”, whether it is a patient, a physician, or any “simple” end user. Such test kits *should be* (and nowadays, *can be*) used by persons with no special training or expertise in chemistry or biology. This trend of decentralization of (bio)chemical analysis is expected to continue and grow. For this to happen, though, the analytical equipment must become smaller, portable, easier to operate, faster in response and at the same time, robust and reliable; the analysis results must be processed and presented in a way that would be easy for the user to interpret [1.1.].

At this point, a recently emerged notion appeared to bridge the gap: in 1990s the concept of Micro Total Analysis Systems (μ TAS) was introduced [1.2.]. The idea of μ TAS builds on performing all the necessary steps that are required for a (bio)chemical analysis on a miniaturized format and thereby offers portability (Fig.1.1.). Automation of the entire analysis process and data processing is also part of the μ TAS concept. In an extreme representation, μ TAS can be compared to a black box where the user needs only to apply the sample and push a start button and simply retrieve the results. At the heart of each μ TAS is a chip in which fractions of microliters of samples and reagents are moved around with very high accuracy. Especially when the samples and reagents are in short supply or very expensive, μ TAS offers a significant decrease in costs by drastically reducing the volumes needed to perform a chemical analysis. The batch fabrication of μ TAS allows the repetition of the same procedure many times, allowing the processing of many samples in parallel.

It is often needed to know how the concentration of an analyte changes in time, i.e., online monitoring. With conventional methods this is very difficult, but the use of μ TAS brings the (bio)chemical analysis close to the place where it needs to be performed since sample handling, analysis, and data processing are all integrated in μ TAS. Thus, the advantages of μ TAS can be summarized in the following: portability, reliability, reduction of sample and reagent consumption, automation of analysis, and online monitoring.

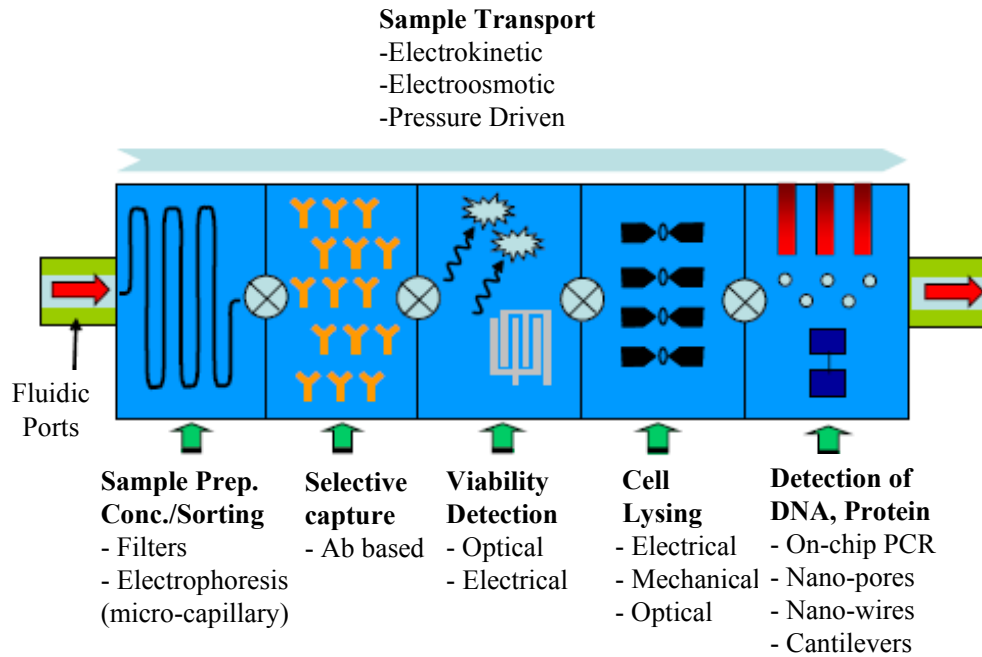


Fig.1.1. Typical structure of a μ TAS integrated platform. Various modules can be used in appropriate combination to detect the desired entity [1.3.].

Along with the development of μ TAS, new terms emerged such as “lab-on-a-chip”, “bioMEMS”, “biochips”, “microarrays”, etc. Nowadays these words are more or less interchangeable, and it is up to the author which one to use. However, there could be a general classification, depending on the complexity of functions realized on those microsystems. On one hand are the μ TAS, lab-on-chips, bioMEMS, and on the other hand are the microarrays. Between the two big categories the following major differences can be identified:

- (i) The number of analytes: in microarrays it is typical to probe some hundreds (even thousands) of samples. They are injected via robotic systems, and usually (or, mostly exclusively) the detection method is label-based, e.g. fluorescence; a pattern of varying intensities of spots is created, which is then “read” by proper scanners and analyzed with computer software. On the contrary, in μ TAS only a few analytes are typically probed.
- (ii) Due to this large number of analytes, the detection method for microarrays is usually label-based; for this reason, the primary objective in detection in a microarray is the answer to a “yes or no” question. In contrast, μ TAS are also focused on additional questions such as “how much” and “how fast”, incorporating kinetics and affinity analysis in their repertoire.
- (iii) Microarrays are mostly passive platforms, which may not actually include other components than the functionalized surface and the spotted receptors, which are solely intended for detection. On the other hand, μ TAS are more complex systems that incorporate a number of microfluidic components such as valves, micropumps, chambers, and microchannels serving particular functions such as fluid propulsion, separation, mixing, etc; even advanced functions can be integrated on-chip, such as electrophoresis, PCR-on-chip,



sample pre-concentration, in addition to biosensing and detection. Thus, even though such microsystems detect less analytes, they exhibit higher complexity and multiplexity of functions.

Within this context, the microsystem described in the current work belongs to the μ TAS classification, since, on one hand, it does not target large number of detected samples, while on the other hand it is a more complex system than just a microarray as it involves a microfluidic module, injection system, a sensor chip, etc.

Such microsystems can, roughly, be divided into two categories according to the users they target: (i) bulky pieces of equipment, having a microsystem as a core, intended for hospitals, diagnostic centers, etc, and (ii) small, hand-held devices, intended for personalized medicine and point-of-care diagnostics. Depending on which category they belong to, their design and fabrication requires different approach. However, in all cases there are some common features: the fluidic cartridge, the fluid handling for liquid dispensing, the biological assay (DNA- or protein-oriented, or both), the microfluidics for fluid processing, and the biosensor. Especially about the latter, no matter what kind of biosensor it is, it always exists at the heart of such a microsystem.

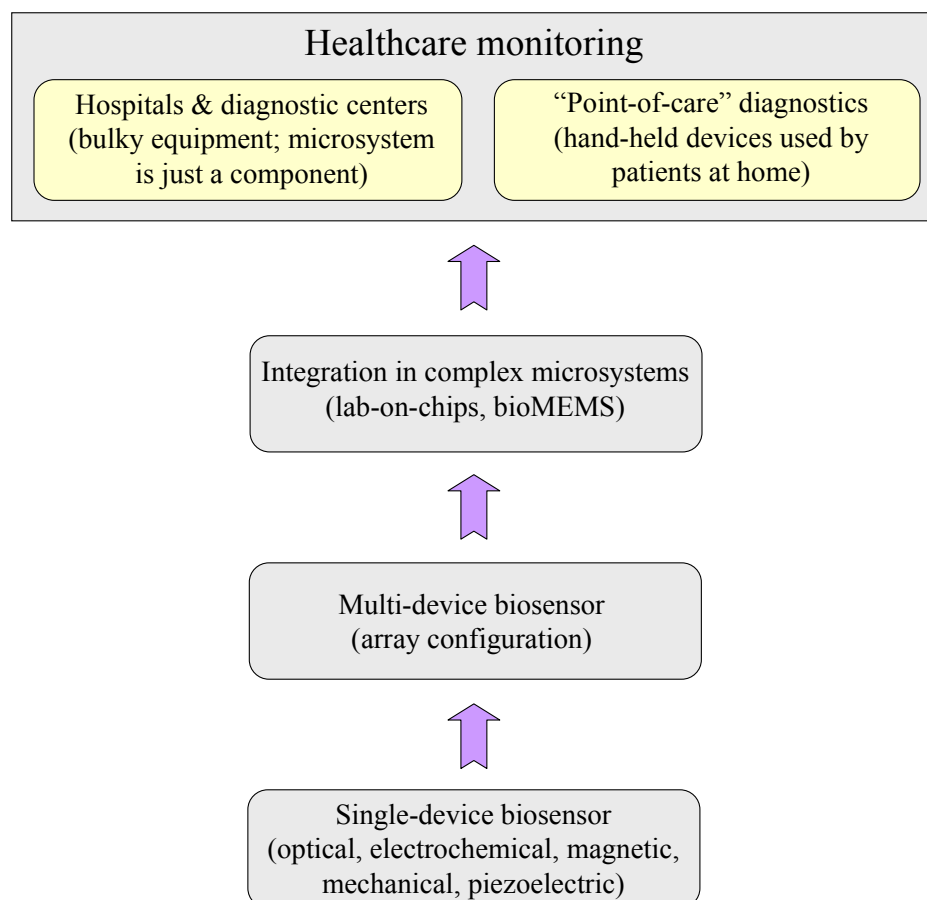


Fig.1.2. Flow chart of development steps towards healthcare monitoring microsystems.



1.2. Investing on microsystems for diagnostics

Being able to perform multi-functional on-chip integrated analysis, μ TAS (or biochips, bioMEMS, etc) are increasingly attracted by clinical diagnostics applications, or, as termed, “In Vitro Diagnostics” (IVD). In fact, the significance of μ TAS is evident via the attention that is given to them by corporate companies, and European Union funding for IVD purposes. Indicatively, only some of the recently initiated European projects under FP7 funding are listed below; the competition for funding (hundreds of relevant projects submitted in each FP7 call) proves the increasing interest as well as the intensive and multi-level research and technology advances in this field. Some of the European Union funded projects under way for the development of point-of-care diagnostics are listed below:

- **“BIOGNOSIS”**: “Integrated biosensor system for label free in-vitro DNA and protein diagnostics in healthcare applications”; targeting the development of an innovative integrated DNA and protein detection system for applications in medical diagnostics [1.4].
- **“POCEMON”**: “Point-of-care monitoring and diagnostics for autoimmune diseases”; aiming at the development of a mobile monitoring and diagnostic platform for detecting a large number of autoimmune diseases [1.5].
- **“NEUROTAS”**: “Microfluidic total analysis system for the early diagnosis of neurodegenerative disorders”; through this project, the aim is to develop a microsystem to detect neurodegenerative diseases, e.g. Alzheimer’s [1.6].
- **“CD MEDICS”**: “Coeliac disease management monitoring and diagnosis using biosensors and an integrated chip system”; the objective is to obtain an instrument that will be a low-cost, non-invasive intelligent diagnosis system for celiac disease, diagnosis and management [1.7].
- **“PYTHIA”**: “Monolithically integrated interferometric biochips for label-free early detection of human diseases”; the project aims at developing a novel integrated optoelectronic biochip for the early diagnosis of diseases [1.8].

In addition to that, many Small and Medium Enterprises (SMEs) have undertaken the development of healthcare microsystems. But also big corporate companies, traditional players in the semiconductor industry, such as Philips, [1.9.] Siemens [1.10.], Sony [1.11.], IBM [1.12.], etc, with huge markets in microelectronics, displays, electronic equipment etc, have foreseen the great importance of microsystems in life sciences and have established divisions specifically oriented towards this goal: the development of microsystems for health monitoring, disease diagnostics and drug development. It is worth mentioning that the global In Vitro Diagnostics market was B€ 22 for 2001, with the main focus areas reported indicatively in the following chart.

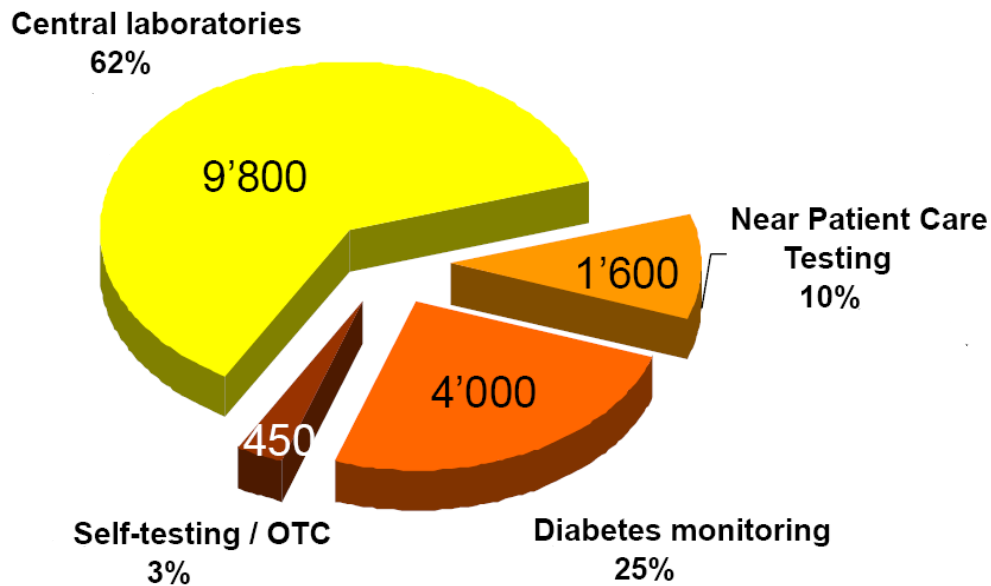


Fig.1.3. Market segments of In Vitro Diagnostics (in M€).

1.3. Going “multi”

Apart from their competence to intergrate on chip a variety of functions and processes, as mentioned before, μ TAS need to increase their analytical capacity. Especially in diagnostics and biomedical analysis, there is a need for tools that are able to integrate multimodal information on multiple biomarkers, rather than independent analysis on single biomarkers, as currently practiced in diagnosis. Thus, one could say that the technology around biosensors goes “multi”.

Multi-sample detection is currently the focus of all the main biosensor developments (sec.1.5.). Being “multi” is not just a matter of multiplicity, but also multiplexity that is achieved through such systems. In other words, these systems, with the proper computer-aided data processing, are capable of not only detecting N independent processes, but N interconnected processes which are all part of a whole. For example, biological pathways generally involve several tens of genes; so it is not sufficient to screen for mutations in one single gene, but in many, in order to understand if, and how a pathway is affected. Similarly for cancer diagnosis, one needs to cross-check a number of involved biomarkers in order to reach a conclusion about a possible tumor development.

Thus, having established some biosensing methods already, the biosensing community proceeds rapidly into increasing the level of complexity and develop platforms capable of detecting a large number of samples (irrespective of the manner, whether it is simultaneous or sequential) with ultimate target their incorporation in diagnosis-oriented μ TAS.

Two typical multi-sensing configurations appear below. In Fig.1.4(a) there are 5 immobilized receptors (the same 5 in each of the 4 chips) and 4 different samples are injected on them, realizing in this way a total of 20 screened interactions, optimizing the high sample throughput in this way. In Fig.1.4(b) there are 20 immobilized receptors, but now only one sample is injected over them; again, 20



interactions are probed, but the maximum received information about the injected sample is achieved.

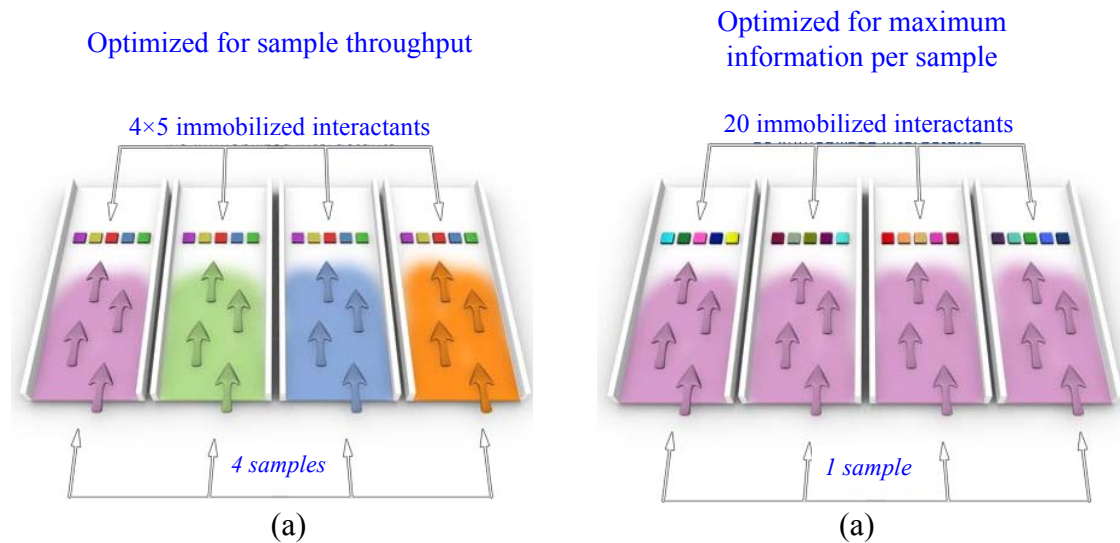


Fig.1.4. Two configurations for multi-sample analysis: (a) optimized for high sample throughput, (b) optimized for maximum information per sample.

1.4. What is a biosensor?

Having spoken about multi-sensing as a general notion, it is necessary to define the basic element, the biosensor itself. “A biosensor is a self-contained integrated device, which is capable of providing specific quantitative or semi-quantitative analytical information using a biological recognition element (biochemical receptor) which is retained in direct spatial contact with a transduction element. The sensing is based on the alteration of some physical/chemical parameter of the sensor” [1.13].

The basic components of a biosensor are (Fig.1.5.):

- The **transducer**: It is based on some labeling (e.g. fluorescent, radio, magnetic nanoparticles, etc.) or on a label-free, physical principle, which changes when a process takes place at its surface, and is the basis of sensing.
- The **biorecognition layer** is immobilized on the sensor surface via some physical or chemical treatment or surface modification, and is responsible for capturing the target analyte.
- The **analyte** is the biological species to be detected, located within the solution in contact with the biosensor surface. It could be found alone or in a mixture in solution.
- The **electronics**, which transform the change in the physical properties of the transducer into a measurable electric signal.

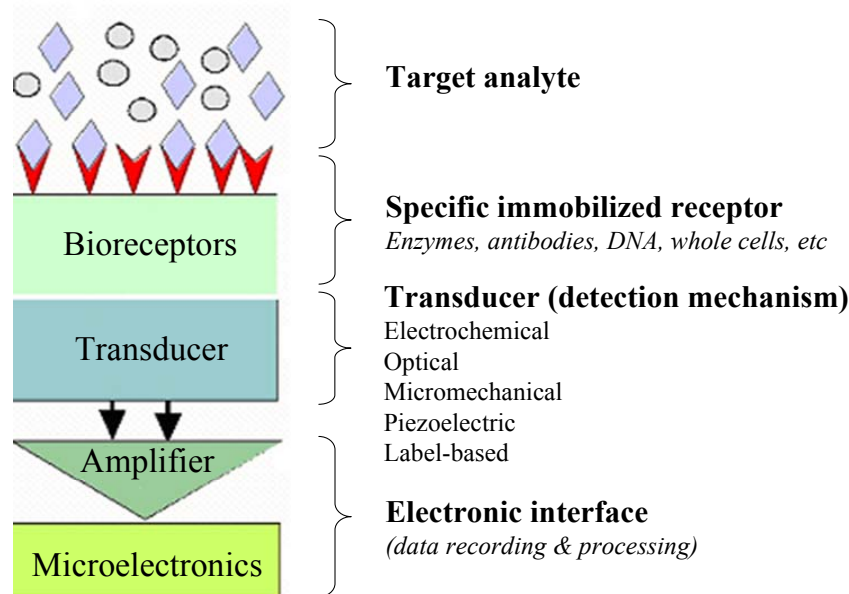


Fig.1.5. Typical components of a biosensor.

Three major characteristics of a biosensor are its *sensitivity*, *selectivity*, and *limit of detection*.

The *sensitivity* of a biosensor depends both on the transducer and the biological element of the sensor. The former determines how many molecules must exist on the surface so that adequate signal is detectable, whereas the latter defines how strong is the relationship between the immobilized receptor molecule and the analyte in solution, thus, how many molecules will bind on the receptor molecules on the surface.

Selectivity is a property that a biosensor must have in high value, especially when applied on medical diagnostics and involves body fluids. What it suggests is essentially that, if a biosensor is exposed to a sample containing a mixture of different species, its signal should depend only on the concentration of *one* analyte, with little or no interference from other species present in the sample. Under this condition it is characterized as highly selective. It is more of a qualitative rather than quantitative property of a transducer and it strongly depends on the sample(s) probed and their interactions with the rest of species present in solutions (i.e., the non-specific interactions). Fluorescently-labeled sensors are inherently more selective than the label-free ones: even if non-labeled molecules bind on the surface, the detector will recognize only the labeled bound ones. That is why there is a lot of work on the development of proper biorecognition layers used with label-free sensors, in order to suppress the non-specific binding.

The *limit of detection (LOD)* refers to the minimum measurable surface density that can be defined. This is done by defining the noise of the sensor signal (blank signal, for example with running buffer); then the lowest signal that can be reliably distinguished from the blank signal is three times the standard deviation of the noise and corresponds to the minimum surface density.



1.5. Multi-sensing in established label-free biosensors

There are several classifications of biosensors which depend on various parameters. A common one for label-free biosensors is based on the physical principle they utilize for the detection, and suggests their classification into electrochemical, optical, micromechanical, and piezoelectric biosensors.

1.5.1. Electrochemical biosensors

Electrochemical biosensors have been studied for a long time and were the first scientifically proposed as well as successfully commercialized biosensors, based on electrochemical principles. Currently, transducers based on semiconductors and screen printed electrodes represent a typical platform for the construction of biosensors. Enzymes or enzyme labeled antibodies are the most common biorecognition components of biosensors. The category of electrochemical biosensors is, by itself, a huge category that can be roughly divided into three large sub-groups according to the operating principle governing the measurement method: (i) amperometric, which involves the electric current associated with the electrons involved in redox processes, (ii) potentiometric, which measures a change in potential at electrodes due to ions or chemical reactions, and (iii) impedimetric transducers, which measure impedance changes associated with changes in the overall ionic medium between the two electrodes. Conductance techniques are attractive due to their simplicity and ease of use since no specialized reference electrode is needed, and have been used to detect a wide variety of entities. Electrical measurements of DNA hybridization using conductance techniques have been demonstrated, where the binding of oligonucleotides functionalized with gold nanoparticles leads to conductivity changes associated with binding events [1.14].

A prerequisite for an electrochemical biosensor to operate is that there should be a suitable enzyme in the biorecognition element that will provide electroactive substances for detection. That makes this group of techniques a little less versatile than the rest of label-free methods, in terms of range of analytes that can be detected. On the other hand, a major advantage of these sensors is their ease of integration with CMOS technology and microelectronics, since most of the materials for electrochemical sensing are CMOS compatible, which brings them closer to commercialization and array/multi-sensor format. In fact, the most common, well-known and first commercially available biosensor, the glucose sensor for the measurement of sugar levels in diabetes patients, has been of electrochemical (amperometric) nature. It has been developed so much that it has already reached the form of a hand-held device for point-of-care diagnostics (Fig.1.6(a)) [1.15].



Fig.1.6. (a) Medisense home blood glucose meters; the original device was invented, designed & developed at Cranfield with Oxford University and launched in 1987, (b) array chip of eSensor[®] for cystic fibrosis detection.

An example of implementation of an electrochemical biosensor array is Osmetech's eSensor[®], an electrochemical detection platform based on a DNA hybridization array on a cost-effective printed circuit board substrate [1.16.]. eSensor[®] has been cleared by FDA for Cystic Fibrosis Carrier Detection (24 cystic fibrosis mutations from DNA isolated from human whole blood). Furthermore, the eSensor[®] platform is readily adaptable to on-chip sample-to-answer genetic analysis using microfluidics technology. Cartridges like the ones in Fig.1.6(b) are inserted into the eSensor[®] 4800 Instrument where the single-stranded targets hybridize to the complementary sequences of the capture probes and signal probes. Detection of the target/probe complexes is achieved using alternating current voltammetry that generates specific electrical signals from the hybridized signal probes [1.17.].

1.5.2. Surface Plasmon Resonance (optical) biosensors

The Surface Plasmon Resonance (SPR) sensor is one of the main representatives of the optical sensors category used for biological detection. SPR is a label-free detection method, which utilizes the interaction of incident light with matter in order to detect deposited (or dissociated) mass. A monochromatic light beam is incident on a gold/glass interface and, at total internal reflection conditions the angle of minimum reflectivity is monitored. The adsorbed biological species change the refractive index of the interface (and thus, the reflectivity minimum) in a way proportional to the surface concentration. Thus, information about the average bound mass and, furthermore, the layer thickness can be extracted over the illuminated area (Fig.1.7.); with real-time monitoring, kinetic and affinity constants can be determined as well.

SPR has been demonstrated in the past decade to be an exceedingly powerful and quantitative probe of interactions including protein-ligand, protein-protein, protein-DNA and protein-membrane binding for applications in medical diagnostics [1.18., 1.19.]. There are several commercially available systems, with Biacore [1.20.] being the most widespread and known one.

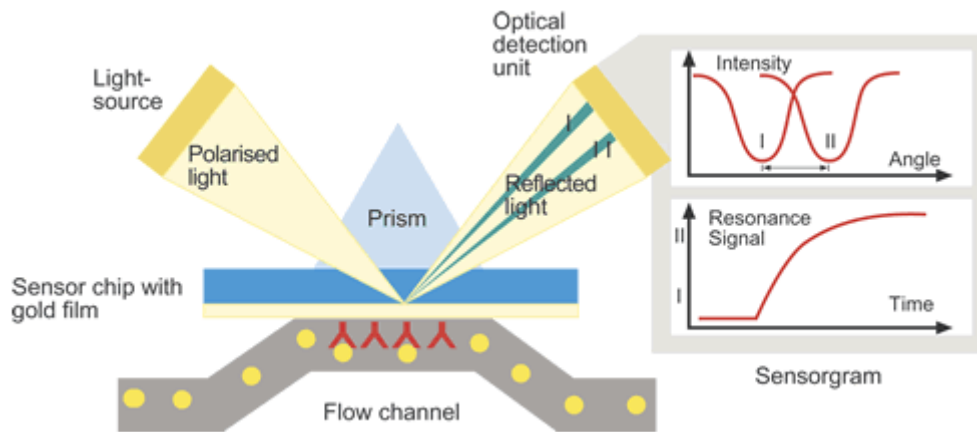


Fig.1.7. Typical configuration of an SPR setup. Receptors are bound on one side of the gold film and light is reflected on the other side; the reflected intensity minimum is monitored.

A variation of SPR operation involves the *imaging* of the gold/glass surface using a lens and a CCD camera to analyze the reflected intensity at each point of the surface [1.21.]. This, then, gives the mass bound to the transducer surface for each pixel analyzed. In an SPR multi-channel transducer a measurement channel is defined solely by the area on which a certain receptor molecule has been deposited, so there is no need for additional gratings or other optical structures [1.22.]. This feature is already exploited in the Biacore instrument, where four measurement channels are available on each gold-coated sensing chip with possibility of independent biomolecule immobilization in each microchannel [1.20., 1.23.]; with specific microfluidic technology the capacity has reached up to 400 spots per sensor surface (Biacore Flexchip model, Fig.1.8.). Further development should allow great improvements in terms of both the number and size of the measurement channels available.

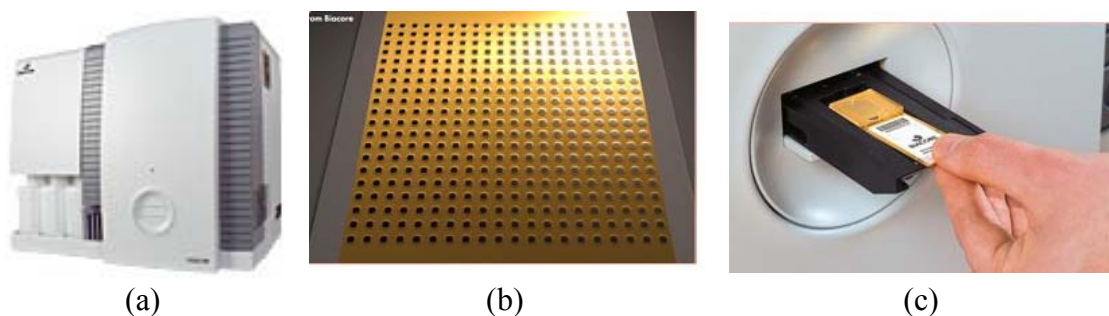


Fig.1.8. (a) Biacore Flexchip equipment, (b) sensor surface with up to 400 interaction spots, (c) insertion of the biochip into Flexchip after flow cell assembly.

1.5.3. Micromechanical biosensors

Cantilevers as a concept were first used at the heart of Atomic Force Microscope [1.24.] for surface topography measurements and later, for other surface properties such as electric, magnetic, nanomechanical, etc. During the evolution of cantilevers as sensors, they were initially tried as physical sensors for measuring



stress, temperature and other properties. Being successful, they were quickly suggested for biosensing as well [1.25.].

In fact there are two “modes” of cantilever operation as biosensor, namely the static (Fig.1.9(a)) and the resonant (Fig.1.9(b)) mode. In the former case, the cantilever is deflected due to surface stresses that are created due to the adsorption and/or binding of biological species on one of its free surfaces and the deflection is then correlated to the deposited mass [1.26.]. In the case of a resonating cantilever, it is the resonance frequency that changes when a process takes place on the cantilever surface, and the shift is, again, correlated to the properties of the biological layer, but this kind of cantilever biosensors suffer from severe viscous damping. Materials used for cantilevers range from silicon and silicon nitride to SU8 according to the desired application and surface functionalization demands.

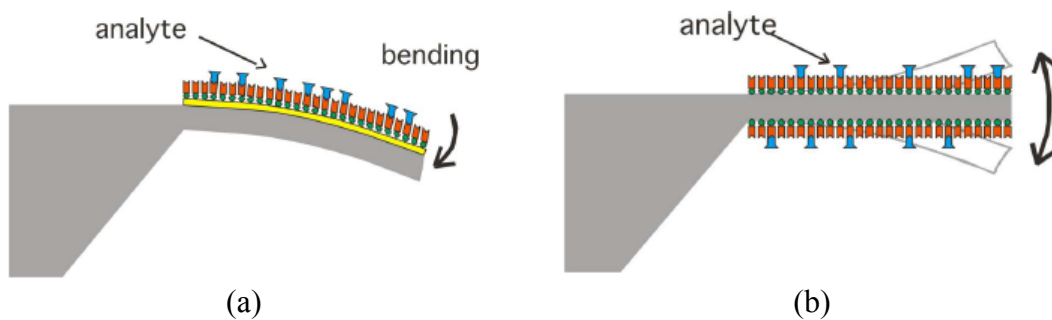


Fig.1.9. (a) Bending of a static microcantilever due to analyte binding, (b) microcantilever operating at resonance mode [1.27.].

Multiplicity is inherent in cantilever-based biosensors, since their fabrication can easily scale up from a single one to an array (Fig.1.10.). The fabrication procedures are standardized, performed by common lithographic methods with few or more lithographic steps, depending on the complexity; they can be produced in batch, since each cantilever of the array has typical dimensions of a few tens to hundreds of microns. Therefore, the fabrication would not be an issue and, indeed, there is an increasing number of reports on establishing a satisfactory cantilever-based multi-sensor [1.28., 1.29.].

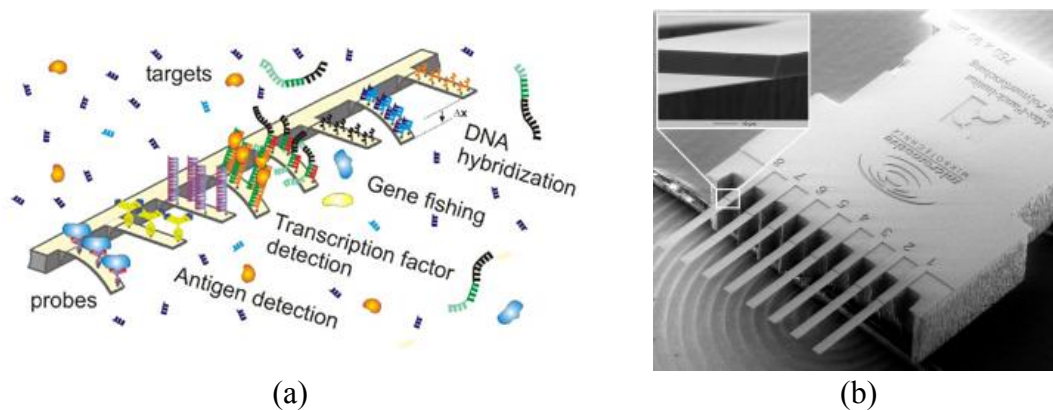


Fig.1.10. (a) Multifunctional cantilever arrays will enable parallel in situ detection of a multitude of genomic and proteomic markers [1.30.], (b) SEM-image of a cantilever chip [1.31.].



However, among the above reported cases, the number of detected samples is rarely (in fact, almost never) as high as the number of cantilevers, which means that the multiplicity that the system, in principle, offers has not been reached yet. The major challenge that these platforms must efficiently overcome is the frequent irreproducibility among the cantilevers' response. It is often needed to use a large number of cantilevers of the array for reference purposes. Thus, the “*different-sample-per-many-cantilevers*” configuration is avoided, and the “*same-sample-per-many-cantilevers*” is used, instead, reducing the number of available cantilevers for multi-sensing. Another challenge is that, according to the standard operation of an AFM, having an array of cantilevers needs an array of optical sources as well. Although this is achievable for a few cantilevers (though complicated) it becomes too demanding for the construction of an array with more than about a dozen of cantilevers.

So, it is evident that, even though this technology has the advantage of low fabrication cost and complexity, it is not in better condition than others as it still has several problems to cope with.

1.5.4. Piezoelectric biosensors

Piezoelectricity was first described in 1880 by Pierre and Jacques Curie and the term describes the generation of electric charges on opposing surfaces of a solid material upon deformation (torsion, pressure, bending, etc.) along an appropriate direction. Conversely, mechanical deformation of the material induced by an external electric field comprises the converse piezoelectric effect. These effects are the fundamental basis of the piezoelectric sensor operating principle, as an oscillating potential difference induces the piezoelectric crystal to oscillate mechanically around its steady-state position. These sensors are also met as “acoustic”. The word has nothing to do with the hearing frequencies (which are of the order of only a few hundreds of Hz). Instead, “acoustic” refers to the *sound* propagation through a medium. Some examples of propagation of sound waves in media appear in Fig.1.11., in a large frequency range.

Acoustic devices have been extensively used in the past for plenty of purposes, such as “electronic noses” and gas sensors for toxic and warfare gas detection [1.32.], materials characterization microsystems for measuring the thickness and viscoelastic properties of organic and inorganic films [1.33.], process monitoring devices for real-time monitoring of physical and/or chemical processes such as adsorption and deposition of thin films [1.34.], measurement devices of physical properties such as pressure [1.35.], temperature, viscosity [1.36.], in food quality control [1.37., 1.38.], etc. Eventually, acoustic devices expanded in the biosensing field as well, after fulfilling the conditions for successful operation in liquid environment. In addition, it is worth noting that a big sub-group of piezoelectric devices are already used in telecommunications as components of mobile phones [1.39.] (in the GHz frequency region), which offers the advantage of low-cost and batch fabrication of such devices.

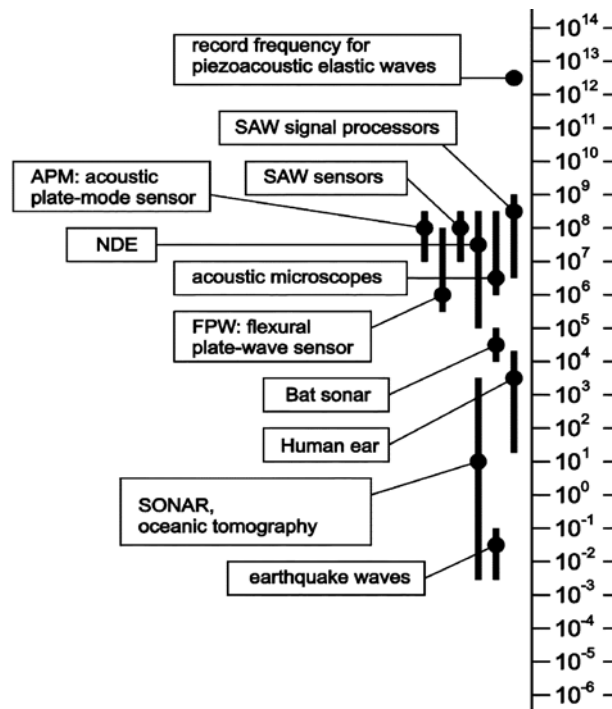


Fig.1.11. Sound wave propagation in various application fields; the frequency is expressed in Hz.

Some advantages of piezoelectric devices as biosensors are the following:

- The sensing principle is of label-free nature, since their function is based on the change of physical parameters, rather than the intensity of a label signal. This is greatly advantageous because labeling in sensing, such as fluorescent- or radio-based, can cause functional problems to the probed molecule/interaction, as it could tamper with the functionality of the molecule(s) involved.
- The processes taking place on the sensor surface can be monitored in real-time, allowing kinetics analysis and determination of association and dissociation constants.
- They are easy to fabricate and use, and can be produced either in miniaturized or larger formats and their sensitivity scales up with operating frequency.
- Acoustic sensors can probe simultaneously two independent parameters of the propagating acoustic wave, corresponding to its energy loss (absorption term) and velocity change (propagation term), which makes them more than just a microbalance; with proper processing of the measured quantities it is possible to extract information about the viscoelastic properties of materials, such as the complex shear modulus, rendering the acoustic sensors a powerful tool for biophysical studies.

Acoustic sensor devices are categorized into two groups, according to their geometry and operation modes: the Quartz Crystal Microbalance (QCM) and the Surface Acoustic Wave (SAW) devices (Fig.1.12.). Since these devices are used throughout this work (the SAW devices, in particular) they will be described in detail



in sec.2. The following section reports the status that SAW-based *multi*-sensors have reached up to date in both gas and liquid sensing. Within this context, the concept of the proposed setup will be discussed: its place in multi-sensing, what gaps it bridges and what novelties it offers.

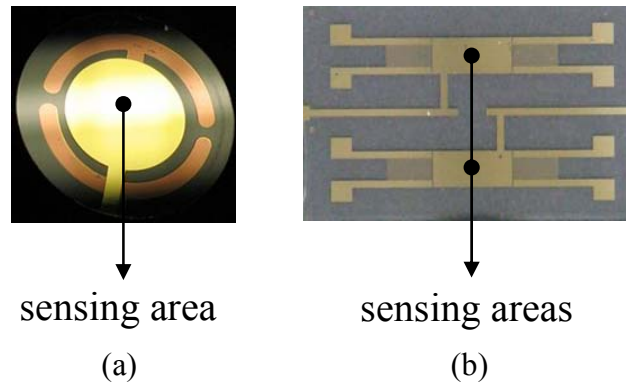


Fig.1.12. Images of (a) a QCM sensor chip, and (b) a SAW dual-sensor chip.

1.6. Existing technology in acoustic multi-sensing platforms

All the well established label-free technologies mentioned in the previous sections try to “go multi” and they are almost “tied” in their race towards developing such systems, because all of them have problems to solve depending on their operating principle. That applies to the piezoelectric sensors as well. Initially, the idea to apply multiplicity in sensing began with the implementation of SAW device arrays for gas sensing (and is still, more or less, confined to that) [1.40. - 1.43.]. Despite their success in gas sensing applications, the challenge remains for SAW-based multi-analysis in biological fields due to the complexity imposed by the liquid nature of the samples.

In Sandia National Laboratories a SAW-based array for gas sensing has been developed, the μ ChemLab [1.44.]. It is a chemical analysis system that combines sample handling (a preconcentrator unit), separation (a miniaturized gas chromatography unit), and detection (the SAW array), i.e., a typical μ TAS (Fig.1.13.).

The Rapp group has developed a gas sensor array (Fig.1.14.) and is recently working on transferring their technology into a biosensor array [1.45.], utilizing eight SAW resonators, operating at 433 MHz; the sensors are intended to be disposable and removable from a polymer housing, which integrates fluidics and electronics. In the meantime, an array-based apparatus was developed in CAESAR research institute, utilizing an array of five SAW devices, operating at 155 MHz (Fig.1.15.) with proper microfluidic housing [1.46.] for protein [1.47.] and DNA [1.48.] applications, currently being commercially launched by Biosensor GmbH [1.49.]. Other groups have used SAW arrays for food quality control purposes [1.50.]. Finally, in QCM-based systems, Qsense has developed a 4-sensor array, as an evolution of their standard equipment.

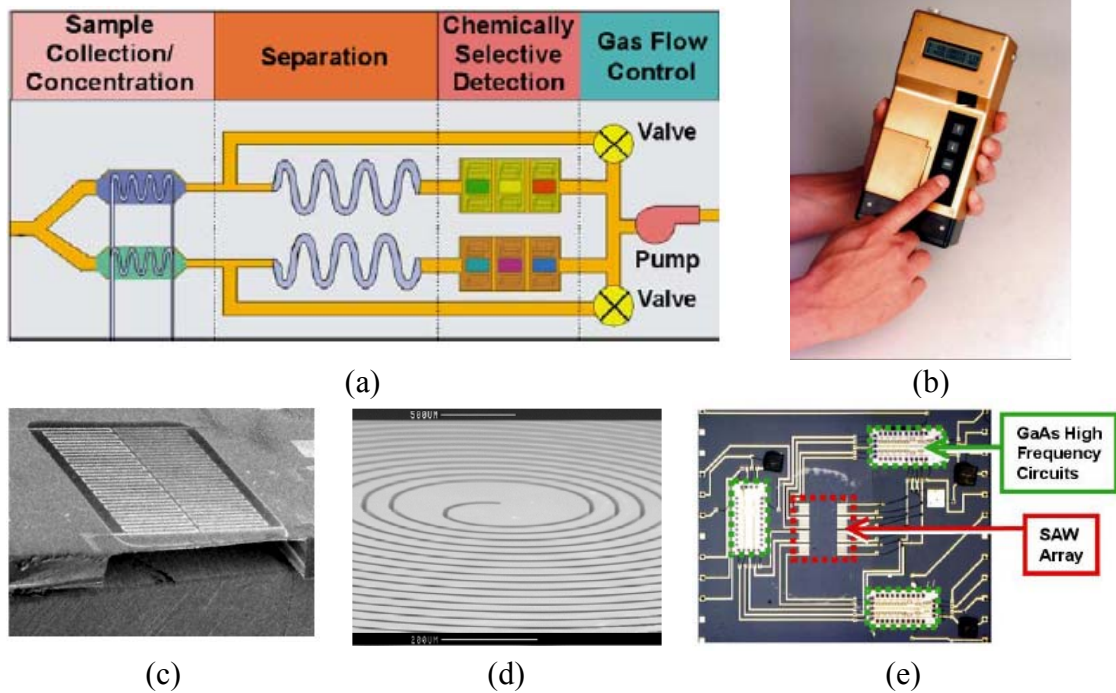


Fig.1.13. (a) Schematic of the $\mu\text{ChemLab}^{\text{TM}}$ analysis and detection system, (b) packaged hand-held $\mu\text{ChemLab}^{\text{TM}}$, (c) concentration unit consisting of a metal film heater and a chemical trap, (d) micromachined gas chromatograph column, (e) SAW array on the electronics board.

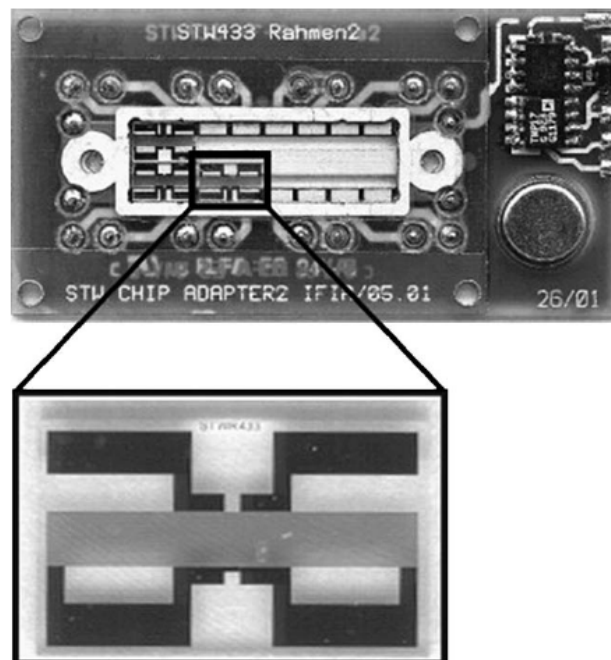


Fig.1.14. SAW-based gas sensor array. Dimensions of the board are $60 \times 30 \text{ mm}^2$. A single microsensors (zoomed area) occupies an area of $4 \times 4 \text{ mm}^2$.

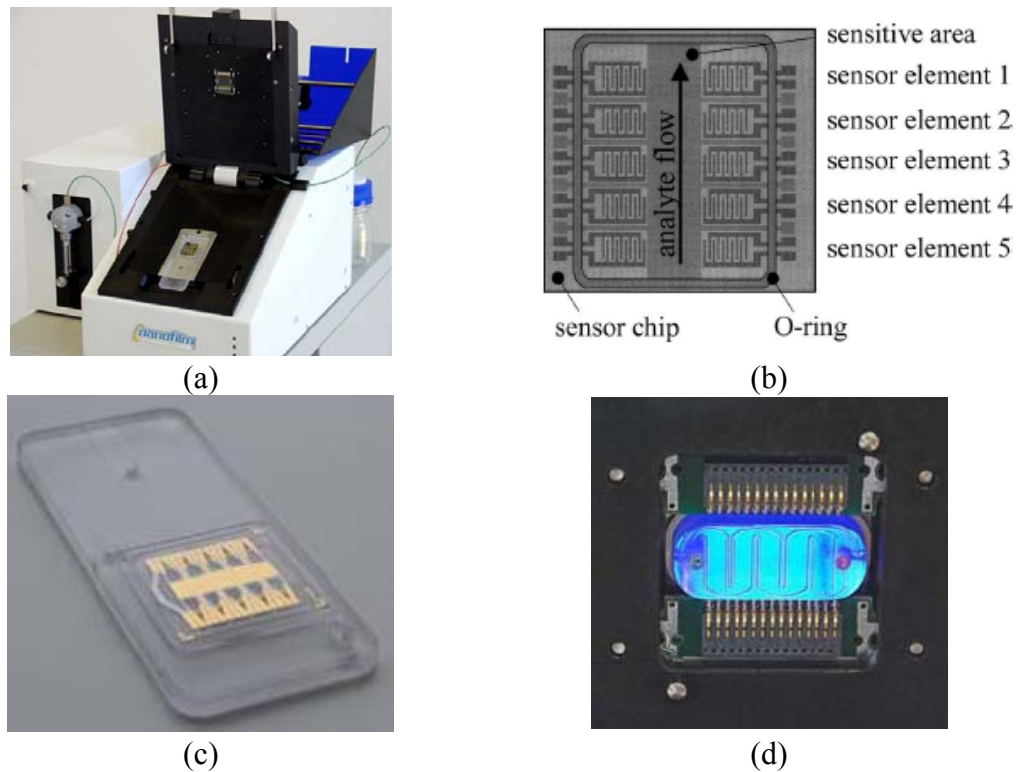


Fig.1.15. S-sens K5 system: (a) Chip reader with chip inserted, (b) schematic of the 5-sensor configuration and fluid flow, (c) K5 chip cartridge, (d) microfluidic cell.

1.7. Novelty of this work: concept and realization

All the above cases (either gas or liquid based multi-sensing configurations) have one common feature: the multiplicity in biosensing is achieved by placing one sensor element next to the other so as to form an array. This approach, is traditionally followed also in the other cases of biosensors mentioned before, e.g. micromechanical, SPR, and electrochemical. However, in the case of SAW, there are some drawbacks in this approach:

1. The detection electronics for one SAW sensor element are quite complicated, so, they become even more complex when an array is to be connected to them, demanding more complex designs, cumbersome and costly fabrication procedures as well as data monitoring systems.
2. Placing a number of SAW sensor elements one next to the other would increase substantially the overall size of the final chip.
3. There is often lack of reproducibility among the SAW elements of an array. This fact results in consuming one or more elements of the SAW array for reference purposes; or in other cases, some sensor elements are used so as to extract an average value, due to the deviation of response among the individual sensors, thus losing the essence of multiplicity.
4. A sensor array is usually a biochip with a fixed number of sensor elements. This means that all the detection electronics and fluidics modules are specifically designed for this particular number of sensor elements. This,



however, is a quite limiting concept: it offers no flexibility and confines the end user to utilize only up to a certain, fixed, number of sensor elements.

Under these circumstances, a new concept of reaching multiplicity is proposed and realized in this work. The traditional concept of an array of *sensor elements* is abandoned, and replaced by the concept of an array of *sensor sub-areas*. In particular, it is suggested to use a single sensor for multi-analysis, by dividing its total sensing area into individual sub-areas. This compartmentalization is proposed to be achieved by means of a microfluidic module, which would create compartments on the sensor surface, dividing it into equal fractions of its total area. In this way, each compartment will host an individual experiment and a single sensor will be transformed into a multi-analyte detection platform. The concept is illustrated in Fig.1.16.

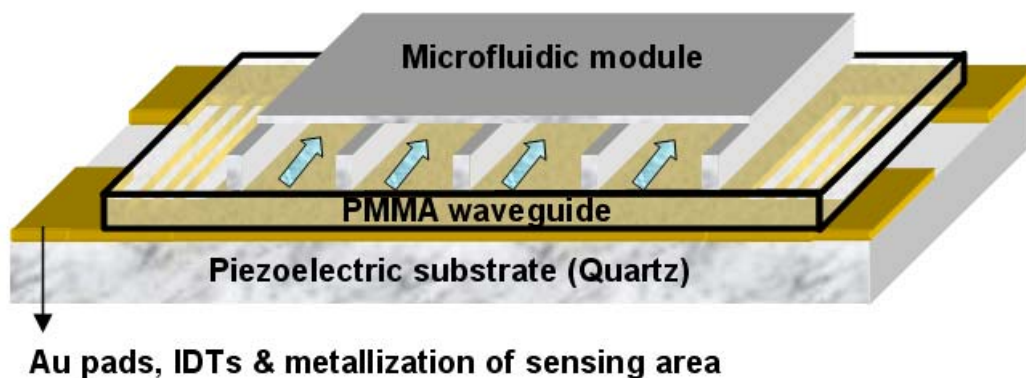


Fig.1.16. 3D representation of a single SAW sensor compartmentalized into four sub-areas.

With respect to the drawbacks faced by the SAW-based multi-sensor setups, mentioned above, the new system has much to improve:

1. The microfluidic module can be adapted to any single-SAW sensor. Thus, the setup can be adjusted to existent monitoring instrumentation, without the need to purchase, modify or upgrade the already existing data acquisition systems.
2. As the multiplicity is not dependent on the number of sensors, but the number of compartments, there is no danger of excessive size of the biochip. In fact, the modified setup has the same size as the standard configuration.
3. In the proposed configuration, the multiple samples are not injected in different sensors, but on the same one. Moreover, during preparation or surface regeneration procedures of the single sensor (waveguide spin-coating, Au thin film deposition, plasma etching, etc, see sec.3.5.) the sensor is uniformly processed. Therefore, there are no inhomogeneities among the sub-areas and any device-dependent inconsistencies (inherently existing in array formats) are eliminated.
4. The fabrication process of the microfluidic module is fast, easy and cheap, so on the same wafer there could be modules with varying number of microchannels (3-, 4-, 5-channel, etc.). Thus, each of them can be used



according to the needs of the user, offering increased flexibility according to the demands of each application.

Two weak points of the proposed system that could be mentioned (but potentially improved) are the following:

- Dividing the area into N sub-areas results in a proportional signal reduction. However, this can be solved by increasing the sensitivity and/or optimizing the geometry of the total sensing area.
- The samples are injected and detected sequentially in the microchannels. Naturally, this way is not as fast as a simultaneous one would be; and there is no way to detect N samples simultaneously on a single sensor (this will be explained in sec.6.2.1.). However, the overall experimental time with an N -channel module is still better than N experiments with a total-area device, taking into account the time for surface cleaning, regeneration, buffer equilibration, etc. Also, the wear of the device is drastically reduced if a sensor is used one time for N experiments, instead of N times for N experiments.

Within this context, this work is based on a novel concept for multi-sample detection. The overall aim is to develop the new setup and establish it as a new means of detecting multiple samples in a versatile, reproducible and reliable way. The specific objectives of this work are the following:

- Selection of the optimum SAW device configuration as the biosensing platform for the new microsystem.
- Design and fabrication of the microfluidic module and test of its functionality.
- Evaluation of reproducibility and sensitivity of the new setup, upon the integration of the microfluidic module with the SAW biochip; establishment of the microsystem's operation for a variety of purposes, such as detection of aqueous solutions, protein adsorption and binding, and kinetics analysis for a variety of biomolecules.
- Validation of the microsystem on samples of clinical interest: detection of 4 different biomarkers responsible for cardiac diseases.

Throughout the thesis, the newly developed setup is termed “ μ F-on-SAW”, as an abbreviation for “microfluidics on SAW devices”.



References

- [1.1.] O. Geschke, H. Klank, P. Telleman, "Microsystem engineering of lab-on-chip devices", Wiley-VCH Verlag GmbH, Weinheim, ISBN: 3-527-30733-8, 2004.
- [1.2.] A. Manz, N. Graber, H.M. Widmer, "Miniaturized total chemical analysis systems: a novel concept for chemical sensing", *Sens. Actuat. B-Chem.*, vol. 1, pp. 244-248, 1990.
- [1.3.] R. Bashir, "BioMEMS: state-of-the-art in detection, opportunities and prospects", *Adv. Drug. Deliv. Rev.*, vol. 56, pp. 1565-1586, 2004.
- [1.4.] <http://www.biognosis-info.de/index.htm>
- [1.5.] <http://www.pocemon.eu>
- [1.6.] <http://www.neurotas.eu>
- [1.7.] <http://www.etseq.urv.es/cdmedics>
- [1.8.] <http://www.pythia-project.eu/index.php>
- [1.9.] http://www.apptech.philips.com/healthcare/projects/magnetic_biosensors.html
- [1.10.] http://w1.siemens.com/innovation/en/publikationen/publications_pof/pof_fall_2004/sensors_articles/biosensors.htm
- [1.11.] <http://www.stuttgart.sony.de/sony-stc/departments/materials-science-laboratory.html#sensing>
- [1.12.] <http://www.zurich.ibm.com/st/bioscience/index.html>
- [1.13.] I.U.P.A.C. "Recommended definitions and classification", *Pure Appl. Chem.*, vol. 71, no. 12, pp. 2333-2348, 1999.
- [1.14.] S.-J. Park, T.A. Taton, C.A. Mirkin, "Array-based electrical detection of DNA with nanoparticle probes", *Science*, vol. 295, pp. 1503-1506, 2002.
- [1.15.] M. Pohanka, P. Skládal, "Electrochemical biosensors - principles and applications", *J. Appl. Biomed.*, vol. 6, pp. 57-64, 2008.
- [1.16.] www.osmetech.com/esensor.htm
- [1.17.] Report, "eSensor[®] Cystic Fibrosis Carrier Detection System 510(k) Summary, 2006.
- [1.18.] L. Huang, G. Reekmans, D. Saerens, J.M. Friedt, F. Frederix, L. Francis, S. Muyltermans, A. Campitelli, C.V. Hoof, "Prostate-specific antigen immunosensing based on mixed self-assembled monolayers, camel antibodies and colloidal gold enhanced sandwich assays", *Biosens. Bioelectron.*, vol. 21, pp 483-490, 2005.
- [1.19.] J.-F. Masson, L. Obando, S. Beaudoin, K. Booksh, "Sensitive and real-time fiber-optic-based surface plasmon resonance sensors for myoglobin and cardiac troponin I", *Talanta*, vol. 62, pp. 865-870, 2004.
- [1.20.] www.biocore.com/lifesciences
- [1.21.] B. Rothenhäusler, W. Knoll, "Surface-plasmon microscopy", *Nature*, vol. 332, pp. 615-617, 1988.
- [1.22.] H.-B. Pyo, Y.-B. Shin, M.-G. Kim, H.C. Yoon, "Multichannel surface plasmon resonance imaging and analysis of micropatterned self-assembled monolayers and protein affinity interactions", *Langmuir*, vol. 21, pp. 166-171, 2005.
- [1.23.] www.rci.rutgers.edu/~longhu/Biacore/pdf_files/Biacore_3000_PIS.pdf
- [1.24.] G. Binnig, C.F. Quate, Ch. Gerber, "Atomic Force Microscope", *Phys. Rev. Lett.*, vol. 56, pp. 930-933, 1986.



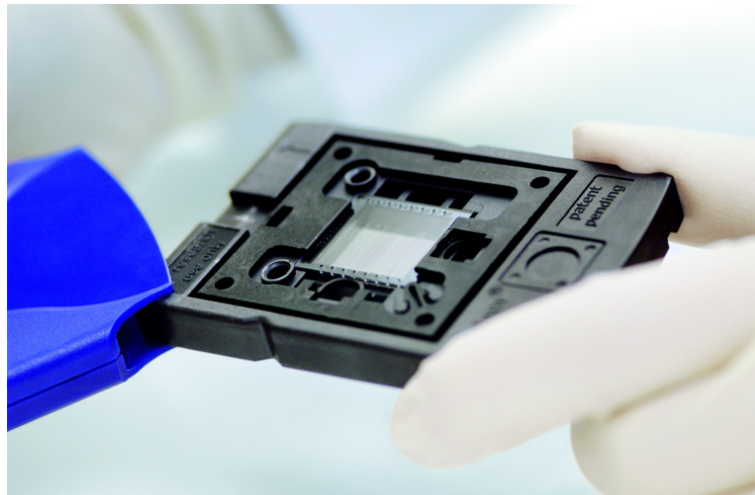
- [1.25.] J. Fritz, M.K. Baller, H.P. Lang, H. Rothuizen, P. Vettiger, E. Meyer, H.-J. Güntherodt, Ch. Gerber, J.K. Gimzewski, “Translating biomolecular recognition into nanomechanics”, *Science*, vol. 288, pp. 316-318, 2000.
- [1.26.] K.Y. Gfeller, N. Nugaeva, M. Hegner, “Micromechanical oscillators as rapid biosensor for the detection of active growth of *Escherichia coli*”, *Biosens. Bioelectron.*, vol. 21, pp. 528–533, 2005.
- [1.27.] K.-U. Kirstein, Y. Li, M. Zimmermann, C. Vancura, T. Volden, W.H. Song, J. Lichtenberg, A. Hierlemann, “Cantilever-Based Biosensors in CMOS Technology”, *Proceedings of the conference on Design, Automation and Test in Europe*, vol. 2, pp. 1340-1341, 2005.
- [1.28.] Y. Arntz, J.D. Seelig, H.P. Lang, J. Zhang, P. Hunziker, J.P. Ramseyer, E.Meyer, M. Hegner, Ch. Gerber, “Label-free protein assay based on a nanomechanical cantilever array”, *Nanotechnology*, vol. 14, pp. 86-90, 2003.
- [1.29.] R. McKendry, J. Zhang, Y. Arntz, T Strunz, M. Hegner, H.P. Lang, M.K. Baller, U. Certa, E. Meyer, H.-J. Güntherodt, Ch. Gerber, “Multiple label-free biodetection and quantitative DNA-binding assays on a nanomechanical cantilever array”, *PNAS*, vol. 99, pp. 9783-9788, 2002.
- [1.30.] http://www.nccr-nano.org/nccr/research/modules/module_01
- [1.31.] http://www.micromotive.de/G/Octosensis_e.php
- [1.32.] C.-Y. Shen, C.-P. Huang, W.-T. Huang, “Gas-detecting properties of surface acoustic wave ammonia sensors,” *Sens. Actuat. B-Chem.*, vol. 101, pp. 1–7, 2004.
- [1.33.] J. Hossenlopp, L. Jiang, R. Cernosek, F. Josse, “Characterization of epoxy resin (SU-8) film using thickness-shear mode (TSM) resonator under various conditions,” *J. Polym. Sci. B, Polym. Phys.*, vol. 42, pp. 2373–2384, 2004.
- [1.34.] S. Kurosawa, T. Hirokawa, K. Kashima, H. Aizawa, D.-S. Han, Y. Yoshimi, Y. Okada, K. Yase, J. Miyake, M. Yoshimoto, J. Hilborn, “Detection of deposition rate of plasma-polymerized films by quartz crystal microbalance,” *Thin Solid Films*, vol. 374, pp. 262–267, 2000.
- [1.35.] M. Jungwirth, H. Scherr, R. Weigel, “Micromechanical precision pressure sensor incorporating SAW delay lines,” *Acta Mech.*, vol. 158, pp. 227–252, 2002.
- [1.36.] A. J. Ricco, S. J. Martin, “Acoustic wave viscosity sensor”, *Appl. Phys. Lett.*, vol. 50, pp. 1474-1476, 1987.
- [1.37.] J. Kondoh, T. Muramatsu, T. Nakanishi, Y. Matsui, S. Shiokawa, “Development of practical surface acoustic wave liquid sensing system and its application for measurement of Japanese tea”, *Sens. Actuat. B-Chem.*, vol. 92 pp. 191–198, 2003.
- [1.38.] D.L. Garcia-Gonzalez, N. Barie, M. Rapp, R. Aparicio, “Analysis of virgin olive oil volatiles by a novel electronic nose based on a miniaturized SAW sensor array coupled with SPME enhanced headspace enrichment”, *J. Agric. Food Chem.*, vol. 52, pp. 7475-7479, 2004.
- [1.39.] K. Y. Hashimoto, “Surface Acoustic Wave devices in telecommunications: modelling and simulation”, ISBN: 354067232X, Springer-Verlag New York, 2008.
- [1.40.] M. Fang, K. Vetelino, M. Rothery, J. Hines, G. C. Frye, “Detection of organic chemicals by SAW sensor array,” *Sens. Actuat. B-Chem.*, vol. 56, pp. 155–157, 1999.



- [1.41.] M. Rapp, J. Reibel, A. Voigt, M. Balzer, O. Bülow, “New miniaturized SAW-sensor array for organic gas detection driven by multiplexed oscillators,” *Sens. Actuat. B-Chem.*, vol. 65, pp. 169–172, 2000.
- [1.42.] J.W. Grate, “Acoustic wave microsensors for vapor sensing,” *Chem. Rev.*, vol. 100, pp. 2627–2647, 2000.
- [1.43.] M. Penza, G. Cassano, F. Tortorella, “Identification and quantification of individual volatile organic compounds in a binary mixture by SAW multisensor array and pattern recognition analysis,” *Meas. Sci. Technol.*, vol. 13, pp. 846–858, 2002.
- [1.44.] <http://www.sandia.gov/mstc/MsensorSensorMsystems/MicroChemLab.html>
- [1.45.] K. Länge, G. Blaess, A. Voigt, R. Götzen, M. Rapp, “Integration of a surface acoustic wave biosensor in a microfluidic polymer chip,” *Biosens. Bioelectron.*, vol. 22, pp. 227–232, 2006.
- [1.46.] M. Perpeet, S. Glass, T. Gronewold, A. Kiwitz, A. Malavé, I. Stoyanov, M. Tewes, E. Quandt, “SAW sensor system for marker-free molecular interaction analysis,” *Anal. Lett.*, vol. 39, pp. 1747–1757, 2006.
- [1.47.] T.M.A. Gronewold, S. Glass, E. Quandt, M. Famulok, “Monitoring complex formation in the blood-coagulation cascade using aptamer-coated SAW sensors,” *Biosens. Bioelectron.*, vol. 20, pp. 2044–2052, 2005.
- [1.48.] T.M.A. Gronewold, A. Baumgartner, E. Quandt, M. Famulok, “Discrimination of single mutations in cancer-related gene fragments with a Surface Acoustic Wave sensor,” *Anal. Chem.*, vol. 78, pp. 4865–4871, 2006.
- [1.49.] <http://www.biosensor-gmbh.de>
- [1.50.] J. Lozano, M.J. Fernandez, J.L. Fontecha, M. Aleixandre, J.P. Santos, I. Sayago, T. Arroyo, J.M. Cabellos, F.J. Gutierrez, M.C. Horrillo, “Wine classification with a zinc oxide SAW sensor array,” *Sens. Actuat. B-Chem.*, vol. 120, pp. 166–171, 2006.



Chapter 2. Description of the microsystem components: acoustic devices and microfluidics



*Geniom Biochip within the plastic cartridge, the core component of febit's
Genomic Services and instruments*

<http://www.febit.com/microarray-sequencing/index.cfm>





Chapter 2. Description of the microsystem components: acoustic devices and microfluidics

2.1. Classification of acoustic waves and devices

The propagation of sound waves in a medium has been studied for years now, including cases where acoustic waves travel across solids, liquids and gases. Even though these waves can exist in all kinds of materials, the acoustic devices are based on piezoelectric materials (as described in sec.1.5.4.) because it is possible to excite the acoustic waves electrically at their surface or bulk. Thus, acoustic (or piezoelectric) devices utilizing these waves for the sensing procedure are categorized according to the type of waves they support for the sensing purpose. Based on a general classification, the acoustic waves can be divided in two major categories: the Bulk Acoustic Waves (BAW) and the Surface Acoustic Waves (SAW); the latter is further divided into the Rayleigh SAW, the Shear-Horizontal SAW, and the Love waves. The devices/sensors that utilize each of these wave categories are named after them, and are briefly described in the following sections.

2.1.1. Bulk Acoustic Waves and devices - Quartz Crystal Microbalance

The term “bulk wave” is generally used to describe waves which are not confined to a surface. Bulk elastic waves can propagate in any direction in any solid, whether elastically isotropic or anisotropic. Three independent types of bulk waves can exist in a medium, namely a longitudinal wave along the wave vector, and two shear waves on a plane perpendicular to the wavevector. Given appropriate crystal symmetry and orientation (satisfied by some piezoelectric materials such as quartz) it is possible that either a shear or a longitudinal component will be produced. Thus, standing shear waves can be produced in a medium under specific conditions.

These principles were exploited for the production of the Bulk Acoustic Wave (BAW) devices and sensors [2.1.]. The most common of this “family” is the Quartz Crystal Microbalance (QCM), or Thickness-Shear Mode (TSM) resonator, shown in Fig.2.1. This device consists of a parallel-sided plate of crystalline quartz sandwiched between two circular electrodes. An external oscillating electrical potential applied on the piezoelectric substrate produces internal mechanical stress, which is essentially a standing acoustic wave between the two metallized sides. The wavelength has to be a multiple of a half wavelength in order for constructive interference to exist, i.e.:

$$d = N \frac{\lambda}{2} \quad (\text{eq.2.1.})$$

$$\text{With } \lambda = \frac{v}{f}, \text{ the above becomes } d = N \frac{v}{2f_N}, \text{ or } f_N = N \frac{v}{2d} \quad (\text{eq.2.2.})$$

where f_N is the N^{th} excited frequency (with $N = 1, 3, 5, \dots$), v is the bulk wave propagation velocity and d is the thickness of the crystal. Thus, keeping the same substrate, the operating frequency is regulated purely by fabrication parameters, i.e., the crystal thickness (e.g., a 5 MHz QCM device is approximately 330 μm thick with



disc diameter around 20 mm). Among the available quartz crystal symmetries AT-cut is mostly preferred, both because it supports shear waves, and due to its tremendous frequency stability ($\Delta f/f = 10^{-8}$) and temperature coefficient (almost zero between 0 and 50 °C [2.2.]). Typical operating frequencies are of the order of few MHz, e.g. 5 MHz for the fundamental and 15, 25, and 35 MHz for the harmonics. However, because the operating frequency is inversely proportional to the quartz thickness, high frequency QCM devices are technically hard to be produced and remain stable, due to their fine thickness and consequently high fragility. Upon loading the QCM resonator with any kind of sample, the shift in resonant frequency peak, Δf , and the damping of the peak, ΔD , are measured, corresponding to various properties of materials, depending on the type of loaded sample (for example, viscosity, viscoelastic properties, film thickness, etc).

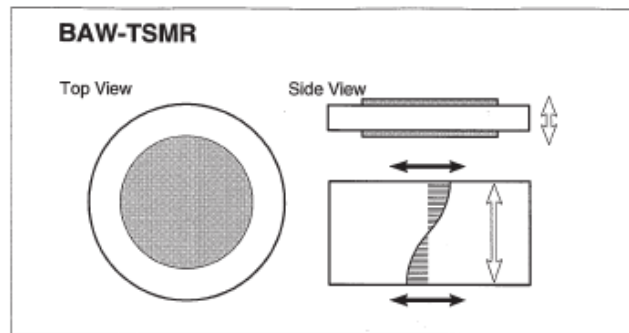


Fig.2.1. Thickness-Shear Mode configuration of a BAW device.

2.1.2. Rayleigh Waves and SAW devices

In contrast to the Bulk Acoustic Waves, when a wave propagates only on the surface or an interface separating two media, it is termed a “Surface Acoustic Wave”. In fact, back in 1887, Lord Rayleigh discovered this propagation mode and the Surface Acoustic Waves were named after himself as “Rayleigh waves”. In this propagation mode, energy is confined very near the surface [2.3.] as the wave amplitude decays exponentially within increasing distance from the surface or interface. Nowadays, the term “Rayleigh SAW” refers to the wave which has compressional and shear components (Fig.2.2.). Under the effect of such a wave, the vector of a particle displacement has three components described by:

$$\vec{u}(x, y, z, t) = e^{(j\omega t - \gamma z)} \sum_{i=1}^3 u_i(y) e^{j\varphi_i} \hat{x}_i \quad (\text{eq.2.3.})$$

revealing an elliptical polarization of the particle trajectory; in eq.2.3. u is the particle displacement, ω is the angular frequency, t is time, γ is the complex wave propagation factor, and φ is the phase of the displacement; the subscript i corresponds to each of the propagation directions [2.4.].

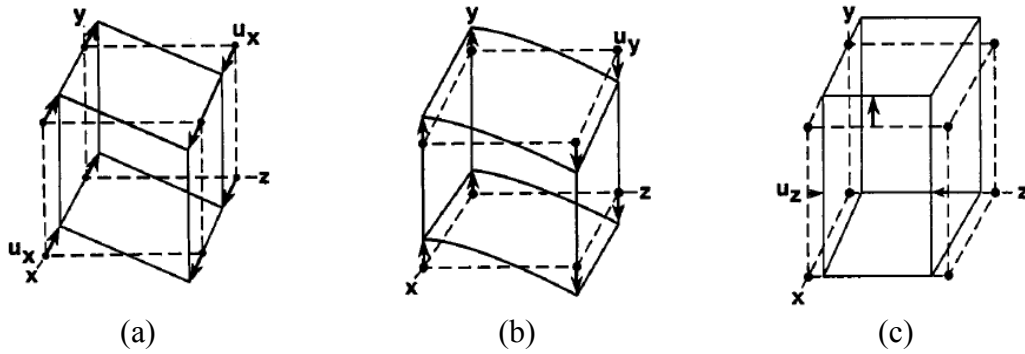


Fig.2.2. Three kinds of particle displacement (considering the xz plane as the sensor surface); (a) transverse shear (shear horizontal), (b) bending, (c) longitudinal compression.

Due to their special propagation characteristics, Rayleigh waves were exploited in sensor technology, as they were extremely sensitive to surface perturbations. Rayleigh waves have been the basis for the development of mass sensitive devices for gas sensing. However, in an effort to use them in liquid sensing, they present a crucial drawback: due to the out-of-plane components of the particle displacement (Fig.2.3.), the interaction of a Rayleigh SAW with a liquid leads to severe damping in its direction of propagation, as a result of energy leakage into the liquid medium. As a result, Rayleigh SAW was soon considered unsuitable for liquid sensing and, consequently, for biosensing.

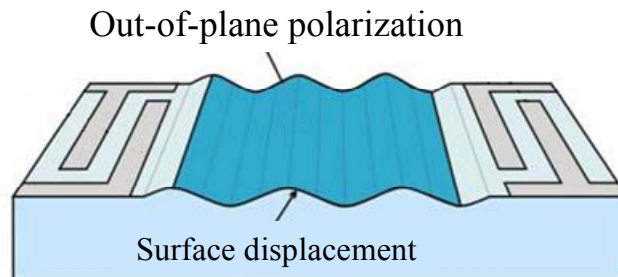


Fig.2.3. Rayleigh mode configuration of a SAW device.

2.1.3. Shear-Horizontal Surface Acoustic Waves and devices

When the particle displacement is perpendicular to the wave propagation direction *and* parallel to the surface plane, then the wave is termed a “Shear-Horizontal Surface Acoustic Wave (SH-SAW)” (Fig.2.4.). In that case, no other polarization of the surface displacement exists (only case (a) in Fig.2.2.) and eq.2.3. has only one component: $\vec{u}(x, y, z, t) = u_x(y) e^{j\varphi_x} e^{(j\omega t - \gamma z)} \hat{x}$. Waves of this polarization exist due to specific crystal orientation and symmetry (ST-cut, as opposed to AT-cut for QCM devices, see sec.2.1.1.).

The SH-SAW devices implement these waves for efficient sensing of liquids. The advantage of SH-SAW over the Rayleigh SAW devices/sensors is that the former do not undergo damping due to the adjacent liquid medium. Therefore, any biological sensing is based on the SH-SAW devices.

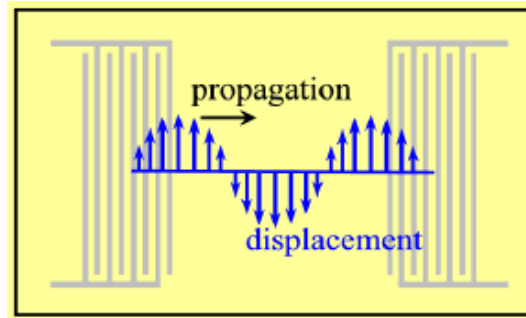


Fig.2.4. Shear-Horizontal mode of a SAW device with in-plane, propagation-normal particle displacement.

2.1.4. Love waves and devices

In a typical SH-SAW, energy is “leaking” into the bulk of the solid medium, along the propagation direction. However, if an elastic layer overlays the medium, a guided SH-SAW, the Love wave, is generated, which exhibits no bulk leaking effects. In order for Love waves to exist, the shear acoustic velocity in the layer must be lower than that in the underlying medium; in addition, specific conditions for the thickness and the acoustic properties of the overlayer must be met in order for it to act as an acoustic waveguide [2.5.]. The overlayer thickness and acoustic properties (density and shear modulus) define the optimum waveguide conditions and the extent to which the acoustic energy is transferred into the overlayer. The sensitivity to mass loading is thereby increased by concentrating the energy in this layer. The optimal thickness of the layer will depend on both the density and the shear velocity, and can be determined both theoretically and experimentally [2.6.].

The concentration of the wave energy in the guiding layer due to its lower shear acoustic velocity than the substrate can be easily viewed from the following mathematical notation. The energy density U and wave velocity v are related via the power density $P = U \cdot v$. Differentiating dU/dv (i.e., how the energy density changes with wave velocity), we get:

$$\frac{dU}{dv} = \frac{d(P/v)}{dv} = -\frac{P}{v^2} = -\frac{Uv}{v^2} = -\frac{U}{v} \Rightarrow$$

$$\frac{dU}{dv} = -\frac{U}{v} \Rightarrow \frac{\Delta U}{U} = -\frac{\Delta v}{v} \quad (\text{eq.2.4.})$$

The latter expresses a fundamental relation between the wave energy density and velocity for a system excited at a given frequency; it theoretically confirms that, in the Love wave configuration where the overlayer has a lower acoustic velocity than the substrate, energy density increases within the waveguide layer.

This fact is exploited in sensing applications. When a guiding layer is placed on an uncoated SH-SAW device it turns into a Love wave device and combines both (i) the shear-horizontal nature of particle displacement (which allows operation in liquids), and (ii) the acoustic energy concentration/“entrapment” near the layer/sample interface (which increases the sensitivity).



2.1.5. Building blocks of a typical Love wave device

Since Love wave devices are the ones used in this work, the “architecture” of a typical such device is analyzed (Fig.2.5.). The main components are: (i) piezoelectric substrate (quartz), (ii) metallization area and InterDigital Transducers (gold), (iii) waveguide layer (polymer), (iv) shear-horizontal particle motion (the signs “ \otimes and \odot ” denote particle displacement perpendicular to the paper plane), (v) liquid sample, sensed within a penetration depth, δ .

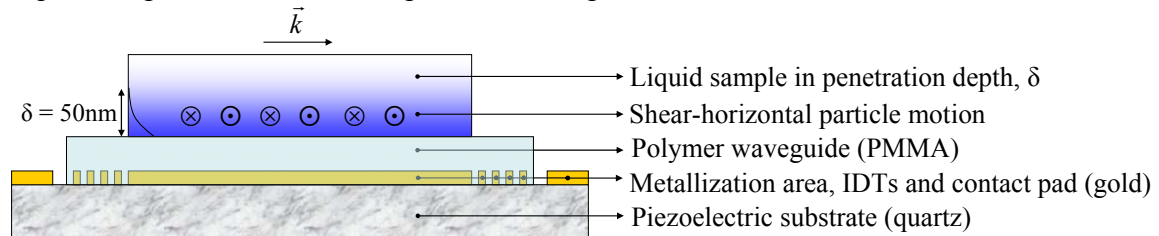


Fig.2.5. Typical components of a Love wave device.

(i) Piezoelectric substrate

The most widely used material for acoustic devices is quartz, a crystalline form of SiO_2 . It offers the advantage of low temperature coefficient compared to other piezoelectric materials, which renders it quite insensitive to environmental temperature changes. It is available in a number of crystallographic orientations according to the desired applications. For example, ST-cut is commonly used for SAW devices, whereas AT-cut quartz for QCM sensors; the crystal cut of the piezoelectric substrate should also be carefully chosen, as it defines whether the acoustic wave will be an SH-SAW (i.e., suitable for liquid applications) or Rayleigh SAW (unsuitable for liquid sensing).

Some special ceramic materials are often used as piezoelectric substrates for SAW sensors, such as lithium niobate and tantalate (LiNbO_3 and LiTaO_3 , respectively), because they have a large acoustomechanical coupling coefficient, i.e., they offer a high conversion efficiency between the electric and the acoustic energy. For this reason, fewer pairs of IDTs (see next section) need to be used than with quartz. Also, sensors based on these materials can even be immersed into liquids, unlike quartz, without severe distortion of the wave, which is of great importance to liquid-based chemical and biosensors. The optimum crystallographic orientations that have been determined for these materials are 41° -rotated Y-cut for LiNbO_3 and 36° -rotated Y-cut for LiTaO_3 . However, these substrate materials suffer from a large temperature coefficient. As a consequence, thermal fragility is a problem, as well as the extreme temperature stability that needs to be kept during the use of these substrates for biosensing.

Other materials used in acoustic wave devices are ZnO and AlN, primarily due to their compatibility with Si technology and processing, as well as their integration capacity.



(ii) InterDigital Transducers (IDTs)

The excitation and detection of SAW is almost exclusively achieved by using InterDigital Transducers (IDTs) (first reported in 1965 [2.7.]) in contrast to previous methods utilizing mechanical coupling between the transducer and the piezoelectric material. The IDTs comprise of a comb-like structure, as shown in Fig.2.6. The design of the IDTs should be carefully made, as it determines the electrical impedance, the operating frequency, bandwidth and sensing area of the device. The metal film used to make the IDTs should be thick enough, to offer low electrical resistance, and thin enough, to avoid excessive mechanical load to the acoustic wave. Typical materials for IDTs are aluminum or gold, with nominal thickness around 100 nm. In case of gold, a thin layer (~10 nm) of chromium or titanium should be deposited between the substrate and the gold for adhesion purposes. Standard photolithographic techniques are used for the IDTs fabrication, which include only a few steps, as the pattern itself is not complex. Deposition methods commonly used are evaporation (thermal or e-beam) or sputtering. In addition, a metallization between the IDT sets (optional, in general, see Fig.2.5.) as well as the contact pads are made of the same metal.

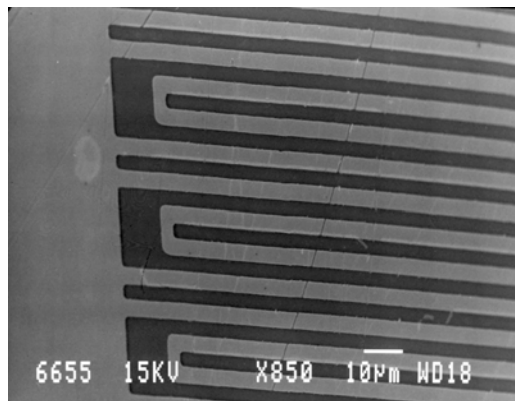


Fig.2.6. SEM image of IDT sets from the 155MHz quartz SAW device used; the thick vertical section is the common metal pad.

When a radio frequency is applied on the input IDT set, the time-varying voltage results in a synchronously varying mechanical deformation of the piezoelectric substrate and, eventually, in the generation of a propagating acoustic wave. The wavelength λ excited by the IDTs is equal to the periodicity of the transducer pattern, d (Fig.2.7.); the velocity v of the wave has a specific value for a given substrate. Thus, the operating frequency is defined by $f_o = v / \lambda$, or, $f_o = v / d$, and it is only dependent on the structural parameter, d , of the device. In general, IDT geometry features, such as electrode width, spacing, number of finger pairs and acoustic aperture are important design parameters for SAW device fabrication, and the optimum specification according to the desired application is most often accomplished with sophisticated computer software and simulations.

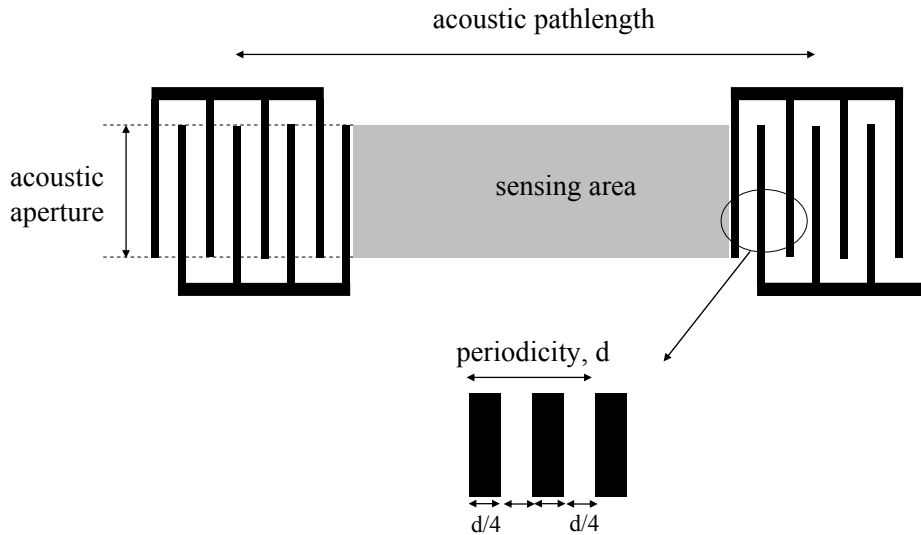


Fig.2.7. Typical features of IDT geometry and sensing area.

(iii) Waveguide layer

As it was mentioned, the Love wave device configuration makes use of a waveguide layer for sensitivity enhancement. The main parameters for the selection of the waveguide material are its density and sound velocity, as well as its thickness. It has been shown that a waveguide becomes more efficient as the material density reduces with parallel reduction of the acoustic velocity in it [2.6.] (Tab.2.1.).

Tab.2.1. Typical SAW waveguide materials.

Material	Shear acoustic velocity (m/s)	Density (kg/m ³)	Thickness (μm)
Fused silica (SiO ₂)	3764	2200	12
Gold	1200	19700	1-2
PMMA	1100	1180	3

In order for a film to act as an acoustic waveguide, it should be quite thinner than the wavelength (the latter being calculated in the film). In addition, the sound velocity in the waveguide material should be smaller than that in the piezoelectric substrate.

Typical materials used as acoustic waveguides are SiO₂ and polymer films. SiO₂ is usually deposited via Plasma Enhanced Chemical Vapor Deposition (PECVD) or other time- and money-consuming processes, and a thickness of a few μm is necessary for efficient waveguiding. On the other hand, polymer films are deposited via spin-coating, which is faster and cheaper method than PECVD and films of up to 1 to 1.5 μm thickness are required to guide the acoustic wave. However, due to the polymeric nature of the waveguide, these devices are not compatible with chemical treatment using organic solvents. In our case, a PMMA waveguide was used, which was spin-coated over the entire sensing area and the IDT sets (the color in Fig.2.5.



corresponding to the waveguide is deliberately semi-transparent, to denote that the film covers the IDTs as well).

2.2. Operating principle

The schematic in Fig.2.8. describes in short the operating principle of acoustic sensors. An oscillating voltage is applied at the input set of IDTs. Due to the piezoelectric nature of the substrate the generated oscillating electric field induces a synchronously harmonic mechanical oscillation which is transmitted through the crystal as an acoustic wave (in particular, having a shear horizontal polarization of particle displacement). Like any wave, it is characterized by amplitude and phase. When a surface perturbation of any kind takes place (for example mass or viscoelastic loading in air or liquid environment, adsorption, binding, etc.) the wave parameters change as a result of this surface perturbation: amplitude change is related to energy losses in the medium where the wave propagates, and phase is related to wave velocity changes due to mass and viscoelastic properties of the sample. Eventually, due to the inverse piezoelectric phenomenon, the perturbed mechanical (acoustic) wave is transformed into an electric field (or, equivalently, electric potential) which is detected by the receiver set of IDTs and is registered as detected signal. Then, it is up to analytical and/or numerical calculations, simulations and models to correlate the signal change with the parameters of interest characterizing each examined sample.

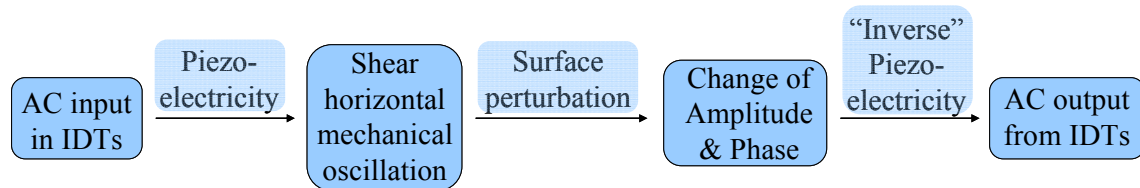


Fig.2.8. Schematic representation of the acoustic wave sensor operating principle.

2.3. Introduction to microfluidics

“Microfluidics” is a multidisciplinary field converging engineering, physics, chemistry, microtechnology and biotechnology, with practical applications to the design of systems in which small volumes of fluids are used, and expands in theoretical, computational and fabrication/production directions. It describes the fluidic behaviors at the micro/nanoscale and the engineering of design, simulation, and fabrication of the fluidic devices for the transport, delivery, and handling of fluid volumes of the order of microliters or smaller. Microfluidic devices and systems handle fluid samples in this range for various applications, including inkjet printing, blood analysis, biochemical detection, chemical synthesis, drug screening/delivery, protein analysis, DNA sequencing, and so on. Microfluidic systems consist of microfluidic platforms or devices for fluidic sampling, control, monitoring, transport, mixing, reaction, incubation, and analysis. To produce microfluidic systems,



microfluidic devices must be functionally integrated on a platform using proper micro/nano fabrication techniques.

Microfluidic devices offer the ability to work with smaller reagent volumes, shorter reaction times, and the possibility of parallel operation. The fundamental hypothesis for all micrometer-scale systems, concerning flow, is the fact that they are dominated by diffusion. The time t_D it takes for a molecule to travel a distance L , during diffusion, is:

$$t_D = \frac{L^2}{D} \quad (\text{eq.2.5.})$$

where D is the diffusion coefficient. Thus, it is obvious that, miniaturizing the dimensions, diffusion time is also reduced proportionally to the square of the dimensions. Thus, a process duration (and furthermore, the time to acquire the response signal in sensors) can be reduced from hours to minutes.

From the technological point of view, the ease and cost-effectiveness of the microfluidics fabrication processes is an additional advantage to their usage. In fact, unlike microelectronics, where there is great competition on “who will be more nano” and as small as possible dimensions are desirable, in microfluidics this is not the case. For fluid transport, channels with dimensions from a few microns to a few hundreds of microns are enough. In addition, inexpensive materials are often used. All the above are important reasons for the catching up of microfluidics. Eventually, even though microfluidics is not the actual final target but just a constituent part of a more complex analytical system (μ TAS, lab-on-a-chip, etc.) the latter would never exist without the microfluidics development. The miniaturized nature of microfluidics is remarkably useful for μ TAS when very little sample quantities are available, and when reduced cost of research (and/or of a potential commercial device) is desired.

2.4. Materials for microfluidics fabrication

Various materials are used for the fabrication of microfluidic devices and systems. Silicon is one of the most popular materials in micro/nano fabrication because its micromachining has been well established over decades. In general, the advantages of using silicon as a substrate or structural material are its good mechanical properties and excellent chemical resistance, the well characterized processing techniques, and the capability for integration of control/sensing circuitry as a semiconductor. Other materials such as glass, quartz, ceramics, metals, and polymers are also used for substrates and structures in micro/nano fabrication, depending on the application. Among these materials, polymers have recently become promising materials for lab-on-a-chip applications, due to their excellent material properties for biochemical fluids and their low cost manufacturability.

2.4.1. Silicon

It is most reasonable to consider that silicon would be the first candidate material for the fabrication of microfluidic devices, since so much processing technology has been developed and established around it [2.8.]. Silicon is structured



mainly by means of wet etching (i.e., immersion of the wafer after proper pre-processing, in a highly chemically active solvent which “eats away” the exposed silicon) or dry etching (see sec.2.5.5.). The fabricated features may have rounded, trapezoidal, or vertical walls, according to the isotropic or anisotropic nature of the etching. However, the use of silicon for microfluidics presents some drawbacks, such as the high operational cost for silicon microstructuring techniques and lack of biocompatibility, which have led the researchers to turn to other materials for microfluidics-oriented purposes.

2.4.2. Glass

The main reasons for using glass for biomedical microdevices are its high mechanical strength, chemical resistance, electrical insulation and wide optical transmission range. A typical example is the use of glass for electrophoresis devices. Special types of glass such as Foturan [2.9.] can also be structured with photolithography after treatment to render them photosensitive. UV-radiated amorphous glass crystallizes and these areas can be removed selectively by a subsequent etch process in hydrofluoric acid. Special types of glass are often processed using laser micromachining.

2.4.3. Polymers

Silicon as a substrate material is not very compatible to biomedical applications. Adding the fact that microfluidic devices are intended to be disposable (especially as parts of diagnostic chips) silicon- and glass-based modules increase substantially the production cost. That is why polymers are often selected, instead, and fully polymeric chips offer the solution to problems of biocompatibility as well. Apart from these major advantages, polymers are optically transparent and they can be surface treated in order to create functional groups or modify them accordingly and tailor their surface properties.

PMMA, also known as plexiglass, is one of the primary polymers used for microfluidic purposes. It can be applied on a substrate in various thicknesses and solidifies by heating. It offers high chemical resistance and good electrical insulation. Its surface properties can be modified chemically to suit its application and it can be processed to form the desired shape by means of hot embossing, laser machining, as well as plasma etching [2.10.].

PDMS is a polymer that has an inorganic siloxane backbone with methyl groups attached to silicon [2.11.]. The prepolymer and curing agent of PDMS are both commercially available. PDMS has an elastomeric nature and can be micromachined using replica molding. Harder versions of PDMS (h-PDMS [2.12.]) have higher modulus and can be used according to the application requirements. Finally it is biocompatible, since even mammalian cells can be cultured directly on this material.

SU8 is an epoxy based resin and can be structured with conventional photolithography. SU8 is a versatile material for microfluidics: it can either be used by itself, as the structuring material for microchannels, or it can play the role of the



mold, with its structures transferred on most polymers through replica molding. It is chemically stable and resistant to most acids and other solvents [2.10.].

Cyclo-Olefin Copolymer (COC) is a promising plastic substrate due to its chemical resistance to acids, bases, and most of the polar solvents. It is optically transparent down to 250 nm and its surface treatment remains more stable in time than PDMS, with most commonly used buffers. On top of that, it exhibits biocompatible properties, which is essential for healthcare-targeted microfluidic systems [2.13.].

2.5. Polymer microfabrication processes for microfluidics production

2.5.1. Replica molding - Soft lithography

Soft lithography [2.14., 2.15.] refers to a family of techniques for fabricating or replicating structures using elastomeric stamps, molds, and conformable photomasks. It is called "soft" because it uses elastomeric materials, most notably PDMS. Soft lithography is generally used to construct features measured on the micrometer to nanometer scale. The development of soft lithography expanded rapidly during the period 1995 to 2005. This method has some unique advantages over other forms of lithography (such as photolithography and electron beam lithography) which are:

- Lower cost than traditional photolithography in mass production
- Well-suited for applications in biotechnology and plastic electronics
- Well-suited for applications involving large or nonplanar (nonflat) surfaces
- Does not need a photo-reactive surface to create a nanostructure

2.5.2. Injection molding

The process of injection molding requires a structured mold and a thermoplastic polymer. The mold consists of two parts, usually made of steel or aluminum, which are brought together; the molding tool is closed, evacuated and heated above the glass transition temperature of the polymer to be structured. The thermoplastic polymer fluid is injected in the mold under high pressure and travels to the cavity walls. Subsequently, both the mold and the polymer are cooled down and the polymer is demolded [2.16.]. Various combinations of this method can be applied, in order to improve the performance of the method and to expand its use to materials that are not thermoplastics.

2.5.3. Hot embossing

In hot embossing, a thermoplastic material is inserted into a molding machine and formed under pressure. Hot embossing requires heat and compression and is performed in a properly structured mold-press. In short, a thermoplastic foil is placed between two mold inserts. The two inserts approach each other and "trap" the foil with simultaneous heating above its softening temperature. Finally, the polymer is cooled and demolded, having acquired the desired structure (and keeping a residual



layer, which is the main disadvantage of this method). Structures in the micro and nano scale may be fabricated, and nickel or silicon molds may be used [2.16.].

2.5.4. Stereolithography

In stereolithography, a computer-driven laser scans a photocurable resin causing photopolymerization in a layer-by-layer manner, building the structure in “planes” from the bottom moving upwards. The design of the desired object is drawn in CAD and is linked to x-y stages for moving the laser. Polymerization takes place at the focal plane of the laser, which can be turned on and off for selective structuring. With refined variations of this method, fine structures down to a few microns can be reached. A major advantage of this method is that it requires no mold, as it is a direct-write technique and it can create 3D structures of arbitrary shape (as long as they can be designed with CAD) and even 3D hollow structures such as tubes, pipes, etc. [2.17., 2.18.].

2.5.5. Plasma etching

Plasma etching and in particular, Deep Reactive Ion Etching (DRIE), is an alternative technology to soft lithography for the fabrication of microfluidic devices [2.19.]. It uses chemically reactive plasma in order to remove material deposited on wafers. The reactive gas depends on the material to be removed, for example SF_6 and O_2 have been used for the etching of PDMS and PMMA, respectively [2.20.]. Under proper conditions, the etched structures have (near) vertical walls, which is the desired condition for microchannels and fluidic chambers. A major difference of this method is the lack of replication methods and the more massive production of devices using a plasma etching chamber.

2.6. Examples of microfluidic devices

The following examples describe microfluidic devices either as components of larger systems, or as a complete system. They are meant to demonstrate that a microfluidic platform does not have to be of complicated nature in order to be functional. On the contrary, the examples in sec.2.6.1. and sec.2.6.2. indicate that simple structures can offer much added value to an integrated microfluidic-based system.

2.6.1. On-chip chromatography

Even though microfluidic components are often of passive nature, adjusting their dimensions and their fabrication material can transform them into valuable components performing liquid processing at a miniaturized level. A typical example is chromatography; this well-known separation technique which needs cumbersome, expensive and bulky bench-top equipment can be transferred on-chip. The idea was to integrate all the components of a typical chromatographic column into a wafer



substrate by micromachining them. In particular, RIE of quartz has been employed to produce a liquid chromatographic chip with an array of 10- μm -high, $5 \times 5 \mu\text{m}$ sized rectangular columns to act as support for the stationary phase in the 4.5-cm-long, 150- μm -wide separation chamber (Fig.2.9(a); columns instead of spheres were used, due to easier fabrication). Moreover, uniformity of distribution (before the column) and collection of analytes (after the column) was essential, and was achieved via a micromachined network (Fig.2.9(b), taken at the entrance of the separation column). The pillars are treated appropriately so that the stationary phase will adsorb on them (e.g., electrostatically [2.21.]) for the actual chromatography procedure.

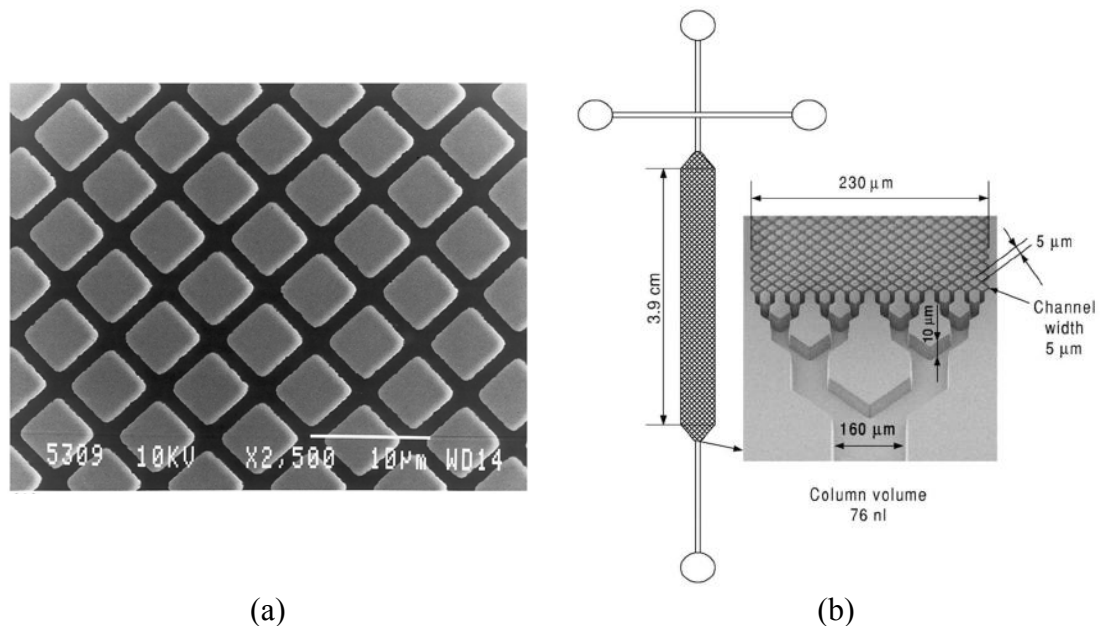


Fig.2.9. SEM image of the inlet splitter (a), and the initial part (b) of a micromachined stationary phase support, intended for microchip chromatography [2.22.]. All features have been etched with RIE.

2.6.2. Micromosaic Immunoassays

A group in IBM Zurich has proposed a simple, easy-to-fabricate and use method to conduct immunoassays based on microfluidic networks (μFN), essentially parallel channels of a few microns in width [2.23.]. Microfluidic networks have high-resolution and high-contrast capabilities for simultaneously patterning lines of proteins onto a surface.

The microchannels were fabricated on a silicon substrate using RIE and then covered with a PDMS substrate. Various methods could be used for fluid propulsion, but they employed the capillary force, due to the size and hydrophilicity of the microchannels' walls. Under these circumstances, various antibodies were loaded at the input pads of the microchannels. As they flowed along the microchannels, stripes of antibodies were patterned on the PDMS sealing surface. After a blocking step with BSA, the μFN was rotated 90° and used again, so as to inject a series of analytes over the pre-patterned antibodies (Fig.2.10(a)). This assay was termed a "micromosaic



immunoassay (μ MIA)” because it places a series of ligands and analytes along micrometer-wide intersecting lines, thus providing a mosaic of signals from cross-reacted zones (Fig.2.10(b)). The resulting binding pattern can then be readily evaluated when analytes are tagged (two-step immunoassays) or can be developed by binding a fluorescent- or enzyme-conjugated antibody to the analyte (sandwich-type immunoassay).

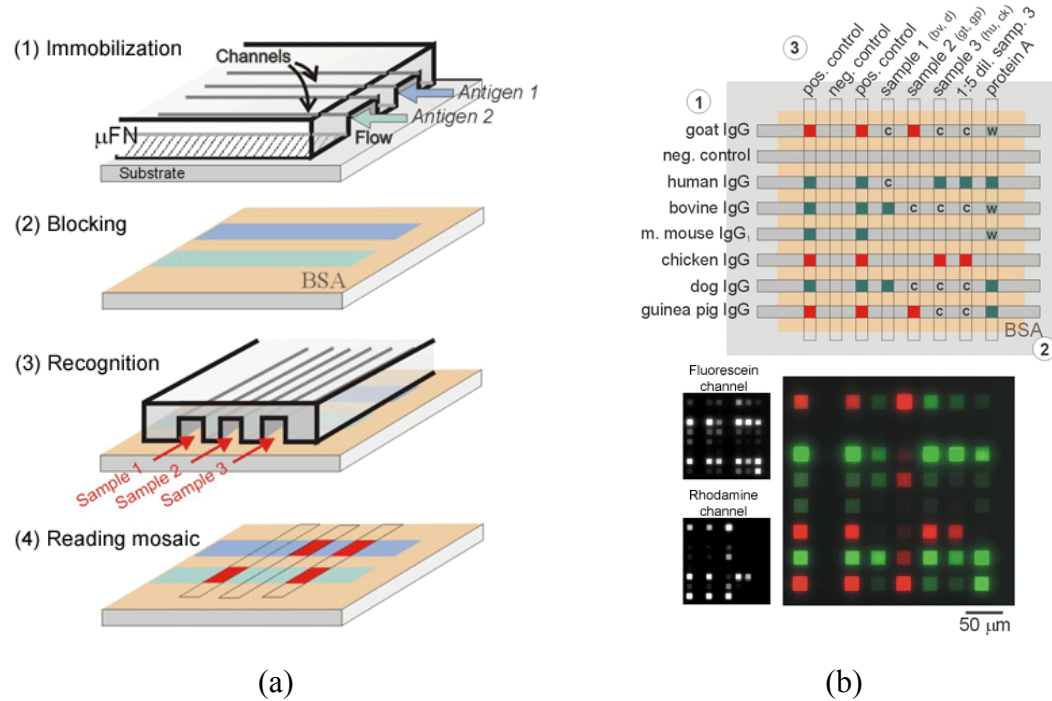


Fig.2.10. (a) Operating principle of μ FN, (b) 8×8 μ MIA representing the experiments and their outcome as revealed simultaneously in the immunofluorescence color channels. The mosaic (bottom) appears to be in agreement with the expected pattern (top).

2.6.3. Microfluidics on a CD

A very interesting and smart application of microfluidic systems is based on a CD-like configuration (Fig.2.11(a)). In a setup like this, several microfluidic functions such as flow sequencing and mixing can be integrated into a CD by balancing the centrifugal and capillary forces. At a static or low speed condition, the liquid does not move due to capillary confinement. By spinning the disc, the capillary force is overcome by the centrifugal force and the fluid is pumped from the center towards the edge of the disc. During this route, the liquid meets reservoirs, mixers and reaction chambers. Whether it stays there and for how long, is controlled by manipulating the spin velocity of the disc, as well as the dimensions of the fluidic components. Samples on the CD can be analyzed by coupling the CD drive with an optical detection system (e.g. absorbance or fluorescence based), compatible with a modified CD reader apparatus (Fig.2.11(b)). This “lab-on-a-disc” platform, as it is termed, has the advantages of low cost fabrication, easy operation, fast response, which make it suitable for point-of-care applications in diagnostic centers.



This configuration has been investigated by several groups [2.24. - 2.26.] and has been used in DNA hybridization, protein analysis, immunoassays, etc. In fact, Gyros company [2.27.] has developed a high throughput system based on this principle. It is capable of accomplishing parallel assays, due to the robotic handling and dispensing of liquids, while the miniaturized reaction chambers allow several tens of reactions to be performed on a CD (Fig.2.12.).

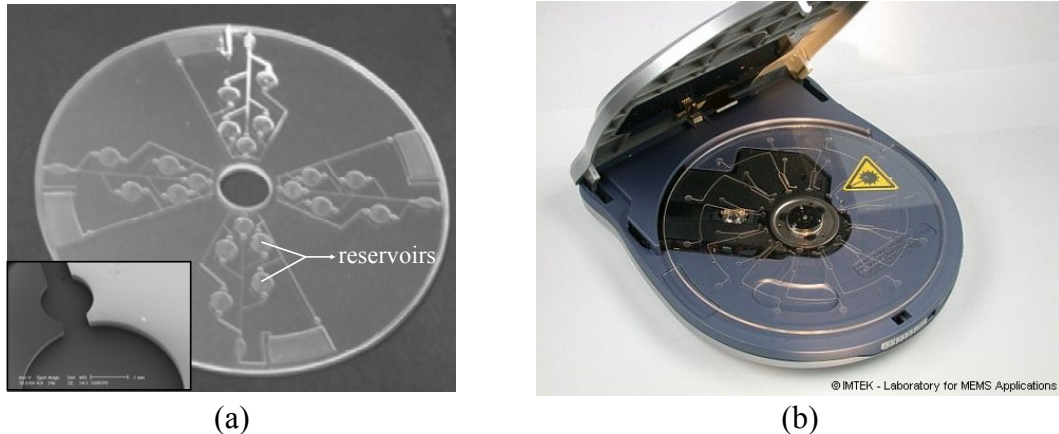


Fig.2.11. (a) CD-based microfluidic platform (inset: SEM image of a reservoir), (b) Bio-Disk reader, developed at IMTEK [2.28.].

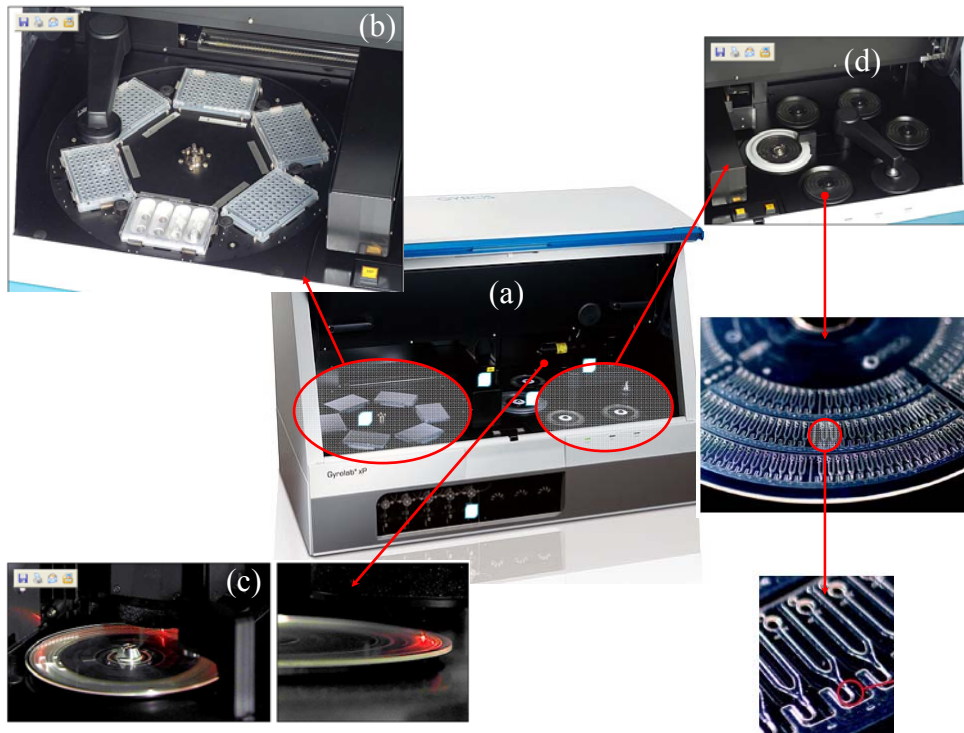


Fig.2.12. Gyrolab xP apparatus: (a) main unit, (b) microplate carousel, (c) laser-induced fluorescence detector, (d) CD spinning station; zoom on a CD area and on a microfluidic unit.



References

- [2.1.] D.S. Ballantine, R.M. White, S.J. Martin, A.J. Ricco, E.T. Zellers, G.C. Frye, H. Wohltjen, "Acoustic Wave sensors", Academic Press Inc., ISBN 0-12-077460-7, 1997.
- [2.2.] A. Janshoff, C. Steinem, "Quartz Crystal Microbalance for bioanalytical applications", *Sensors Update*, vol. 9, pp. 313-354, 2001.
- [2.3.] Lord Rayleigh, "On waves propagating along the plane surface of an elastic solid", *Proc. London Math. Soc.*, vol. 17, pp. 4-11, 1885.
- [2.4.] S.J. Martin, G.C. Frye, S.D. Senturia, "Dynamics and response of polymer-coated Surface Acoustic Wave devices: effect of viscoelastic properties and film resonance", *Anal. Chem.*, vol. 66, pp. 2201-2219, 1994.
- [2.5.] E. Gizeli, "Study of the sensitivity of the acoustic waveguide sensor", *Anal. Chem.*, vol. 72, pp. 5967-5972, 2000.
- [2.6.] A.C. Stevenson, E. Gizeli, N.J. Goddard, C.R. Lowe, "Acoustic Love plate sensors: a theoretical model for the optimization of the surface mass sensitivity", *Sens. Actuat. B-Chem.*, vol. 13-14, pp. 635-637, 1993.
- [2.7.] R.M. White, F.W. Voltmer, "Direct piezoelectric coupling to Surface Acoustic Waves", *Appl. Phys. Lett.*, vol. 7, pp. 314-316, 1965.
- [2.8.] D.J. Harrison, P.G. Glavina, A. Manz, "Towards miniaturized electrophoresis and chemical-analysis systems on silicon: an alternative to chemical sensors", *Sens. Actuat. B-Chem.*, vol. 10, pp. 107-116, 1993.
- [2.9.] D. Hülsenberg, "Glasses for microsystems technology", *Microelectron. J.*, vol. 28, pp. 419-432, 1997.
- [2.10.] R. Bashir, S. Wereley, "BioMEMS and Biomedical Nanotechnology", vol. 4, pg.96, Springer, ISBN 0-387-25566-4, 2006.
- [2.11.] J.C. McDonald, D.C. Duffy, J.R. Anderson, D.T. Chiu, H. Wu, O.J.A. Schueller, G.M. Whitesides, "Fabrication of microfluidic systems in poly(dimethylsiloxane)", *Electrophoresis*, vol. 21, pp. 27-40, 2000.
- [2.12.] H. Schmid, B. Michel, "Siloxane polymers for high-resolution, high-accuracy soft lithography", *Macromolecules*, vol. 33, pp. 3042-3049, 2000.
- [2.13.] D. Paul, A. Pallandre, S. Miserere, J. Weber, J.-L. Viovy, "Lamination-based rapid prototyping of microfluidic devices using flexible thermoplastic substrates", *Electrophoresis*, vol. 28, pp. 1115-1122, 2007.
- [2.14.] Y. Xia, G.M. Whitesides, "Soft Lithography", *Angew. Chem. Int. Ed. Engl.*, vol. 37, pp. 551-575, 1998.
- [2.15.] Y. Xia, G.M. Whitesides, "Soft Lithography", *Annu. Rev. Mater. Sci.*, vol. 28, pp. 153-184, 1998.
- [2.16.] M. Hecke, W.K. Schomburg, "Review on micro molding of thermoplastic polymers", *J. Micromech. Microeng.*, vol. 14, pp. 1-14, 2004.
- [2.17.] A. Bertsch, personal correspondence, 2005.
- [2.18.] A. Bertsch, S. Zissi, J.Y. Jezequel, S. Corbel, J.C. Andre, "Microstereolithography using a liquid crystal display as dynamic mask-generator", *Microsyst. Technol.*, vol. 3, pp. 42-47, 1997.
- [2.19.] P. A. Clerc, L. Dellmann, F. Grétilat, M. A. Grétilat, P. F. Indermühle, S. Jeanneret, P. Luginbuhl, C. Marxer, T. L. Pfeffer, G. A. Racine, S. Roth, U. Staufer,



- C. Stebler, P. Thiébaud, N.F. de Rooij, “Advanced deep reactive ion etching: A versatile tool for microelectromechanical systems,” *J. Micromech. Microeng.*, vol. 8, pp. 272–278, 1998.
- [2.20.] M.E. Vlachopoulou, A. Tserepi, N. Vourdas, E. Gogolides, K. Misiakos, “Patterning of thick polymeric substrates for the fabrication of microfluidic devices,” *J. Phys., Conf. Ser.*, vol. 10, pp. 293-296, 2005.
- [2.21.] B. He, F. Regnier, “Microfabricated liquid chromatography columns based on collocated monolith support structures”, *J. Pharmaceut. Biomed. Anal.*, vol. 17, pp. 925–932, 1998.
- [2.22.] B. He, N. Tait, F.E. Regnier, “Fabrication of nanocolumns for liquid chromatography,” *Anal. Chem.*, vol. 70, pp. 3790–3797, 1998.
- [2.23.] A. Bernard, B. Michel, E. Delamarche, “Micromosaic Immunoassays”, *Anal. Chem.*, vol. 73, pp. 8-12, 2001.
- [2.24.] M.J. Madou, L.J. Lee, S. Daunert, S. Lai, C.-H. Shih, “Design and fabrication of CD-like microfluidic platforms for diagnostics: microfluidic functions”, *Biomed. Microdev.*, vol. 3, pp. 245-254, 2001.
- [2.25.] J. Steigert, M. Grumann, M. Dube, W. Streule, L. Riegger, T. Brenner, P. Koltay, K. Mittmann, R. Zengerle, J. Ducree, “Direct hemoglobin measurement on a centrifugal microfluidic platform for point-of-care diagnostics”, *Sens. Actuat. A-Phys.*, vol. 130–131 pp. 228–233, 2006.
- [2.26.] J.M. Chen, P.-C. Huang, M.-G. Lin, “Analysis and experiment of capillary valves for microfluidics on a rotating disk”, *Microfluid. Nanofluid.*, vol. 4, pp. 427-437, 2008.
- [2.27.] www.gyros.com
- [2.28.] http://www.imtek.de/anwendungen/content/workinggroups/lab-on-a-chip/lab-on-a-chip_biodisk_b1_en.php



Chapter 3. Experimental instrumentation



*Microarray-based diagnostic AmpliChip CYP450 Test, by Roche Diagnostics
<http://www.amplichip.us>*





Chapter 3. Experimental instrumentation

This section describes the measurement instrumentation and experimental techniques used throughout the project. They are summarized in this chapter as they were repeatedly used in the experiments with all kinds of samples, no matter whether the standard flow configuration was used, or the μ F-on-SAW one. Figure 3.1. shows the connections among the various instruments/components as they were used in measurements with μ F-on-SAW setup. The various components and instruments are described in the following sections of this chapter.

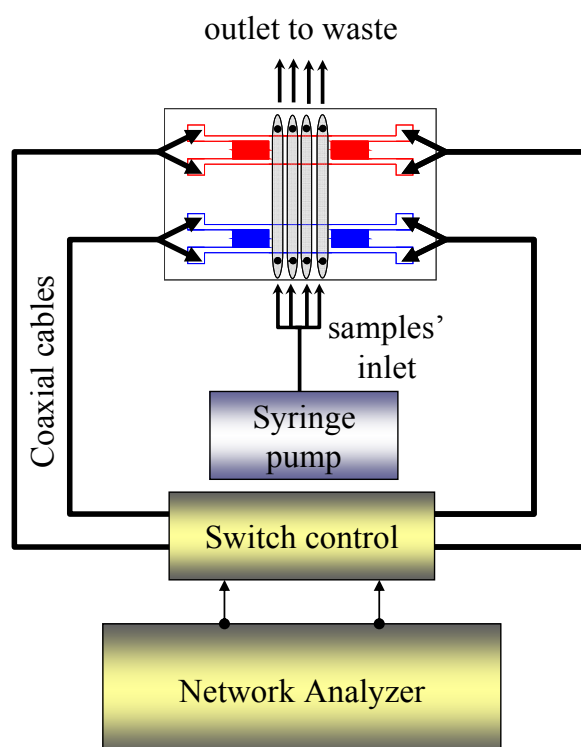


Fig.3.1. Schematic of the connections between components in a typical biosensing experiment using the μ F-on-SAW configuration.

3.1. Network Analyzer

As it was described in sec.2.2., the operating principle of an acoustic sensor is the interaction of an acoustic wave with matter. However, the input (as well as the output) of an acoustic device is actually an electric signal, which is “transformed” into a mechanical oscillation only due to the piezoelectric phenomenon. Thus, what is eventually measured, is some electrical properties, which are then correlated to the wave characteristics (amplitude and phase). For this reason, an electronic apparatus is needed in order to probe the change in electrical features of the sensor. This apparatus is called Network Analyzer and, although misleading, the term “network” clearly has nothing to do with computer networks; it refers to electric networks, instead. Such a machine is used to measure electrical parameters of devices, systems, components, etc, which are connected to it.



More specifically, in our case it is used to measure the transmission coefficient, or scattering parameter (S_{21}), i.e. the ratio of output over input voltage:

$$S_{21} = \frac{V_{out}}{V_{in}} = \frac{V_{o,out} e^{i\omega t}}{V_{o,in} e^{i\omega(t-\phi)}} \quad (\text{eq.3.1.})$$

The scattering parameter, S_{21} , is the one (among others) that corresponds to the transmitted signal. As both V_{in} and V_{out} are complex quantities, their ratio is complex as well, and the Network Analyzer measures both the magnitude of S_{21} (usually the *logarithmic* magnitude, termed “insertion loss”, expressed in *dB*) and its phase, expressed in degrees (*deg*). Because the insertion loss corresponds to the amplitude, these two terms will be interchanged in the text.

Insertion loss and phase are plotted against a span of frequencies, revealing the frequency response of the sensor; the frequency peak is selected as the operating frequency, as it is the one where the losses are minimum and thus, the maximum energy is transmitted through the device. A typical spectrum of insertion loss and phase vs. frequency appears in Fig.3.2., indicating how the signal change is measured.

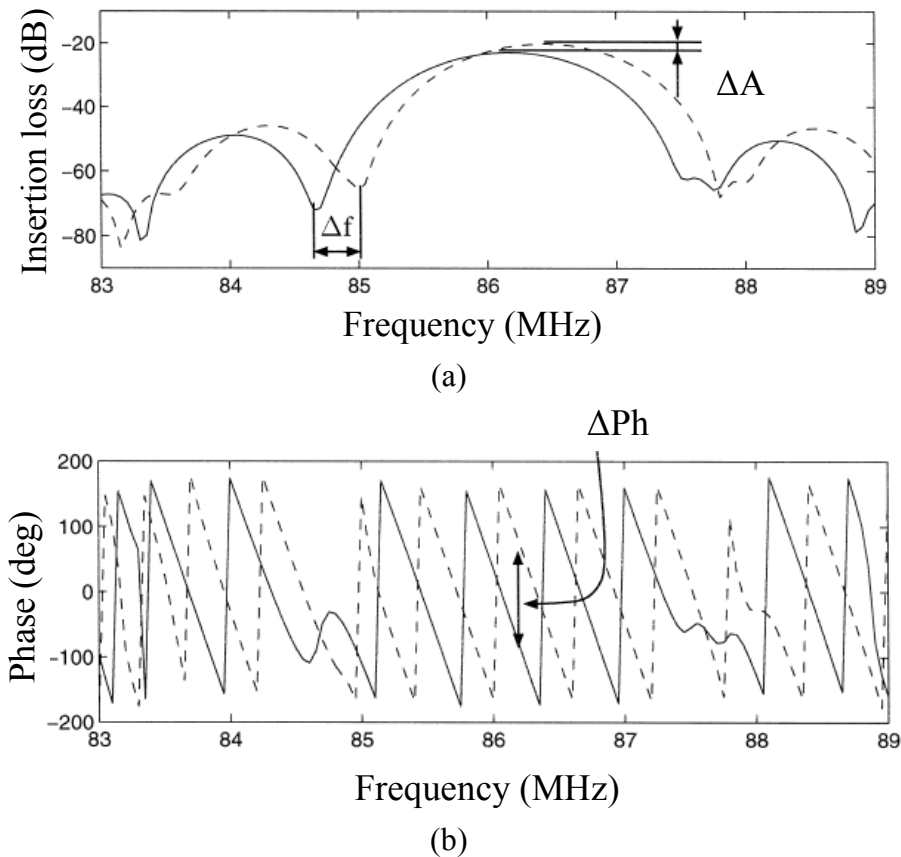


Fig.3.2. (a) Insertion loss vs. frequency during the propagation of the acoustic wave, (b) phase vs. frequency. Dashed and solid lines correspond to a sensor response prior and after sample loading, respectively.

The apparatus that was used for all the experiments was an HP 8753ES Network Analyzer (NA) (Fig.3.3.). A switch control unit (Agilent 3499A) was connected to the Network Analyzer in order to probe both sensor elements of the dual chip simultaneously. Measurements of amplitude and phase changes (ΔA and ΔPh ,



respectively) were performed at the transmission regime and an HPVVEE software was used for data acquisition. A marker was “following” the peak of the insertion loss vs. frequency spectrum (Fig.3.2.) probing the damping and shift of the peak (corresponding to the insertion loss and phase changes). Data points were recorded every 30 s.

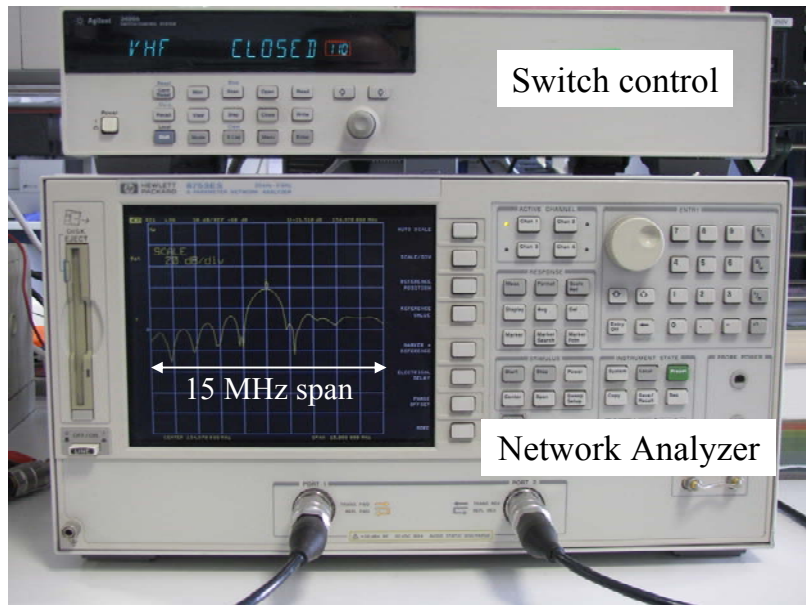
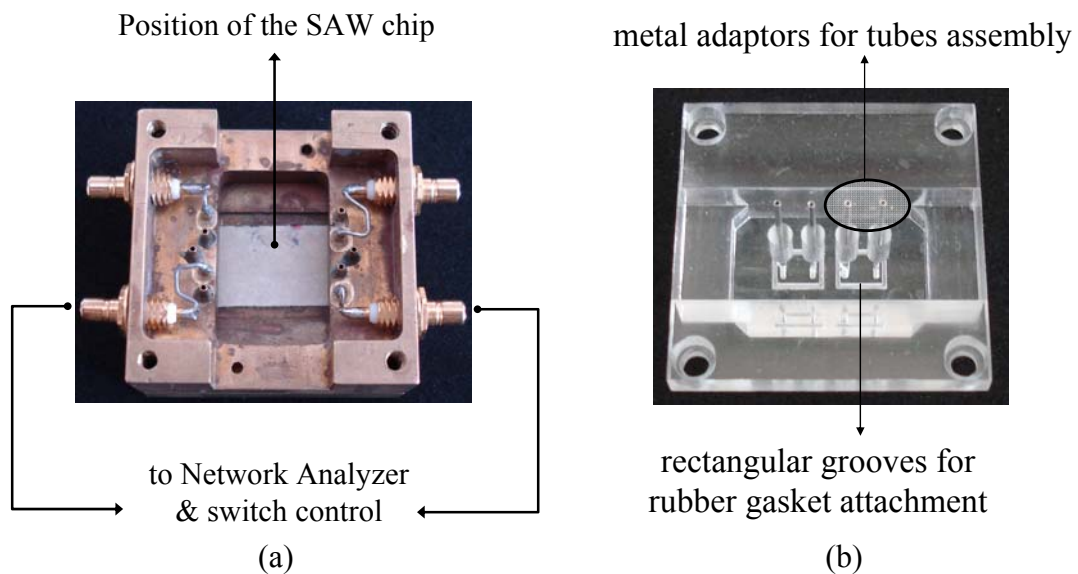


Fig.3.3. Network Analyzer and switch control unit. The insertion loss vs. frequency spectrum is visible on the screen for a 15 MHz frequency span.

The sensor chip was tightly mounted on a metal holder and was connected to the Network Analyzer via coaxial cables. For the experiments utilizing the total sensing area, the standard flow cell was used (dual flow cell for the dual sensor chip). It is made of plexiglass, with four metal tubings permanently fixed for fluid in- and outlet. In addition, a rectangular rubber gasket was used to facilitate smooth contact between the flow cell and the pressure-sensitive device (Fig.3.4.).



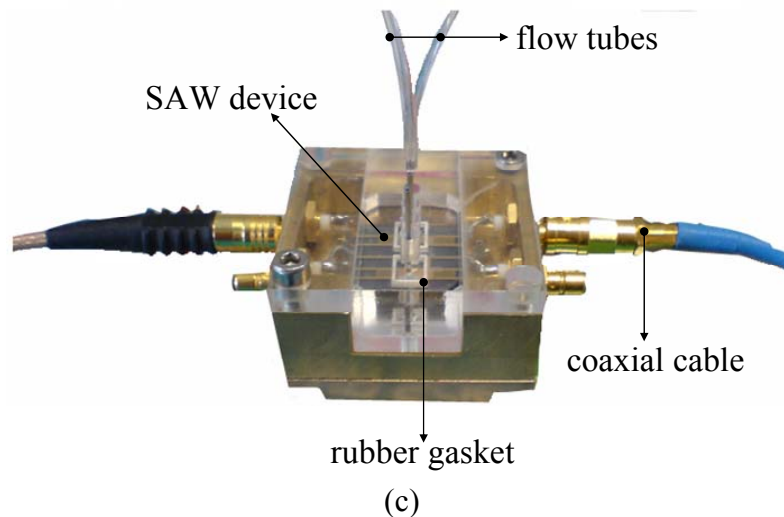


Fig.3.4. (a) Metal holder, (b) flow cell, and (c) assembled components of a standard SAW configuration.

3.2. Surface Plasmon Resonance

The Surface Plasmon Resonance (SPR) optical biosensor SR7000 from Reichert (Fig.3.5(a)) was used in order to verify some results that emerged from the acoustic measurements (sec.9.). SPR principle was briefly described in sec.1.5.2. In the particular system the laser beam was at 780 nm wavelength. The sensor chip (XanTec bioanalytics GmbH), like the majority of the SPR chips, was a 1×1 cm glass slide, with a 50 nm gold layer on top (Fig.3.5(b)). The chip was mounted on the apparatus and sealed with a plastic flow cell; the sensing area, as defined by the laser spot, was 12 mm².



(a)



(b)

Fig.3.5. (a) The SPR SR7000 apparatus used, (b) typical sensor chip mounted on the SPR biosensor.

In a typical SPR setup a gold-coated glass slide is in contact with liquid (from the gold side) and the reflected light beam on the glass side is detected. When a light beam hits the chip there is a particular incidence angle above which total internal reflection (TIR) takes place. Although no light is coming out of the prism in TIR, the electric field of the photons is not zero, but extends about a quarter of a wavelength beyond the reflecting surface. For a specific incidence angle, the photons interact with the electron clouds of the gold, and are transformed into surface plasmons. This



happens when the wave vector of light equates the plasmon wave vector. This resonance effect enhances the electric field amplitude, which is of evanescent nature and decays within a penetration depth of a few hundreds of nanometers into the liquid. The plasmon resonance (and energy loss from the photons) appears as a sharp drop in the reflected intensity reaching the detector. The angle at which this intensity minimum occurs changes proportionally to the refractive index at the surface, which, in turn, is proportional to the bound mass, i.e., the surface concentration, Γ . Thus, surface concentration is calculated via the change in the angle of resonance minimum. As soon as Γ is known, the film thickness, d , can be deduced from [3.1.]:

$$d \cdot \Delta n = \frac{dn}{dc} \Gamma \quad (\text{eq.3.2.})$$

where Δn is the refractive index difference between the pure buffer and the pure protein film, the latter being taken as 1.41 [3.2.], [3.3.]. The refractive index increment, dn/dc expresses the proportionality between the refractive index of protein solutions and their bulk mass concentration and is given by $dn/dc = 0.188 \text{ ml/g}$ [3.4.]. This value has been observed for a variety of proteins and for solutions up to very high concentrations (almost 50 % w/w); thus, extrapolation from bulk protein solutions to protein films (where the concentration is typically higher than 50 %) can be made.

3.3. Pumping systems

The biosensing experiments carried out throughout the project were performed in a flow-through manner, rather than static one, making the use of pumping systems necessary. In particular two types of pumps were used:

- (i) Peristaltic pump: For the experiments with the standard flow cell (when the total sensor surface was used) a Gilson peristaltic pump promoted fluid propulsion (Fig.3.6(a)). The flow rate was kept at 20 $\mu\text{L}/\text{min}$; PVC tubes of 0.25 mm inner diameter were adjusted to the flow cell.
- (ii) Syringe pump: For the experiments where the newly developed μF -on-SAW setup was used, a syringe pump (HARVARD PHD2000 programmable, Fig.3.6(b)) was considered more appropriate due to its better flow stability and compatibility with the narrow capillary tubes attached to the microsystem. The flow rate was set 5 $\mu\text{L}/\text{min}$; 1 mL plastic disposable syringes were used with the pump and special capillary tubes were attached (see sec.5.4.). The syringe pump was preferred over the peristaltic (used with the standard configuration) for the μF -on-SAW setup because it can reach lower and more stable flow rates, which is reflected at the signal as smooth baseline.



(a)



(b)

Fig.3.6. Pumps used during the experiments: (a) peristaltic pump, for the experiments with the standard flow cell, (b) syringe pump, suitable for the μ F-on-SAW setup.

3.4. Spin coating

Spin-coating was used in order to deposit the polymer waveguide on the sensor chip. It is a fast and easy procedure, without need of sophisticated equipment. The thickness of the deposited film depends primarily on the spinning speed: the higher the speed the thinner the film. Other deposition parameters that affect the thickness are the spinning time, as well as the acceleration steps before reaching the final coating step; temperature, solvent and concentration of the solution are some other affecting parameters.

In our case, the various waveguide thicknesses were achieved by keeping the spinning parameters constant and altering the concentration of the PMMA solutions, which were 8%, 14%, and 17%. The % concentration in this case was calculated as $g_{PMMA} / g_{solvent}$, where solvent was 2-ethoxyethyl acetate-EET (>99%, Aldrich). The film thickness was measured experimentally with profilometry and was in agreement with published data [3.5.]. The correspondence between PMMA solution concentration and film thickness (error is $\pm 0.10 \mu\text{m}$) was:

- 8% PMMA $\rightarrow 0.35 \mu\text{m}$
- 14% PMMA $\rightarrow 0.70 \mu\text{m}$
- 17% PMMA $\rightarrow 1.10 \mu\text{m}$

The following table and corresponding figure indicate the procedure during spinning (“ramp” represents the acceleration and refers to the time needed to reach the desired speed).

Thermal treatment in an oven at 200°C for 2 h followed the spin-coating of the device, in order to achieve solvent evaporation and PMMA solidification. It should also be noted that the uniformity of PMMA thickness is essential for the proper operation of the μ F-on-SAW setup, especially for the reproducibility of sensitivity among the sub-areas.



Tab.3.1. Spin coating protocol

Parameters	Values
Speed-1 (rpm)	1900
Accelleration-1 (“ramp1”, s)	6
Time-1 (s)	3
Speed-2 (rpm)	3000
Accelleration-2 (“ramp2”, s)	2
Time-2 (s)	2
Speed-3 (rpm)	4000
Accelleration-3 (“ramp3”, s)	3
Time-3 (s)	30
Deceleration (“ramp4”, s)	10



Fig.3.7. P6700 spin-coater model, Specialty Coating Systems Inc.

3.5. Gold sputtering and plasma etching

On top of PMMA waveguide a 20-nm-thick Au layer was sputter coated to facilitate biomolecule adsorption. A Bal-Tec SCD 050 sputter coater was used. Au targets were also acquired from Bal-Tec. Argon was the sputtering gas and the chamber pressure was set at 4×10^{-2} mbar prior to sputtering, with the current being 40 mA. During the sputtering procedure of the SAW sensor chip, an in-house mask was used, with which: (i) the IDT areas were protected so as to avoid short circuiting via Au deposition between the IDTs, and (ii) both devices' sensing areas were simultaneously coated with Au. After sputtering, the device was baked at 150 °C for 30 min to ensure better adhesion between the Au and PMMA.

As the biochips were not disposable, their full re-usability should be ensured by regenerating the Au surface after each experiment. Chemical methods with organic solvents for removal of the adsorbed biomolecules were avoided, as they would dissolve the PMMA waveguide. Thus, a physical (in contrast to chemical) process was followed for surface cleaning and regeneration; plasma cleaning. Plasma cleaning involves the removal of impurities and contaminants from surfaces through the use of energetic plasma created from gaseous species (atmospheric air in our case). Lower energy plasmas are used for plasma cleaning versus plasma etching purposes. The plasma is created by using high radio-frequency to ionize a low pressure gas. The energetic, ionic species diffuse towards the surface, adsorb and react with species on the surface to be cleaned. Gaseous products are often formed, which are removed by a vacuum system (a mechanical pump in our case). The energetic species also clean the surface by collision with the surface, knocking off species from the surface.

The used system was the Expanded Plasma Cleaner & Plasma Flo™ (Fig.3.8.). The etching conditions were 600 mTorr chamber pressure, 5 min etching time with 30 W power applied to the RF coil. With proper calibration, it was observed that under these conditions, no substantial removal of the top gold layer existed, so the biochip was re-used for several times.

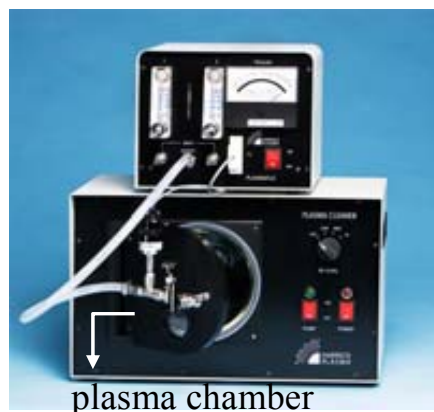


Fig.3.8. Expanded Plasma Cleaner & Plasma FloTM from Harrick Scientific Corp.

3.6. Biomolecules used in the work

The biomolecules used in this work are the following (just mentioned here because their description and reasons why they were selected are discussed appropriately in the suitable section where they belong):

- Neutravidin (Pierce) and Protein G (Calbiochem) for binding with biotinylated molecules (b-PrG, b-PrA, b-BSA, b-IgG, from Sigma) and IgG, respectively. For details, see sec.6.3.2.
- Cardiac biomarkers and their corresponding antibodies for the clinical application: Creatine Kinase MB (CK-MB) and a-CK-MB mAb were purchased from RayBiotech Inc. and Santa Cruz Biotechnology Inc., respectively. Cardiac Reactive Protein (CRP) and a-CRP mAb, D-dimer and a-D-dimer mAb, Pregnancy Associated Plasma Protein-A (PAPP-A) and a-PAPP-A mAb were all purchased from HyTest. For details see sec.8.3.

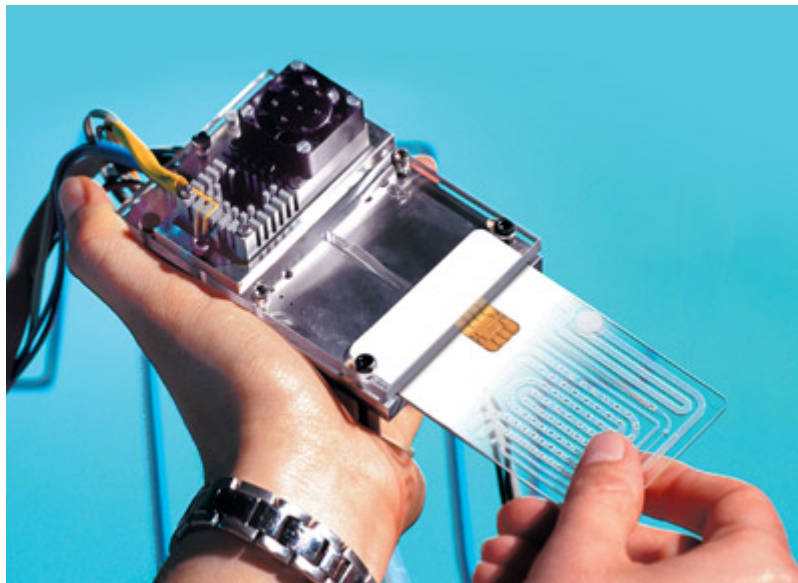
In addition, the processes involved in microfluidics fabrication (soft lithography) as well as the materials involved in it will be thoroughly described in sec.5.3., as they are by themselves part of the experimental work of the project.

References

- [3.1.] J.A. de Feijter, J. Benjamins, F.A. Veer, “Ellipsometry as a tool to study the adsorption behavior of synthetic and biopolymers at the air-water interface”, *Biopolymers*, vol. 17, pp. 1759-1772, 1978.
- [3.2.] L.K. Wolf, Y. Gao, R.M. Georgiades, “Sequence-dependent DNA immobilization: specific versus non-specific contributions”, *Langmuir*, vol. 20, pp. 3357-3361, 2004.
- [3.3.] S. Lousinian, S. Logothetidis, “Optical properties of proteins and protein adsorption study”, *Microelectron. Eng.*, vol. 84, pp. 479-485, 2007.
- [3.4.] H.J. Hinz, “Structural and Physical Data I”, vol. 2a, pp. 8001-8008, Springer-Verlag ISBN 978-3-540-56083-8, 2003.
- [3.5.] D.B. Hall, P. Underhill, J.M. Torkelson, “Spin coating of thin and ultrathin polymer films”, *Polym. Eng. Sci.*, vol. 38, pp. 2039–2045, 1998.



Chapter 4. Selection of the optimum device configuration for μ F-on-SAW



Siemens' Quicklab for DNA tests on handheld devices
<http://www.mtbeurope.info/news/2005/506024.htm>





Chapter 4. Selection of the optimum device configuration for μ F-on-SAW

4.1. Introduction

One of the two main components of the microsystem is the sensor itself. Even though the fabrication of the SAW devices was not a scope of this work and, thus, they were provided by manufacturers and collaborators, there was a large number of device configurations with varying operating parameters which should be investigated in the beginning of the work. The objective was to compare all the available configurations and balance their pros and cons, so as to select the most suitable one for the desired application of multi-sensing. The following three parameters varied in the compared devices:

- (i) Piezoelectric substrate material: Lithium tantalate (LiTaO_3) vs. quartz (Q)
- (ii) Operating Frequency: 50 vs. 155 MHz
- (iii) Polymer waveguide thickness (0, 0.35, 0.70, 1.10 μm)

Under various combinations of the above parameters, 12 different device configurations emerged, which are summarized in the following Table.

Tab.4.1. SAW device configurations emerging from variations of their functional parameters.

Substrate material	Quartz				LiTaO_3							
Operating frequency (MHz)	155				50				155			
Waveguide thickness (μm)	0	0.35	0.70	1.10	0	0.35	0.70	1.10	0	0.35	0.70	1.10
Abbreviations	Q155_0	Q155_0.35	Q155_0.70	Q155_1.10	L50_0	L50_0.35	L50_0.70	L50_1.10	L155_0	L155_0.35	L155_0.70	L155_1.10
 <div style="display: flex; justify-content: space-around; margin-top: 5px;"> Q155 L155 </div>	<p><i>Fig.4.1. Real size pictures of the two different designs used. The L50 device has the same geometrical design as the L155.</i></p>											



In order to be characterized, the devices were subjected to various kinds of surface perturbations, namely:

- (i) Au deposition, representing pure mass loading
- (ii) Aqueous glycerol solutions of various concentrations representing pure viscous loading of a broad viscosity range, spanning both Newtonian and Maxwellian regions
- (iii) Adsorption of proteins
- (iv) Viscoelastic layer loading in air and liquid

This systematic study led to sensitivity evaluation and derivation of solid conclusions about the interaction of acoustic waves with the various types of surface perturbations. Furthermore, not only did this study reveal the optimum configuration for the development of the multi-sensor platform, but it also pointed out the strong and weak points of *all* the above device configurations, suggesting the applications that each one is most suitable for.

4.2. Analysis of SH-SAW perturbations

The interaction of acoustic waves with matter is the physical effect behind the function of the SH-SAW devices as sensors. There are several kinds of perturbations that an SH-SAW may undergo, depending on the kind of sample that is loaded on the acoustic sensor. Three case studies have been traditionally analyzed according to the type of material under test: case 1, a rigid mass layer [4.1.]; case 2, a purely viscous liquid [4.2.]; case 3, a viscoelastic film [4.3.], but also combinations of the above in biological materials, such as protein multi-layer structures [4.4.], DNA [4.5.], or liposomes [4.6.]. A surface perturbation always changes the wave characteristics, i.e., amplitude and velocity. The complex propagation factor γ of the acoustic travelling plane wave (eq.2.3.) is related to the wave energy and velocity as follows [4.7.]:

$$\frac{\Delta\gamma}{k_o} = \frac{\Delta\alpha}{k_o} - j \frac{\Delta v}{v_o} \quad (\text{eq.4.1.})$$

where k_o , α , v_o , and v are the wavenumber, the attenuation and the phase velocity before and after the perturbation of the acoustic wave, respectively; $\Delta\alpha/k_o$, $\Delta v/v_o$ are the normalized wave attenuation and fractional change in wave velocity, respectively.

These wave-related quantities, $\Delta\alpha/k_o$ and $\Delta v/v_o$, are directly proportional to the Network Analyzer measured quantities, change in amplitude (ΔA) and phase (ΔPh) of the acoustic wave, respectively. The former set is preferred when a common graph axis is used, as they are both measured in “parts per million (ppm)” and also because they are directly related to the surface mechanical impedance (see below); the latter set is preferred when direct correlation with the N.A. quantities is desired. Throughout the text both notations will be used according to the occasion, and the equations relating them are the following [4.4.]:

$$\Delta Ph(\text{deg}) = L_s k_o \cdot \frac{360}{2\pi} \cdot \frac{\Delta v}{v_o} \quad (\text{eq.4.2(a)})$$

and

$$\Delta A(\text{dB}) = 20 \log(e) \cdot L_s k_o \cdot \frac{\Delta\alpha}{k_o} \quad (\text{eq.4.2(b)})$$

where L_s is the length of the propagation path of the wave.



For every case of surface perturbation there is a corresponding (complex) surface mechanical impedance, Z , which describes it. In all cases, Z is related to the wave parameters in the following way [4.8.], [4.9.]:

$$\frac{\Delta\alpha}{k_o} - j \frac{\Delta v}{v_o} = c \cdot Z \quad (\text{eq.4.3.})$$

The term c depends on the device material and geometry, the surface particle velocity and the wave power density; as long as the device used is the same, the value of c remains constant [4.9.]. The mechanical (or acoustic) impedance is characteristic of the nature of each loaded sample, and through that, materials' properties are evaluated, as will be described in the following theoretical and experimental sections.

4.2.1. Case 1: Mass loading

The simplest perturbation of an acoustic sensor rises from rigid mass loading on its surface. The mechanical impedance is then given by the term:

$$Z_{mass} = j \cdot \omega \rho h \quad (\text{eq.4.4.})$$

where ω , ρ , h are the angular operating frequency, the mass density, and the thickness of the deposited film, respectively [4.8.]. In this case a rigid/elastic solid (the term "elastic" is used as a contrast to the terms "viscous" and "viscoelastic" used later) follows synchronously the oscillation of the sensor (Fig.4.2.) resulting in zero change in amplitude, i.e., zero energy losses, a result of equating the real and imaginary parts of eq.4.3. and eq.4.4. Then the fractional change in velocity is directly proportional to the layer thickness.

In a simplified representation incorporating the Network Analyzer measured parameters:

$$\Delta Ph = S_m \Delta m \quad (\text{eq.4.5.})$$

where Δm is the deposited mass and the proportionality constant S_m represents the mass sensitivity. Equation 4.5. is equivalent to the Sauerbrey relation [4.1.].

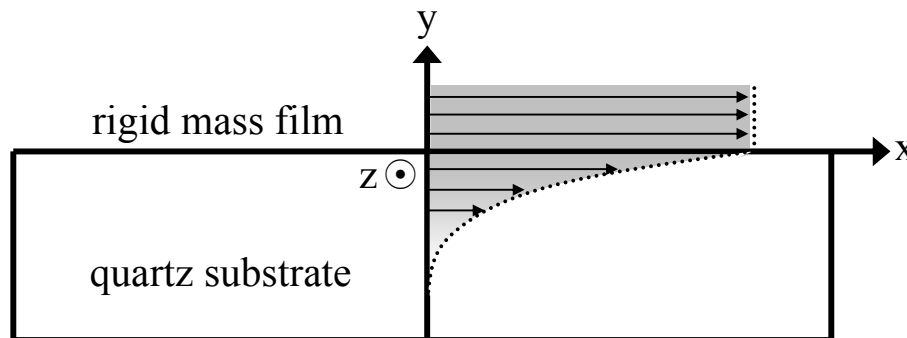


Fig.4.2. Cross-sectional view of a shear-horizontal wave particle displacement (propagation along z-axis) in an ideal mass layer; as it appears, the mass layer follows synchronously the shear oscillation at the surface.



4.2.2. Case 2: Viscous loading (Newtonian liquid)

The surface perturbation that rises from loading of non-adsorbing pure viscous liquids or solutions on the sensor is characterized by the following mechanical impedance [4.8.], [4.10.], [4.11.]:

$$Z_{visc} = (1 + j) \sqrt{\frac{\omega \rho \eta}{2}} \quad (\text{eq.4.6.})$$

where ρ and η are the density and viscosity of the liquid, respectively.

From the above equation it is evident that viscous loading gives rise to *both* amplitude and phase change. The fact that dissipation/damping is introduced in a liquid sample makes the wave decay within a penetration depth, δ , in the liquid (Fig.4.3.):

$$\delta = \sqrt{\frac{2\eta}{\rho\omega}} \quad (\text{eq.4.7.})$$

As the penetration depth is frequency dependent, for the 155 MHz device used, $\delta = 50 \text{ nm}$ (for buffer or water samples, with $\rho = 1000 \text{ kg/m}^3$, $\eta = 0.001 \text{ Pa}\cdot\text{s}$).

Equating the real and imaginary parts of eq.4.3. and eq.4.6. we get:

$$\frac{\Delta\alpha}{k_o} = \frac{\Delta v}{v_o} = c \sqrt{\frac{\omega \rho \eta}{2}} \quad (\text{eq.4.8.})$$

and the relation between the NA measured quantities and the liquid properties (ρ , η) becomes:

$$\Delta A = S_{visc,A} \sqrt{\rho\eta} \quad (\text{eq.4.9(a)})$$

and

$$\Delta Ph = S_{visc,Ph} \sqrt{\rho\eta} \quad (\text{eq.4.9(b)})$$

The proportionality constants $S_{visc,A}$ and $S_{visc,Ph}$ include c and ω and represent the sensitivity of amplitude and phase, respectively, upon loading samples with varying $(\rho\eta)^{1/2}$. Therefore, according to the above equations, both wave propagation parameters are proportional to the square root of density-viscosity product [4.2.], [4.10.], [4.11.], [4.12.] and in practice, the sensitivity is expressed by the slope of a ΔPh vs. $(\rho\eta)^{1/2}$ (or, ΔA vs. $(\rho\eta)^{1/2}$) plot.

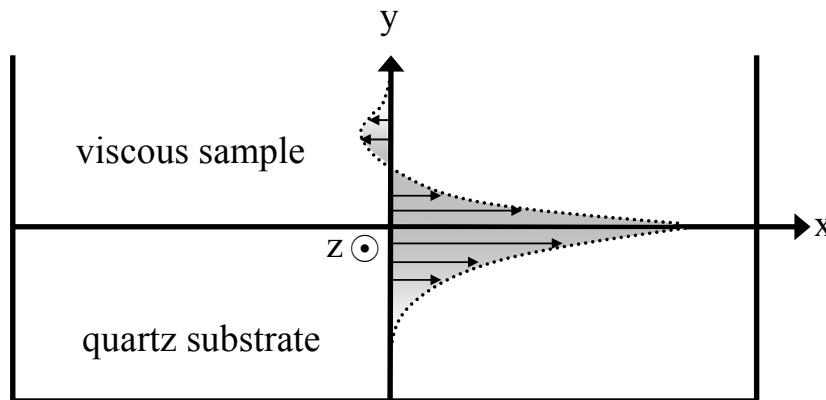


Fig.4.3. Cross-sectional view of a shear-horizontal wave particle displacement (propagation along z-axis) in a Newtonian liquid; the displacement profile of the liquid particles appears to be decaying rapidly within a penetration depth, δ , in the fluid.



4.2.3. Case 3: Viscous loading (Maxwell liquid)

The relationships expressed in eq.4.9(a) and eq.4.9(b) remain linear up to a critical viscosity value η_c , where the sample behaves as Newtonian fluid. Beyond that, the signal reaches saturation and the sensor response can be explained by considering the liquid as Maxwellian and modeling it accordingly [4.13.]. The Maxwell model introduces a viscoelastic response of liquids at high frequencies. The model consists of a spring and a dashpot connected in series. The dashpot represents energy losses and is characterized by η , the viscosity, whereas the spring represents the energy storage and is characterized by μ , the elastic (shear in our case) modulus, also known as the “high frequency rigidity modulus”, G_∞ . These two quantities are related through the relaxation time, τ , which is the characteristic time for the transition between viscous and elastic behavior [4.14.], [4.15.]:

$$\tau = \frac{\eta}{\mu} \quad (\text{eq.4.10.})$$

Although for complex materials a distribution of relaxation times is necessary for their complete description, the Maxwell model uses a single relaxation time, which is enough to characterize pure liquids and solutions [4.12.], [4.13.]. The viscoelastic behavior of liquids under oscillatory deformation (shear direction in our case) is expressed through the complex shear modulus G^* , given in its general form as [4.14.], [4.16.]:

$$G^* = G1 + jG2 = \frac{j\omega\eta}{1 + j\omega\tau} \quad (\text{eq.4.11(a)})$$

or:

$$G^* = \left[\mu \frac{\omega^2 \tau^2}{1 + \omega^2 \tau^2} \right] + j \cdot \left[\mu \frac{\omega \tau}{1 + \omega^2 \tau^2} \right] \quad (\text{eq.4.11(b)})$$

The critical quantity $\omega\tau$ depends both on the test sample through τ and on the angular frequency in use, ω . The following regimes are identified:

- (i) For $\omega\tau \ll 1$ the oscillation time ($T_{SAW} = 1/\omega$) is greater than the relaxation time and the sample has sufficient time to respond to the shear “deformation”. In that case, $G2$ is the dominant factor (with $G2 \rightarrow \omega\eta$ and $G1 \rightarrow 0$) and the liquid exhibits purely viscous behavior.
- (ii) For $\omega\tau \gg 1$ the oscillation time is smaller than the relaxation time and the sample does not have sufficient time to respond to the shear deformation. Energy is not lost in the form of viscous dissipation but it is stored elastically as the liquid exhibits an amorphous solid-like behavior. In that case $G1$ dominates and reaches the value μ of the Maxwell model.
- (iii) For $\omega\tau = 1$ the transition from Newtonian to Maxwellian regime takes place.



4.2.4. Case 4: Viscoelastic layers in air and liquid

The samples that are loaded on an acoustic sensor are often deviating from the ideal cases of mass and viscous loading. Polymer films in air, protein and DNA biological layers and multi layers in contact with overlying liquid are some of these examples. The interactions of acoustic waves with these materials are, still, obeying to eq.4.3. only that the acoustic impedance is much more complicated for these cases.

In case of a viscoelastic film in air, the acoustic impedance is given by the following formula incorporating a hyperbolic tangent component (\tanh):

$$Z_{air} = \sqrt{\rho_F G} \cdot \tanh\left(j\omega h \sqrt{\frac{\rho_F}{G}}\right) \quad (\text{eq.4.12.})$$

where ρ_F and h are the film density and thickness, and $G = G_1 + jG_2$ the complex shear modulus of the film. The formula takes into account the propagation of the wave in the viscoelastic medium and the profile of particle displacement within it.

In cases when non-ideal samples (like pure mass and/or liquid) are combined, the linear combination of the individual acoustic impedances is not correct. Thus, for a viscoelastic film in contact with liquid (the typical representation of a protein film with buffer, Fig.4.4.), the acoustic impedance is not given by the linear combination of eq.4.12. with eq.4.6. but is expressed in eq.4.13. taking into account an interdependence between the liquid and the viscoelastic film:

$$Z_{liq} = \sqrt{\rho_F G} \frac{\sqrt{j\omega\rho_L\eta_L} \cdot \cosh\left(j\omega h \sqrt{\frac{\rho_F}{G}}\right) + \sqrt{\rho_F G} \cdot \sinh\left(j\omega h \sqrt{\frac{\rho_F}{G}}\right)}{\sqrt{\rho_F G} \cdot \cosh\left(j\omega h \sqrt{\frac{\rho_F}{G}}\right) + \sqrt{j\omega\rho_L\eta_L} \cdot \sinh\left(j\omega h \sqrt{\frac{\rho_F}{G}}\right)} \quad (\text{eq.4.13(a)})$$

or,

$$Z_{liq} = \sqrt{\rho_F G} \frac{\sqrt{j\omega\rho_L\eta_L} + \sqrt{\rho_F G} \cdot \tanh\left(j\omega h \sqrt{\frac{\rho_F}{G}}\right)}{\sqrt{\rho_F G} + \sqrt{j\omega\rho_L\eta_L} \cdot \tanh\left(j\omega h \sqrt{\frac{\rho_F}{G}}\right)} \quad (\text{eq.4.13(b)})$$

where ρ_L and η_L are the density and viscosity of the overlying liquid, respectively.

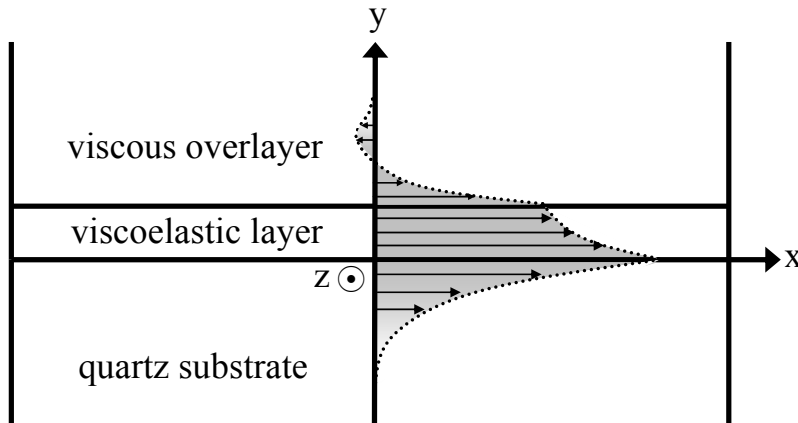


Fig.4.4. Cross-sectional view of a shear-horizontal wave particle displacement (propagation along z-axis) in a combination of a finite viscoelastic layer and a semi-infinite Newtonian liquid; in principle the linear combination of the two is not valid.



Equating the real and imaginary parts of Z_{air} (and Z_{liq}) with their corresponding real and imaginary parts of $\Delta\gamma/k_o$ in eq.4.3., information about the film properties can be deduced. It is clear though, that neither eq.4.12. nor eq.4.13. can be directly separated analytically into real and imaginary parts, so that they are equalized with $\Delta\alpha/k_o$ and $\Delta v/v_o$, which is why it is often needed to turn to computational methods.

Only under conditions can eq.4.12. be simplified to some extent, by substituting $\tanh(jx)$ with $j\tan(x)$ and performing the Taylor series of $\tan(x) = x + x^3/3$. In that case, and after algebraic calculations, it is possible to separate Z_{air} analytically into distinct real and imaginary parts:

$$\frac{\Delta\alpha}{k_o} = c \frac{\omega^3 h^3 \rho^2}{3} \frac{G2}{G1^2 + G2^2} \quad (\text{eq.4.14(a)})$$

$$\frac{\Delta v}{v_o} = c \left(\omega \rho h + \frac{\omega^3 h^3 \rho^2}{3} \frac{G1}{G1^2 + G2^2} \right) \quad (\text{eq.4.14(b)})$$

However, this is not the case for eq.4.13. An additional difficulty, is the fact that in eq.4.12. and eq.4.13. there are too many unknown quantities ($G1$, $G2$, ρ_F , h , etc.) while only two known measured quantities (ΔA , ΔPh). Thus, there should either be some assumptions for some of the unknown parameters so that they are reduced, or, alternatively, measure the same sample in more than one frequency and extract two or three pairs of measured quantities (i.e., having more input numbers, equal to the number of unknown ones; this is done by the Qsense apparatus and simulation software. Even though it was beyond the scope of this work to deal with numerical solutions and simulation of the above equations to extract protein layer properties, in chapter 9 it is described how a quantitative determination of proteins' viscoelastic properties (under assumptions/conditions) can be derived.

Finally, a useful qualitative derivation out of eq.4.13., which will be used in sec.9., is the following: plotting the imaginary part (representing ΔPh , or $\Delta v/v_o$) against the film thickness, h , reveals a linear relation between the two, up to the penetration depth (Fig.4.5., for $h < 50 \text{ nm}$, assuming that $G1 = 5 \times 10^5 \text{ N/m}^2$, $G2 = 5 \times 10^6 \text{ N/m}^2$, and $\rho_{film} = 1050 \text{ kg/m}^3$, which are reasonable values as discussed in sec.9.5.). Due to this linearity, it is safe to assume that the phase change is proportional to the mass uptake within the penetration depth (whereas for thicknesses beyond the penetration depth the proportionality ceases, Fig.4.5. for $h > 50 \text{ nm}$).

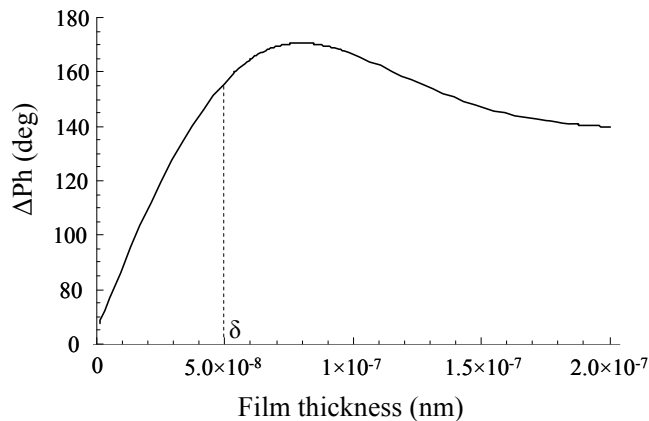


Fig.4.5. Theoretical representation of ΔPh with film thickness, when a viscoelastic layer with a liquid overlayer is deposited on the sensor. It appears that within the penetration depth ($\sim 50 \text{ nm}$) a linear relation can be assumed.



The various expressions for complex acoustic impedance depending on the loaded material are summarized in Tab.4.2. and the “flow” of actions taken in order to characterize a material with a SAW sensor, in general, is shown in Fig.4.6.

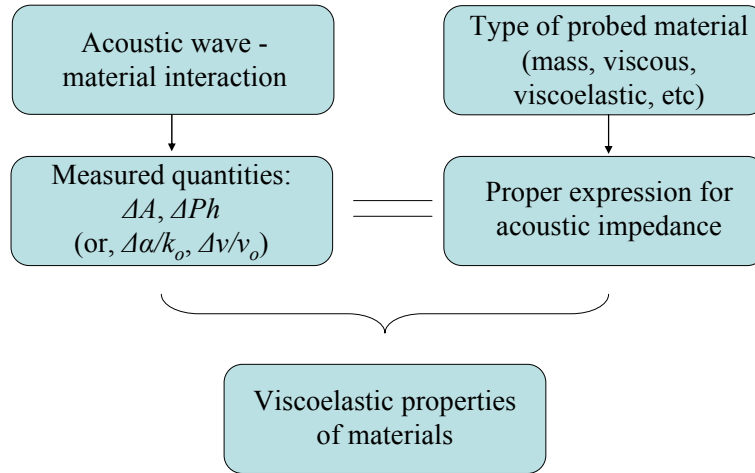


Fig.4.6. Flow of actions for the determination of materials’ properties using SAW devices.

Tab.4.2. Expressions for various kinds of acoustic impedance.

Type of loaded sample (surface perturbation)	Expression for acoustic (mechanical) impedance	
pure mass	$Z_{mass} = j \cdot \omega \rho h$	
pure viscous	$Z_{visc} = (1 + j) \sqrt{\frac{\omega \rho \eta}{2}}$	
viscoelastic in air (semi-infinite)	$Z_{air} = \sqrt{\rho_F G} \cdot \tanh(j\omega h \sqrt{\frac{\rho_F}{G}})$	
	$\frac{\Delta\alpha}{k_o} = c \frac{\omega^3 h^3 \rho^2}{3} \frac{G2}{GI^2 + G2^2}$	$\frac{\Delta v}{v_o} = c(\omega \rho h + \frac{\omega^3 h^3 \rho^2}{3} \frac{G1}{GI^2 + G2^2})$
viscoelastic in air (finite thickness)	$Z_{air} = \sqrt{\rho_F G}$	
viscoelastic in liquid	$Z_{liq} = \sqrt{\rho_F G} \frac{\sqrt{j\omega \rho_L \eta_L} + \sqrt{\rho_F G} \tanh(j\omega h \sqrt{\frac{\rho_F}{G}})}{\sqrt{\rho_F G} + \sqrt{j\omega \rho_L \eta_L} \tanh(j\omega h \sqrt{\frac{\rho_F}{G}})}$	



4.3. Experimental procedure

4.3.1. SAW devices used

One group of sensor chips used was based on a 0.5-mm-thick Y-cut quartz crystal. Two sets of 100-nm-thick Au interdigital transducers (IDTs) were photolithographically patterned on top of quartz, while a 20-nm-thick Cr film was used as an adhesive layer between quartz and Au. The IDTs had a split finger design with a period of 32 μm (and operating frequency of 155 MHz).

The other group of devices was based on a 36° rotated Y-cut, X-propagating Lithium tantalate crystal (36°YX-LiTaO₃). One set of these devices operated at 50 MHz, with 32 IDT pairs and 80 μm wavelength, whereas the other set operated at 155 MHz, with 25 IDT pairs and 26.5 μm wavelength. As before, IDTs are made of gold (200 and 650 nm thick for L50 and L155, respectively) and the sensing area was metalized (Au). A Ti adhesion layer was used instead of Cr. The acoustic aperture (IDT overlap), determining the width of the sensing area, was 1.6 and 2 mm, for quartz and LiTaO₃, respectively; the total available length of the sensing area was 5.65 and 10.8 mm for the quartz and LiTaO₃ devices, respectively. For Au deposition the whole sensing area was used, whereas for liquid experiments (glycerol and protein solutions) the used area was restricted by the flow cell length, which was 4.65 and 4 mm for quartz and LiTaO₃, respectively. Thus, for liquid-based experiments, the actual sensing areas were $1.6 \times 4.65 = 7.44 \text{ mm}^2$ for quartz, and $2 \times 4 = 8 \text{ mm}^2$ for LiTaO₃. Both perturbed areas are well within the acoustic aperture of the devices.

4.3.2. Materials for sensor characterization

(i) *Au thin film deposition*

For the deposition of Au thin films the instrumentation of sec.3.5. was applied. Au was sputtered in the same way both to evaluate mass loading (i.e., thin Au films of various thicknesses) and to facilitate biomolecule adsorption (thin Au film of fixed thickness 20 nm).

(ii) *Aqueous glycerol solutions*

Aqueous glycerol (99.6% purity, Biomol, Hamburg, Germany) solutions were prepared (concentrations from 15 to 88 wt%) and their viscosity was either measured experimentally using a concentric-cylinder-geometry viscometer (“DV-2P” Anton Par GmbH, Austria) or extrapolated from published data [4.17.]. All viscometry and acoustic experiments were carried out at 25° C. The concentration, density, and viscosity of the tested samples are summarized in Tab.4.3. For the examination of the glycerol solutions on the sensor the standard flow cell configuration was used (Fig.3.4.). For the case of quartz the total sensing area exposed to liquid was 7.44 mm^2 , whereas for LiTaO₃ it was 8 mm^2 . To compare results from both designs, the acoustic signal changes were normalized to surface area in all cases. All sample



solutions were injected with a peristaltic pump at a flow rate of 10 $\mu\text{l}/\text{min}$; rinsing was done with water.

Tab.4.3. Concentration, viscosity, and density of the tested aqueous glycerol solutions

Glycerol wt% ($\text{g}_{\text{gly}}/\text{g}_{\text{total}}$)	Viscosity (cP) at 25°C	Density (g/cm^3) at 25°C
15.4	1.4	1.017
25.6	1.9	1.029
32.9	2.7	1.038
37.3	3.1	1.044
42.3	3.8	1.050
46.7	4.6	1.055
52.2	5.9	1.062
62.1	10.2	1.075
72.0	21.9	1.087
75.9	33.2	1.093
80.0	49.5	1.098
84.0	81.8	1.104
88.0	128.1	1.109

(iii) Adsorbing protein solutions

Neutravidin (Pierce) solutions were prepared in phosphate buffer (PBS, pH 7.4, Sigma-Aldrich); PBS was used for sample rinsing as well. The solution was injected at a concentration 200 $\mu\text{g}/\text{ml}$ and at flow rate 10 $\mu\text{l}/\text{min}$, for 7.5 min.

4.4. Results and Discussion

4.4.1. Mass loading

The evaluation of the device response to mass loading was realized by means of Au deposition. Each sputtering procedure lasted 10 s; the acoustic signal was measured immediately before and after the Au deposition. The relation between sputter time and Au film thickness is known by the manufacturer (10 s \rightarrow 2.6 nm Au) for the particular deposition conditions and parameters. Thus, it was possible to directly relate the change in signal with the deposited mass (Au mass density 19.3 g/cm^3).

For pure mass loading it is expected that the change in acoustic wave amplitude (normalized wave attenuation) is negligible with respect to film thickness. This is confirmed in our case, as it is shown in Fig.4.7.

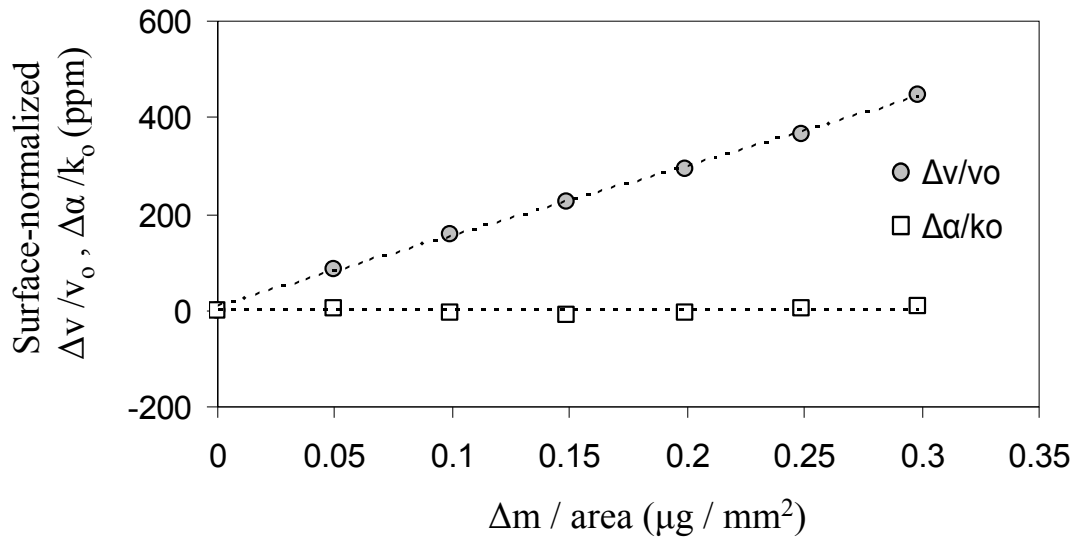


Fig.4.7. Surface-normalized acoustic wave parameters plotted against deposited Au mass per area for Q155 device without PMMA waveguide (based on eq.4.2(a) and eq.4.2(b)).

This graph shows both normalized quantities of the acoustic wave in the same units (parts per million, ppm). Fig.4.7. clearly shows an increase in the (absolute value of) $\Delta v/v_0$, while $\Delta \alpha/k_0$ remains constant (practically zero), indicating that the deposited Au layer causes no significant wave energy loss since the rigid layer oscillates synchronously with the sensor surface. The same holds true for all devices tested (data not shown).

The sensitivity of the devices to deposited mass is expressed in this section by the change in phase signal with respect to loaded mass. It is represented by the slope of a $\Delta Ph/\text{area}$ vs. $\Delta m/\text{area}$ plot, expressed in $\text{deg}/\mu\text{g}$. Such a plot appears in Fig.4.8. and summarizes the response of all configurations.

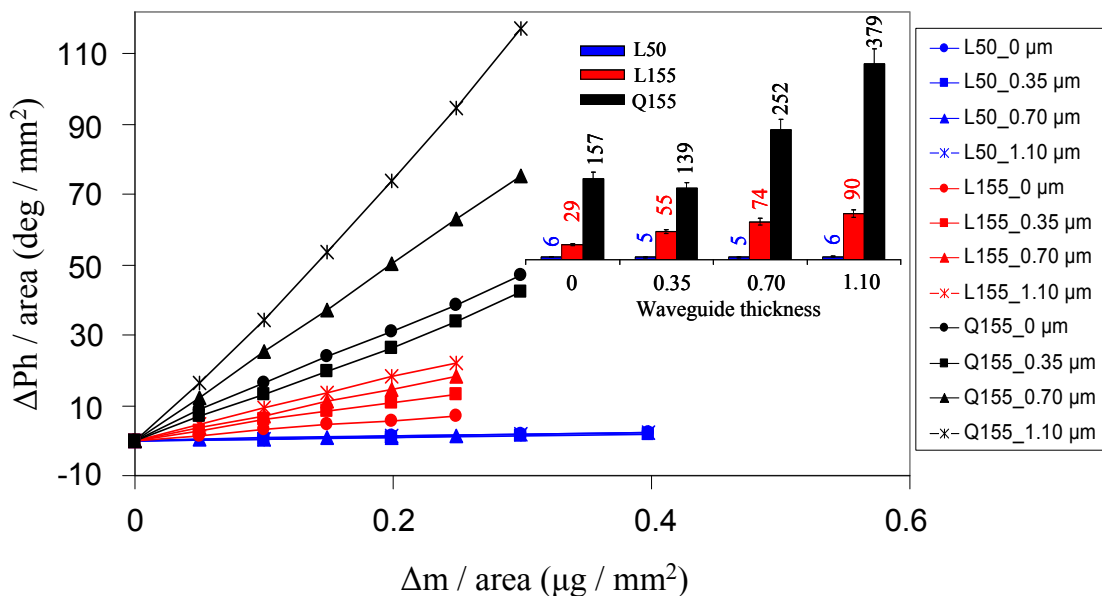


Fig.4.8. Comparative diagram of surface-normalized phase change vs. deposited mass per area for all device configurations. Inset: mass sensitivity values ($\text{deg} / \mu\text{g}$) with respect to PMMA waveguide thickness (μm).



It is clear that for all cases the phase change is directly proportional to the deposited mass, thus the linearity holds for all types of sensors and for all waveguide layers. The slopes of the trendlines, representing the sensitivity profiles, are summarized in the inset of Fig.4.8. as a bar diagram. As it appears, the mass sensitivity of the L50 device hardly changes with increasing thickness of the PMMA layer, indicating that the particular device is insensitive to waveguiding, at least for the examined PMMA thicknesses. These experimental results confirm the theoretical report that a LiTaO₃ substrate supports predominantly an SH-SAW which is already guided near the surface without significant diffraction (energy leak) into the bulk and therefore, remains unaffected by a waveguide coating. However, L155 does exhibit an increase in its mass sensitivity as the PMMA thickness increases, even though it is based on a LiTaO₃ substrate as well. The contrast in this behavior apparently comes from the higher operating frequency of L155, which leads to higher sensitivity to surface perturbations and, thus, higher sensitivity to waveguiding effects.

In the case of Q155, the devices appear to have the highest mass sensitivity, even though they operate at the same frequency as the L155. This difference is in agreement with theoretical considerations which report that the mass sensitivity of a quartz and a LiTaO₃ device, both operating at the same frequency, is higher for quartz due to higher SH-SAW velocity in this material ($v_Q = 4960$ m/s while $v_L = 4120$ m/s for the particular cut and orientation of the substrates used) [4.18.], [4.19.].

Finally it should be noted that the ratio of mass sensitivity values between Q155 and L155 of *same* PMMA (e.g. $\frac{S_m^{Q155}}{S_m^{L155}}$) does not exhibit any trend as the PMMA thickness increases (as a proof of that, for example, 0.35 μm thick waveguide has no effect on Q155 but causes an almost twofold sensitivity increase on L155). This indicates that, the PMMA waveguiding effect does not change linearly as the PMMA thickness increases, in either L155 or Q155.

4.4.2. Viscous loading – Low viscosity regime

The response of the devices to viscous loading was examined through sequential injections of aqueous glycerol solutions on the PMMA surface. Glycerol has not been observed to bind on PMMA; in addition, the PMMA surface does not exhibit roughness sufficient for liquid entrapment, i.e., mass loading effects. Therefore, these solutions are ideal for studying the interaction of SH-SAW with purely viscous samples.

In order to evaluate the devices' sensitivity to viscous loading, the samples of the low viscosity (Newtonian) region were used, due to the linear relation between ΔPh and $(\rho\eta)^{1/2}$ (eq.4.9(b)). Figure 4.9. summarizes the surface-normalized change in phase with respect to $(\rho\eta)^{1/2}$ for the twelve different device configurations (amplitude changes exhibit a similar trend, data not shown). The slopes of the lines, representing the viscosity sensitivity based on phase, $S_{visc,Ph}$, are summarized in the inset of Fig.4.9. As can be seen in Fig.4.9. the lines do not cross zero point; this is because the signal was measured with respect to the water, rather than air. In all cases, for $\Delta Ph \approx 0$, $(\rho\eta)^{1/2}$ is ≈ 1 , i.e. the value for water.

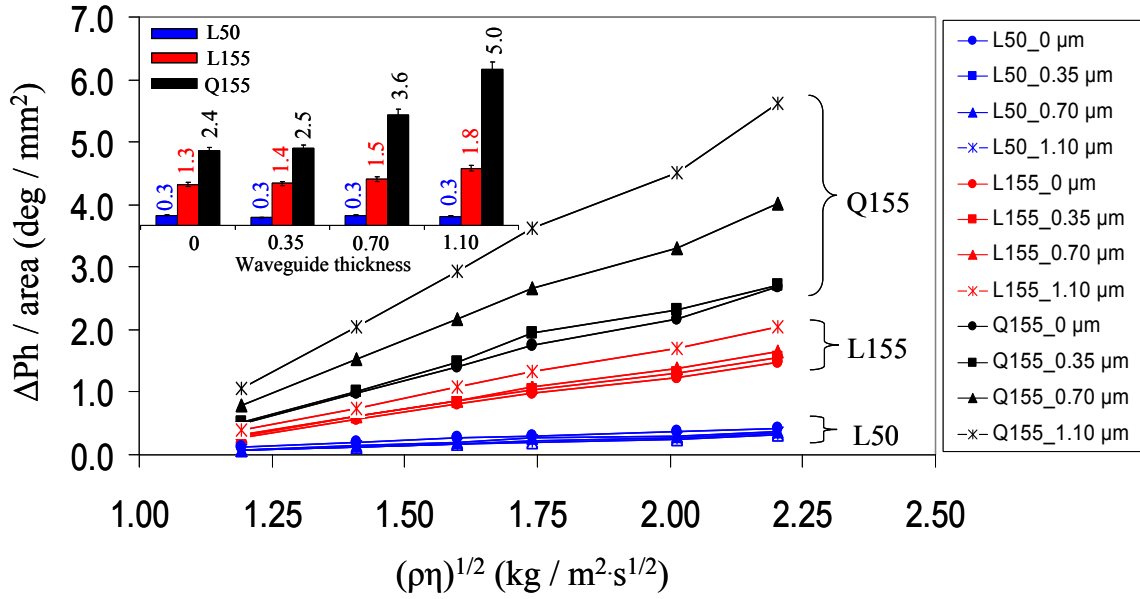


Fig.4.9. Surface-normalized phase change with respect to square root of density-viscosity product. Inset: viscosity sensitivity values ($\text{deg m}^2 \text{s}^{1/2} / \text{mm}^2 \text{kg}$) with respect to PMMA waveguide thickness (μm).

Comparing the sensitivity values for the various PMMA thicknesses of L50 (Fig.4.9., inset) it appears that there is essentially no influence of the waveguide on the sensitivity to viscous loading, just as in Au deposition. Performing an equivalent comparison for L155 we see that the (viscosity-related) sensitivity increases little (38%) when waveguide is added (e.g. $\frac{S_{\text{visc,Ph}}^{L155}(1.10\mu\text{m})}{S_{\text{visc,Ph}}^{L155}(0\mu\text{m})} = 1.38$), relatively to the case of mass loading for L155 ($\frac{S_m^{L155}(1.10\mu\text{m})}{S_m^{L155}(0\mu\text{m})} = 3.10$) which represents an increase of 210%.

Examining the increase rate of the viscosity- and mass-related sensitivities of the Q155 devices it is clear that the former exhibits a smaller increase, as with L155, suggesting a device independent observation.

Overall our data suggest that increase of the mass sensitivity of the SH-SAW device (e.g. by adding a PMMA waveguide) results in a correspondingly higher viscous loss, resulting in a trade-off between the mass sensitivity and the output signal level of the device [4.7.]. Moreover, one major difference between mass and viscous loading, even when they take place on identical sensor configurations, is that the “initial status” of the device before sample loading is different. More specifically, when adding a mass layer, the surrounding environment is air. However, when adding a glycerol solution, the surrounding environment is *already* liquid medium (the water in equilibrium) which has *already* caused wave damping and energy losses before any glycerol sample is injected. Consequently, the potential of the sensor to give higher signal values in viscous loading is reduced as shown experimentally by the comparable or greater values of any combination of sensitivity ratios of column “mass” compared to column “visc” in Tab.4.4.



Tab.4.4. Comparison of sensitivity to mass and viscous loading for the various examined device configurations. Reported values are averages of at least three experiments ($\pm 8\%$).

Part (a)			
	Sensitivity ratios	Mass	visc
Quartz	$\frac{S^{Q155}(0.35\mu\text{m})}{S^{Q155}(0\mu\text{m})}$	0.89	1.04
	$\frac{S^{Q155}(0.70\mu\text{m})}{S^{Q155}(0\mu\text{m})}$	1.61	1.50
	$\frac{S^{Q155}(1.10\mu\text{m})}{S^{Q155}(0\mu\text{m})}$	2.41	2.08
Part (b)			
	Sensitivity ratios	Mass	visc
LiTaO₃	$\frac{S^{L155}(0.35\mu\text{m})}{S^{L155}(0\mu\text{m})}$	1.90	1.08
	$\frac{S^{L155}(0.70\mu\text{m})}{S^{L155}(0\mu\text{m})}$	2.55	1.15
	$\frac{S^{L155}(1.10\mu\text{m})}{S^{L155}(0\mu\text{m})}$	3.10	1.38
Part (c)			
	PMMA thickness (μm) (% g/g)	Mass	Visc
$\frac{S^{Q155}}{S^{L155}}$	0 (0%)	5.41	1.85
	0.35 (8%)	2.53	1.79
	0.70 (14%)	3.41	2.40
	1.10 (17%)	4.21	2.78

4.4.3. High viscosity regime - Maxwell behavior

In order to examine the sensor behavior at higher viscosities, three of the twelve configurations were selected; L50, L155, and Q155, all with a $0.35\ \mu\text{m}$ thick waveguide. The highest measured glycerol concentration was 88 wt% exhibiting viscosity 128.1 cP. Practical hurdles did not allow reaching higher viscosities because the corresponding glycerol solutions were very viscous, resulting in blocking of tubes as well as severe distortion of the signal. The examined range though was adequate to extract some interesting features, as they appear in Fig.4.10. and are discussed below.

A striking feature in Fig.4.10. is that for Q155 there is a deviation from the linear behavior between ΔPh and $(\rho\eta)^{1/2}$ as well as ΔA and $(\rho\eta)^{1/2}$, as the solution



viscosity increases. Moreover, this deviation reaches a saturation level, after which there is practically no change in the acoustic signal, despite the significant change in $(\rho\eta)^{1/2}$. The two distinct regions, indicated by the dashed lines, denote the Newtonian and Maxwellian liquid regimes.

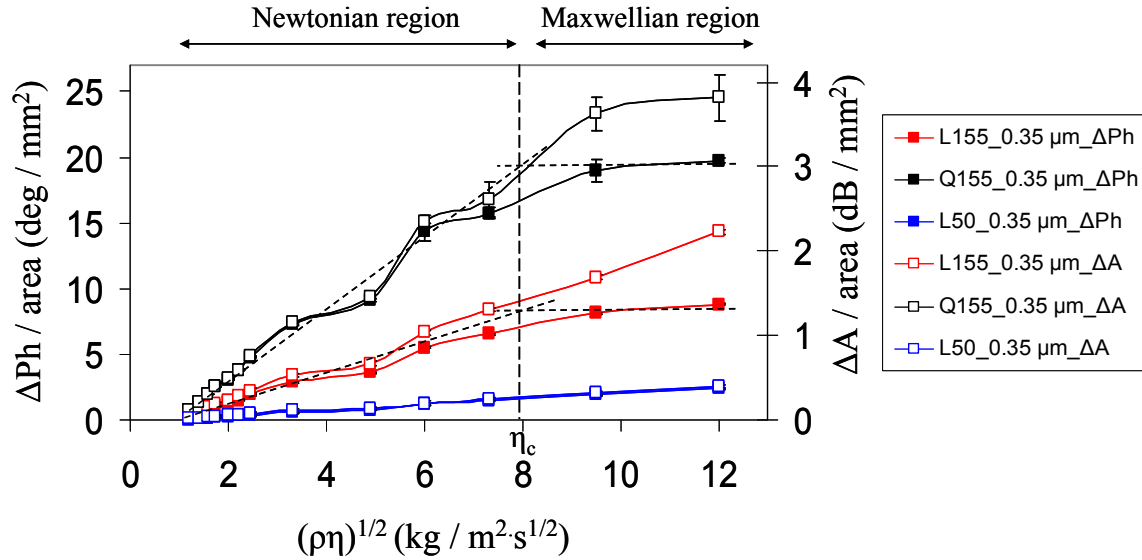


Fig.4.10. Surface-normalized acoustic signals upon liquid loading for the three different devices with the same PMMA layer ($0.35 \mu\text{m}$). The transition from the Newtonian to Maxwellian region is indicated by dashed lines.

It should be noted that the deviation from linearity for L155 appears at the same η_c as for Q155, within experimental error. This indicates that this phenomenon is independent of the device substrate and is only frequency related. It should also be noted that for L155 the deviation appears only for phase and not for amplitude; although the dependence of both acoustic signals (phase and amplitude) on $(\rho\eta)^{1/2}$ is the same for the Newtonian region as expected theoretically from eq.4.9(a) and eq.4.9(b), it changes when the fluid enters the Maxwell region. This is in agreement with published data [4.7.], [4.20.], [4.21.] and is depicted as a “delay” in deviation for the amplitude.

The critical viscosity value at which the transition takes place is approximately $\eta_c = 54.6 \text{ cP}$, which corresponds to glycerol concentration $82 \pm 2 \text{ wt}\%$. This value is in excellent agreement with [4.12.] where the operating frequency was 159 MHz. It is also worth noticing that, for $\eta_c = 54.6 \text{ cP}$, the characteristic relaxation time of glycerol is $\tau = 1.09 \text{ ns}$, which is equal to the $T_{SAW} = 1/\omega = 1.03 \text{ ns}$. For the calculation of τ , a variety of values for μ have been used in the literature [4.17.] ranging from 10^7 to 10^9 N/m^2 with $\mu = 5 \times 10^7 \text{ N/m}^2$ giving the best fit for glycerol [4.13.], [4.14.]. The ratio of the characteristic relaxation time (τ) over the characteristic time of shear deformation (T_{SAW}) is in fact the Deborah number which expresses how liquid- or solid-like behavior a liquid exhibits when it is probed at a particular shear rate (or, frequency, in our case). High Deborah numbers correspond to solid-like behavior whereas low Deborah numbers correspond to liquid-like behavior [4.22.]. As a result, when the ratio equals unity, the operating T_{SAW} becomes comparable to the liquid relaxation time and the latter begins to exhibit a solid-like behavior. In our system,



i.e., viscous glycerol solutions on a 155 MHz SAW device, Deborah numbers lie in the range of 0.027 to 2.495 from 15 to 88 wt% glycerol solutions, indicating that at the specific frequency, the glycerol liquids indeed transit from a liquid-like to solid-like behavior.

Supplementary to the above results deriving from acoustic measurements, and in order to cross-check the results with independent measurements, the values of $G1$ and $G2$ were calculated. What is usually done in materials characterization is that a sample is probed in a frequency spectrum so that a range of $\omega\tau$ values is derived and a plot of $G1(\omega)$ and $G2(\omega)$ is extracted. In our case, the probing frequency is single; however, the range of glycerol concentrations is quite broad, and because each solution is characterized by an individual η_i it is attributed a relaxation time τ_i . Therefore, a range of $\omega\tau$ is acquired by probing *several* samples with *one* frequency, instead of spanning *several* frequencies for *one* sample. $G1$ and $G2$ are calculated by eq.4.11(b) using $\mu = 5 \cdot 10^7 N/m^2$ and plotted against glycerol concentration in Fig.4.11.

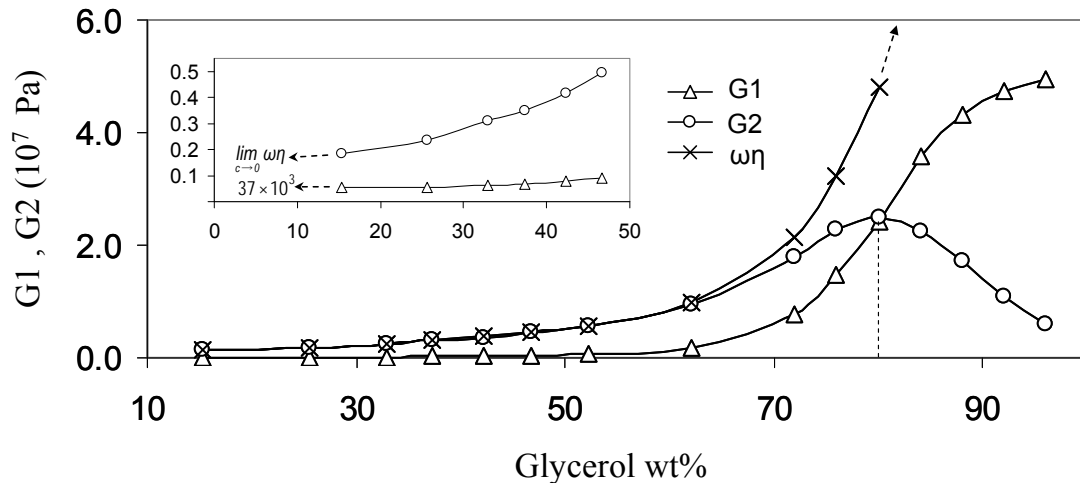


Fig.4.11. Calculation of $G1$ and $G2$ from viscosity η , and plot versus wt% of glycerol solutions. Inset: Magnification of the 10 to 50% glycerol concentration region. Same axes and units in both figures.

The following features are of interest in Fig.4.11.:

- (i) For low viscosities, $G1$ is quite small, whereas $G2$ tends to a finite value ($\approx\omega\eta$) following eq.4.11(b); (circles and crosses coinciding in Fig.4.11.). The actual values for low viscosity (15 wt%) are $G1 \rightarrow 37 \times 10^3 Pa$ and $G2 \rightarrow 1.6 \times 10^6 Pa$, i.e., $G2$ is 45 times higher than $G1$ (Fig.4.11., inset). For $c \rightarrow 0$ this difference in behavior is expected to be more pronounced.
- (ii) For high concentrations (i.e., high viscosities) the value of $G1$ increases substantially with respect to $G2$ and approaches the value of $\mu = 5 \cdot 10^7 N/m^2$. On the other hand, $G2$ is no longer given by the Newtonian expression $\omega\eta$; (circles and crosses deviating in Fig.4.11.). This indicates the necessity to express high viscosity liquids as Maxwellian fluids rather than Newtonian.



- (iii) It is known that the point where $G1$ and $G2$ plots intersect denotes a change in material behavior [4.14.]. In our plot, the intersection point of $G1$ and $G2$ lies at a concentration between 80 and 84 wt%, which means that this is where the behavior of the liquid begins to change from Newtonian to Maxwellian (result extracted from the *viscosity* measurements). This is in agreement with the value that was extracted from the *acoustic* measurements, through the deviation from linearity of the ΔPh vs. $(\rho\eta)^{1/2}$ plot (Fig.4.10.). This agreement appears graphically in Fig.4.12. (the notation of normalized wave quantities was used here in order to graphically view both quantities in the same axis due to uniformity of their units), where it appears that the intersection point between $G1$ and $G2$ coincides with the point where the acoustic signal trend changes from linear to saturation.

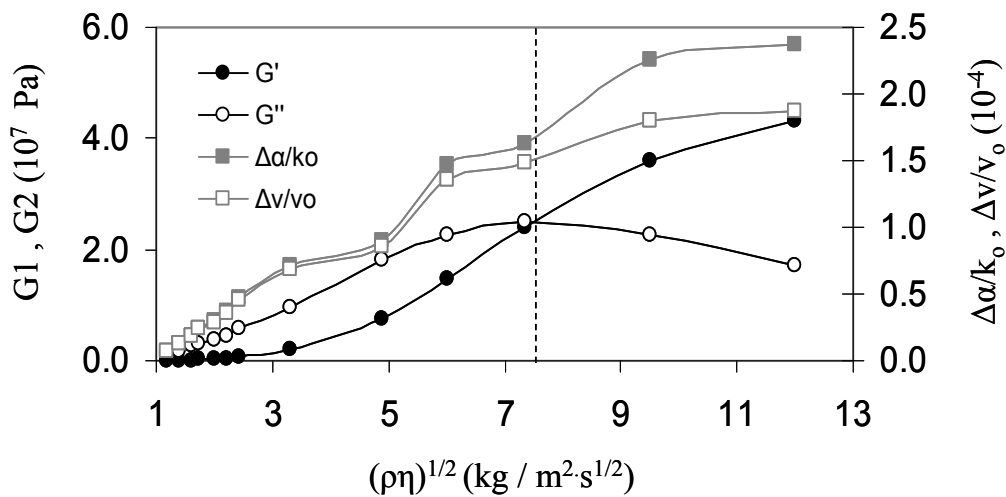


Fig.4.12. Combinatorial graph of the materials' viscoelastic properties and the measured acoustic wave parameters for Q155 with $0.35 \mu m$ thick waveguide. The intersection of $G1$ and $G2$ coincides with the transition point from linear to saturation region of the acoustic signal.

The intersection point of $G1$ and $G2$, however, is not only a function of glycerol concentration (or equivalently, relaxation time, or viscosity), but depends on the probing frequency as well. For this reason, a theoretical study was carried out, based on eq.4.10., eq.4.11(a), and eq.4.11(b) by varying the operating frequency for all the glycerol samples. The results are summarized in Fig.4.13., where the solid and dashed lines indicate theoretical calculations (since devices of such frequencies were not available), whereas the lines with points indicate actual experimental cases.

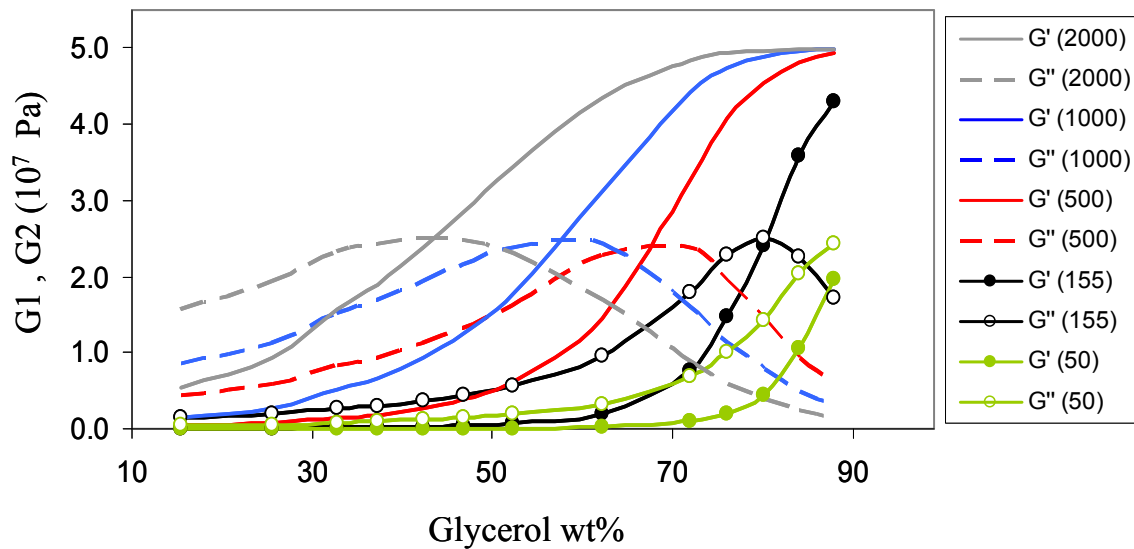


Fig.4.13. G_1 and G_2 for various operating frequencies (see legend, in MHz) for the used glycerol concentrations (i.e., measured viscosities). Calculated (lines) and experimental data (lines with points) are shown.

Clearly the higher the sensor operating frequency the earlier the intersection point of G_1 and G_2 appears, and, equivalently, the earlier the saturation of the sensor response is expected to be reached (based on Fig.4.12. as well). For example, a 500 MHz sensor would reach saturation at glycerol concentrations below 70 wt%. As for a 2 GHz device, even though it would present the highest sensitivity among all (sensitivity increases with operating frequency [4.23.]) it would not be able to distinguish glycerol solutions above 40 wt%. The above theoretical calculation included the 50 MHz operating frequency in order to cross-check if it is compatible with our experimental results. According to Fig.4.13. for 50 MHz there is no intersection point of G_1 and G_2 , meaning that for the concentration range probed by the particular frequency there is no saturation point in the sensor's function. Indeed, this is confirmed through the acoustic experiments (Fig.4.10.) where it appears clearly that L50 device exhibits no deviation from the linear relation between surface-normalized ΔPh and $(\rho\eta)^{1/2}$.

Therefore, an interesting feature is revealed; even though it was shown that L50 devices exhibit the lowest sensitivity when compared to their corresponding L155 and Q155 ones (Fig.4.9.), in fact they possess a significant advantage; their dynamic range of viscosity measurement is broader and they can detect high viscosity changes without reaching any saturation, unlike L155 and Q155. In a theoretical approximation, L50 would start reaching the saturation at viscosities of approximately 160 cP (i.e., 90 wt%).

4.4.4. Protein adsorption

The final step in the evaluation of the tested device configurations involves the study of their response to protein sample loading. The neutravidin samples (200 $\mu\text{g/ml}$) were left for sufficient time for physisorption on the Au surface to reach saturation. The phase change was taken at saturation and after buffer rinsing with



respect to the buffer equilibrium prior to injection. Moreover, the non-zero values in amplitude per area (0.01-0.03 dB/mm² for L155 and 0.05-0.1 dB/mm² for Q155) imply the deviation of such samples from pure mass loading (Au thin films). The real-time signal change upon protein adsorption and the absolute values of phase change for all twelve configurations examined are summarized in Fig.4.14. and Fig.4.15., respectively.

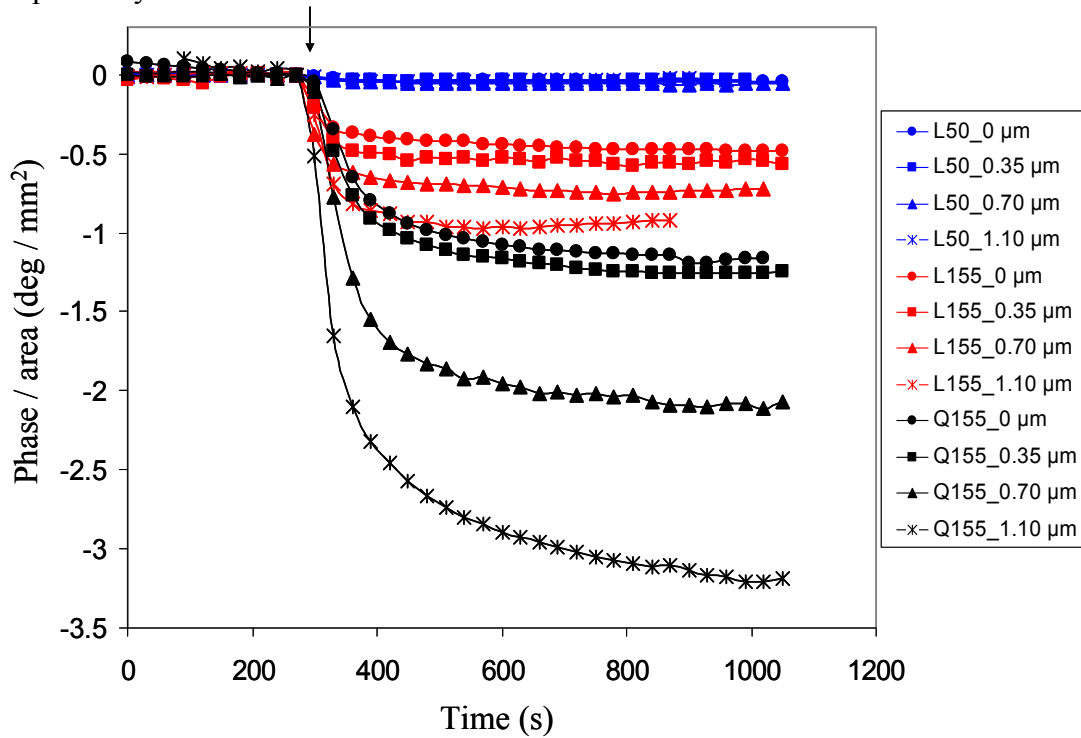


Fig.4.14. Real-time diagrams of 200 $\mu\text{g/mL}$ neutravidin adsorption on the twelve Au-coated device configurations; the arrow indicates the first contact of the sample on the surface.

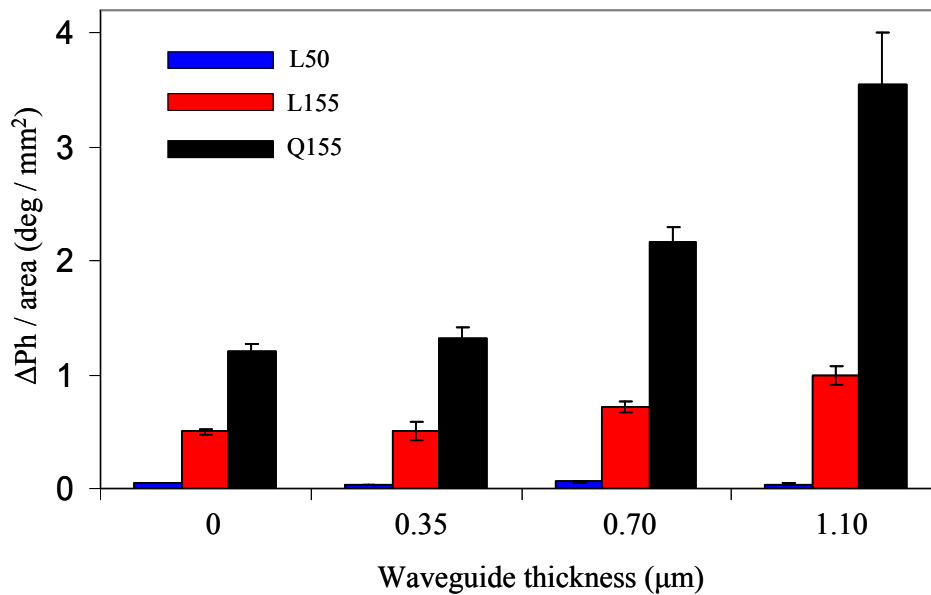


Fig.4.15. Surface-normalized phase change values upon neutravidin adsorption; comparison among all devices and waveguide thicknesses 0, 0.35, 0.70, and 1.10 μm .



After the theoretical and experimental analysis of the previous sections, the data in Fig.4.14. and Fig.4.15. evaluating the comparison among the various configurations on protein loading, are more or less expected, even though in this section we refer to absolute values of signal change rather than sensitivity. Q155 presents the highest values, followed by L155 and finally the L50 device. Also, there is no unexpected trend concerning the device response to PMMA waveguiding; the sensor response increases with waveguide thickness although not linearly (Fig.4.15.).

4.4.5. Viscoelastic properties of waveguide films

In the parametric investigation carried out for the selection of the optimum device configuration, three different PMMA layers were tested. Although it was not among the main objectives of this work, the viscoelastic properties of these films were quantified, so as to indicate the expanded potentials of SAW sensors into viscoelastic materials characterization.

Solving eq.4.14(a) with regard to $\frac{1}{GI^2 + G2^2}$ and substituting in eq.4.14(b), it is possible to calculate the loss tangent, $G2/G1$:

$$\frac{G2}{G1} = \frac{\frac{\Delta\alpha/k_o}{\Delta v/v_o - c \cdot \omega\rho h}}{1} = \tan\theta (= a) \quad (\text{eq.4.15.})$$

where θ is the angle between $G1$ and G^* in the complex plane representation (Fig.4.16.); the smaller the θ the closer to elastic behavior; the higher the θ the closer to viscous behavior, with θ around 45° being the transition area.

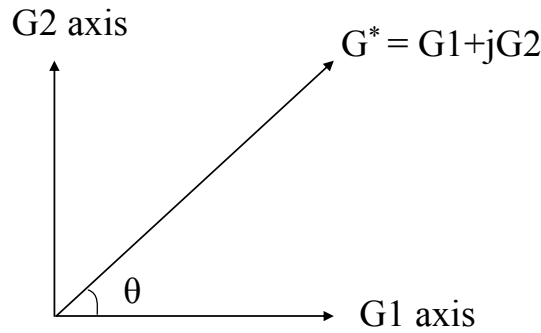


Fig.4.16. Complex representation of $G1$, $G2$.

Once $\tan\theta (=a)$ is known, $\frac{G2}{GI^2 + G2^2}$ becomes equal to

$$\frac{G2}{\left(\frac{G2}{a}\right)^2 + G2^2} = \frac{1}{\left(1 + \frac{1}{a^2}\right)G2}, \text{ and eventually: } G2 = \frac{c}{\frac{\Delta a}{k_o}} \frac{\omega^3 h^3 \rho^2}{3\left(1 + \frac{1}{a^2}\right)} \quad (\text{eq.4.16.}),$$

with $G1 = G2/a = G2/\tan\theta$.

The value of constant c was determined by mass loading (gold sputtering) on an uncoated Q155 device. This is mentioned in order to clarify that PMMA in the calculations of this section is not considered as waveguide but as the loaded sample itself, thus, the c of the uncoated Q155 device should be used.



Table 4.5. summarizes the calculations for the PMMA films that were tested as waveguides, plus one more with higher thickness; the logarithm values of $G1$, $G2$ are plotted against film thickness in Fig.4.17.

Tab.4.5. Viscoelastic properties of PMMA films with respect to their thickness.

h (nm)	G1 (Pa)	G2 (Pa)	G2/G1 = $\tan\theta$
350	7.89×10^7	4.21×10^6	0.053
700	6.01×10^8	5.25×10^7	0.087
1050	1.70×10^9	1.50×10^8	0.089
1420	2.91×10^9	1.32×10^8	0.045

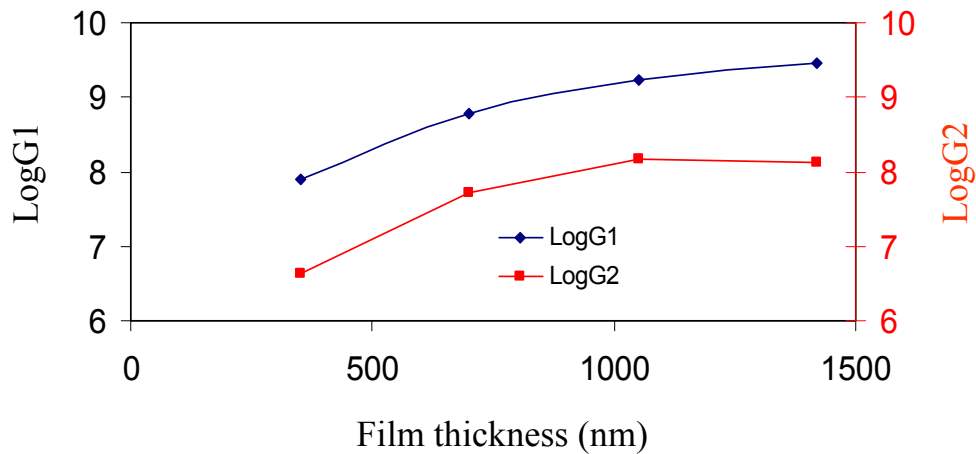


Fig.4.17. Storage and loss moduli of PMMA films as a function of film thickness.

As it appears, in all cases, $\tan\theta \ll 1$ (i.e., $G1 \gg G2$) which implicitly indicates the more elastic than viscous behavior of the PMMA films. It should be noticed that there is some expected error in the values for $G1$, $G2$, deriving from the assumption that eq.4.12. can be approximated by eq.4.14(a) and eq.4.14(b). This holds true when the $\omega h \sqrt{\frac{\rho_F}{G}} \ll 1$; physically this means that the upper surface of the film moves almost synchronously with the lower surface (i.e., the sensor surface). For $\omega h \sqrt{\frac{\rho_F}{G}} = 1$, film resonance effects take place. In our case this happens for $h \cong 940$ nm. Thus, in Tab.4.5. “safe” measurements hold for $h = 350$ and $h = 700$ nm. Above $h \cong 940$ nm the full eq.4.12. should be used to accurately determine $G1$ and $G2$. However, in published work, the simplified expressions have been used and SU8 films (with proximal viscoelastic properties with PMMA) have been characterized in this way, and the order of magnitude calculated in the present work fits in good agreement [4.24.].

Finally, it must be noted that as the operating frequency decreases the film resonance effect appears at higher film thicknesses. Thus, the approximation of $\tan x$ is valid for a broader film thickness range, and the viscoelastic properties can be more accurately calculated for a broader thickness range. In particular, theoretical calculations revealed that for a 155 MHz device the film resonance takes place at $h \sim 2$



μm , whereas for a 50 MHz one it takes place at $h \sim 6 \mu\text{m}$. This is another evidence that, even though high frequency devices are more sensitive, in general, they are not suitable for all applications, but proper design and consideration should be given according to the demands of the experiment (like for the high viscosity liquids in sec.4.4.3.).

4.5. Conclusions

A parametric study of the performance of various configurations of SH-SAW devices under various perturbation mechanisms was undertaken. Mass sensitivities were calculated via Au deposition. Q155 exhibited the maximum sensitivity, followed by the L155 and L50. Coating with a PMMA waveguide improved the sensitivity of both Q155 and L155 (yet, retaining the trend $S_m^{Q155} > S_m^{L155}$) but left the S_m^{L50} unaffected.

For the case of liquid loading, a wide range of glycerol concentrations (15 to 88 wt%, viscosities from 1.4 to 128.1 cP) was used. In the *low viscosity* region (Newtonian), the signal was found to be linear with $(\rho\eta)^{1/2}$, as theoretically expected. Comparison of the sensitivity among the uncoated devices revealed the highest sensitivity in Q155, followed by L155 and L50. Coating the devices with PMMA and comparing them, the trend remained ($S_{visc}^{Q155} > S_{visc}^{L155} > S_{visc}^{L50}$), with sensitivities increasing with PMMA thickness. In the *high viscosity* region (Maxwellian, above approximately 80 wt%), the signal of Q155 and L155 reached saturation, revealing the discrete existence of two regions at this frequency, which was confirmed by the crossing of $G1$ and $G2$ curves. This distinction of regimes is independent of the substrate, but dependent on the frequency, as it was not identifiable in L50. Thus, L50, even though less sensitive in all examined cases, is more suitable for high viscosity measurements than L155 and Q155, as it is expected to reach saturation at higher viscosity (> 160 cP).

Investigation of the viscoelastic properties of the PMMA waveguides (probed as samples themselves, rather than waveguides) revealed the potential of the devices to calculate the storage and loss moduli of such samples and assess their elastic vs. viscous regime. The results were comparable with work reported in literature. Moreover, it was shown (theoretically) that the lower frequency devices can measure properties of a broader range of PMMA thicknesses than the high frequency ones (similarly to the case of Maxwellian fluids) before the film-resonance effect comes into effect.

Finally, experiments with protein adsorption indicated that, as biosensors, the quartz devices exhibited the highest signal response, which increased with PMMA thickness. Although the highest response was observed for the thickest PMMA waveguide (1.10 μm), it exhibited a large standard deviation upon averaging the experiments.

Thus, as an overall conclusion and objective of this chapter, the selected configuration to use in the μ F-on-SAW setup was the quartz-based device, operating at 155 MHz with 0.70 μm PMMA waveguide due to both high sensitivity *and* reproducibility.



References

- [4.1.] G. Sauerbrey, "Verwendung von schwingquarzen zur wägung dünner schichten und zur mikrowägung", *Zeitschrift Phys.*, vol. 155, pp. 206-222, 1959.
- [4.2.] K.K. Kanazawa, J.G. Gordon, "The oscillation frequency of a quartz resonator in contact with a liquid", *Anal. Chim. Acta*, vol. 175, pp. 99-105, 1985.
- [4.3.] S.J. Martin, G.C. Frye, "Surface acoustic wave response to changes in viscoelastic film properties", *Appl. Phys. Lett.*, vol. 57, pp. 1867-1869, 1990.
- [4.4.] M. Weiss, W. Welsch, M. von Schickfus, S. Hunklinger, "Viscoelastic behavior of antibody films on a shear horizontal surface acoustic wave sensor", *Anal. Chem.*, 70, pp. 2881-2887, 1998.
- [4.5.] A. Tsortos, G. Papadakis, K. Mitsakakis, K.A. Melzak, E. Gizeli, "Quantitative determination of size and shape of surface-bound DNA using an acoustic wave sensor", *Biophys. J.*, vol. 94, pp. 2706-2715, 2008.
- [4.6.] K.A. Melzak, F. Bender, A. Tsortos, E. Gizeli, "Probing mechanical properties of liposomes using acoustic sensors", *Langmuir*, vol. 24, pp. 9172-9180, 2008.
- [4.7.] S.J. Martin, A.J. Ricco, T.M. Niemczyk, G.C. Frye, "Characterization of SH Acoustic Plate Mode liquid sensors", *Sensor Actuator*, vol. 20, pp. 253-268, 1989.
- [4.8.] G. Kovacs, M.J. Vellekoop, R. Haueis, G.W. Lubking, A. Venema, "A Love wave sensor for (bio)chemical sensing in liquids", *Sens. Actuat. A-Phys.*, vol. 43, pp. 38-43, 1994.
- [4.9.] S.J. Martin, G.C. Frye, S.D. Senturia, "Dynamics and response of polymer-coated surface acoustic wave devices: Effect of viscoelastic properties and film resonance", *Anal. Chem.*, vol. 66, pp. 2201-2219, 1994.
- [4.10.] J. Kondoh, S. Shiokawa, "A liquid sensor based on a shear horizontal SAW device", *Electron. Comm. Jpn. 2*, vol. 76, pp. 69-82, 1993.
- [4.11.] T. Nomura, A. Saitoh, Y. Horikoshi, "Measurement of acoustic properties of liquid using liquid flow SH-SAW sensor system", *Sens. Actuat. B-Chem.*, vol. 76, pp. 69-73, 2001.
- [4.12.] A.J. Ricco, S.J. Martin, "Acoustic wave viscosity sensor", *Appl. Phys. Lett.*, vol. 50, pp. 1474-1476, 1987.
- [4.13.] F. Josse, Z. Shana, "Effects of liquid relaxation time on SH surface waves liquid sensors", *J. Acoust. Soc. Am.*, vol. 85, pp. 1556-1559, 1989.
- [4.14.] A.J. Matheson, *Molecular Acoustics*, John Wiley & Sons Ltd, Bristol, ISBN 0-471-57620-4, 1971.
- [4.15.] G. McHale, M.I. Newton, M.K. Banerjee, J.A. Cowen, "Acoustic wave-liquid interactions", *Mat. Sci. Eng. C*, vol. 12, pp. 17-22, 2000.
- [4.16.] G. McHale, M.I. Newton, F. Martin, "Theoretical mass, liquid, and polymer sensitivity of acoustic wave sensors with viscoelastic guiding layers", *J. Appl. Phys.*, vol. 93, pp. 675-590, 2003.
- [4.17.] F. Teston, G. Feuillard, L. Tessier, L.P. Tran Hu Hue, M. Lethiecq, "Analysis of the coupling between shear horizontal plate waves and liquids: Application to the measurement of the shear rigidity modulus of glycerol solutions", *J. Appl. Phys.*, vol. 87, pp. 689-694, 2000.



- [4.18.] E. Gizeli, F. Bender, A. Rasmusson, K. Saha, F. Josse, R. Cernosek, Sensitivity of the acoustic waveguide biosensor to protein binding as a function of the waveguide properties, *Biosens. Bioelectron.*, vol. 18, pp. 1399-1406, 2003.
- [4.19.] S. Shiokawa, J. Kondoh, "Surface Acoustic Wave sensors", *Jpn. J. Appl. Phys.*, vol. 43, pp. 2799-2802, 2004.
- [4.20.] H.L. Bandey, S.J. Martin, R.W. Cernosek, A.R. Hillman, Modeling the responses of TSM resonators under various loading conditions, Sandia National Laboratories Report (SAND99-0631), Mar. 1999
- [4.21.] V. Raimbault, D. Rebière, C. Dejous, M. Guirardel, V. Conedera, "Acoustic Love wave platform with PDMS microfluidic chip", *Sens. Actuat. A-Phys.*, vol. 142, pp. 160-165, 2008.
- [4.22.] H.A. Barnes, J.F. Hutton, K. Walters, An Introduction to Rheology, Rheology Series vol. 3, Elsevier, The Netherlands, 1993
- [4.23.] H. Wohltjen, "Mechanism of operation and design considerations for surface acoustic wave device vapor sensors", *Sensor Actuator*, vol. 5, pp. 307-325, 1984.
- [4.24.] J. Hossenlopp, L. Jiang, R. Cernosek, F. Josse, "Characterisation of epoxy resin (SU-8) film using Thickness-Shear mode (TSM) resonator under various conditions", *J. Polym. Sci. Pol. Phys.*, vol. 42, pp. 2373-2384, 2004.



Chapter 5. Design and fabrication of the microfluidic module



*Microfluidics based ELISA with GRAVITM - Cell, from DiagnoSwiss
<http://www.diagnoswiss.com>*





Chapter 5. Design and fabrication of the microfluidic module

5.1. Introduction

This chapter describes the microfluidic module, the component of the microsystem that renders it a multi-analyte platform. The considerations that led to the final design based on geometrical and functional issues are initially discussed. Then, the fabrication procedure is described with detailed protocols and descriptions of the various steps. Post fabrication processes are also outlined, leading to the final assembly with the SAW biochip. In addition, comparison of the microfluidic module with the standard flow cell is done, and some features of the microchannels flow behavior are listed.

5.2. Design considerations

5.2.1. Material selection

In sec.2.4. a variety of materials was suggested for microfluidics fabrication. Among those, silicon could not be used due to its minimum biocompatibility, increased process cost and time. Glass was also rejected due to the high pressure it would place upon the sensing area of the device, endangering the functionality of the latter. In addition, it must be considered that the microfluidic module intended for the desired application has the form of a “seal”, which will be assembled on top of the SAW biochip. For such an objective, both silicon and glass were considered unsuitable. That is why a polymeric material was used, instead.

Among the candidate polymer materials, PDMS was selected. PDMS is a hybrid polymer, also called “silicone rubber”. It is a siloxane and has an alternating inorganic siloxane backbone and organic methyl groups (Fig.5.1.) and was preferred to others due to a number of advantages that it exhibits.

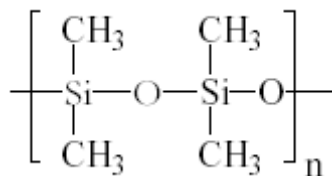


Fig.5.1. Chemical formula of PDMS monomer

Advantages of PDMS:

- It exhibits substantial chemical resistance.
- It conforms well on surfaces and deforms reversibly.
- It is transparent in the visible range, which can render it suitable for flow inspection, but also useful for cell measurement under microscopes.
- It is easy to handle, cheap and fast to process using soft lithography.



- It binds well upon plasma treatment (not used in the current work, but potentially in future development targeting disposable biochips).
- It presents good swelling behavior, i.e., it does not swell when in contact with a variety of fluids [5.1.].
- It can be easily functionalized and hydrophilized, mostly with plasma treatment (even though it loses its hydrophilicity shortly after treatment).

5.2.2 Geometrical features

The design was done according to the following considerations. The microfluidic module is intended to separate the total SAW surface into distinct sub-areas in order to achieve multi-sample detection. Thus, the design of the module suggests a rectangular shape for the microchannels, of equal width and of parallel configuration, with PDMS walls of appropriate thickness to separate them.

Having this in mind, there are in principle two possible arrangements, depending on the microchannels' axis being: 1) parallel or 2) perpendicular to the direction of wave propagation (the k -vector) (Fig.5.2.). In the first case the dotted and white regions represent sub-areas with and without any sample on them, respectively (assuming a total area divided into $N = 2$ sub-areas). As the acoustic wavefront propagates, the part above the empty area will remain unaffected whereas the part propagating through the filled region will undergo some delay due to its interaction with the sample. Having N samples, the wavefront would, consequently, "break" into N parts as it undergoes different time delays during its interaction with the different samples. Eventually, the receiver IDT set would sense an interference signal between the N parts of the wavefront which would not be a true representation of the wave-sample interaction. This effect was experimentally verified by poor quality results and lack of reproducibility of signal change upon sample loading (data not shown).

On the other hand, such irregularities do not hold for the second case (Fig.5.1(b)). An acoustic wavefront crosses one sample at each timeframe, thus, undergoing a uniform time-delay along its length (that is why no "break" appears). As a result, the second configuration was selected for the setup.

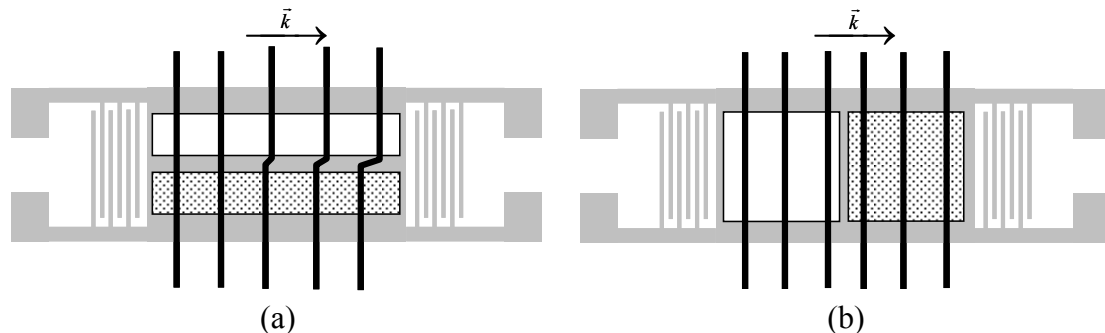


Fig.5.2. (a) "Break" of the acoustic wavefront resulting in interference of the "partial" waves at the receiver IDT set of the device, (b) no effect of wavefront "break", as the wave crosses one sample at each time frame.

Having selected the microchannel orientation, the next step involved the design of microchannels' dimensions. These were selected considering two key factors: 1) the contact area between the sensor and the module, and 2) the active area



per microchannel. To elaborate, each microchannel is separated by its neighboring one by a PDMS “wall,” which should be thick enough to facilitate good contact of the walls with the sensor surface and prevent leakage. Figure 5.3(a) shows a “leaking” microchannel, whereas Fig.5.3(b) a functional one.

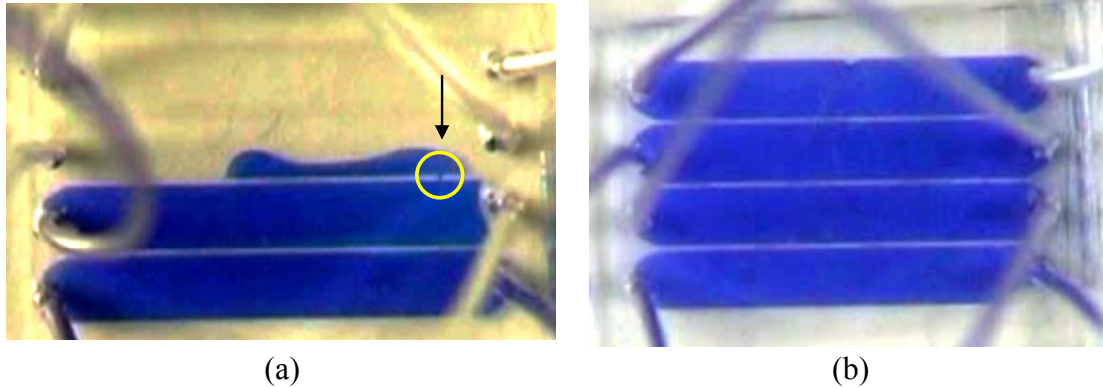


Fig.5.3. (a) Faulty microfluidic module possibly due to bad contact, (b) well-functioning module.

On the other hand, a major concern that had to be taken into consideration was the piezoelectric nature of the SAW sensor; excessive contact area between the sensor and the module would lead to high damping of the wave and/or malfunction of the device due to signal distortion. Therefore, to compensate the pros and cons of the thickness of PDMS walls, the values were chosen for the wall thickness to be around 100-120 μm . The height of the microchannels was 100 μm , as defined by the fabrication procedure (see sec.5.3.2.). With these dimensions, the active sample volumes are drastically minimized; volumes of 150-250 nL correspond to each sensing sub-area, in contrast to typically 3.5 μL that correspond to the total sensing area of the standard flow cell (Tab.5.1.). Finally, speaking of channel dimensions, it should be noted that for all samples used in the experiments (water, glycerol and PBS buffer) the swelling ratio of PDMS was 1.0 [5.1.], which indicates no swelling of the material and, thus, no change in its dimensions or properties upon its contact with the particular liquids.

The length of the microchannels was designed big enough to allow liquid flow above both sensors of the chip. Even though one device would be enough for the multi-sensing, using both was a practical way to increase the number of acquired data points. Therefore, each channel's length was fixed at 12.75 mm, allowing the input and output of the liquid to take place outside the sensing areas to avoid any possible effect on the signal. The liquid input and output regions of the microchannels were designed to be curved instead of rectangular so as to avoid bubble formation and sample remnants at these regions as well as incomplete wash-off, which could be possible in the case of rectangular-shape-edged microchannels (Fig.5.4.).

Another special feature of the design derives from the liquid nature of the samples. The operation of the IDT electrodes on quartz-based SAW devices is incompatible with liquid. Therefore, it is imperative that the IDT areas should be kept out of contact with the fluid under test, otherwise severe distortion of the wave would be caused. One option would be to simply let the module cover the IDT sets. This,



however, would impose pressure on the IDT region and would, again, cause severe damping of the wave and distortion of the output signal. For this reason, the design includes a hollow “safety shell” located above all the IDT sets in order to prevent their contact with both the liquid and the bulk material of the module (shown in Fig.5.4. with semi-transparent black color).

Taking into consideration the above design parameters and special features of the SAW sensor chip, the optimum dimensions of channel width and PDMS-wall thickness for the cases of three-, four-, and five-channel modules are summarized in Tab.5.1. and a typical design for a 4-channel module appears in Fig.5.4.

Tab.5.1. Typical dimensions for three types of microfluidic modules.

Number of microchannels	Channel width (μm)	PDMS wall thickness (μm)	Sub-area (mm ²)	Microchannel volume (μl)	
				Total	Above each sub-area
3	1550	120	2.48	1.97	0.248
4	1100	120	1.76	1.40	0.176
5	900	110	1.44	1.14	0.144

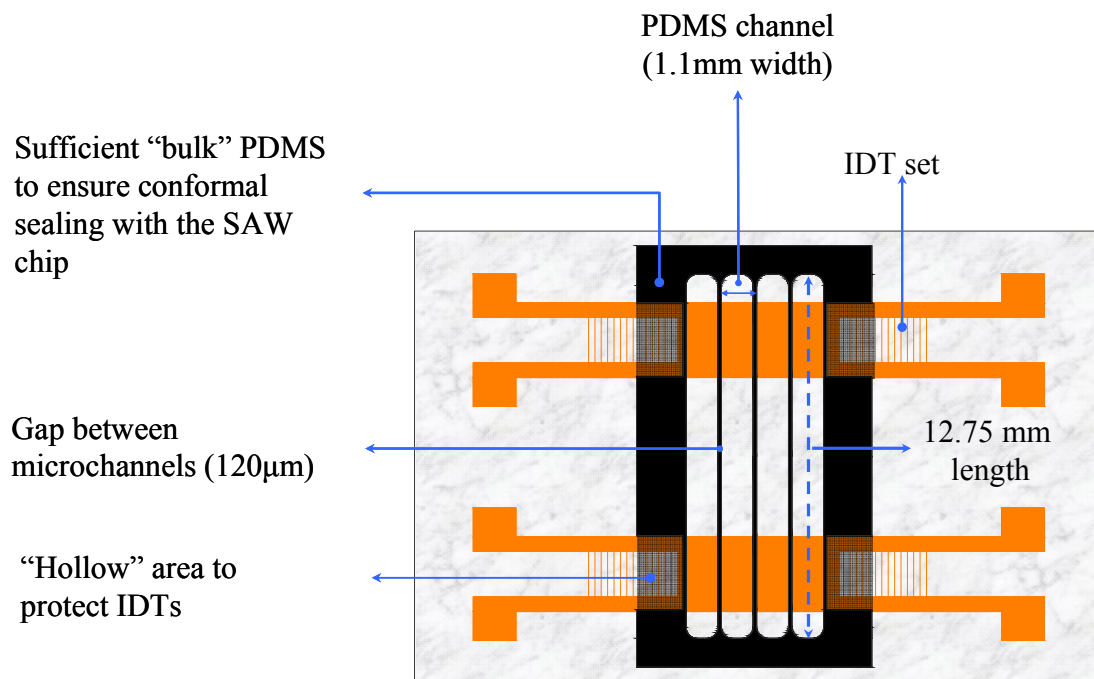


Fig.5.4. AutoCAD design of a 4-channel microfluidic module (black color, top view) attached on the two sensors (orange) of the biochip.



5.3. Fabrication process: Soft Lithography

The microfluidic module was fabricated by means of soft lithography. This method includes a group of procedures, which allows fast, cost-effective, and simple fabrication of microfluidic devices. Rapid prototyping is one major step, during which a master prototype is designed and fabricated with standard photolithographic techniques (and used over and over again as a mold). In the subsequent processing step, replica molding, PDMS is cast on the mold, and after specific thermal treatment, it acquires the negative pattern of the mold [5.2.], [5.3.], [5.4.]. In the following sections, the procedure followed towards the fabrication of the microfluidic modules is presented in detail.

5.3.1. Mask design and fabrication

The mask design was made with AutoCAD software (Fig.5.5.) and printed on a transparency using a high resolution (above 2400 dpi) commercial printer. The black areas of the design represent the areas that microchannels will eventually be formed. Each numbered rectangle represents a complete microfluidic module of arbitrary (N) microchannels. As it appears, plenty of modules fit in a 3-inch wafer (76 mm diameter), which is one of the reasons that make soft lithography a desirable method for microfluidics production.

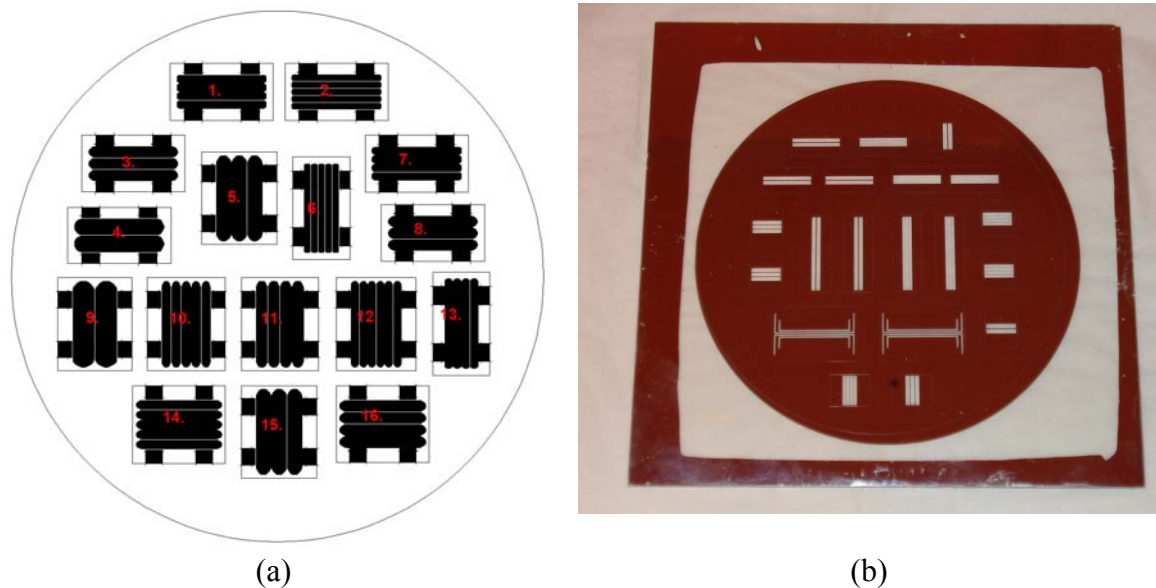


Fig.5.5. (a) Design of the mask. The round-shaped endings of the microchannels are visible, as well as the square areas intended for the protective hollow shells of the IDTs (on either sides of microchannels), (b) actual image of the Al-mask; the microchannels will eventually be formed at the Al-removed areas.

The transparency was used as an initial temporary mask for patterning a 500-nm-thick Al-coated piece of glass (Al was deposited by thermal evaporation). This was done by means of negative photolithography of AZ(5214E) photoresist and subsequent wet etching of the Al with a mixture of H_3PO_4 and isopropyl alcohol 1:1.



In this way, the patterns were directly transferred from the transparency to the Al-mask (Fig.5.5(b)), which was then used for all (the rest of) photolithography processes.

5.3.2. SU8 mold fabrication

The material used for mold fabrication was the negative epoxy type photoresist SU8 100 from MicroChem Corp. The processing of SU8 includes the following steps, which are schematically summarized in Fig.5.6.

- *Substrate pretreatment*, involving thorough wet cleaning of the 3-in. Si wafer (acetone, isopropanol and deionized water) and subsequent surface dehydration with baking at 120 °C for 15 min.
- *Spin-coating* of SU8 on the Si substrate (Karl Suss RC8 spinner) and formation of a 100- μm -thick SU8 layer. This thickness defines the depth of the microchannels. Spinning took place in two steps: (i) spread cycle; ramp up to 500 rpm speed with 100 rpm/s acceleration and leave for 10 s in order for the resist to cover the whole wafer surface, (ii) spin cycle: ramp up to 2200 rpm final speed at 300 rpm/s acceleration and leave for 30 s.
- *Soft bake* in two steps: at 65 °C for 20 min, followed by 95 °C for 50 min, both on a hot plate, in order to remove the solvent and densify the film.
- *Exposure to i-line UV* (365 nm) with a Karl Suss MJB3 mask aligner at contact photolithography mode (Fig.5.7.); various exposure times between 20 and 25 min were examined for optimum crosslinking. Two kinds of filters were used: a narrow band-pass filter with a FWHM of 55 nm in combination with a step-like filter that cuts off wavelengths below 365 nm. The second filter was necessary because SU8 presents too high absorbance at this region and could result in too high exposure of the top part and therefore highly non-vertical walls [5.5.].
- *Post-exposure bake* on a hot plate for 1 min at 65 °C and 20 min at 95 °C, which completed the cross-linking of the exposed sites (initiated through the UV exposure).
- *Development* with immersion of the SU8-coated Si wafer in methoxy-2 propyl acetate (PGMEA) for 15 min under continuous stirring. Regions that were exposed to UV radiation through the apertures of the Al-mask, and therefore cross-linked, remained intact while the rest was dissolved in the developer. Development was followed by rinsing with isopropanol and drying with nitrogen flow.
- *Hard bake* was the final step, realized at 160 °C for 15 min on a hot plate, in order to remove possible cracks on the crosslinked SU8 film.
- Upon completion of the processing, the structures were examined under an optical microscope in order to validate the efficiency of the procedure and the accuracy of the structures; very little profile of the SU8 walls was observed, i.e. deviation from the ideal vertical shape/orientation, of the order of maximum 10%, which does not affect the purposes of the current work.



Fabrication steps

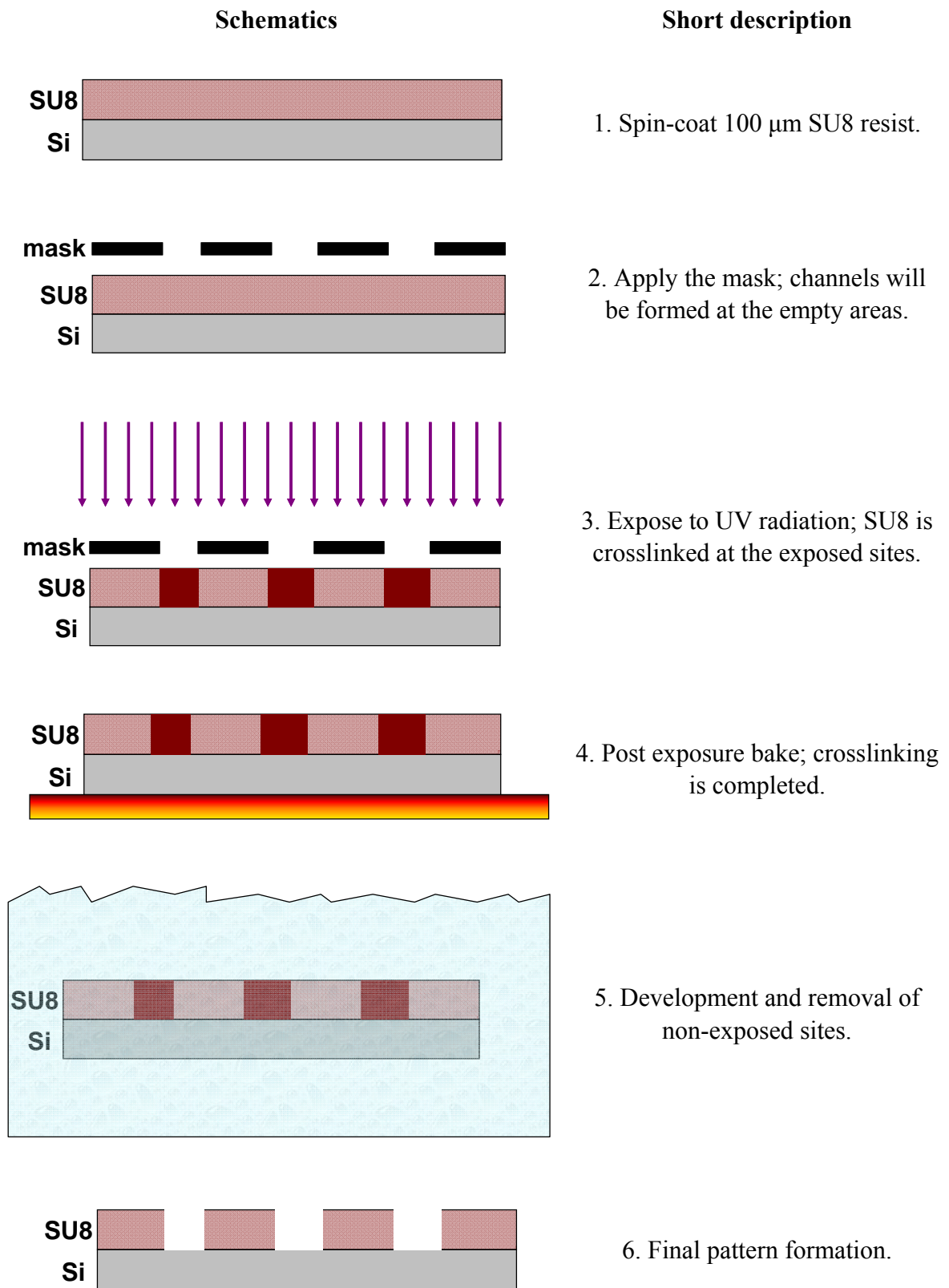


Fig.5.6. Process flow of fabrication steps.

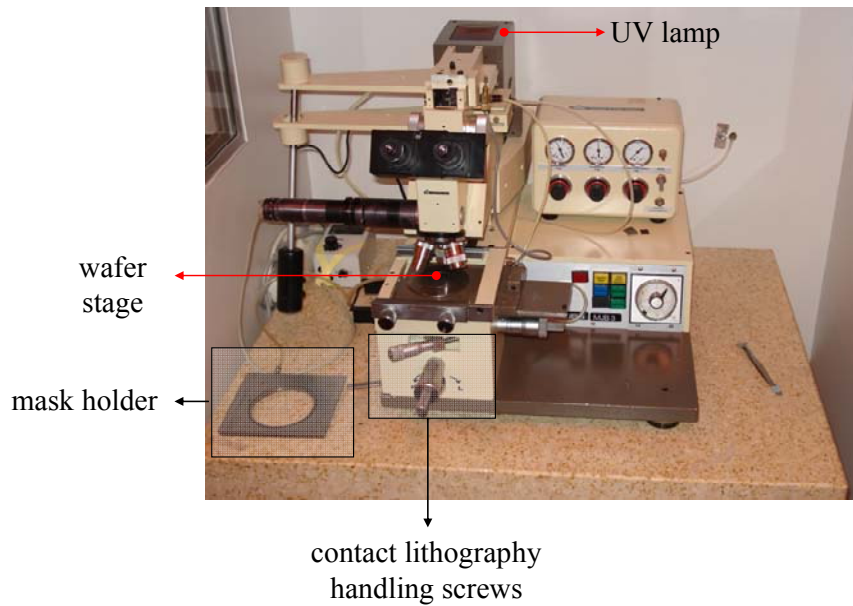


Fig.5.7. Karl Suss MJB3 mask aligner that was used for the exposure of the SU8 coated Si wafer and the formation of the structures.

5.3.3. PDMS processing and replica molding

Upon completing the structuring of the SU8-coated Si wafer with the desired patterns, processing of PDMS was the next part of the procedure, and it can be distinguished in the following steps:

- *Preparation of the PDMS* involved mixing of the base resin with the curing agent Sylgard 184, supplied from Dow Corning Corporation, in a 10 : 1 ratio and degassing till complete removal of the bubbles.
- *Casting of the PDMS prepolymer mixture* on the SU8 mold, which was located at the bottom of a 4-mm-deep metal holder, with diameter slightly larger than 3 inches (i.e., as wide as the wafer).
- *Thermal curing* of PDMS on a hot plate, at 100 °C for 1 h.
- *Peeling off* of the thermally solidified PDMS from the SU8 mold followed. The “elastomeric wafer” of 4 mm thickness (as much as the depth of the metal holder) was more easily peeled off when a thin Teflon film was spin-coated on the SU8 wafer, in order to facilitate less sticking. The PDMS modules were diced from the “elastomer wafer” with a razor edge and some of them were indicatively inspected with Scanning Electron Microscope (Fig.5.8.). It clearly appears that the end-to-end width is the same for all chips, as they are all intended to fit in the same sensing area of the SAW sensor. The difference in the microchannels width is noticeable, as well as part of the “safety shell” at both sides of the microchannels for the IDTs protection.

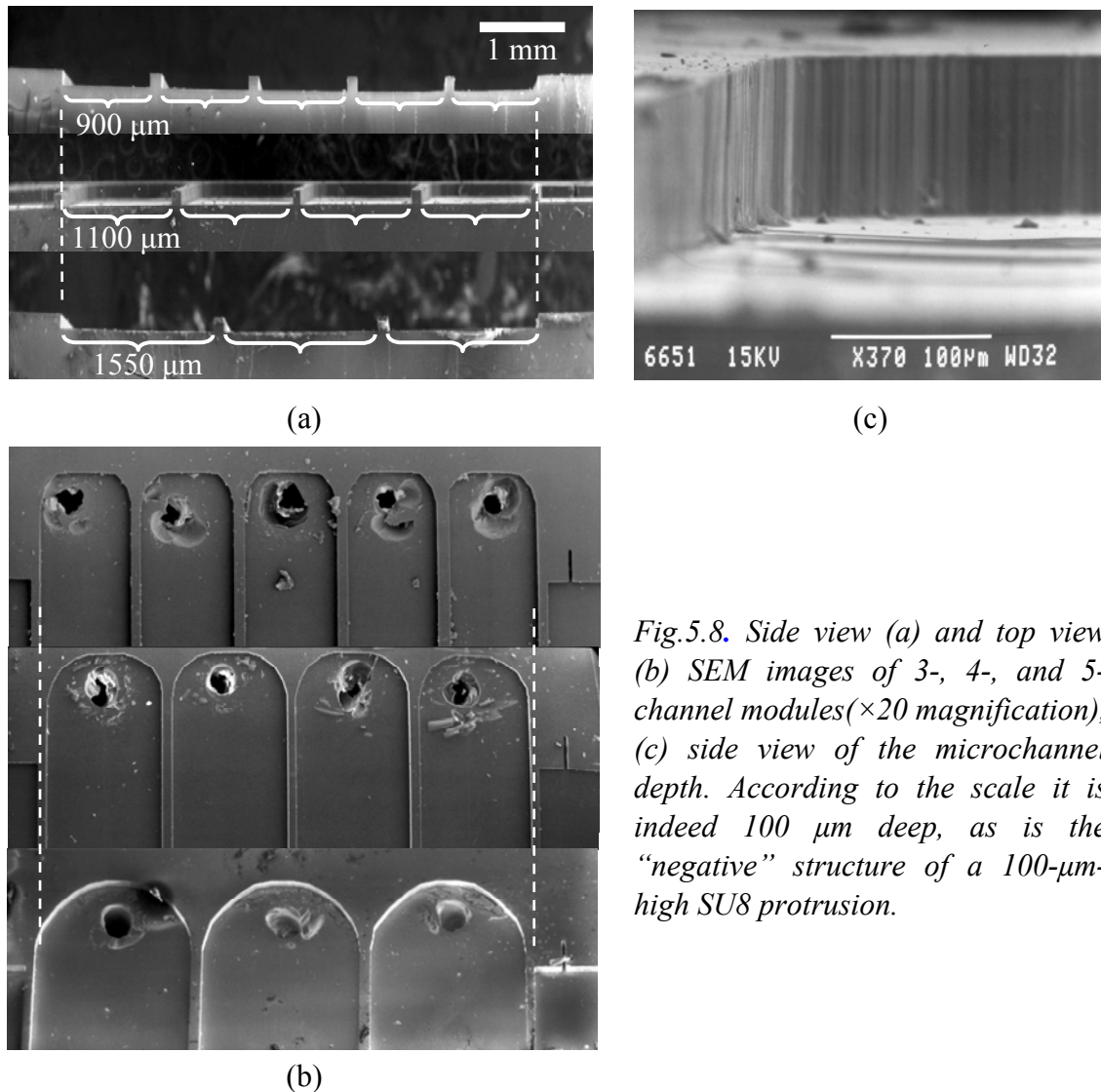


Fig.5.8. Side view (a) and top view (b) SEM images of 3-, 4-, and 5-channel modules ($\times 20$ magnification), (c) side view of the microchannel depth. According to the scale it is indeed $100\ \mu\text{m}$ deep, as is the “negative” structure of a $100\text{-}\mu\text{m}$ -high SU8 protrusion.

5.4. Post fabrication processing - fluidic interconnects

Having the diced PDMS module in hand, there are a number of further actions that need to be taken before assembling the module on the SAW chip in a fully functional way. These are listed below:

- *Opening vias* for fluid inlet and outlet in the microchannels. This was done by means of a bench drill machine (TBM 220, Proxxon). X-Y stage and vision through a $\times 4$ magnification microscope ensured the precise drilling of 0.5-mm -diameter vias (Fig.5.8(b)). A larger diameter (e.g. $1\ \text{mm}$) was avoided due to the danger of drilling on two microchannels simultaneously, which would lead to fluid leakage from one to the other.
- *Capillary tubing attachment* made of low density polyethylene - PE (Scientific Commodities, Inc.) for fluid inlet and outlet (Fig.5.9(a)). Their outer diameter was $0.5\ \text{mm}$ (for precise fitting in the vias) and inner diameter was $0.2\ \text{mm}$. The capillaries were manually fixed on their correspondent drilled positions on the PDMS module. The lack of glue or any other adhesive means was a great



advantage because: 1) it eliminated the danger of via blocking or module contamination, and 2) it allowed the replacement and/or cleaning and drying of one or more capillaries at any moment without having to dispose of the PDMS module.

- Interfacing with the external syringe pump was achieved by special tip adaptors (EFD[®] - Engineered Fluid Dispensing[®]) with outer and inner diameters of 200 and 100 μm , respectively, which were attached to 1 mL syringes for fluid propulsion (Fig.5.9(b)).
- *Micromodule mounting on the SAW sensor chip:* To ensure the reusability of the PDMS modules and the uniform regeneration of the sensor surface after each experiment, the modules were reversibly bound to the sensor surface. Specifically, the PDMS modules formed reversible sealing on the sensor when pressed against the latter; a slight pressure was enough to seal the module on the sensor. This reversible sealing is possible because PDMS is flexible and can conform to minor imperfections in a “flat” surface making van der Waals contact with this surface. This method of sealing is water tight and fast and occurs at room temperature. Simply peeling the PDMS off the flat surface breaks this reversible seal [5.3.]. Furthermore, to ensure the stability of the module, a plastic cover was screwed on top of PDMS module in order to apply constant and uniform gentle external pressure on the latter. Properly designed openings allowed the protrusion of the capillaries without obstruction by the rest of the plastic lead (Fig.5.10.).



Fig.5.9. (a) Capillary tubing, (b) various types of syringe adaptors.

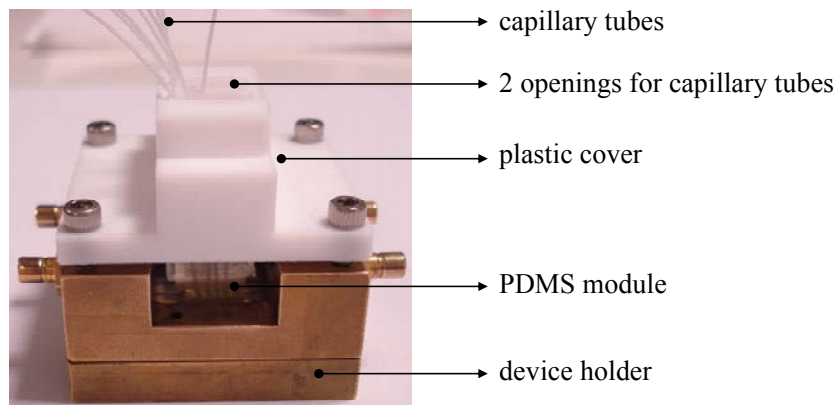


Fig.5.10. Plastic lead (white component) screwed gently on the PDMS module applying the necessary force for conformal and reversible sealing; blocking of capillary tubes is avoided via the two openings.



5.5. Verification of suitability

5.5.1. Hermeticity of the microfluidic module

The quality of the micromodule sealing on the sensor was tested with a syringe pump at the flow rate of interest, 5 $\mu\text{L}/\text{min}$ (the pump operated at an “INFUSE” mode, rather than “REFILL”, i.e., at a “liquid-push” rather than “liquid-pull” mode). Using blue-dye fluid, no leakage was observed in the vast majority of the cases, neither between the microchannels, nor at the entrance and exit points of the fluids, nor at the attachment points of the vias with the capillaries. Also, long duration of flow was tried, again, without faults. In order to detach the two components (sensor chip and PDMS module), the complex was immersed in water for some minutes and then the module was gently removed manually; no marks of the module were left on the sensor surface.

In addition, it must be noted that the hermetic sealing did not cause severe damping of the insertion loss (potentially due to the piezoelectric nature of the sensor). In fact, the damping was only half of that caused by the standard flow cell, which was so, because the total contact area of the micromodule was half of the contact area of the standard flow cell.

5.5.2. Flow regime; Reynolds number

Speaking about liquid flow through a rectangular microchannel, the flow characteristics through such a “tube” (general term) should be mentioned. The type of flow is traditionally indicated by means of the Reynolds number, a dimensionless number in fluid mechanics, which qualitatively describes the domination of inertia or viscous forces during the flow of a liquid, and is given by the formula:

$$Re = \frac{\rho Dv}{\eta} \quad (\text{eq.5.1.})$$

where ρ and η are the mass density and viscosity of the fluid, respectively, v its average (linear) velocity, which is given by the ratio of flow rate, Q , over the cross-sectional area, A ; D is a typical length scale, which for non-cylindrical cross-section is called the “hydraulic diameter”, $D_h = \frac{4A}{P_{wet}}$ (eq.5.2.), where P_{wet} is the wetted perimeter. For our case (rectangular-shaped cross-section with height H and width W) D_h is [5.6.]:

$$D_h = \frac{2WH}{W + H} \quad (\text{eq.5.3.})$$

The ratio in eq.5.1. qualitatively indicates the “competitiveness” between the inertia and viscous forces. High ratio, i.e., domination of inertial contribution, indicates turbulent flow, and is more typical of flows in the macro world. In contrast,



low Re values indicate domination of the viscosity term, which is a feature of the flow at smaller dimensions. The transitional flow regime, between turbulent (unpredictable, chaotic) and laminar (steadier, more well-behaved) flow, has been empirically determined at $2000 < Re < 3000$. Eventually, in our case, $Re \cong 0.14$, so the flow in our microchannels is laminar, as expected.

The pressure drop, Δp , inside the microchannel can be estimated using the following equation [5.7.]:

$$\Delta p = f \frac{L}{D_h} \frac{v^2}{2} \quad (\text{eq.5.4.})$$

where L is the channel length and f the friction coefficient, which depends on the H/W ratio. The calculation gives $\Delta p = 12 \text{ Pa}$, which is well below the maximum pressure that PDMS walls can withstand (few psi [5.3.]).

5.6. Conclusions

The conclusion of this chapter is essentially the successful design and fabrication of the microfluidic module and its assembly with the SAW biochip. In this way, the four microchannels cross the sensing areas of the two sensors in such way that an array of eight sub-areas altogether is formed (Fig.5.11.).

Consequently, the micromodule is ready to be used.

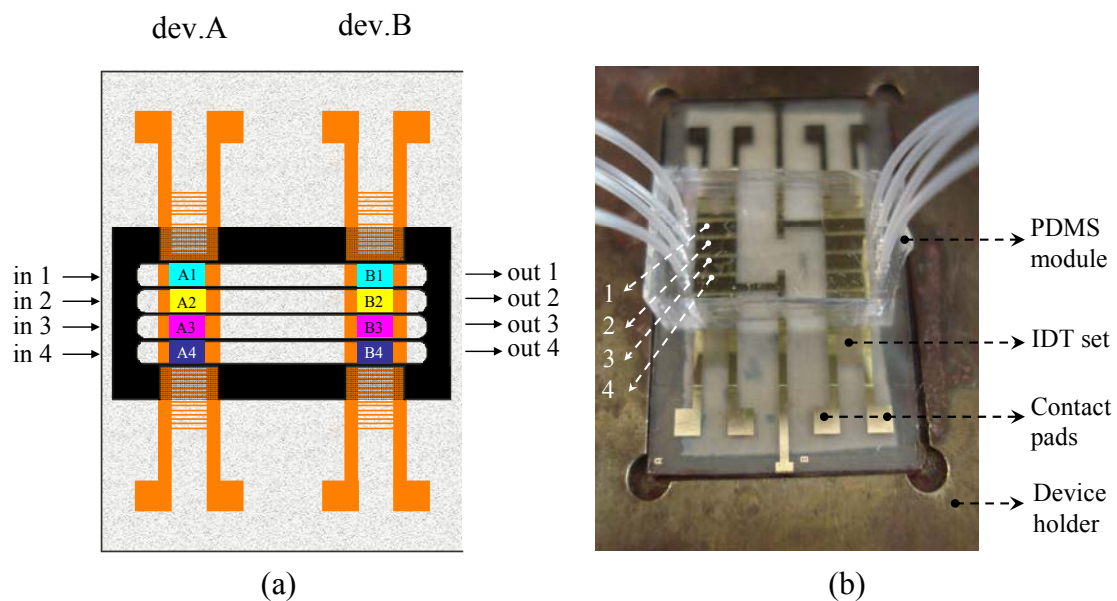


Fig.5.11. (a) Schematic top view of the design as the microchannels cross the devices, forming eight distinct sub-areas (A1, A2, . . . , B3, B4); the arrows indicate the input and output of the samples, (b) image of the PDMS module mounted on the dual-sensor chip; # 1–4 denotes the microchannels.

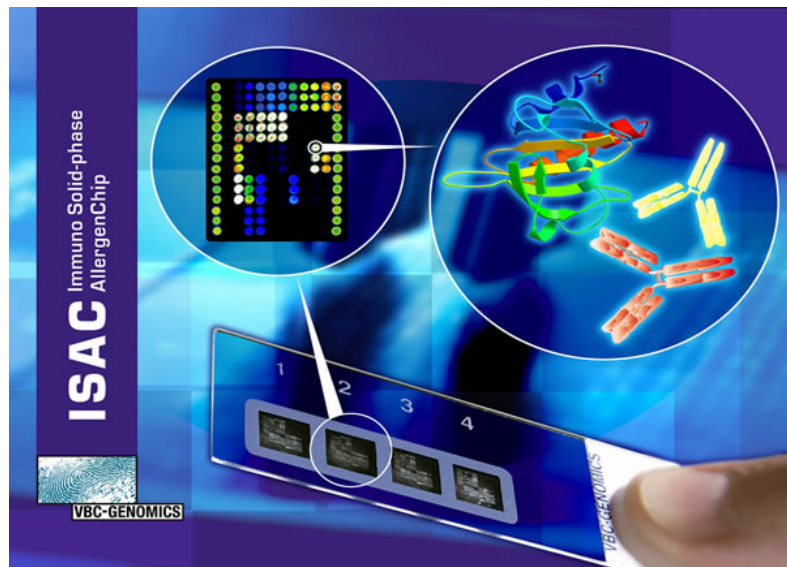


References

- [5.1.] J. N. Lee, C. Park, G. M. Whitesides, “Solvent compatibility of poly(dimethylsiloxane)-based microfluidic devices,” *Anal. Chem.*, vol. 75, No. 23, pp. 6544–6554, 2003.
- [5.2.] S. K. Sia, G. M. Whitesides, “Microfluidic devices fabricated in poly(dimethylsiloxane) for biological studies,” *Electrophoresis*, vol. 24, no. 21, pp. 3563–3576, 2003.
- [5.3.] J. C. McDonald, D. C. Duffy, J. R. Anderson, D. T. Chiu, H. Wu, O. J. A. Schueller, G. M. Whitesides, “Fabrication of microfluidic systems in poly(dimethylsiloxane),” *Electrophoresis*, vol. 21, no. 1, pp. 27–40, 2000.
- [5.4.] B.-H. Jo, L. M. van Lerberghe, K. M. Motsegood, D. J. Beebe, “Three-dimensional micro-channel fabrication in polydimethylsiloxane (PDMS) elastomer,” *J. Microelectromech. Syst.*, vol. 9, no. 1, pp. 76–81, 2000.
- [5.5.] M. E. Vlachopoulou, A. Tserepi, N. Vourdas, E. Gogolides, K. Misiakos, “Patterning of thick polymeric substrates for the fabrication of microfluidic devices,” *J. Phys., Conf. Ser.*, vol. 10, pp. 293–296, 2005.
- [5.6.] Y. Son, “Determination of shear viscosity and shear rate from pressure drop and flow rate relationship in a rectangular channel”, *Polymer*, vol. 48, pp. 632-637, 2007.
- [5.7.] N.-T. Nguyen, S. T. Wereley, “Fundamentals and Applications of Microfluidics”, Artech House, Boston, pp. 36–38, 2002.

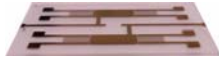


Chapter 6. Evaluation of the μ F-on-SAW performance



*Allergens detection by the Immuno Solid-Phase AllergenChip, by VBC-GENOMICS
<http://www.vbc-genomics.com/en>*





Chapter 6. Evaluation of the μ F-on-SAW performance

6.1. Introduction

Having proven that the microsystem does not suffer from fluid leakage around the microchannels, as well as at the junction between tubing and module, we assure the functionality of the new setup at the “hardware” level. Like every new system that is developed, its sensitivity, signal response and limits, as well as its reproducibility need to be checked. Moreover, for our case, as the microsystem suggests a multi-analyte detection capability due to the formation of various spatially discrete sub-areas, a critical challenge emerges, concerning the actual reliability of the system.

As the multiplicity in μ F-on-SAW is based on the formation of N sub-areas on a single sensor, it is essential that these sub-areas are equivalent in their response to the same analytes. In other words, it should be tested whether the signal response depends on the series of sample loading, and more importantly, on the location of the sub-area on the sensor. In order to test this issue, same samples were injected in all microchannels in order to extract an average and standard deviation of the signal. This deviation from an average value will be an indicator of the error (or, inversely, the reproducibility) among the sub-areas. It is desirable to know how much is the signal deviation among the sub-areas, and if it is larger than the standard deviation of experiments carried out on different days.

Thus, in this chapter, the reproducibility of μ F-on-SAW is investigated at first by applying the same viscous solutions on the different sub-areas (the condition and the ideal case is described schematically in Fig.6.1.). Then, the same principle is tested with biomolecules, checking the reproducibility of protein adsorption and subsequent specific binding. Finally, there is a comparison of the performance of the two configurations, the standard one and the μ F-on-SAW.

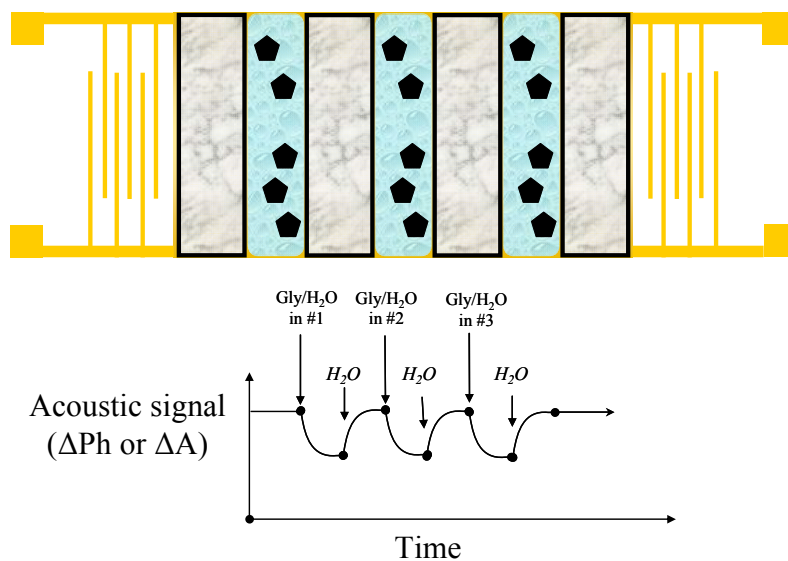


Fig.6.1. Ideal case for μ F-on-SAW setup. The repeated signal change upon loading the same sample in different microchannels indicates full reproducibility among the sub-areas.



6.2. Evaluation of μ F-on-SAW upon viscous loading

6.2.1. Sequence of sample loading

One feature of the Love wave sensors that needs to be taken into consideration is that the output IDT set receives the signal change that has taken place on the *average* of the total sensor surface. This is of no concern in the standard configuration because the used area is the total area, itself. In the new setup though, there are N available areas, and the most favorable procedure for sample loading needs to be investigated.

The desirable case would be to inject N samples at the same time and acquire the N signals simultaneously. Such an approach would drastically reduce the experimental time. However, since the output signal is the average of what happens on the surface, what we would get from a simultaneous injection is the *sum* of the sub-signals. Thus, it will be impossible to distinguish which part of the signal comes from each part of the sensor (i.e., split the output signal in parts and assign each part to an event on a particular sub-area). For this reason, the sequential injection of samples was selected, so that every moment there is an event taking place on *only one* sub-area. A detailed view of the content of each microchannel is described in Tab.6.1. in a typical experiment with glycerol solutions. During the injection of a sample through microchannel # i , water remains in the used microchannels in a “static” way, i.e. without flow, and air still exists in the unused ones. To ensure that the existence of non-flowing water in the rest of microchannels -other than the one in use- does not affect the acquired signal, water was injected and left in the microchannels for a sufficient duration of time; no change in the baseline of the signal was observed.

Although the sequential mode of sample loading could imply longer duration of the experiment, in reality this was not the case as it was proven by initial tests for time trade-off between the standard and the μ F-on-SAW setups. Moreover, the use of the μ F-on-SAW configuration with biological samples saved time from the surface regeneration procedures and reduced the device wear.

Tab.6.1. Content of each microfluidic channel during a typical experiment. “Active” microchannels (i.e., where some sample is loaded) are marked white.

μ F #4	μ F #3	μ F #2	μ F #1
water for baseline equilibrium	air	Air	air
gly#6	air	Air	air
rinse	air	Air	air
gly#5	air	Air	air
rinse	air	Air	air
rest of samples & rinse	air	Air	air
“static” water	water for baseline equilibrium	Air	air



“static” water	gly#6	air	air
“static” water	rinse	air	air
“static” water	gly#5	air	air
“static” water	rinse	air	air
“static” water	rest of samples & rinse	air	air
“static” water	“static” water	water for baseline equilibrium	air
“static” water	“static” water	gly#6	air
“static” water	“static” water	rinse	air
“static” water	“static” water	gly#5	air
“static” water	“static” water	rinse	air
“static” water	“static” water	rest of samples & rinse	air
“static” water	“static” water	“static” water	water for baseline equilibrium
“static” water	“static” water	“static” water	gly#6
“static” water	“static” water	“static” water	Rinse
“static” water	“static” water	“static” water	gly#5
“static” water	“static” water	“static” water	rinse
“static” water	“static” water	“static” water	rest of samples & rinse
End of experiment			

6.2.2. Signal response and sensitivity of μ F-on-SAW; comparison with the standard configuration

Moving to the actual experimental section, six aqueous glycerol solutions of increasing concentration (15 - 45 wt%) and viscosity (all in the Newtonian region) were used for the first characterization of the setup in terms of its signal response and sensitivity evaluation (Tab.6.2.). The reasons that glycerol was chosen were analyzed in sec.4.2.2. In fact, only one solution in all microchannels would be enough to compare the signal response and derive conclusions about the reproducibility among the sub-areas. However, to evaluate the sensitivity, a number of solutions need to be measured in order to derive the $\Delta Signal$ vs. $(\rho\eta)^{1/2}$ plots and extract the sensitivity from the slope (see sec.4.4.2.).

Figure 6.2. shows the real-time response of the μ F-on-SAW in terms of the amplitude of the acoustic wave, when the 4-channel microfluidic module was used; a similar response was observed for the phase of the acoustic wave. Each group of six signal changes corresponds to successive injections of the six glycerol solutions through microchannels #4, 3, 2, and 1. Following the injection of each sample the signal drops accordingly and, on rinsing, it returns at its initial baseline, which ensures that glycerol does not adsorb on PMMA, nor that there are any mass loading effects due to surface roughness-induced liquid trapping. A very small signal drift or deviation from complete return of the baseline is due to temperature fluctuations



and/or other environmental reasons and is not relevant to the use of the microfluidic module, since it is also observed in experiments using the standard flow cell.

Tab.6.2. Features of glycerol samples used in the experiments.

Sample serial No		Glycerol concentration (w/w)	Square root of density-viscosity product ($\text{kg} \cdot \text{m}^{-2} \cdot \text{s}^{-1/2}$)
(a)	gly#6	46.72%	2.20
(b)	gly#5	42.29%	2.05
(c)	gly#4	37.34%	1.92
(d)	gly#3	32.87%	1.74
(e)	gly#2	25.63%	1.55
(f)	gly#1	15.37%	1.41

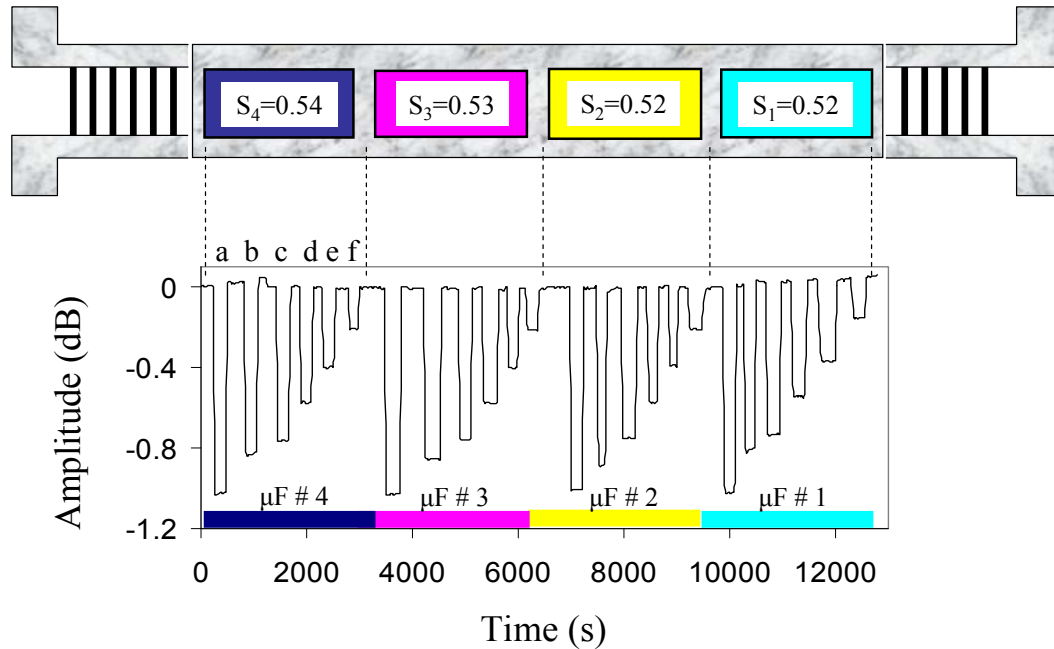


Fig.6.2. Real-time representation of the acoustic wave amplitude during sequential injection of six glycerol solutions in each microchannel. The same sequence was followed in all microchannels. The serial number of the samples corresponds to a specific concentration, as it appears in Tab.6.2. S_1 - S_4 represent the sub-areas' sensitivity expressed in $\text{dB m}^2 \text{s}^{1/2} / \text{mm}^2 \text{kg}$.

Interestingly, the pattern of Fig.6.2. resembles much the ideal concept of Fig.6.1. In particular, it was observed that when one sample (e.g. gly#1) was injected in different microchannels, the signal response obtained was essentially the same. The maximum observed deviation between microchannels was 6% for amplitude and 8% for phase change. This suggests that the sensor response is independent of the sub-area location. The above result applies to the whole range of glycerol concentrations that were tested, with maximum deviations for the rest of glycerol solutions of the order of only 6% and 6-8% for amplitude and phase changes respectively. The surface-normalized ΔA values stemming from Fig.6.2. are summarized in the bar



diagram in Fig.6.3. (similar trend for ΔPh). The last bar of each group represents the surface-normalized signal change when the standard configuration was used (exploiting the total sensing area). As it appears, there is a satisfactory agreement between the two setups (upon surface normalization of the signal) with very few exceptions of deviation up to 10%, a value which is considered to be within the experimental error. This finding allows us to use the surface-normalized signal and make direct comparisons between the two setups.

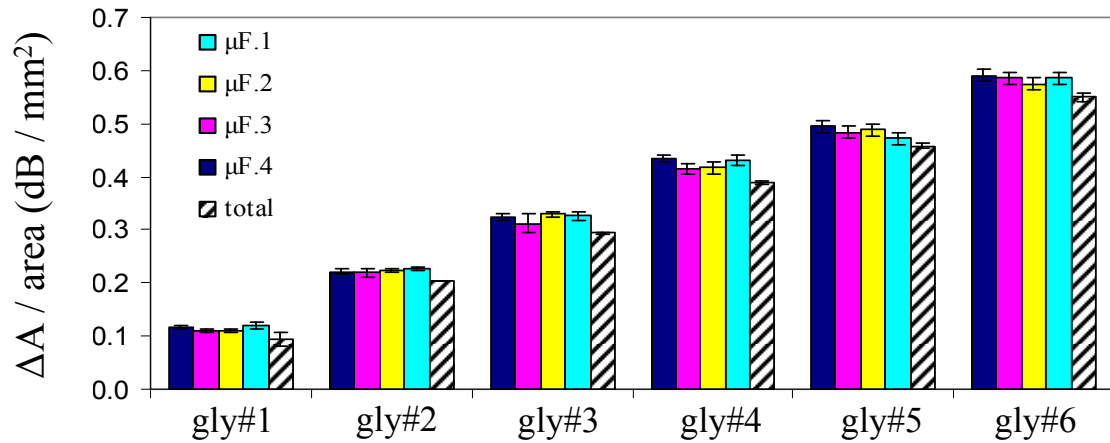


Fig.6.3. Surface-normalized amplitude change for each sample and in each microchannel.

Furthermore, as the setup utilized *two* SAW sensors, it was worth making a comparison between results from the same microchannels but different sensors, i.e., A1 vs. B1, A2 vs. B2, etc. This comparison is depicted in Fig.6.4. The figure has been drawn in a way that each rectangle corresponds to a sub-area of the $\mu\text{F-on-SAW}$ (see Fig.5.11.). The values correspond to the surface-normalized ΔA of one of the glycerol solutions (gly#3). It clearly appears that the reproducibility holds not only between the sub-areas of the same sensor, but also between the two sensors. Thus, all eight sub-areas can be used as equal, for sensing purposes.

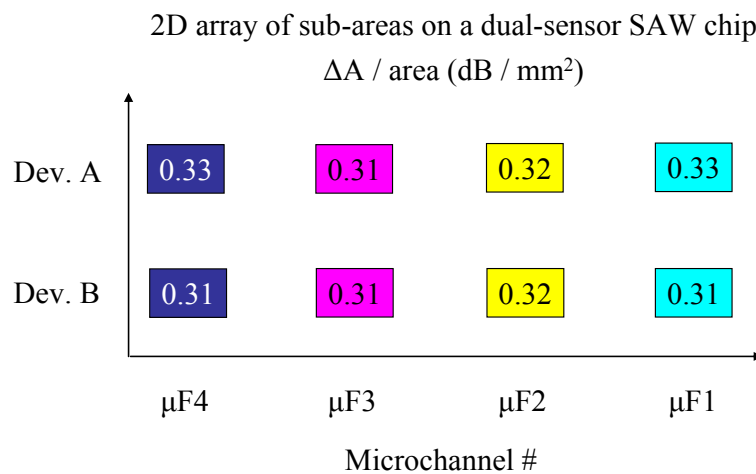


Fig.6.4. Surface-normalized amplitude change for a particular glycerol sample (32.8 % w/w) at each of the eight sub-areas formed on the microsystem (corresponding to Fig.5.11.).



The sensitivity of the SAW system upon viscous loading is evaluated through the surface-normalized change of the acoustic signal with respect to the sample's $(\rho\eta)^{1/2}$ (eq.4.9(a), eq.4.9(b)). The relationship of these quantities is linear for the total area and for the viscosity range that was used. Figure 6.5. summarizes the $\Delta A/\text{area}$ vs. $(\rho\eta)^{1/2}$ plot for all microchannels and the standard flow cell (similarly for $\Delta Ph/\text{area}$ vs. $(\rho\eta)^{1/2}$, not shown). It is noticeable that, for the examined viscosities, the linearity between ΔA (and ΔPh) with respect to $(\rho\eta)^{1/2}$ remains valid in the case of the microchannels, despite the fact that the total area has been divided into four sub-areas. The overlap of the points and the fact that they follow the same trend is a significant issue (trendlines are not shown for simplicity reasons, but the linear equations appear as inset in Fig.6.5.). It indicates that, although the sub-areas are located at different sites on the sensor, they are identical in their performance when their compartments are loaded with the same viscous liquid. The slopes for all microchannels are the same and, therefore, the sensitivity profile of their sub-areas is uniform and does not depend on their location on the sensor. In numbers, comparison of the slope values (i.e. sensitivity) among the sub-areas gives a maximum deviation of 4% and 3% when it is expressed in terms of amplitude and phase, respectively.

Furthermore, even though the absolute signal value in the $\mu\text{F-on-SAW}$ setup is N times less than that of the standard configuration, the sensitivity (based on the surface-normalized signals) remains the same, which is a very useful finding for the future application of the $\mu\text{F-on-SAW}$.

Apart from comparison between the microchannels' performance, another interesting feature from Fig.6.5. rises through the comparison of the total area sensitivity profile with that of each sub-area. Some net values of normalized signal change taken from the total area and a single sub-area revealed a deviation of approximately 10%, as described before. However, this deviation did not hold for sensitivity and was quite lower, only 1-5% and 2-3% for amplitude and phase, respectively. This indicates clearly that confining a sample in a smaller, rectangular-shaped sub-area of the sensor does not affect the sensitivity profile.

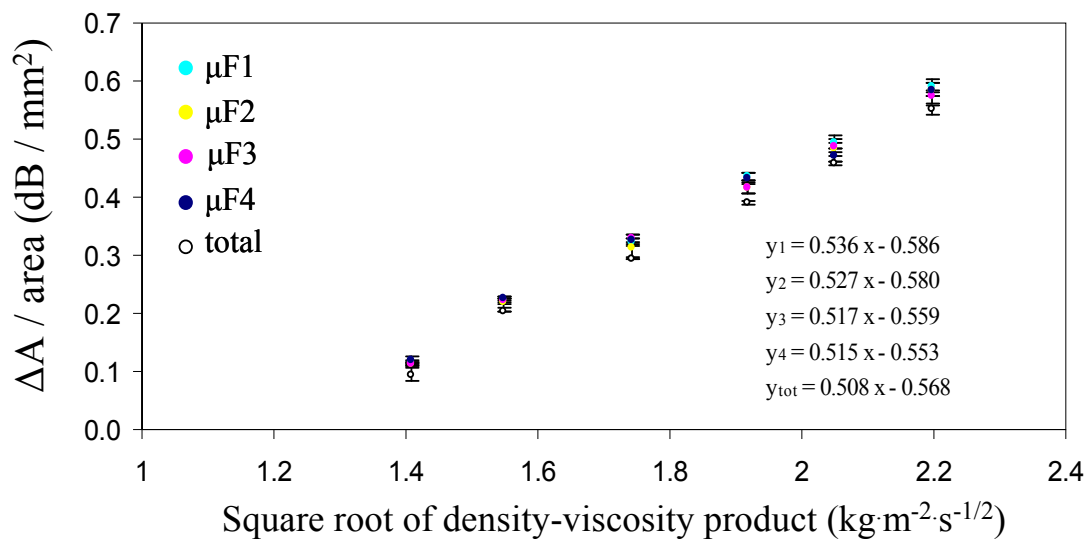


Fig.6.5. Surface-normalized amplitude change as a function of the square root of density-viscosity product. The equations refer to the linear trendlines. The slopes represent the sensitivities of the four sub-areas and the total area.



In the course of experiments, various sequences of injections were tried, for example μ F4 $\rightarrow\mu$ F3 $\rightarrow\mu$ F2 $\rightarrow\mu$ F1 (following the wave propagation direction), then μ F1 $\rightarrow\mu$ F2 $\rightarrow\mu$ F3 $\rightarrow\mu$ F4 (reverse), μ F3 $\rightarrow\mu$ F4 $\rightarrow\mu$ F1 $\rightarrow\mu$ F2 (arbitrary sequence), and others. No dependence of the signal on the injection sequence was ever observed.

6.3. Evaluation of μ F-on-SAW upon protein adsorption and specific protein binding

6.3.1. Necessity to use biomolecules for evaluation

In the previous section, the potential of μ F-on-SAW for use with liquid samples was investigated, where it was proven that it operates reproducibly in a remarkable way among the sub-areas, upon viscous loading (operating, thus, even as a “multi-viscosimeter”).

However, as the final objective for μ F-on-SAW is biosensing applications (adsorption, biomolecular interactions, kinetics analysis, etc.) the reproducibility issues among the sub-areas, described in the previous section must be verified for biological samples as well, before proceeding to the actual multi-analyte detection. The reason that the verification with simple viscous solutions is not enough, by itself, is that the nature of acoustic wave interaction with non-adsorbing viscous solutions (such as glycerol solutions) is different from that with adsorbing (visco)elastic samples (such as biological layers); this is evident also from the governing equations of these interactions (see Tab.4.2.). Moreover, when glycerol solutions were used for tests, upon rinsing there was no remaining sample on the sub-area (recall the non-adsorbing nature of glycerol). On the contrary, when a protein adsorbs on a sub-area it is not removed and when a protein adsorbs on the next sub-area there is already a “history” on the sensor, which should be examined if it has any influence on the reproducibility. For these reasons, it is essential to characterize the μ F-on-SAW performance (and especially reproducibility) with biological samples too, apart from the evaluation with glycerol solutions.

For experiments with proteins, the phase change of the acoustic signal instead of the amplitude was used in order to probe the biomolecular processes. This was done under the assumption that, phase change is predominantly dependent on the mass uptake rather than any viscoelastic phenomena. This is close to reality when proteins, especially globular ones (like the ones we use) are used with thicknesses up to the penetration depth (see sec.4.2.4.).

Unlike the reproducibility experiments with glycerols, where the top layer of the sensor chip “exposed” to the sample was PMMA, for the protein-based tests, a 20-nm-Au layer was sputter-coated on top of PMMA to facilitate more efficient adsorption of the biomolecules. For surface regeneration purposes, a standard procedure described in sec.3.5. was followed. For fluid flow, a syringe pump was used at 5 μ L/min flow rate.



6.3.2. Reproducibility of μ F-on-SAW upon biomolecular interactions

For the reproducibility tests, two types of interactions were investigated:

- (i) Biotin-avidin, by means of neutravidin adsorption and biotinylated BSA (b-BSA) binding.
- (ii) Protein G adsorption and IgG binding.

Biotin-avidin interaction was selected because it is a well known and characterized one. Apart from the commercially available biotinylated molecules, there are available biotinylation kits, which can easily tag one or more biotins to a biomolecule (protein, DNA, etc.) without tampering the molecule's biological activity, achieving specific interaction with avidin. The biotin-avidin bond is the strongest known bond in nature (dissociation constant of the order of $\sim 10^{-14} \text{ M}^{-1}$ [6.1.]) which makes the formation of the complex practically irreversible and, thus, resistant to various solution conditions (such as multiple washings, pH changes, etc).

Neutravidin (neu) is a deglycosylated version of avidin with a mass of approximately 60 kDa. It has a near-neutral pI (6.3 ± 0.3) which minimizes non-specific interactions [6.2.]; this was the main reason for its selection over the standard streptavidin. It has four available binding sites, when in solution, which are reduced in maximum two, when it adsorbs on a surface. The latter was the case in our experiments, where it was adsorbed on each sub-area to form a monolayer and it was followed by b-BSA binding. The concentrations of neu and b-BSA were 200 and 50 $\mu\text{g/mL}$, respectively, in PBS (pH 7.4).

ProteinG-IgG interaction is also a well-known and studied one [6.3.] and it was selected because it is the basis for immunological, antibody-antigen, interactions. Similarly, PrG was left for adequate time to adsorb on the surface and then the IgG was injected for binding. The concentrations of PrG and IgG were 200 and 50 $\mu\text{g/mL}$, respectively, in PBS (pH 7.4).

Thus, the reproducibility was eventually tested in the following four manners:

- adsorption of neu in all μ Fs
- binding of b-BSA on neu in all μ Fs
- adsorption of PrG in all μ Fs
- binding of IgG on PrG in all μ Fs

In detail, a typical experiment for binding detection with μ F-on-SAW took place in the following stages, assuming sequential injections of the samples in each microchannel:

- (a) PBS for equilibration in μ F4
- (b) neutravidin 200 $\mu\text{g/mL}$ (or PrG 200 $\mu\text{g/mL}$)
- (c) PBS rinsing
- (d) injection and specific binding of b-BSA 50 $\mu\text{g/mL}$ on neutravidin (or, specific binding of IgG 50 $\mu\text{g/mL}$ on PrG)
- (e) PBS for rinsing

...the above sequence was followed in μ F3 $\rightarrow\mu$ F2 $\rightarrow\mu$ F1.

The sensor diagrams taken from the μ F-on-SAW during the above mentioned interactions appear in Fig.6.6. and Fig.6.8. In principle, when the status of a microchannel changes from “empty” to “PBS filled”, a large phase change is caused.



However, this was omitted from the figures for simplicity purposes, as it would “visually” block the actual ΔPh of interest. This does not affect the data analysis, anyway, as it is a mere shift in the graph. Moreover, Fig.6.8. has emerged from a graph of similar nature to Fig.6.6., by shifting all injections to zero; this helps to visualize better the equivalence of the sub-areas upon injection of the same samples.

The ΔPh values of the examined molecules are then presented in bar diagrams (Fig.6.7. and Fig.6.9.). In order to derive the ΔPh for each protein in a specific microchannel, values from different days (but in the same microchannel) were averaged. It can be deduced from the following graphs that the reproducibility among sub-areas holds for proteins as well, in cases of both adsorption, and specific binding, within a 10% error, which is considered well accepted.

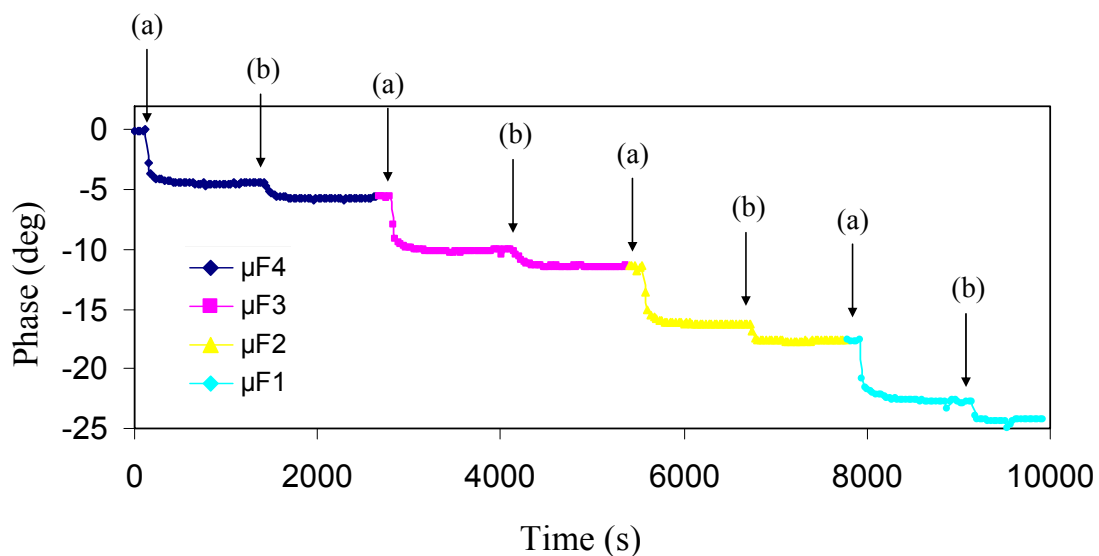


Fig.6.6. Real-time phase change: “(a)” and “(b)” correspond to neutravidin and b-BSA injection times, respectively. Rinsing steps after each sample are not marked with arrows for simplicity reasons.

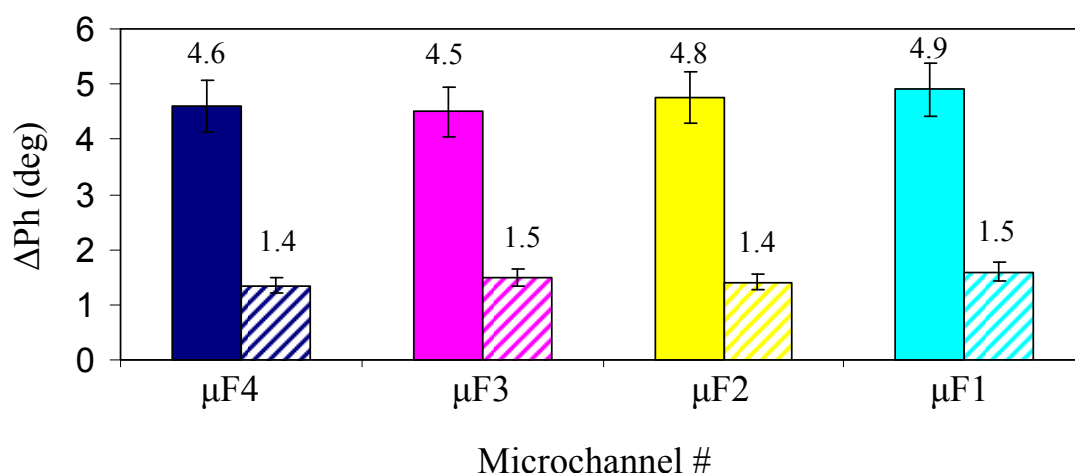


Fig.6.7. Phase change for neutravidin adsorption (filled bars) and b-BSA binding (striped bars).

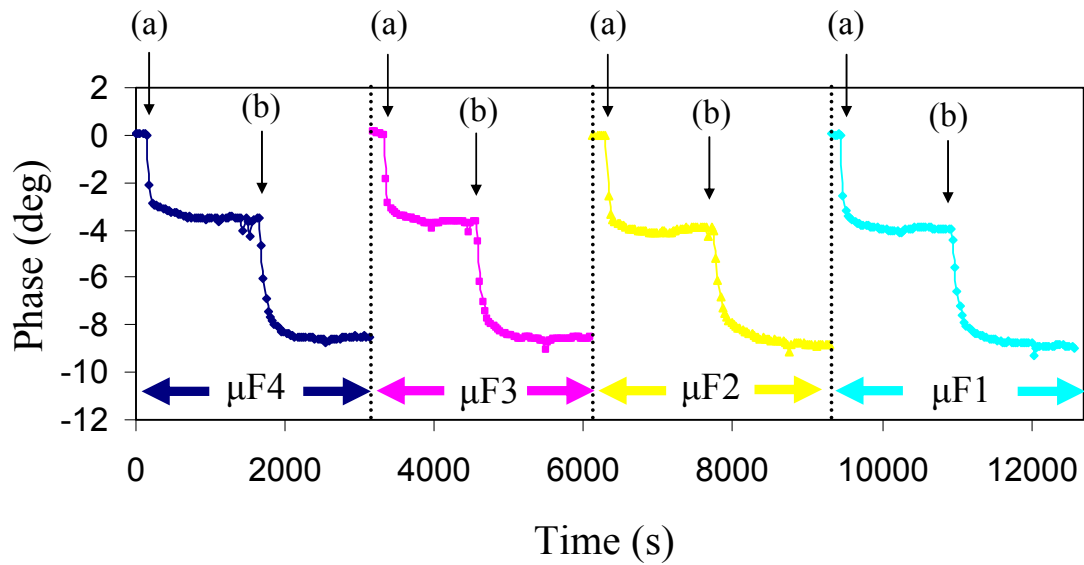


Fig.6.8. Real-time phase change due to: (a) PrG adsorption on Au, and (b) IgG binding, in all 4 microchannels. Rinsing steps after each sample are not marked with arrows for simplicity reasons.

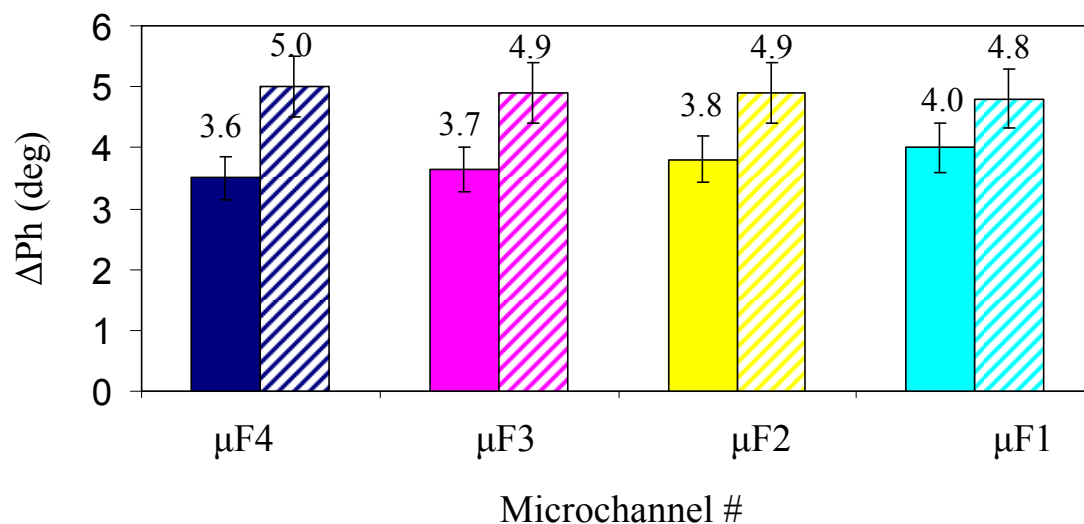


Fig.6.9. Phase change for PrG adsorption (filled bars) and IgG binding (striped bars)

6.3.3. Signal-to-surface proportionality

Concerning the proportionality of the signal to surface area, the reasonable question that rises is whether it is valid for biomolecule detection as it was for glycerol solutions (sec.6.2.2.). The following two graphs give the answer. Figure 6.10. is a combined plot of the phase due to neutravidin adsorption on the *total area*, and on *all sub-areas* sequentially. The graphs were both shifted to zero initial signal in order to simplify the comparison. The total area is 7.44 mm^2 and each sub-area is 1.76 mm^2 , i.e., the four microchannels add up to 7.04 mm^2 , 5% less than the total area, but still it is less than the experimental error of the sensor. It clearly appears that the sum of the signals from each sub-area corresponds to the signal from the total area. Similar real-time trend exists for PrG (data not shown) and the surface-normalized phase change is



summarized in Fig.6.10(b) for neu and PrG, where it clearly appears that the signal-to-surface proportionality holds for biomolecule samples, like it did for glycerol.

This finding can be used in a more “advanced” version of μ F-on-SAW. If, for example, among the N samples under test, there is one that gives smaller phase change, this sample can be given more “space” on the surface in order to increase the signal response (confining, simultaneously, molecules giving bigger response, to a smaller sub-area). Thus, an “asymmetric” μ F-on-SAW can be formed, compensating the phase change from small- and big-signal molecules.

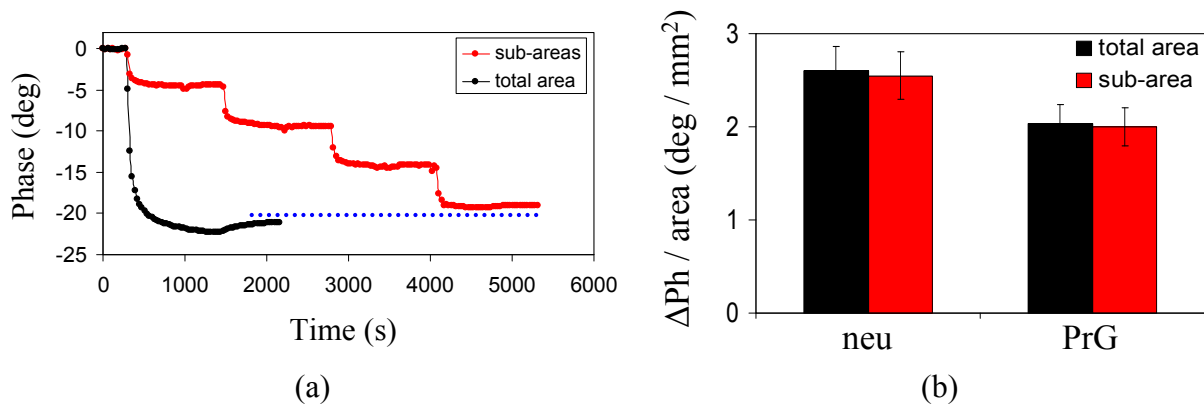


Fig.6.10. (a) Phase change of neutravidin adsorption on the total area and on all sub-areas, (b) surface-normalized ΔPh indicating signal-to-surface proportionality between the standard and the μ F-on-SAW configurations.

6.4. Conclusions

The evaluation of the μ F-on-SAW setup revealed very interesting points. Comparison of the results deriving from the four sub-areas showed remarkable uniformity along its compartmentalized sub-areas, regarding the net values of signal change as well as the sensitivity profiles of those areas. No dependence of the results on the location of the sub-areas on the sensor was observed, neither on the sequence that the microchannels were used (i.e. $1 \rightarrow 2 \rightarrow 3 \rightarrow 4$, reverse, or arbitrary order). Moreover, in the case of protein samples it was shown that the signal acquired from an “active” microchannel is not affected by the “history” on the other sub-areas. Thus, no matter where or when a sample is injected in the microchannels, the latter are equivalent in their response, allowing the system to be safely and reliably used with various samples. This ensures a reliable multi-detection dependent only on the different nature of the samples and not on sensitivity inhomogeneities. Thus, highlight conclusions of this chapter regarding the acquired signal from the N sub-areas is summarized below:

- (i) It is independent of the history of the device, i.e., what already exists on other sub-areas.
- (ii) It is independent of the location of the sub-area.
- (iii) It is independent of the injection sequence or direction.

These facts encourage the use of μ F-on-SAW for reliable and reproducible multi-analyte detection.

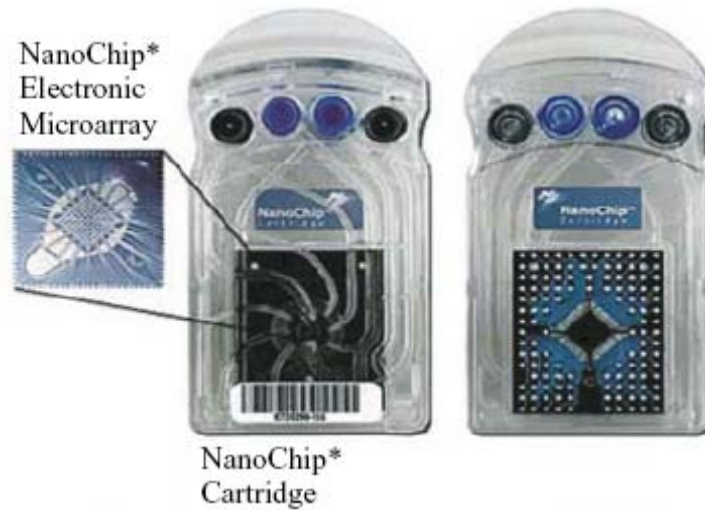


References

- [6.1.] H.F. Launer, H. Fraenkel-Conrat, "The avidin-biotin equilibrium", *J. Biol. Chem.*, vol. 193, pp. 125-132, 1951.
- [6.2.] Y. Hiller, E.A. Bayer, M. Wilchek, "Nonglycosylated avidin", *Methods Enzymol.*, vol. 184, pp. 68-70, 1990.
- [6.3.] U. Sjöbring, L. Björck, W. Kastern, "Streptococcal Protein G: Gene structure and protein binding properties", *J. Biol. Chem.*, vol. 266, pp. 399-405, 1991.



Chapter 7. Multi-sample detection using μ F-on-SAW



*Nanochip electronic microarray for diagnostics, produced by Nanogen
<http://www.nanogen.com/products/customassays>*





Chapter 7. Multi-sample detection using μ F-on-SAW

7.1. Introduction - biomolecules used for multi-analysis

In this chapter the multi-sensing capacity of μ F-on-SAW is investigated using four different samples. Having made the preliminary tests with neutravidin – b-BSA and PrG – IgG interactions and having some feedback about how these systems work, it is reasonable to proceed to multiplicity using one of these two interaction pairs. Due to the broad availability of biotinylated molecules of various sizes and features, compared to antibodies, the avidin-biotin pair was selected as the basis for the multiple experiments.

The selected biotinylated molecules were Protein G (PrG), Protein A (PrA), Bovine Serum Albumin (BSA) and Immunoglobulin G (IgG).

- *Protein G (PrG) and Protein A (PrA)*: They are surface-bound bacterial cell wall proteins, deriving from *Streptococcus* and *Staphylococcus aureus*, respectively. Both proteins exhibit affinity for the Fc fragment of immunoglobulins. The earlier discovered PrA is known to have distinct types of binding activity: a primary reaction with IgG and other classes of Ig at sites located in the Fc region and a weaker reaction localized to a region outside the antigen combining site [7.1.]. The affinity of PrG for IgG is higher than that of PrA although over a narrower spectrum of Ig classes. PrG binds monoclonal antibodies from mouse and rat, a property that is poor in PrA. Therefore, PrG is considered a more general and versatile IgG binding reagent [7.2.]. The above properties make the two proteins of primary interest to immunoassay and chromatography applications.
- *Bovine Serum Albumin (BSA)* is a heart-shaped protein. It is a serum protein, but in biosensors community it is widely used as a “blocking agent”, i.e., to block non-specific interactions and/or fill gaps on the sensor surface after incomplete receptor adsorption.
- *Immunoglobulin G (IgG)* belongs to the immunoglobulins family, where other types are included, such as IgA, IgE, etc., among which IgG is the most abundant (see sec.8.4. for more details).

The above commercially available proteins were selected in their biotinylated form as standard molecules of well known size to test the newly developed μ F-on-SAW system. Moreover, all the above proteins have, in general, a globular nature (i.e., not linear, fibrous or another special shape which could affect in some way the acoustic signal, as it has been shown [7.3.]). Finally, another major reason towards their selection was their *MW*: first, they span a large spectrum, from 30 to 150 kDa, and second, the small proteins have quite close values in their *MW*, which is a challenge for the system’s ability to “discriminate” the proteins with close *MW*, i.e. explore the system’s “resolution”, as it is widely termed. Table 7.1. summarizes the various features of the four proteins that were used (in their non-biotinylated form, as the biotin conjugate does not alter their properties).



Tab.7.1. Properties of biomolecules used in multi detection.

	PrG [7.4.]	PrA	BSA	IgG [7.5.]
MW (kDa) *	30	42	66	150
Shape	globular	globular	heart-like shape	rectangular prism
Size **	$3 \times 4 \times 5$	$2.5 \times 3.5 \times 4.5$	$3 \times 3 \times 8$ nm	$23 \times 23 \times 4$ nm
Biotins / molecule (Sigma datasheet)	2-4	3-8	3-6	N/A

* As $MW_{biotin} = 244$ Da, the MW of the biotinylated molecules was considered to be equal to that of the non-biotinylated ones (error in this assumption was less than 5%)

** The size was verified via the RCSB protein data bank (www.pdb.org)

7.2. Multiple detection with μ F-on-SAW

In all experiments, neutravidin was first injected in each microchannel and was left to adsorb so as to form a monolayer that would, subsequently, capture the biotinylated molecules. Since the specific binding detection and kinetic analysis was the objective of this chapter, the non-specific binding was minimized by injecting 1 mg/mL BSA blocking solution after the neutravidin adsorption. All biotinylated proteins were injected in concentrations that were high enough to saturate the neutravidin layer. The injection sequence in each microchannel was the following:

- PBS for equilibrium in μ F4
- neutravidin 500 μ g/mL
- PBS rinsing
- BSA for blocking (1 mg/mL)
- PBS rinsing
- b-BSA 50 μ g/mL (or b-PrG in μ F3, b-IgG in μ F2, b-PrA in μ F1)
- PBS rinsing

The above steps are followed in all the rest microchannels and the biomolecules distribution over the sub-areas on the sensor chip after protein binding appears schematically in Fig.7.1. Furthermore, based on the finding that all sub-areas are reproducible in terms of signal response, the four biotinylated proteins were injected in any microchannel.

Figure 7.2. shows the real-time phase change for the four sequentially detected biomolecules in the four compartments of the same sensor. Occasional spikes in the real-time signal exist due to sample change. During this procedure the pump is stopped, the sample syringe is removed, the buffer syringe is positioned, and the pump is set on again. Such a pressure change often results in a signal spike (which is a factor that needs to be optimized, as discussed in the future plans section). There are other causes of signal spikes, such as air bubbles passing from the surface; however, a pressure change spike is recognizable because the signal returns to its initial baseline.

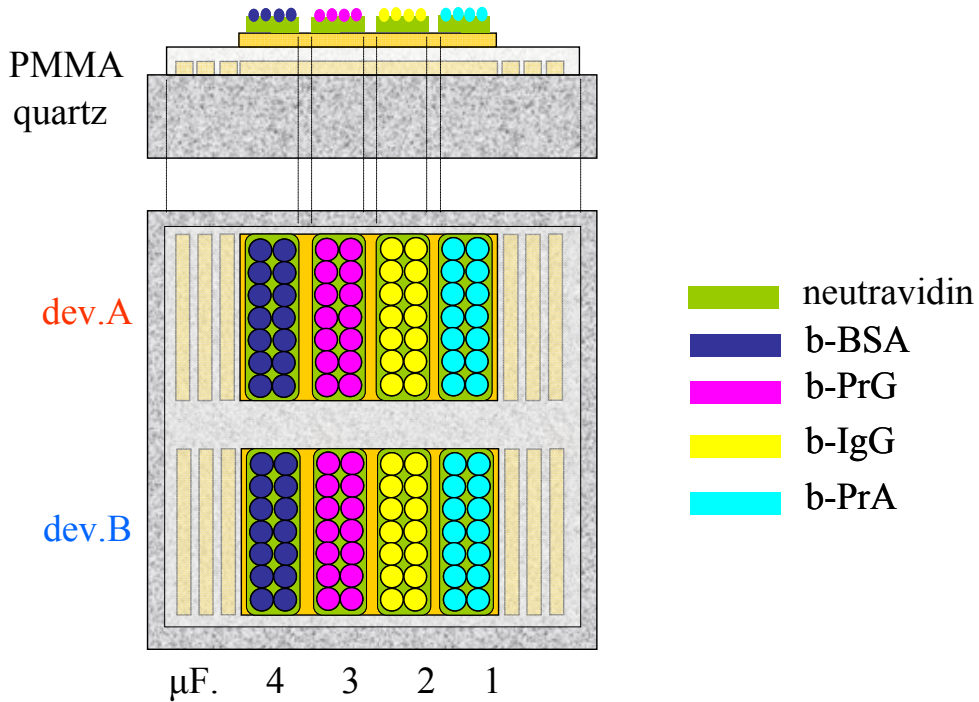


Fig.7.1. Schematic representation of the biomolecules' distribution forming an 8-area biomolecular array.

The phase change is depicted in a bar diagram in Fig.7.3. (the colors between Fig.7.1., Fig.7.2., and Fig.7.3. are equivalent). It is clearly shown that even though there is proximity of MW between three proteins, the μ F-on-SAW is capable of distinguishing the signals among them. Moreover, the non-specific binding was investigated by injecting *non*-biotinylated molecules on neutravidin (after BSA addition, data not shown). No phase change was observed, ensuring the minimum non-specific binding, which allows the safe assumption that the signal change stemmed purely from the biotin-avidin interaction.

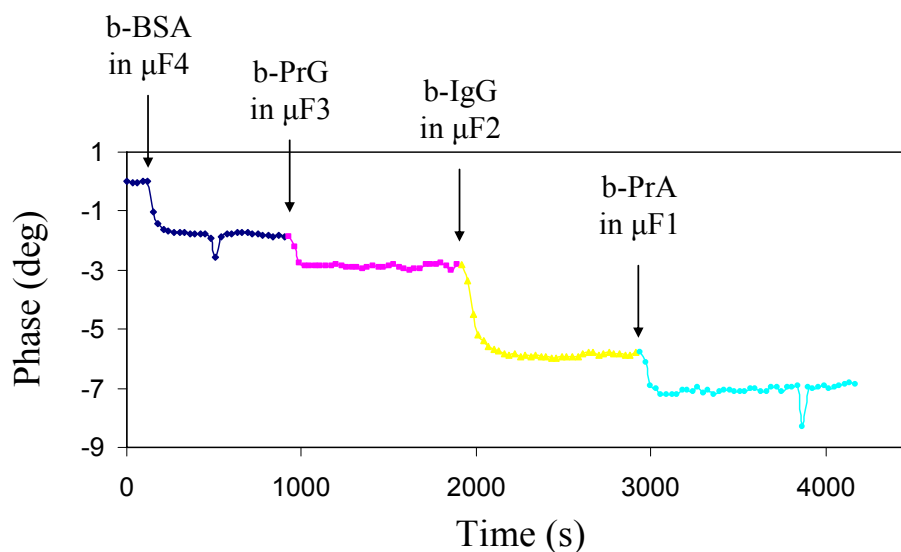


Fig.7.2. Sequential detection of four different biomolecules with μ F-on-SAW.

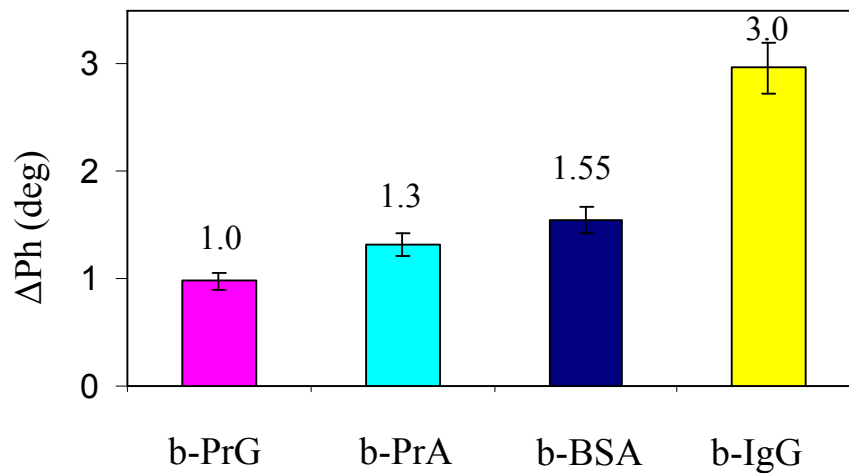


Fig.7.3. Phase change for the four examined molecules.

7.3. Full exploitation of 4×2 sub-areas: multiplexing with μ F-on-SAW

As the μ F-on-SAW consists of two devices and four microchannels crossing them, a 2D array of eight sub-areas is formed; thus, eight interactions can potentially be probed. However, due to its configuration, a sample flowing in a microchannel passes from both devices; thus, only four interactions are in reality detected in duplicates and only half the capability of μ F-on-SAW is exploited (even if more than 2 devices were used, the maximum detected interactions would, again, be limited to the number of microchannels). In this section, we demonstrate that under proper conditions, it is possible to exploit the full capacity of the μ F-on-SAW in its current configuration, in order to probe $2 \times 4 = 8$ biomolecular interactions.

This was achieved by setting different receptor molecules on the two devices. More particularly, devices A and B were pre-treated with different molecules, namely neutravidin (in dev.A) and PrG (in dev.B). A custom made double-well PDMS module was used with two rectangular openings of the size of the total sensing areas, in order to prevent the protein solutions to expand on the IDT areas and also to prevent them from intermixing. The solutions of the two molecules (80 μ L volume of 1 mg/mL concentration for both proteins) were poured on top of the two total sensing areas and left to adsorb for 30 min at room temperature, followed by PBS rinsing and drying under nitrogen. This procedure was repeated a few times so as to ensure the reproducibility of the physical adsorption of neutravidin and PrG in a static condition.

The microfluidic module was then carefully attached on the pre-functionalized chip and the typical experimental procedure standardized for μ F-on-SAW setup followed (1 mg/mL BSA was injected in all microchannels prior to any sample, in order to block possible “empty spaces” on the surface).

Since nothing changed on the “hardware” of the setup, a sample flowing through μ F_i flowed, again, through both dev.A and B. However, since dev.A and B were pre-functionalized with different receptors, *two* interactions were probed instead of *one*. For example, injecting b-BSA through μ F₄, the sample flowed above both neu and PrG, probing both neu – b-BSA and PrG – b-BSA interactions. Repeating a similar procedure with the other three microchannels (injecting the other three



samples) 8 different interactions were analyzed, which are summarized in Tab.7.2. and schematically drawn in Fig.7.4. (the colors do not correspond with the previous figures).

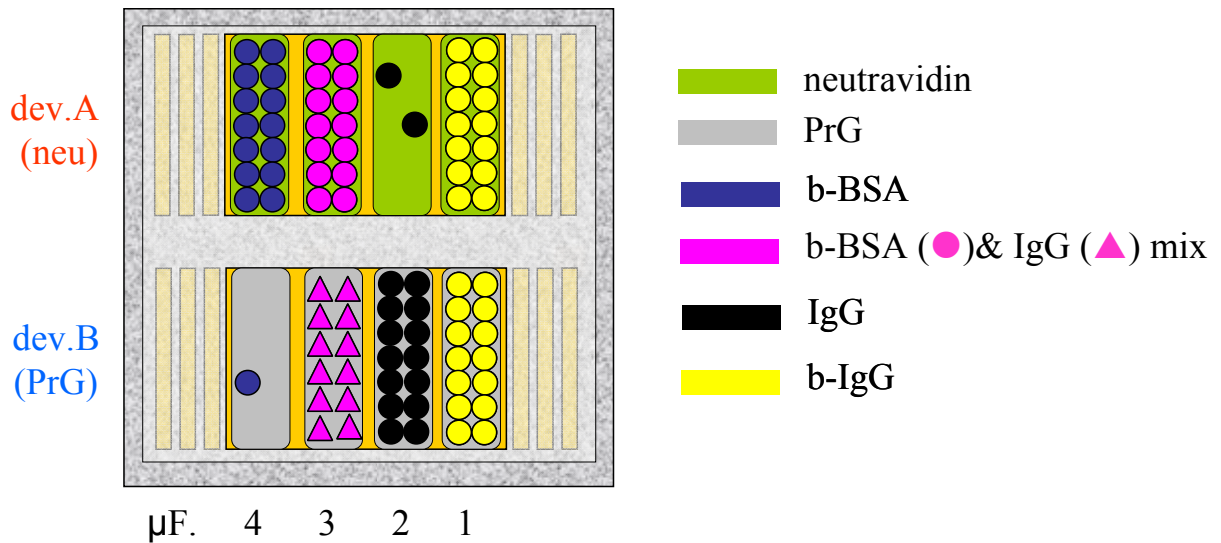


Fig.7.4. Schematic representation of the eight probed interactions.

Tab.7.2. Combination of 2 pre-functionalized device surfaces with 4 injected analytes to achieve the monitoring of 8 different interactions (average ΔPh values in deg, with standard deviation $\pm 8-10\%$).

Pre-functionalized devices	Samples injected in microchannels			
	μ F4 (b-BSA)	μ F3 (b-BSA + IgG)	μ F2 (IgG)	μ F1 (b-IgG)
dev.A (neu)	neu + b-BSA (1.5)	neu + mix (1.3)	neu + IgG (<0.4)	neu + b-IgG (3.0)
dev.B (PrG)	PrG + b-BSA (<0.2)	PrG + mix (4.8)	PrG + IgG (4.7)	PrG + b-IgG (4.3)

Table 7.2. is drawn in such way as to fully correspond *spatially* to the μ F-on-SAW setup: the 4 columns correspond to the four microchannels, and the 2 rows correspond to the 2 sensor devices; thus, each of the eight cells corresponds to each of the sub-areas of the setup. Clearly it appears that eight different interactions are probed, and the signals they give are summarized in Fig.7.5., where each bar corresponds to a particular sub-area of the μ F-on-SAW.

Note that a mixture of two proteins was also tested in order to study interference effects and analyte binding specificity. In particular, the protein mixture consisted of b-BSA and IgG. This pair was selected because: (i) the former is known to interact only with neutravidin and the latter only with PrG, (ii) b-BSA exhibited negligible non-specific binding to PrG (sub-area B4); similarly for IgG on neutravidin (sub-area A2), (iii) no interaction between the two mixture components was experimentally observed, allowing the assumption that they are separate in the solution, forming no molecular complex.

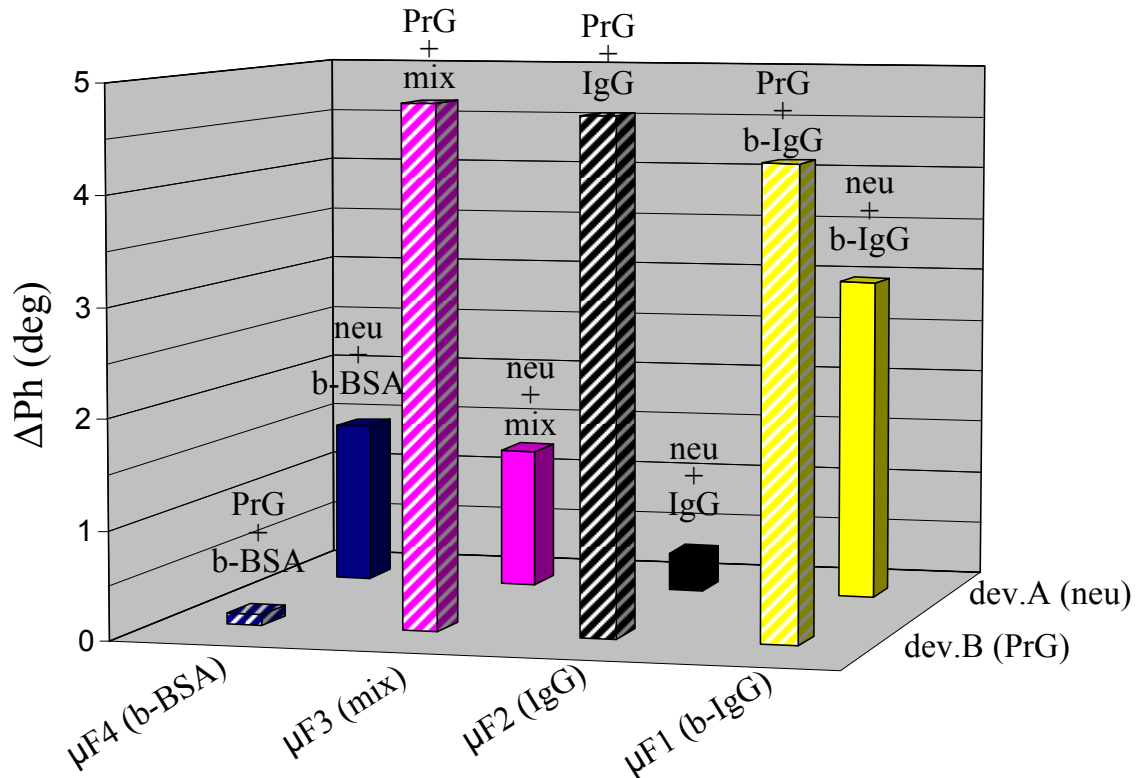
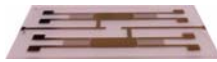


Fig.7.5. Multiplexed interactions probed with μ F-on-SAW (standard deviation was of the order of 8-10%, not depicted on the figure due to software restrictions in 3D mode).

A close look at Fig.7.5. reveals the following interesting points:

- In A4, the neu – b-BSA interaction gave a signal change, which was typical to this interaction (see also Fig.7.3.).
- In B4, the PrG – b-BSA showed minimum non-specific binding as expected.
- In A3, the neu – mixture interaction gave a signal change which was equal to that observed in A4, proving that the IgG presence in the mixture does not affect the neutravidin – b-BSA binding.
- In B3, the PrG – mixture signal was almost as much as that observed in B2 and B1, indicating again, that IgG binds with PrG in the same way, no matter if it is in mixture, or not.
- In μ F2, IgG bound only to PrG (B2) and minimally to neutravidin (A2), as expected for the specific and non-specific interaction, respectively.
- In μ F1, b-IgG molecule has in principle two specific binding options; biotin to neutravidin (A1), and IgG Fc fraction to PrG (B1) and is expected to interact with both pre-functionalized surface receptors. Indeed, not only does b-IgG bind to neutravidin, but it also appears that biotin molecules do not interfere with the PrG-IgG interaction since $\Delta Ph_{PrG - b-IgG} = \Delta Ph_{PrG - IgG}$.

Thus, in this section the feasibility of exploiting the full potential of μ F-on-SAW was investigated and successfully proven. Small deviations from the expected values may have derived from possible rinsing off of the neu and PrG after the pre-functionalization and prior to attachment of the microfluidic module. However, the main objective of these experiments was achieved: the full-scale multiplexity of the



μ F-on-SAW was demonstrated by pre-functionalizing the surfaces of the sensors *prior* to mounting of the microfluidic module. This pre-functionalization can be achieved in a simple way, by letting the receptors adsorb for a sufficient time, or by using more sophisticated methods, such as surface nanopatterning techniques. Indicatively, micro-contact printing, dip-pen nanolithography, inkjet spotting and standard bio-compatible lithographic methods can be used to precisely pre-functionalize the surface with an array of rectangular spots (corresponding to the sub-areas that are formed on the μ F-on-SAW) with (up to) 8 receptors and detect 8 different biomolecular interactions.

7.4. Binding affinities and kinetic analysis

In this section the capacity of the microsystem is further investigated during the equilibrium and kinetic analysis of binding processes detected via the μ F-on-SAW. Firstly, the affinity constants are assessed via the equilibrium analysis, assuming Langmuir binding isotherms to govern the interactions. Kinetic analysis follows and the protocol for data processing is briefly described, accompanied by some basic mathematical formulation for the processing. Affinity constants calculated through kinetic data are compared with the values inferred from the equilibrium analysis. Furthermore, the binding rate constants are evaluated, which is something that can be done only via the kinetic and not through the equilibrium analysis. Various theoretical approaches have been published in the literature for processing real-time and equilibrium data [7.6.], [7.7.], [7.8.], [7.9.] a summary of which is described in sec.7.4.1. and sec.7.4.2.

7.4.1. Theory on equilibrium analysis

A biomolecular binding interaction between a receptor R and a ligand L, forming a molecular complex RL can be described by:



In such interactions it is of interest to know the strength of the binding, which is quantitatively annotated by the association (K_A) or dissociation (K_D) constants of the complex formation. Both K_A and K_D , also referred to as affinity constants, are measured under equilibrium conditions and are related to each other through $K_A=1/K_D$. The term “equilibrium” implies a dynamic state where complexes are being formed and dissociated at a constant rate, with no longer change in the concentrations of free and bound species. In our case, dissociation was either not existent, or not observed with our detection method. This could imply inability to define dissociation rate and affinity constants. However, owing to the data processing protocol that was followed, all constants were determined through kinetic analysis using only the association curves prior to equilibrium by proper fitting (see sec.7.4.2.).

A relation between the affinity constants and the concentrations of the interacting molecules is given by:



- association constant: $K_A = \frac{[RL]}{[R][L]} = \frac{k_a}{k_d}$ (measured in M^{-1}) (eq.7.2(a))
- dissociation constant: $K_D = \frac{[R][L]}{[RL]} = \frac{k_d}{k_a}$ (measured in M) (eq.7.2(b))

The terms k_a (in $M^{-1}s^{-1}$) and k_d (in s^{-1}) appearing in the equations are the association and dissociation rate constants, respectively, and denote how fast the compound RL is formed and dissociated, respectively, i.e., they are related to the actual kinetics of the (forward and reverse) interactions. From the above it can be inferred that an interaction with high affinity constant will most likely have a large k_a and small k_d .

It is important to notice that the affinity constants can be measured directly (see processing below) without knowing the constants k_a and k_d ; however, the inverse is not possible, which is why the equilibrium analysis is not enough for the calculation of the rate constants, but kinetic analysis is needed, instead.

Taking into consideration that the total concentration of R includes the free and the bound quantities of R, i.e., $[R]_{tot} = [R] + [RL]$ (same for L) eq.7.2(b) can be rearranged as:

$$\frac{[RL]}{[R]_{tot}} = \frac{[L]}{[L] + K_D} \quad (\text{eq.7.3.})$$

$\frac{[RL]}{[R]_{tot}}$ represents the fraction of R which is in the form of RL complex, referred to as the “fraction bound”, and is, essentially, equal to the relative surface coverage, Γ (Langmuir binding isotherm):

$$\Gamma = \frac{[RL]}{[R]_{tot}} = \frac{[L]}{[L] + K_D} \quad (\text{eq.7.4.})$$

The surface coverage is proportional to the sensor signal (this applies not only to piezoelectric sensors, but to optical, label-based, etc). Thus, in our case and for a certain concentration, c , of the ligand, the above equation becomes:

$$\Delta Ph_c = \frac{\Delta Ph_{max} c}{c + K_D} \quad (\text{eq.7.5.})$$

ΔPh_c (corresponding to $[RL]$) is the phase change for a particular ligand concentration at equilibrium conditions (e.g. c_1, c_2 in Fig.7.6(a)); ΔPh_{max} (corresponding to $[R]_{tot}$) is the phase change at high concentrations, where ΔPh remains constant, irrespective of the ligand concentration increase (e.g. c_3, c_4 in Fig.7.6(a) and Fig.7.6(b)); K_D is the dissociation constant, expressed in M; thus, the concentration at which $\Delta Ph = 0.5 \times \Delta Ph_{max}$ equals K_D . However, for more accurate calculations, non-linear curve fitting of eq.7.5. was done, as well as linearization of eq.7.5. and subsequent linear fitting (sec.7.4.3.).

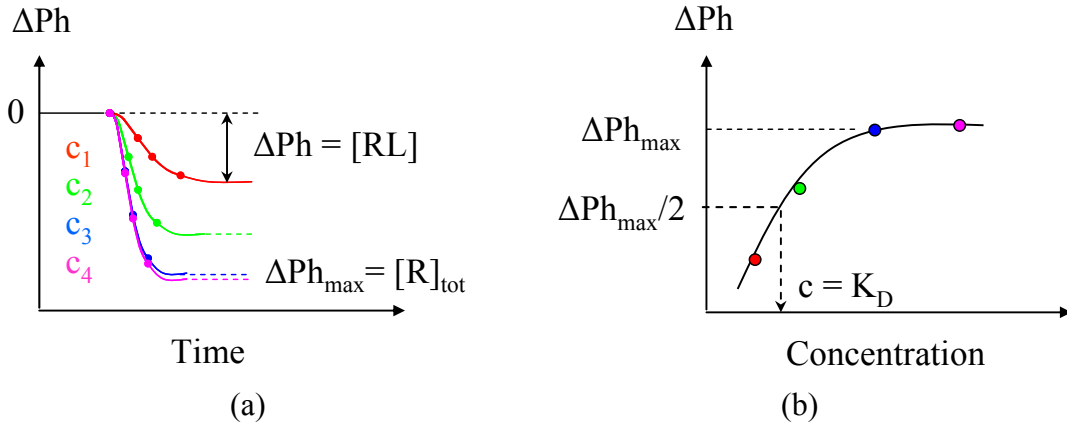


Fig.7.6. (a) Schematic representation of four ligand concentrations, reaching saturation at c_3 and c_4 , (b) isotherm curve derived from (a). Colors from (a) correspond to (b).

7.4.2. Theory on kinetic analysis

With the previous formulation it was shown how the affinity constants can be measured via calculations at equilibrium state. On the other hand, another interesting question to answer is “how fast” an interaction takes place. This is described by the rate of association and dissociation, i.e., the change in concentrations of reactants and products over time as the reaction approaches equilibrium; this is done via kinetic studies and analysis, in order to define the association and dissociation rate constants (k_a and k_d , respectively).

In the typical single-step biomolecular binding reaction, described in eq.7.1., the rate of association (i.e. how fast R and L bind) is given by:

$k_a[\text{R}][\text{L}]$, where k_a is measured in $M^{-1}\text{s}^{-1}$,

and the rate of dissociation is given by:

$k_d[\text{RL}]$, where k_d is measured in s^{-1} .

The rate of product formation $d[\text{RL}]/dt$ as equilibrium is approached takes into account both forward and reverse reaction rates, i.e:

$$\frac{d[\text{RL}]}{dt} = k_a[\text{R}][\text{L}] - k_d[\text{RL}] \quad (\text{eq.7.6.})$$

where “R” in this case is the neutravidin, and “L” is the biotinylated molecule. The total concentration of receptors on the surface can be expressed as the sum of free receptors and bound receptors in the form of RL complex, thus, $[\text{R}]_{\text{tot}} = [\text{R}] + [\text{RL}]$. Equation 7.6. is then transformed into:

$$\frac{d[\text{RL}]}{dt} = -(k_a[\text{L}] + k_d)[\text{RL}] + k_a[\text{R}]_{\text{tot}}[\text{L}] \quad (\text{eq.7.7.})$$

$(k_a[\text{L}] + k_d)$ can be defined as the “observed” rate constant, k_{obs}



which is a differential equation of the form: $\frac{dy}{dt} = -by(t) + a$ and its solution is given

by $y(t) = \frac{a}{b}(1 - e^{-bt})$. Solving eq.7.7. according to the above we get (assuming that $t_0 = 0$ and $[RL](0) = 0$):

$$[RL](t) = \frac{k_a [R]_{tot} [L]}{k_a [L] + k_d} (1 - e^{-(k_a [L] + k_d)t}) \quad (\text{eq.7.8(a)})$$

Dividing by k_a :

$$[RL](t) = \frac{[R]_{tot} [L]}{[L] + K_D} (1 - e^{-(k_a [L] + k_d)t}) \quad (\text{eq.7.8(b)})$$

where K_D is the dissociation constant. The term before the parenthesis is actually what was derived from the equilibrium analysis (eq.7.5.), which is reasonable since equilibrium happens for $t \rightarrow \infty$, when the exponential decays to zero. Also, the $[RL](t)$ is the corresponding ΔPh_c at any time instant, and $[L]$ is the concentration of the analyte, c . Thus:

$$\Delta Ph_c(t) = \frac{\Delta Ph_{max} c}{c + K_D} (1 - e^{-k_{obs}t}) \quad (\text{eq.7.9.})$$

In this way both rate constants are directly calculated (because they are incorporated in k_{obs}), and they can be further used to calculate the binding affinity constant K_A (the experimental protocol described in sec.7.4.4.).

7.4.3. Experimental results on equilibrium analysis

A typical graph showing the real-time phase change for neu – b-IgG interaction at various b-IgG concentrations is shown in Fig.7.7. Similar plots represent the binding of the other three biotinylated molecules on neutravidin. For each concentration of each molecule, experimental repetition of at least 3 times took place. The samples were prepared in $\mu\text{g/mL}$ units, so in order to convert the x-axis from $\mu\text{g/mL}$ into M the following relation was used: $x \frac{\mu\text{g}}{\text{mL}} = \frac{x}{10^3 MW} M$ (Tab.7.3.).

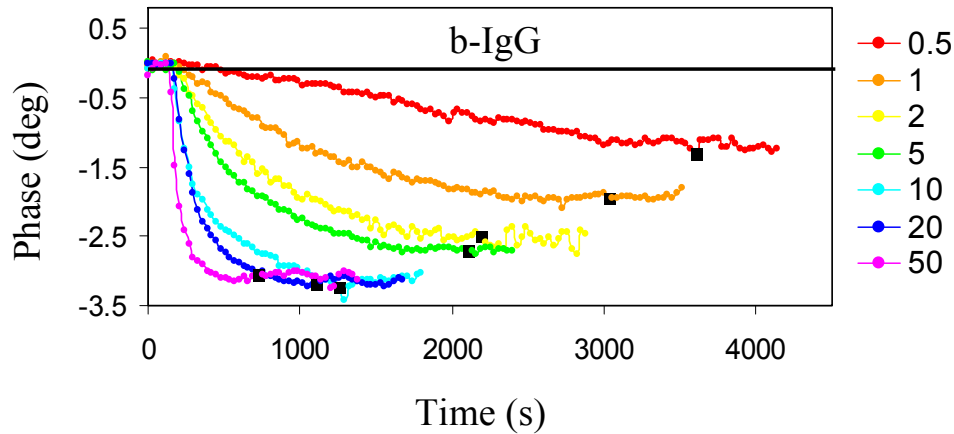


Fig.7.7. Real-time phase change for neu – b-IgG interactions in various examined concentrations (presented here in $\mu\text{g/mL}$). The black squares indicate buffer injection.



Tab.7.3. Concentrations of the used samples, in $\mu\text{g/mL}$ and M units.

Concentration (in $\mu\text{g/mL}$)	b-PrG concentration (in M)	b-PrA concentration (in M)	b-BSA concentration (in M)	b-IgG concentration (in M)
0.5	1.67×10^{-8}	1.19×10^{-8}	7.58×10^{-9}	3.33×10^{-9}
1	3.33×10^{-8}	2.38×10^{-8}	1.52×10^{-8}	6.67×10^{-9}
2	6.67×10^{-8}	4.76×10^{-8}	3.03×10^{-8}	1.33×10^{-8}
5	1.67×10^{-7}	1.19×10^{-7}	7.58×10^{-8}	3.33×10^{-8}
10	3.33×10^{-7}	2.38×10^{-7}	1.52×10^{-7}	6.67×10^{-8}
20	6.67×10^{-7}	4.76×10^{-7}	3.03×10^{-7}	1.33×10^{-7}
50	1.67×10^{-6}	1.19×10^{-6}	7.58×10^{-7}	3.33×10^{-7}

The experimental protocol for determining the affinity constants via the Langmuir isotherms was the following:

1. The interactants (neutravidin and the biotinylated molecule) were left to equilibrate (monitoring the real-time phase change).
2. When the signal reached saturation, PBS was used for rinsing till, again, equilibration (this was done in case of dissociation and to eliminate any potential non-specific binding).
3. The ΔPh value between the time before analyte injection and after rinsing was recorded.
4. The above steps were repeated for various protein concentrations.
5. ΔPh vs. c was plotted (in M units).
6. The data were fit using appropriate mathematical functions (based on eq.7.5).

The fitting was done using the function $y = \frac{Bx}{K+x}$ of the “Origin” software (“Pharmacology - One site bind”) with variables x and y corresponding to ΔPh_c and concentration, respectively. Comparing with eq.7.5. we get from the fitting process that: $B = [R]_{tot}$ and $K = K_D$. The binding isotherms of the four biotinylated molecules on neutravidin, as probed in the four microchannels, are indicated in Fig.7.8.; each ΔPh data point (for b-IgG, for example) corresponds to one real-time curve of Fig.7.7.

In an alternative way, K_A and K_D were calculated via the linearization of Langmuir equation. In particular, inverting eq.7.5. we get:

$$\frac{1}{\Delta Ph} = \frac{c + K_D}{\Delta Ph_{max} c} \Rightarrow \frac{1}{\Delta Ph} = \frac{c}{\Delta Ph_{max} c} + \frac{K_D}{\Delta Ph_{max} c} \Rightarrow \frac{1}{\Delta Ph} = \frac{1}{\Delta Ph_{max}} + \frac{K_D}{\Delta Ph_{max} c}$$

of the form $Y = A * X + B$ ($A = 1/\Delta Ph_{max}$, and $B = K_D/\Delta Ph_{max}$).

Figure 7.9. shows the linearized Langmuir graphs for all b-proteins and the values for K_D and $K_A (=1/K_D)$ for the four proteins are summarized in Tab.7.4. (the difference in the affinity values calculated in the two ways -Langmuir, and linearized Langmuir- is due to the mathematical processing: in the former case a non-linear fitting is executed, which is prone to larger error than the linear fit of the latter case).

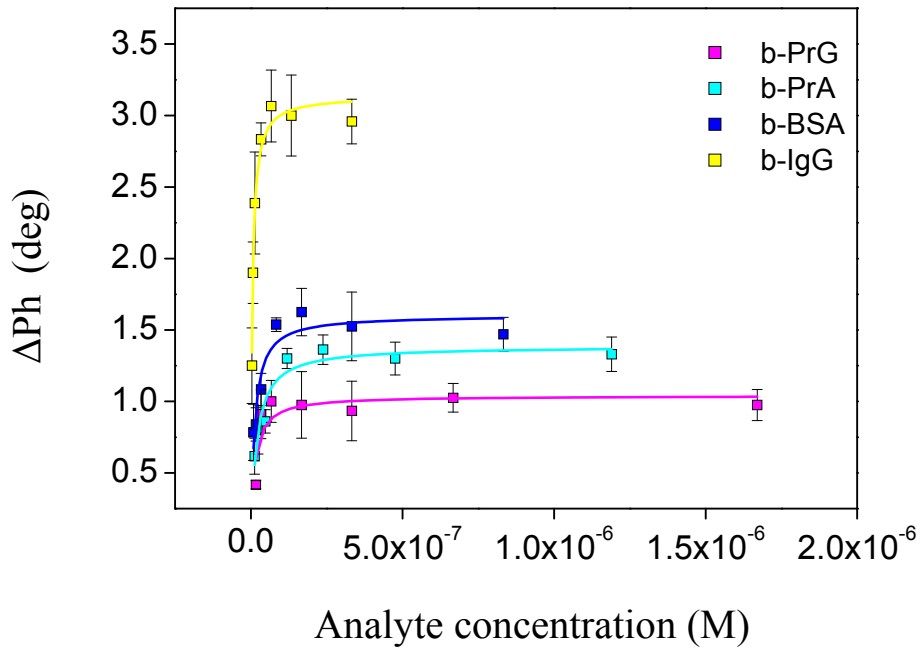


Fig.7.8. Comparative plot of the binding isotherms of all biotinylated molecules on neutravidin.

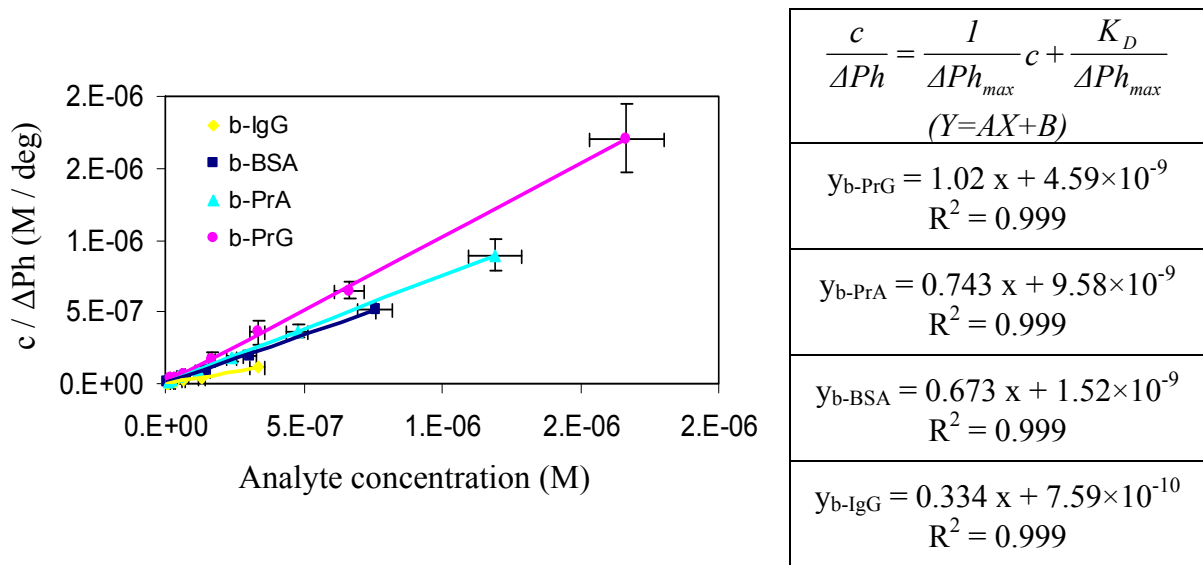


Fig.7.9. Linearization of Langmuir binding curves for all biotinylated proteins.

7.4.4. Experimental results on kinetic analysis

As it was mentioned before, with equilibrium analysis it is possible to extract the binding constants, but not the rate constants. In order to calculate the latter, kinetic analysis of the real-time results (Fig.7.10) was carried out. The protocol, based on the equations of sec.7.4.2., was as follows:

1. The *Phase vs. time* real-time graph was plotted for one concentration till the graph appeared to change no more, upon protein binding.

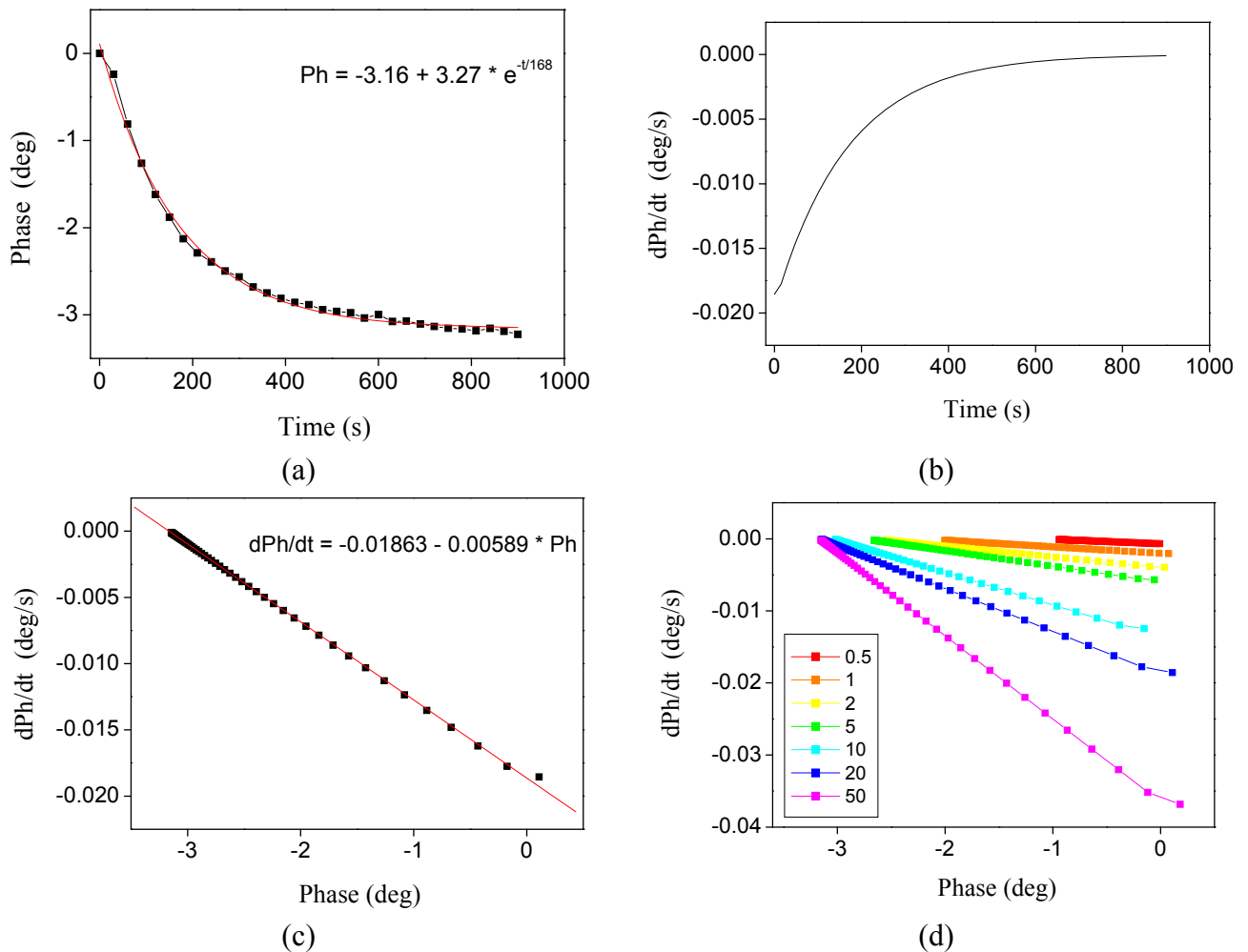


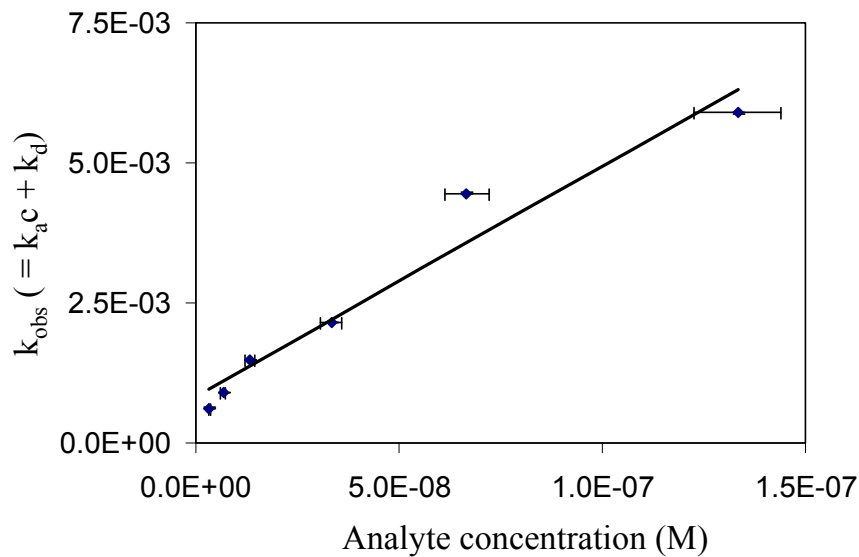
- The real-time data points were fit to a first order exponential function (Origin software function: $y = y_o(1 - e^{-x/A})$ where $y: \Delta Ph$, $x: time$).
- The first derivative $d\Delta Ph/dt$ of the fit function was taken which, according to eq.7.7. (and the equivalences $\Delta Ph_c \rightarrow [RL]$ and $\Delta Ph_{max} \rightarrow [R]_{tot}$) is equivalent to

$$\frac{d\Delta Ph}{dt} = -k_{obs} \Delta Ph + k_a [R]_{tot} c_i \quad (\text{eq.7.10.})$$

- The phase derivative was plotted against the phase ($d\Delta Ph/dt$ vs. ΔPh) and according to eq.7.10. the slope is equal to k_{obs} for the particular concentration c_i .
- Steps 1 to 4 were repeated for all concentrations.
- The k_{obs} was linearly plotted vs. c ; due to the k_{obs} definition (eq.7.7.) the slope is equal to k_a and the abscissa is equal to k_d .

The above steps are summarized graphically in Fig.7.10. They indicatively refer to b-IgG, but similar processing and graphs correspond to the other biotinylated molecules as well (Fig.7.10(a) to (c) correspond to b-IgG concentration $c = 20 \mu g/mL$). Table 7.4. then summarizes the calculated parameters from the above kinetic analysis.





(e)

Fig.7.10. (a) Fitting of raw data with a single exponential decay function, (b) first derivative of the fit line, (c) plotting $d\Delta Ph/dt$ vs. ΔPh and linear fit, (d) same as (c) but for all concentrations (in $\mu\text{g/mL}$) examined for one molecule, (e) Plotting the seven slopes of (d), i.e., the k_{obs} , vs. concentration: k_a equals the slope and k_d equals the abscissa.

Tab.7.4. Affinity constants (derived from Langmuir non-linear curve fitting, Langmuir linearization, and kinetic analysis) and binding rates from kinetic analysis.

Constants	b-PrG	b-PrA	b-BSA	b-IgG
Affinity constants from equilibrium (<i>non-linear Langmuir fit</i>)				
K_A (M^{-1})	8.06×10^7	5.92×10^7	9.09×10^7	2.24×10^8
K_D (M)	1.24×10^{-8}	1.69×10^{-8}	1.10×10^{-8}	4.46×10^{-9}
Affinity constants from equilibrium (<i>linearization of Langmuir curves</i>)				
K_A (M^{-1})	2.22×10^8	7.76×10^7	4.43×10^8	4.40×10^8
K_D (M)	4.50×10^{-9}	1.29×10^{-8}	2.26×10^{-9}	2.27×10^{-9}
Binding rate and affinity constants (<i>kinetic analysis</i>)				
K_A (M^{-1})	7.46×10^7	1.24×10^7	2.44×10^7	2.91×10^7
K_D (M)	1.34×10^{-8}	8.06×10^{-8}	4.1×10^{-8}	3.44×10^{-8}
k_a ($\text{M}^{-1}\text{t}^{-1}$)	1.27×10^4	2.23×10^4	4.63×10^4	3.20×10^4
k_d (t^{-1})	1.70×10^{-3}	1.80×10^{-3}	1.90×10^{-3}	1.10×10^{-3}



(it must be noted that, because the proportionality of signal-to-surface area was proven between the μF -on-SAW and the standard setup, the affinity constants are not expected to change when using one system or the other, so there is full compatibility in the results between the two).

7.4.5. Comments on the results

Having the K_A values for all four proteins, it is interesting to analyze and compare them in the following ways: (i) what is the relation between the K_A of the neutravidin – biotinylated molecule interaction and the avidin-biotin one, available in the literature, and (ii) compare the affinity and kinetic constants among the four proteins themselves.

It is reported in literature that the avidin-biotin interaction has a K_A of the order of 10^{13} to 10^{15} M^{-1} , which is approximately 10^5 - 10^7 times higher than the one we experimentally defined. At first sight there seems to be a huge, inexplicable inconsistency. Looking at published references, they mostly refer to avidin-biotin (or streptavidin-biotin) binding in solution. In our case, even if we assume that neutravidin has similar behavior as streptavidin in terms of biotin-binding (which is true according to some studies showing that the biotin-binding activity of neutravidin remains largely unaffected by the deglycosylation [7.10.]), we can not disregard two main differences, which are likely to explain the discrepancy between our values and the literature ones:

- (i) Instead of *free* (strept)avidin in solution we have neutravidin *adsorbed* on a solid substrate, which is a major difference. Due to this constraint, neutravidin has only two out of its potentially four binding sites exposed to the solution of the analyte (biotinylated molecule), which could play a significant role to the reduction of binding affinity constant. In support of this argument, there are some reported studies in which neutravidin has been genetically modified as to suppress the functionality of one, two or three of its binding sites, without tampering with any other characteristic of the molecule (e.g., size, shape, MW, etc.) [7.11.], [7.12.]. These studies report that the affinities of such mutated molecules to biotin-binding are dramatically reduced. These conditions (blocked neutravidin sites due to adsorption and blocked sites due to mutation) could be considered equivalent, and thus this could be a reason for the reduced observed affinity.
- (ii) In addition, instead of simple biotin, in our work we use biotinylated molecules. By default this means bigger biomolecules, which need more time to diffuse to the binding sites so, in principle, comparison with pure biotin-avidin interaction may even be groundless.

The above assumptions for the explanation of the discrepancy of the affinity constants between avidin-biotin (literature) and neutravidin – b-molecules (experiments) should also take into consideration the following issue: as it was mentioned in sec.7.4.1. the concentration at which $\Delta Ph = 0.5 \times \Delta Ph_{max}$, equals K_D . Therefore, the evaluation of K_D somehow depends on the detection limit of the biosensing platform. The microsystem used has a detection limit for analyte



concentration of the order of 1 nM; therefore, even if K_D is much lower than 1 nM, it will not be detected. Therefore, even if the K_D of the biotinylated biomolecules was, indeed, lower than the calculated one (close to the avidin-biotin range) it corresponds to concentrations too low to be detected with the μ F-on-SAW platform.

Comparing the affinity constants among the biomolecules, there seems to be some small scattering depending on the calculation method. On the other hand, there seems to be no apparent trend (for example as the MW of the biotinylated molecule increases) which leads to the conclusion that all molecules have essentially the same binding constants. Comparing the binding rate constants among the four biotinylated molecules it appears that the values are of the same order of magnitude and, in fact, quite close between them. This is additional evidence that there is essentially no difference in the binding behavior between the four biotinylated molecules with neutravidin. It is neither their size nor MW that make one of them interact faster or more favorably with neutravidin. This does not mean that a much smaller or bigger biotinylated molecule will have similar rate constants (tested under the same conditions on the same device) but at least for the range of MW and sizes that were tested in this work, no significant difference in k_a or k_d was observed.

7.5. Conclusions

This chapter reported the first application of μ F-on-SAW setup as multi-sample detection platform. Four different biomolecules were used, having their biotinylated nature in common, and they all interacted with neutravidin. Discrimination of their close MW was achieved and individual detection of each biomolecular interaction in each microchannel was performed. In addition, the full capacity of μ F-on-SAW at its current configuration to detect 8 different interactions was explored and successfully tested, by pre-treating the two sensors of the biochip, opening the way for further investigation of this issue via more sophisticated biomolecular patterning techniques. Finally, the microsystem was proven successful also in performing affinity and kinetic analysis, via the determination of binding and rate constants of the interactions between the four biotinylated molecules and neutravidin. Results on this field indicated that, due to the large size of molecules and the adsorbed state of neutravidin (as opposed to free in solution) the affinity constants were reduced with respect to known values from literature for avidin-biotin. However, this “size effect” did not appear to induce some trend in the values of the constants (when the four molecules were combined between them) which allows us to deduce that, despite the lower calculated affinity constants, it was eventually the nature of avidin-biotin interaction that was observed.

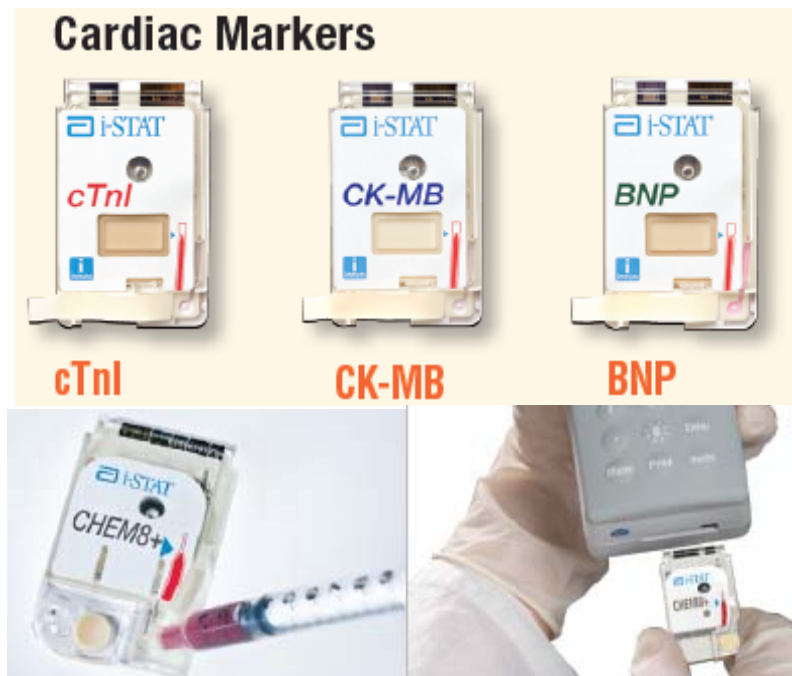


References

- [7.1.] J. Langone, *Adv. Immunol.*, vol. 32, pp. 157-241, 1982.
- [7.2.] M. Bendayan, S. Garzon, "Protein G-gold complex: comparative evaluation with Protein A-gold for high resolution immunocytochemistry", *Histochem. Cytochem.*, vol. 36, pp. 597-607, 1988.
- [7.3.] A. Tsortos, G. Papadakis, K. Mitsakakis, K.A. Melzak, E. Gizeli, "Quantitative determination of size and shape of surface-bound DNA using an acoustic wave sensor", *Biophys. J.*, vol. 94, pp. 2706-2715, 2008.
- [7.4.] http://en.wikipedia.org/wiki/Protein_G
- [7.5.] C.G. Gölander, E.J. Kiss, "Protein adsorption on functionalized and ESCA-characterized polymer films studied by ellipsometry", *J. Colloid Interface Sci.*, vol. 121, pp. 240-253, 1988
- [7.6.] R. Karlsson, A. Michaelsson, L. Mattsson, "Kinetic analysis of monoclonal antibody-antigen interactions with a new biosensor based analytical system", *J. Immunol. Methods*, vol. 145, pp. 229-240, 1991.
- [7.7.] J.A. Goodrich, J.F. Kugel, "Binding and kinetics for molecular biologists", Cold Spring Harbor Laboratory Press, New York, ISBN 0-87969-736-9, 2007.
- [7.8.] E. Gizeli, C.R. Lowe, "Biomolecular sensors", pg. 87, Taylor & Francis, ISBN 0-7484-0791-X, 2002.
- [7.9.] J.D. Andrade, V. Hlady, "Protein adsorption and materials biocompatibility: A tutorial review and suggested hypotheses", *Adv. Polym. Sci.*, vol. 79, pp. 1-63, ISBN 978-3-540-16422-7, Springer, 1986.
- [7.10.] Y. Hiller, E.A. Bayer, M. Wilchek, "Nonglycosylated avidin", *Methods Enzymol.*, vol. 184, pp. 68-70, 1990.
- [7.11.] M. Howarth, D. J.-F. Chinnapen, K. Gerrow, P.C. Dorrestein, M.R. Grandy, N.L. Kelleher, A. El-Husseini, A.Y. Ting, "A monovalent streptavidin with a single femtomolar biotin binding site", *Nature Methods*, vol. 3, pp. 267-273, 2006.
- [7.12.] G.O. Reznik, S. Vajda, T. Sano, C.R. Cantor, "A streptavidin mutant with altered ligand-binding specificity", *PNAS*, vol. 95, pp. 13525-13530, 1998.



Chapter 8. Clinical application: cardiac markers



i-STAT Point-of-care diagnostic kit for cardiac markers, by Abbott
<http://www.abbottpointofcare.com/ISTAT/index.asp>





Chapter 8. Clinical application: cardiac markers

8.1. Introduction - what are biomarkers?

The *early* and *accurate* diagnosis of a pathological condition, such as tumor or heart disease, is of critical importance for the efficient treatment of a patient. The diagnosis should take place in a quick, precise, reliable and minimally invasive way. The detection of biomarkers in body fluids (blood, saliva, urine) greatly helps towards this scope. A biomarker is a biomolecule (usually a protein) that, in a pathological situation either appears in the body fluids (contrary to its non-existence during physiological conditions), or increases in concentration. A genetic biomarker is a mutated DNA fragment/sequence which results in a defective protein and thus, a malfunction; genetic biomarkers are not detected via measurement of the concentration levels, but by means of hybridization of their complementary sequence; in this sense, their detection is more qualitative (i.e., “yes or no”) than quantitative in nature. In fact, the official definition of the National Institute of Health (NIH) for a biomarker is: “*a characteristic that is objectively measured and evaluated as indicator of normal biological processes, pathogenic processes, or pharmacologic responses to therapeutic intervention*”.

Biomarker molecules can be categorized as *disease-related* and *drug-related* ones. Disease-related biomarkers indicate whether there is a threat of disease (risk indicators or predictive biomarkers), if a disease already exists (diagnostic biomarker), or in what way such a disease may develop in an individual case (prognostic biomarker). In contrast, drug-related biomarkers indicate whether a drug will be effective in a specific patient and how the patient’s body will process it. In drug development, biomarkers may be used to (i) determine how a drug works in the body, (ii) assess a biologically effective dose of a drug, (iii) define whether a drug is safe or effective, and (iv) identify patients most likely to respond to a treatment, or least likely to suffer an adverse event when treated with a drug.

As healthcare is a serious issue and the results need to be as much cross-checked as possible, the more methods used the better. Thus, the purpose of using biomarkers for diagnostics is not to replace the use of other established methods, such as electrocardiographs, sonographs, imaging methods (for cancer) etc. On the contrary, biomarker-based diagnosis aims at developing an additional method for prognostics, of analytical nature, which will act in a complementary, rather than competitive, way to the already existing methods for better and fully characterizing a patient’s condition and potentially individualize treatment, realizing the so called “personalized medicine/healthcare.”

That is why there is intensive work currently taking place on the discovery and development of innovative and more effective biomarkers. These “new” biomarkers have become the basis for preventive medicine, meaning medicine that recognises diseases or the risk of disease early enough, and takes specific countermeasures to prevent the development of a disease. Biomarkers are also seen as the key to “personalized medicine”, i.e., treatments individually tailored to specific patients for highly efficient intervention in disease processes.



8.2. Why cardiac biomarkers with μ F-on-SAW

Here lies a bidirectional question: (i) why were cardiac markers chosen as an application for the μ F-on-SAW and, (ii) why would cardiac marker diagnostics need a multi-sample detector.

Firstly, biomarker results should be fast and, at the same time, efficient. In standard biochemical tests, where results come out in a few days, the necessity for a fast procedure is not obvious: one would wonder “what is the difference in hearing the results immediately or after two days, if I suffer from a problem for a long time already”. However, there are cases where minutes are crucial. In pre- and post-operative conditions in intensive care units that continuous monitoring is essential, the results should come out fast, desirably within some minutes [8.1.]. Towards this scope, miniaturized systems and point-of-care analytical microdevices can play a significant role.

With respect to the actual application of cardiac markers it is well known that elevation of the concentration of *only one* marker *does not necessarily* indicate the break out of a disease but could stem from other causes too (smoking, stress, or heart irrelevant disease, etc). Thus, several markers need to be checked in order to verify that the contents in blood have elevated due to pathological origins, rather than other causes. That is why the development of a system capable of performing multiple tests is necessary. And not only that: although the tumor markers are more or less one-to-one related to a disease, this is not the case for cardiac markers. There is a strong interdependency of cardiac markers with respect to the heart-related diseases they indicate [8.2.], [8.3.]: one marker is indicative of more than one problems; and inversely, one disease is relevant with the increase of more than one biomarker levels. Thus, there is a high level of multiplexity among cardiac markers. This makes multi-sample testing vital for cardiac marker assessment, and, conversely, it makes cardiac markers an excellent group of molecules to be used on a multi-sensing setup. These reasons led to the selection of this application.

The nature of biomarker-based diagnostics imposes multiplexity, by itself. Especially for cardiovascular diseases where plenty of non-biological reasons cause increase in concentration levels of these substances and/or heart problems (like smoking, obesity, stress, etc) it is necessary to investigate and cross-check as many biomarkers as possible in order to diagnose the actual source of problem and reliably assess in favour of, or against a cardiovascular risk condition.

8.3. Cardiac markers examined in this work

The cardiac markers selected to be applied on the μ F-on-SAW for multi-sensing are: Creatine Kinase MB (CK-MB), C-Reactive Protein (CRP), D-dimer, and Pregnancy Associated Plasma Protein A (PAPP-A). Some functional information about these biomarkers as well as their role in critical heart conditions are summarized in sec.8.3.1. to sec.8.3.4.

The concept for choosing these particular molecules was that the combination of the examined biomarker group should include both traditional and newly emerged markers. CK-MB and CRP satisfied the first condition. In fact, CK-MB along with



Troponins I and T, as well as Myoglobin, are used in tests either alone, or in combinations of two or three [8.4.]. CK-MB has the highest MW among these molecules, which is another reason it was selected. Among the “newly-emerged” biomarkers, D-dimer and PAPP-A were chosen. Furthermore, it was desirable that the molecules spanned a wide range of molecular weights, so that the correlation with signal could be investigated. This was another reason in favor of selecting PAPP-A, due to its high molecular weight.

It must be noted that, since the field of cardiac markers is of great importance to human healthcare, there has already been research and progress on this field [8.4.]; and even though there have been some cases where only some of the biomarkers have been tested on a micro/biochip [8.5.], [8.6.], [8.7.], [8.8.], none of the examined ones in this work (except CRP [8.9.]) has ever been investigated with an acoustic biosensor, in general. Furthermore, it is one of the very few studies of *on-chip* investigation of *multiple* cardiac markers, which offers additional novelty to this work.

8.3.1. Creatine Kinase - MB (CK-MB)

CK-MB is a dimeric enzyme composed of either M (muscle type) or B (brain) type subunits. These subunits associate to form three isoenzyme forms: BB, MB, and MM. These isoenzymes are expressed at different levels in various tissues in humans: CK-BB is predominantly found in brain tissue and CK-MM in skeletal and heart muscle (Fig.8.1.); CK-MB is the 86kDa isoenzyme of creatine kinase, found in heart muscle, which is why this one is used.

Clinical value and existing tests: Assays for serum levels of CK-MB have long been used in cases of suspected heart muscle disease. In fact, CK-MB is extensively used to aid in the diagnosis of myocardial infraction, even in regular biochemical tests [8.10.]. Its use is not confined to prognosis, but also to post-operational monitoring of a patient’s condition [8.11.]. Normal values of CK-MB concentration are considered below ~ 10 ng/mL.

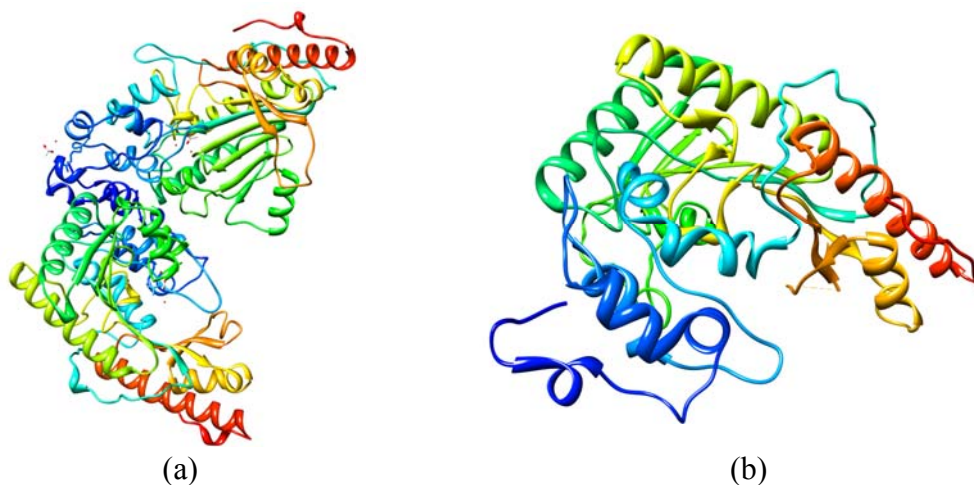


Fig.8.1. Creatine Kinase isoenzymes: (a) CK-BB, (b) CK-MM.



8.3.2. Cardiac Reactive Protein (CRP)

It is a 125 kDa pentameric protein. The monomers are non-covalently associated and are symmetrically arranged around a central pore (Fig.8.2.). For decades CRP had been known as liver-derived protein. However, recent data showed significant level of CRP expression in other tissues, such as blood vessel wall and coronary artery smooth muscle cells.

Clinical value and existing tests: CRP is a widely known and used marker for inflammation [8.12.] and for the early diagnosis of acute coronary syndromes [8.13.]. Patients with elevated CRP levels have an increased risk for heart attack, stroke, sudden death, and vascular disease. In 2003, the Centers for Disease Control and Prevention (CDC) and the American Heart Association (AHA) issued a statement identifying CRP as the inflammatory marker best suited for use in current clinical practice to assess cardiovascular risk [8.14.]. In pathology, CRP concentration has an enormous dynamic range, from 0.05 to 500 $\mu\text{g/mL}$. The CDC/AHA guidelines support the use of CRP in primary prevention and set cut-off points according to relative risk categories: low risk ($<1 \mu\text{g/mL}$), average risk (1-3 $\mu\text{g/mL}$), and high risk ($>3 \mu\text{g/mL}$).

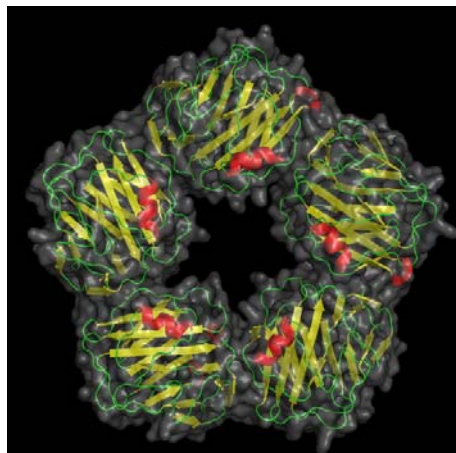


Fig.8.2. The pentameric structure of CRP forming a pore in the middle.

8.3.3. D-dimer

D-dimer is a fibrin degradation product, formed during the blood coagulation cascade. It is a 195 kDa protein and the dimeric form is held by two isopeptide bonds between C-terminal parts of γ -chains (Fig.8.3.).

Clinical value and existing tests: D-dimer is a marker of substantial value for the early diagnosis of hypercoagulability, i.e., excessive thrombus formation. D-dimer level in healthy individuals is less than 0.5 $\mu\text{g/ml}$; elevated levels were found in the blood of patients with pulmonary thromboembolism, deep vein thromboses and atherosclerosis; elevated level of D-dimer in blood indicates a risk of myocardial infarction and is believed to be a reliable marker of pathological coagulation that underlies pathogenesis of most cardiovascular diseases [8.16.]. Also, clinical tests have shown that this protein exhibits significantly increased concentration levels in patients with acute ischemic events (myocardial infarction and unstable angina) than in nonischemic patients [8.17.].

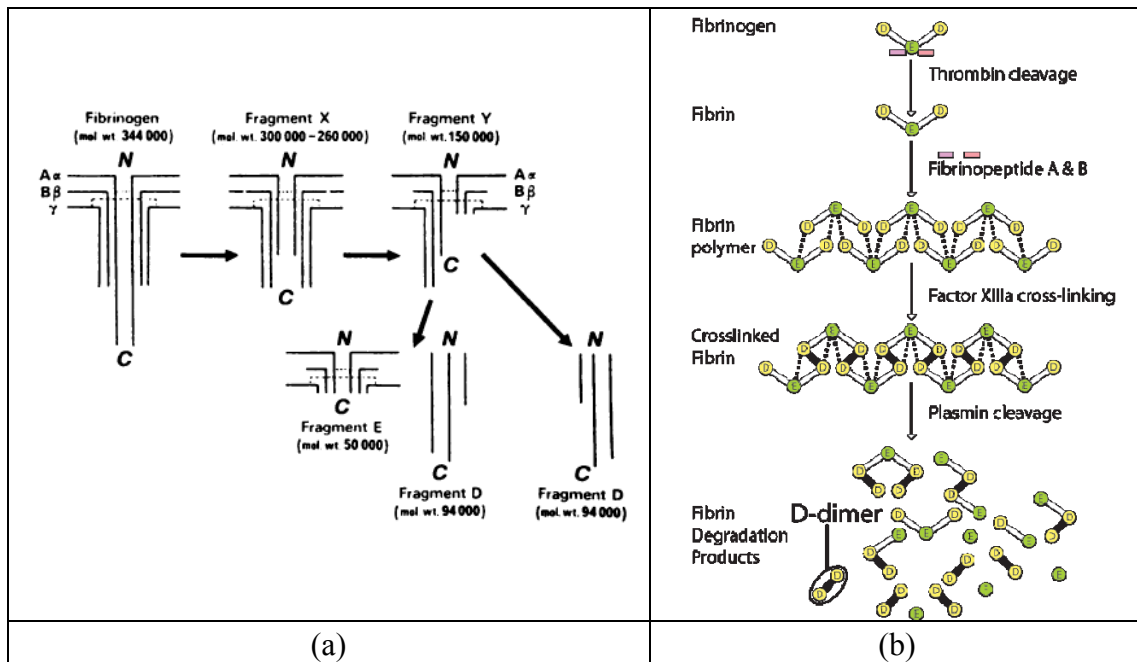


Fig.8.3. Schematic of conversion of fibrinogen D-dimer [8.15.].

8.3.4. Pregnancy-Associated Plasma Protein-A (PAPP-A)

In the blood of pregnant women PAPP-A exists as a covalent (disulfide bridged) heterotetrameric complex, consisting of two 200 kDa PAPP-A subunits and two 50-90 kDa subunits (proMBP) forming a complex with total *MW* of approximately 540 kDa. Such complex is denoted as heterotetrameric PAPP-A (PAPP-A/proMBP or htPAPP-A, Fig.8.4.).

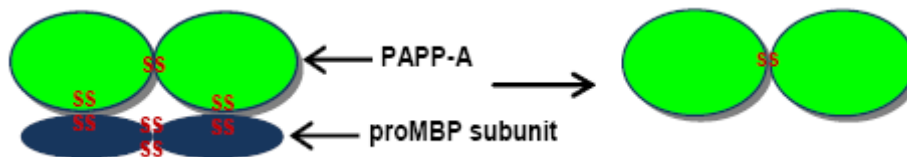


Fig.8.4. Left: heterotetrameric form htPAPP-A; Right: homodimeric form dPAPP-A.

Clinical value and existing tests: The htPAPP-A form is widely recognized biochemical marker of Down syndrome. Recently, though, it was shown that the homodimeric form of PAPP-A (dPAPP-A) with molecular mass about 400 kDa, is abundantly expressed in unstable coronary atherosclerotic plaques. Recent studies have revealed that its dimeric form (dPAPP-A) can be used as a marker of acute coronary syndromes (ACS) [8.18.]. It has been demonstrated that dPAPP-A is abundantly present in unstable atherosclerotic plaques, and its circulating level is significantly elevated in patients with unstable angina or acute myocardial infarction in comparison with patients with stable angina and control subjects [8.19.]. *Note: due to too high cost of dPAPP-A (€ 2300 for 50 µg, www.hytest.fi) the htPAPP-A form was used in our experiments, instead of dPAPP-A. However, the mAb was selected such that captures PAPP-A at its dimeric sub-unit (green areas in Fig.8.4.), which is common for dPAPP-A.*



8.4. Immunoassays

The experiments with cardiac markers were, essentially, immunoassay tests. An immunoassay is a bio(chemical) test used to detect or quantify a specific substance, the analyte, in a body fluid such as blood, using an immunological reaction, i.e., the interaction of an antibody with its antigen. Immunoassays are highly sensitive and specific due to the antibody-antigen interaction. They measure the formation of antibody-antigen complexes and detect them via a biosensing method. Immunoassays may be qualitative (positive or negative) or quantitative (amount measured). An example of a qualitative assay is an immunoassay test for pregnancy, in which the presence of human chorionic gonadotropin (hCG) in urine or serum is detected.

8.4.1. Antibodies

At the core of an immunoassay lies the interaction of the antigen (analyte) with the capture antibody (immobilized on the surface of the sensor, biochip, etc.). An antibody is a protein (immunoglobulin) produced by B-lymphocytes (immune cells) in response to a stimulation by an antigen, which could be bacteria, viruses, harmful toxins, etc [8.20.]. An antibody consists of two large heavy and two small light immunoglobulin (Ig) chains (Fig.8.5.). Several different types of heavy chains exist that define the class or isotype of an antibody. Two regions can be identified on an antibody: the *variable* region gives the antibody its specificity for binding an antigen (which is of non-covalent nature between the antigen-binding site on the antibody and a portion of the antigen called the epitope). The *constant* region determines the mechanism used to destroy the antigen. According to their constant region, structure and immune action, antibodies are divided into five classes: IgM, IgG, IgA, IgD, and IgE.

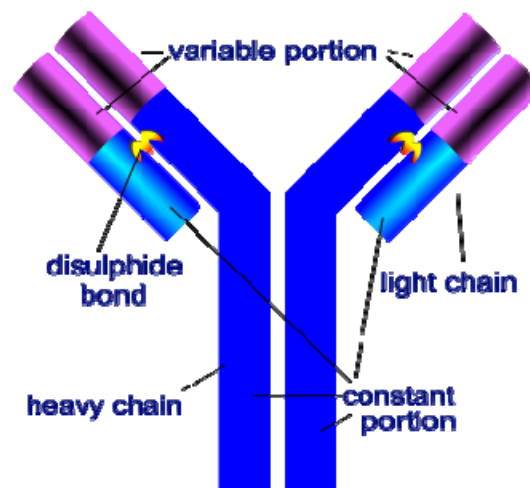


Fig.8.5. Schematic of a typical antibody structure.



8.4.2. Polyclonal and monoclonal antibodies

Polyclonal antibodies are derived from different B cell lines. They are a heterogeneous mixture of immunoglobulin molecules secreted against a specific antigen, each recognizing a different epitope (i.e., multiple different, antibodies that bind the same antigen). Specific polyclonal antibodies are typically produced by immunization of a suitable mammal, such as a mouse, rabbit or goat (the antigen is injected into the mammal). This induces the B-lymphocytes to produce IgG immunoglobulins specific for the antigen. This polyclonal IgG is then purified from the mammal's serum. Due to their nature and heterogeneity, polyclonal antibodies are often used when large entities are to be captured, so that various areas of theirs can be recognized.

Monoclonal antibodies (mAbs) are specific for a single epitope of an antigen. To produce monoclonal antibodies, B-cells are removed from the spleen of an animal that has been injected with the relevant antigen. These B-cells are then fused with myeloma tumor cells that can grow indefinitely in culture (myeloma is a B-cell cancer). This fusion is performed by making the cell membranes more permeable. The fused hybrid cells (called hybridomas), being cancer cells, multiply rapidly and indefinitely and produce large amounts of the desired antibodies. Given almost any substance, it is possible to create monoclonal antibodies that specifically bind on that substance and serve in its detection and/or purification. Polyclonal and monoclonal antibodies are often purified using protein A/G or antigen-affinity chromatography [8.21].

In our application, all four markers are relatively big molecules (especially D-dimer and PAPP-A with 195 and 540 kDa, respectively) so in principle, polyclonal antibodies could be used to capture them more easily. On the other hand, as monoclonal antibodies bind to only one site of a particular molecule, they provide a more specific and accurate detection, less easily affected by the presence of other molecules; and because a crucial part of the experiments was the selective capturing of one biomarker out of a mixture, and the elimination of any non-specific interactions, monoclonal antibodies were eventually used. *(The purchased monoclonal antibodies were, indeed, highly specific to the purchased antigens: anti-CKMB was reported to have no cross-reaction with the other isoenzymes of creatine kinase; anti-D-dimer was reported to have no cross-reaction with D-monomer or fibrinogen).*

8.5. Experimental procedure

Having defined the method of biomarker detection, it is necessary to define the means of antibody immobilization. The objective is to immobilize them (i) without losing their activity, and (ii) having as much orientation as possible with their Fab sites facing the analyte solution.

Chemical methods were rejected due to incompatibility of the biosensing setup with harsh wet environments. Another method could be to use biotinylated antibodies which would bind on a neutravidin-modified surface. However, even though the biotin linkers are known not to affect the functionality of the molecules, they would



still be randomly distributed all over the antibody. This would increase the possibility of a biotinylated antibody to bind neutravidin with its “useful” site facing the surface, rendering it practically useless. The same problem would exist if the antibodies were simply left to adsorb on the gold surface: the molecule could adsorb through the Fab ends or the Fc tail, lie on its “side” or even denature and become non-functional.

That is why the immobilization was eventually accomplished via the PrG-IgG interaction; PrG reacts with IgG at sites located in the Fc region, leaving the “useful” side of the antibody intact (see sec.7.1.). The assay sequence was the following and is schematically shown in Fig.8.6. (the bullet-letters below correspond to the illustrations in Fig.8.6.).

- (a) PBS buffer for signal equilibrium.
- (b) Surface modification with PrG layer, by means of physical adsorption (500 µg/mL PrG concentration).
- (c) Injection of one antibody in each microchannel; its specific interaction with PrG causes the antigen-binding site of the antibodies to be exposed towards the solution (20 µg/mL antibody concentration).
- (c-i) BSA (1 mg/mL) injection for blocking (not appearing in Fig.8.6.).
- (d): Injection of one biomarker per microchannel (concentrations in Tab.8.1.).
- (e): Binding of the marker and rinsing of its excess quantity.

(note: PBS buffer was used for rinsing in between all the above steps)

Tab.8.1. Biomarkers’ concentrations that were tested (in µg/mL and nM).

Concentration (in µg/mL)	CK-MB concentration (in nM)	CRP concentration (in nM)	D-dimer concentration (in nM)	PAPP-A concentration (in nM)
0.25		2.0		
0.5	5.8	4.0		0.9
1	11.6	8.0		1.9
2	23.3	16.0	10.3	3.7
5	58.1	40.0	25.6	9.3
10	116.3	80.0	51.3	18.5
20	232.6	160.0	102.6	37.0

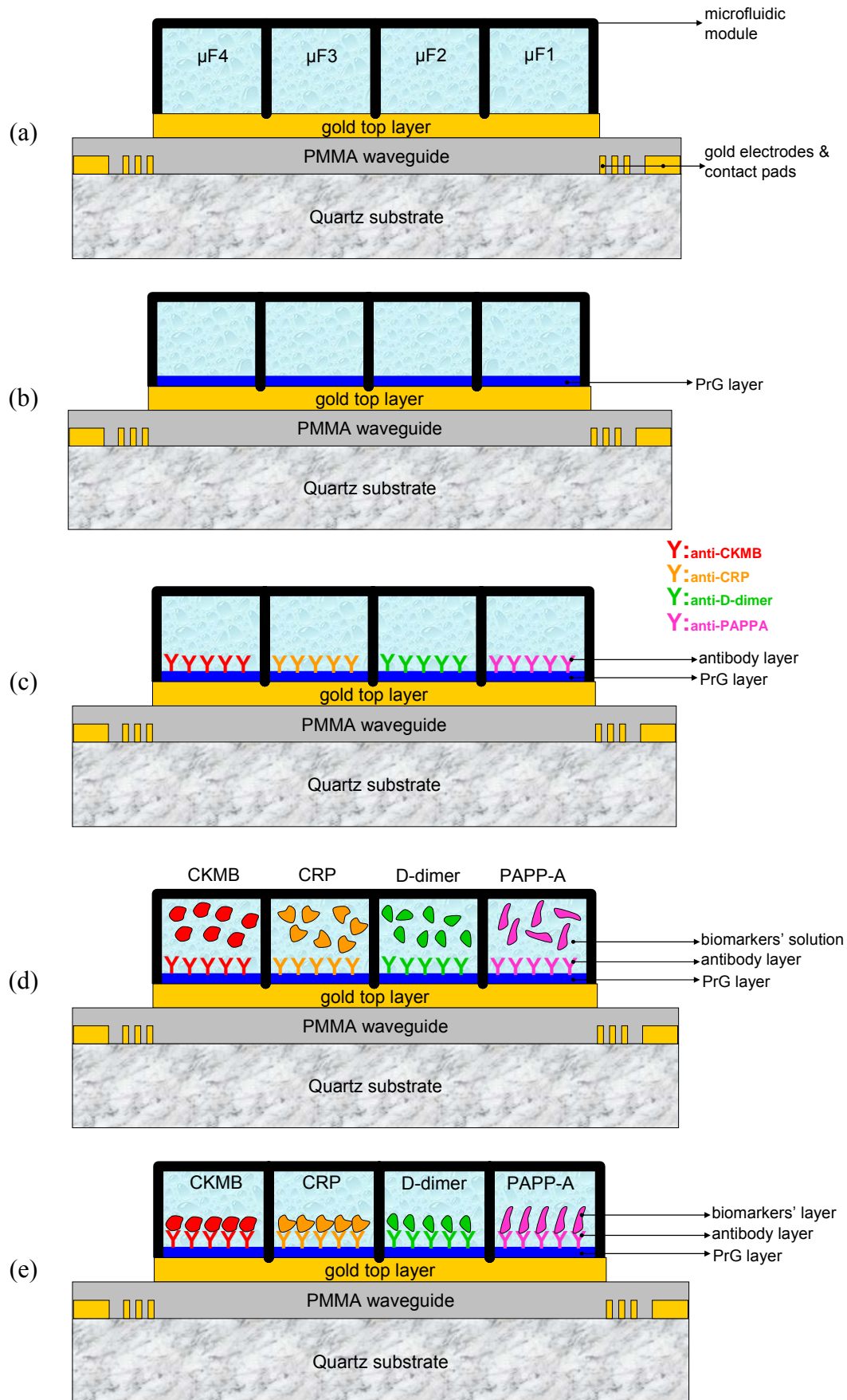


Fig.8.6. Experimental steps during biomarker detection.



The sensogram corresponding to the sequential injection of the four biomarkers in the four microchannels appears in Fig.8.7. The real-time curves of all proteins correspond to the maximum concentration used, 20 $\mu\text{g/mL}$, where the signal appears to reach saturation (see sec.8.6.); Fig.8.7. is accompanied by a bar diagram indicating the phase change values for each of the four biomarkers (still at 20 $\mu\text{g/mL}$) proving that all four of them are detectable and distinguishable (Fig.8.8.). The colors between Fig.8.7. and Fig.8.8. are equivalent; however, each bar of Fig.8.8. is the average of many experiments, whereas each line in Fig.8.7. represents a single experiment and does not fully correspond, in ΔPh value, to the bar of the same color.

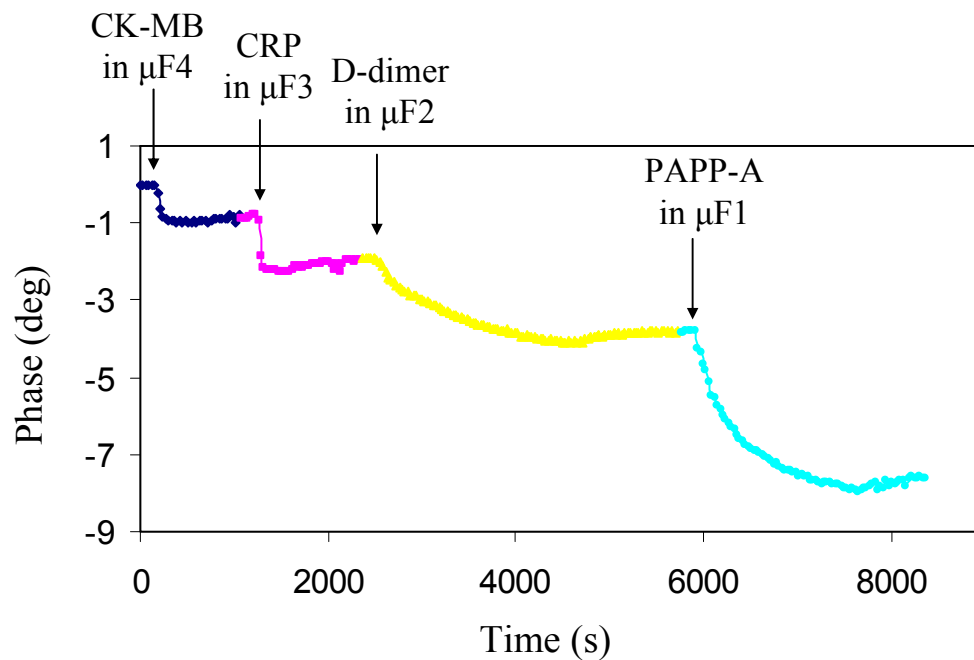


Fig.8.7. Real-time phase change during the sequential injection of the four biomarkers in the four microfluidic compartments.

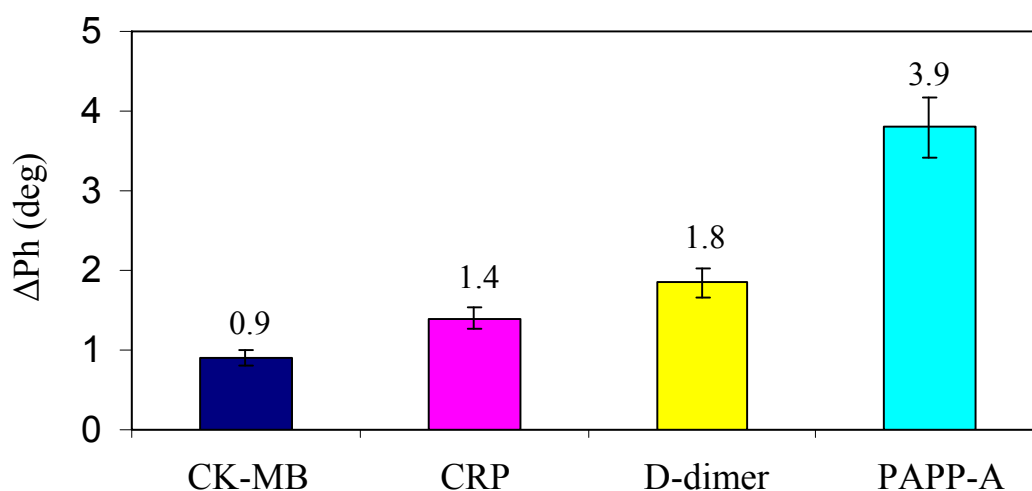


Fig.8.8. Phase change for the four biomarkers.

It appears from Fig.8.7. that the four molecules have different rate of phase change. In fact, for the same concentration (in $\mu\text{g/mL}$) the two big molecules (in terms



of their MW) seem to have quite slower binding rate than the two smaller molecules. Indicatively, an exponential fit for these curves (based on eq.7.9.) reveals the time needed to reach half of the maximum signal change ($T_{1/2} = t_{max} \ln 2$):

$$T_{1/2}^{CK-MB} = 53 \ln 2 = 37s$$

$$T_{1/2}^{CRP} = 35 \ln 2 = 24s$$

$$T_{1/2}^{D-dimer} = 519 \ln 2 = 360s$$

$$T_{1/2}^{PAPP-A} = 463 \ln 2 = 321s$$

i.e., about 10 - 15 times higher for the two big molecules than for the two smaller ones. One explanation is the fact that the above comparison was done in terms of $\mu\text{g/mL}$ units of concentration; transforming the units into M, which is directly proportional to the number of molecules, it appears that there are less molecules available for the two big biomarkers, than for the two smaller ones. In addition, the size of the bigger molecules makes them harder to diffuse to the surface and reach their capture antibodies.

8.6. Binding and kinetic analysis

During the experiments for kinetic and equilibrium analysis, various concentrations of all markers were probed, and in all cases the assay sequence described in sec.8.5. and Fig.8.6. was followed. The real-time binding curves appear in Fig.8.9. (indicatively PAPP-A is shown, but similar trends are valid for the other markers too).

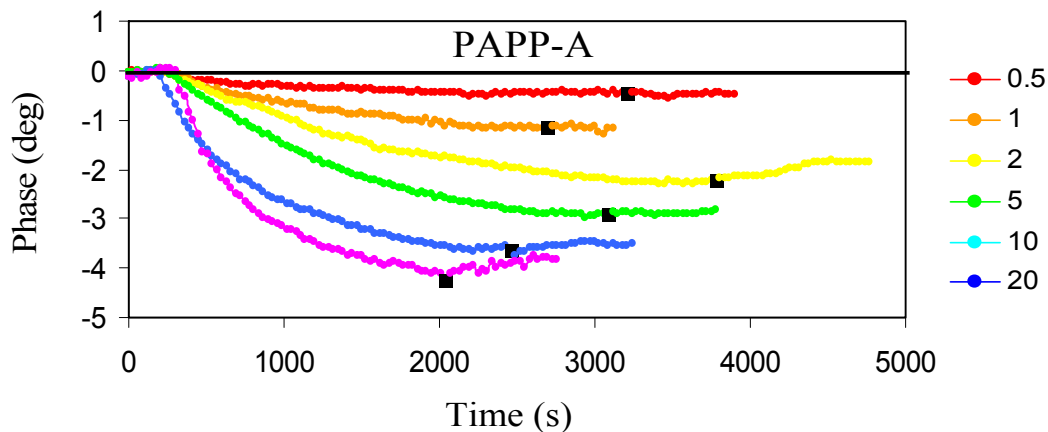


Fig.8.9. Real-time phase change for various concentrations of PAPP-A (expressed in $\mu\text{g/mL}$). The black squares indicate buffer injections.

The data analysis for the assessment of the binding affinity and rate constants was done using the protocols of sec.7.4.3. and sec.7.4.4. The values of k_a and k_d are summarized in Tab.8.2.; the process described in Fig.7.10. is not shown, since the concept is the same. For the equilibrium analysis, each ΔPh_c from all the above concentrations was a data point of a ΔPh vs. c plot (see schematic in Fig.7.6.) giving rise to the comparative graph shown in Fig.8.10., for all markers. In addition, the linearized transformation of the Langmuir equation is plotted in Fig.8.11. and the values calculated from all these methods are summarized in Tab.8.2.

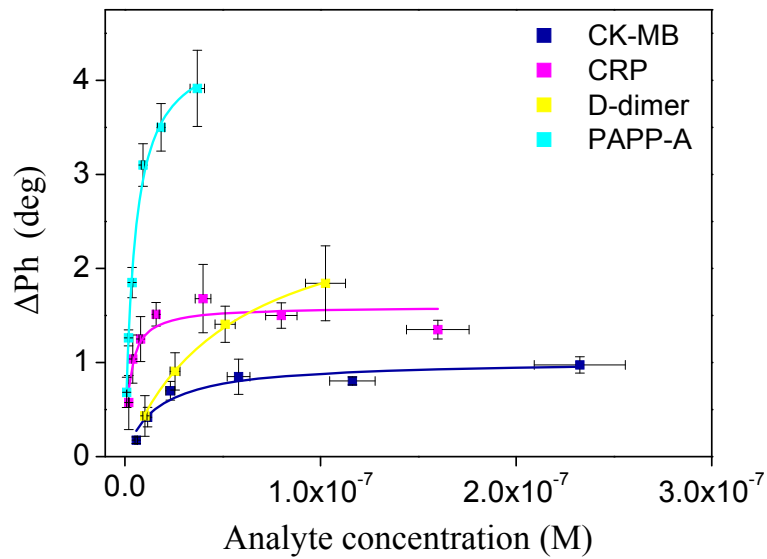
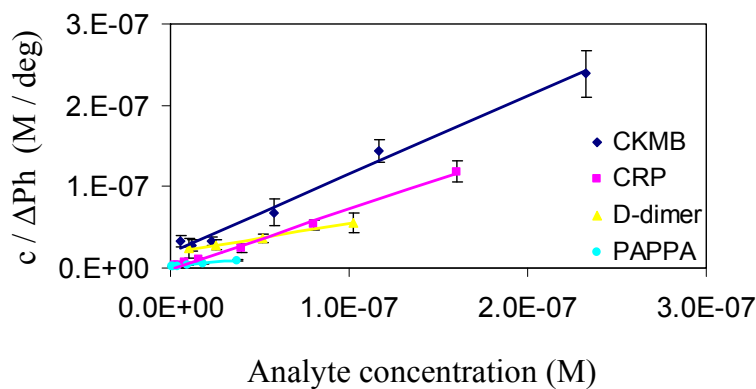


Fig.8.10. Binding isotherms of the four biomarkers upon the interaction with their corresponding antibodies.



$\frac{c}{\Delta Ph} = \frac{1}{\Delta Ph_{max}} c + \frac{K_D}{\Delta Ph_{max}}$ $(Y=AX+B)$
$y_{CK-MB} = 0.962 x + 1.92 \times 10^{-8}$ $R^2 = 0.989$
$y_{CRP} = 0.726 x - 7.48 \times 10^{-10}$ $R^2 = 0.995$
$y_{D-dimer} = 0.232 x + 1.30 \times 10^{-8}$ $R^2 = 0.998$
$y_{PAPP-A} = 0.226 x + 1.08 \times 10^{-9}$ $R^2 = 0.999$

Fig.8.11. Linearization of Langmuir isotherm curves for all cardiac markers. The trendlines are summarized on the right.

Tab.8.2. Affinity constants and binding rate constants for the interaction of the cardiac markers with their antibodies.

Constants	CK-MB	CRP	D-dimer	PAPP-A
Affinity constants from equilibrium (<i>non-linear Langmuir fit</i>)				
$K_A (M^{-1})$	6.29×10^7	4.12×10^8	1.86×10^7	2.10×10^8
$K_D (M)$	1.59×10^{-8}	2.43×10^{-9}	5.38×10^{-8}	4.77×10^{-9}



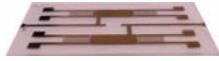
Affinity constants from equilibrium (<i>linearization of Langmuir curves</i>)				
K_A (M ⁻¹)	5.01×10^7	9.71×10^8	1.79×10^7	2.09×10^8
K_D (M)	2.00×10^{-8}	1.03×10^{-9}	5.59×10^{-8}	4.78×10^{-9}
Binding rate and affinity constants (<i>kinetic analysis</i>)				
K_A (M ⁻¹)	1.20×10^8	7.75×10^8	4.63×10^8	1.01×10^8
K_D (M)	8.36×10^{-9}	1.29×10^{-9}	2.16×10^{-9}	9.89×10^{-9}
k_a (M ⁻¹ t ⁻¹)	7.88×10^4	1.24×10^5	1.83×10^4	4.71×10^4
k_d (t ⁻¹)	6.59×10^{-4}	1.60×10^{-4}	3.95×10^{-5}	4.66×10^{-4}

It is worth noticing that the dissociation constant K_D of CRP, as calculated from the Langmuir non-linear fitting was found very close to the one given in the product datasheet, provided by the supplier (for mAb “C2”: $K_D = 1.93 \times 10^{-9}$ M, calculated via a Biacore SPR biosensor). Unfortunately no similar information was available in the datasheet of the other molecules.

Comparing the values of the above constants, and within the scattering existing among the different analysis methods, it can be safely concluded that there is no significant difference between the binding affinities of the four examined biomarkers. This was expected, as all interactions are of the antibody-antigen nature, which has typical K_A , K_D values of the order of magnitude that was experimentally measured.

8.7. Relation between detected values and clinical values

As the multi-analysis is ultimately intended to be implemented in diagnostics, “real-life” data must be taken into account and evaluate the μ F-on-SAW performance according to them. That is why Tab.8.3. reports the concentration “borders” between the healthy and critical conditions concerning the particular biomarkers. In combination with that, Fig.8.12. depicts the dynamic range of the μ F-on-SAW for all the tested molecules, in a ΔPh -vs- $Logc$ plot. $Logc$ was selected for the x-axis in order to appear in a linear form (equivalently, the concentration could be plotted in log-scale). In addition, among the concentrations tested (Tab.8.1.) only those in the linear region were kept, since the saturation region of signal vs. concentration is not of interest (gives no information) in the analytical performance of μ F-on-SAW. The four colored lines at the top of the figure represent the biomarkers’ concentration at the onset of critical situations. These values stem from clinical evaluation, but are indicative, as they may differ according to peoples’ gender, predisposition, obesity and other factors.



Tab.8.3. Concentration range of healthy and critical heart conditions related to the examined biomarkers and dynamic range of the μ F-on-SAW.

	CK-MB	CRP	D-Dimer	PAPP-A
Critical condition ($\mu\text{g/mL}$)	$> 0.01 \mu\text{g/mL}$	$1 - 10 \mu\text{g/mL}$	$> 0.5 \mu\text{g/mL}$	$> 0.05^*$
Dynamic range of μF-on-SAW ($\mu\text{g/mL}$)	0.5 - 20	0.25 - 20	2 - 20	0.5 - 20

*Cut-off value for PAPP-A was reported at 10 mIU/L [8.22.], with conversion factor: 1 mIU/mL = 4.5 mg/L = 4.5 $\mu\text{g/mL}$ [8.23.].

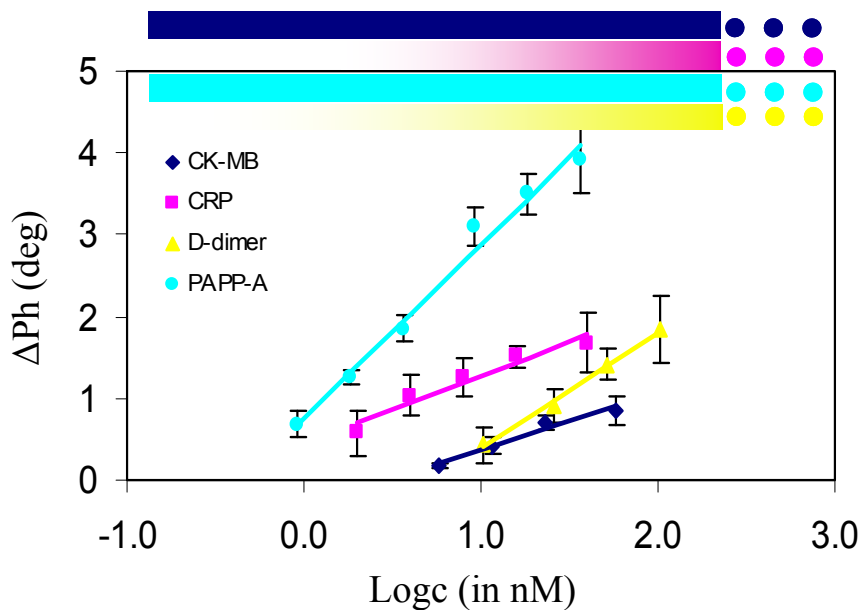


Fig.8.12. Dynamic range diagram for the examined markers, correlating the signal to the analyte concentration.

As it appears, the dynamic range of μ F-on-SAW lies within the critical concentration regions for all markers. The solid dark blue and cyan lines in Fig.8.12. (CK-MB and PAPP-A, respectively) denote that some part of the healthy (low) concentration range is not detectable by the μ F-of-SAW. This is clearly a matter of sensitivity and in order to be solved, further investigation for improvement of the sensitivity should take place, focusing on the microfluidic module and the operational features of the SAW sensor (e.g., size of total sensing area, operating frequency, etc.). Nevertheless, for CRP and D-dimer the μ F-on-SAW is already capable of detecting the whole region of interest, from the low to middle and high risk cases (faded magenta and yellow, with the white part at the left indicating healthy-state values; faded instead of sharp “border” was used on purpose, because of the vagueness in the cut off values due to various factors). The linearized analytical curves are summarized in Tab.8.4. so that, measuring the acoustic signal, it is possible to determine the analyte concentration in the solution.



Tab.8.4. Signal-concentration analytical curves (from Fig.8.12); c is expressed in nM.

$\Delta Ph_{CKMB} = 0.689 \times \text{Log}c_{CKMB} - 0.318$
$\Delta Ph_{CRP} = 0.828 \times \text{Log}c_{CRP} + 0.446$
$\Delta Ph_{D-dimer} = 1.426 \times \text{Log}c_{D-dimer} - 1.041$
$\Delta Ph_{PAPP-A} = 2.124 \times \text{Log}c_{PAPP-A} + 0.755$

8.8. Biomarker detection from a multi-marker mixture

So far it has been shown that the μ F-on-SAW setup is capable of successfully detecting the four cardiac markers, and was used in a broad concentration range with values both in the healthy and critical region according to the occasion. Experimental conditions of this kind followed a one-marker-per-microchannel regime, i.e., only one marker was injected in every microchannel. In reality, however, body fluids like serum contain many species which are potential blockers of the desired interaction. In order to investigate the capability of μ F-on-SAW to operate successfully under such conditions of increased complexity, the following major question must be answered:

“is it possible for an immobilized antibody to capture its homologous antigen from a mixture of injected molecules without complications”?

In fact, this is the highlight of the verification of μ F-on-SAW as multi-sensing platform. This ideal situation is illustrated in Fig.8.13., where it appears that, upon injection of a mixture of the four biomarkers in each microchannel compartment (multi-marker-per-microchannel regime), only the homologous antibody-antigen interaction takes place.

Along with the multi-marker experiments, it is essential to have a view of the interaction patterns between non-homologous antibody-antigen pairs. These were the negative control experiments that were carried out by testing each antibody against all the three non-homologous antigens (e.g. immobilized anti-CKMB + injected CRP, etc). These experiments were done also in the one-marker-per-microchannel regime and all twelve possible combinations were tested.

Then, the multi-marker experiments were carried out in a similar way like those described earlier in this chapter:

- One antibody was immobilized on each of the four sub-areas.
- A mixture of all four biomarkers was injected (sequentially) in each microchannel (in Fig.8.13. they all appear simultaneous for simplicity reasons).
- Only the proper biomarker is (expected to be) bound on its homologous antibody.
- The other three markers are rinsed off.

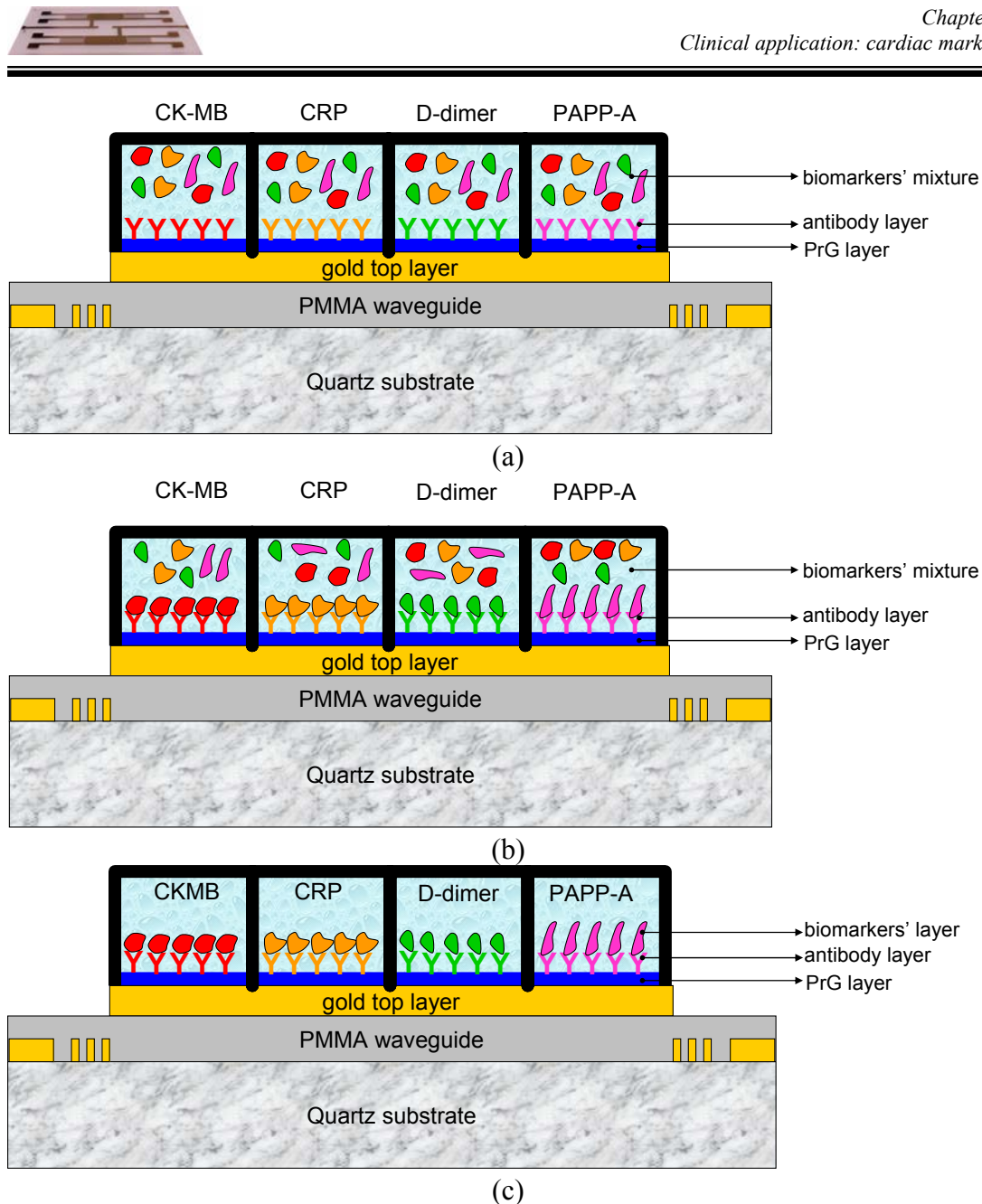


Fig.8.13. (a) Injection of the 4 biomarker mixture in each microchannel, with one pre-immobilized antibody in each compartment, (b) homologous pairs bind with minimum non-specific binding, (c) only homologous pairs are detected upon rinsing. Note the different injection regime between (a) here and Fig.8.6(d).

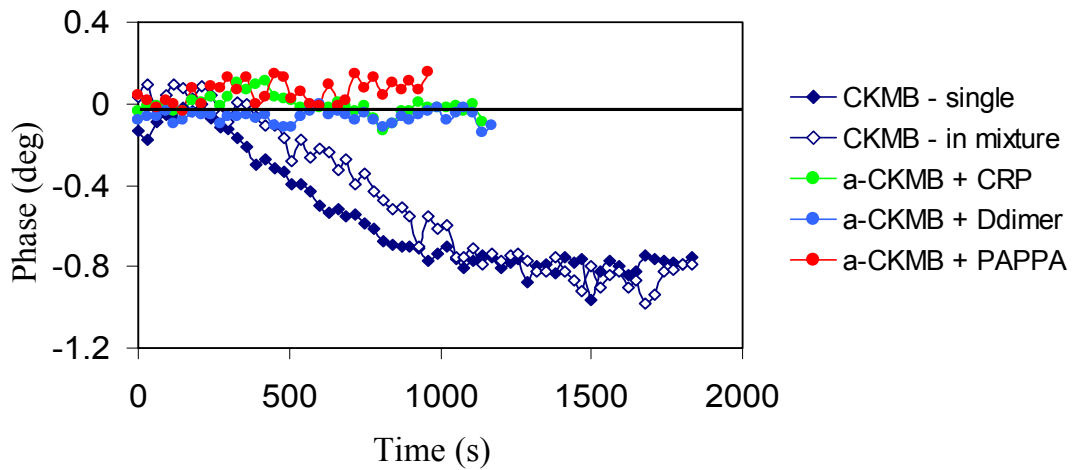
In order to visualize the results, four multi-sensograms were plotted, each corresponding to one biomarker (Fig.8.14.). Each of the four graphs includes 5 real-time curves, which correspond to the following interactions (all antigens were injected in 5 $\mu\text{g}/\text{mL}$ concentrations, both in the single and in the mixture regime):

- antibody-antigen, when the antigen is injected *single* in the microchannel
- antibody-antigen, when the antigen is injected in a *mixture* with the other markers
- 3 control experiments of the interaction of one antibody with all the three non-homologous antigens.

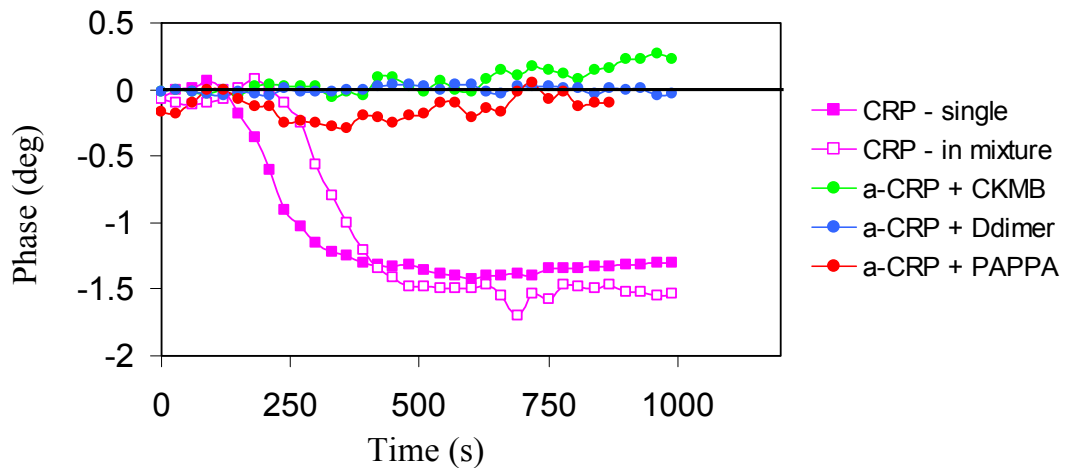


Two very important features are evident from these graphs:

1. The negative controls are (within error or drift) horizontal lines, essentially not changing with time. This is a clear indication that the non-specific binding between non-homologous antibody-antigen pairs is minimum and does not interfere with the measurements.
2. The lines corresponding to an antibody-antigen interaction when the latter is *single* and in *mixture* almost overlap and irrespective of the kinetic decay, the signal change is essentially the same; e.g. $\Delta Ph_{CKMB(single)} = \Delta Ph_{CKMB(mixture)}$, the same applying for the other three biomarkers. This result enhances the previously mentioned zero non-specific binding and implies one more issue: that there is also zero non-specific binding between the biomarkers themselves; they do not seem to form any aggregate, otherwise the $\Delta Ph_{mixture}$ would be much different from the ΔPh_{single} .



(a)



(b)

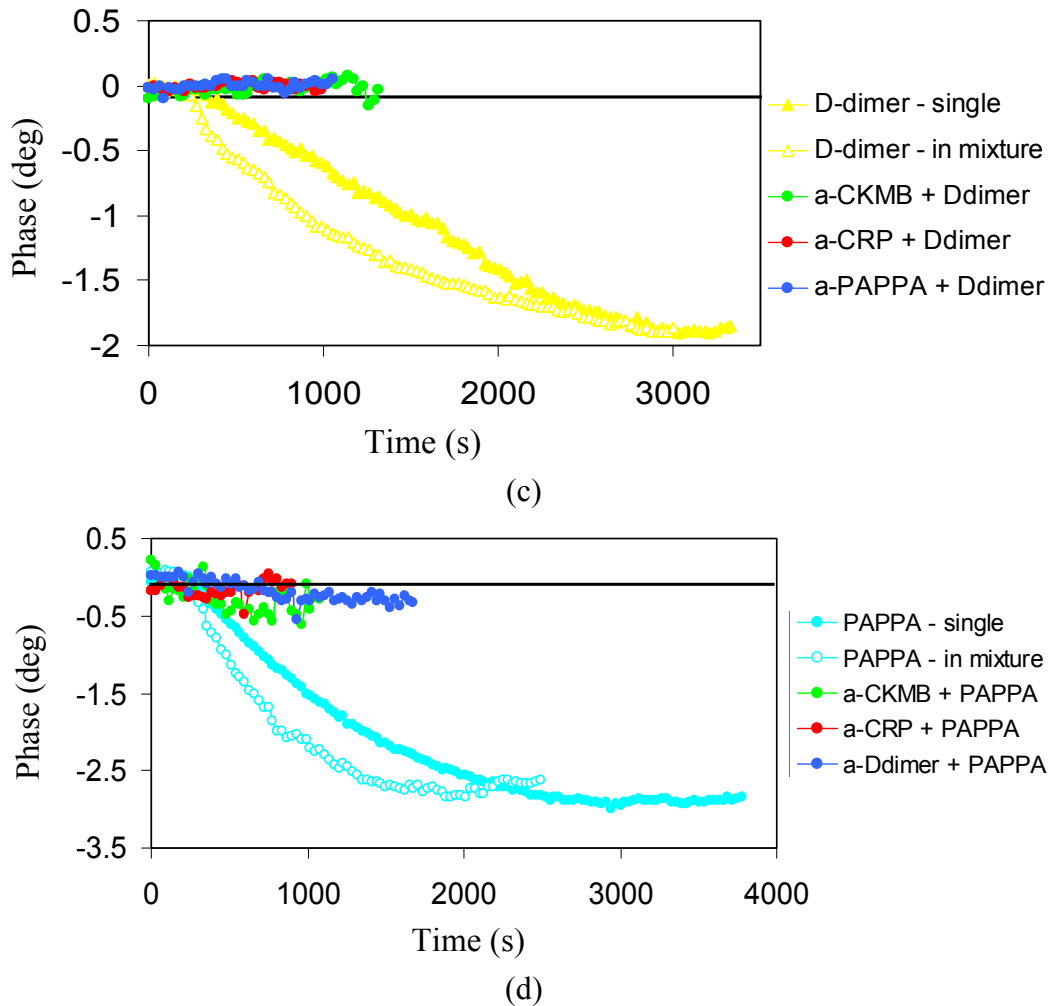


Fig.8.14. Multi-marker detection, selectively capturing the right antigen from a mixture. The concentrations in all cases were $5 \mu\text{g/mL}$.

8.9. Conclusions

In this chapter the $\mu\text{F-on-SAW}$ microsystem was implemented for the detection of four cardiac biomarkers, a clinical application of high importance for diagnostics and healthcare. Various concentrations were tested in order to explore the limits of the setup and analytical immunoassay curves were plotted, correlating the signal to the concentrations of the solutions. The dynamic range of the system was proven to be well within the critical concentration values of the markers, even reaching the health levels of two of them (with sensitivity improvement needed for the other two). Finally, in an experiment of increased complexity, where mixtures of all markers were injected in all microchannels (with different immobilized antibody in each microchannel) the result was remarkably promising: each antibody captured only its corresponding marker with minimum non-specific binding and interference from the other biomolecules present. These results are very important in the verification of $\mu\text{F-on-SAW}$ as a multi-marker detector. Essentially they prove that the sensor can detect a specific interaction in the same way, no matter if the analyte exists alone in the solution or in mixture; there is no screening from other present molecules and, thus, $\mu\text{F-on-SAW}$ can potentially be used with complex body fluids.



References

- [8.1.] G.X. Brogan, J.L. Bock, “Cardiac marker point-of-care testing in the emergency department and cardiac care unit”, *Clin. Chem.*, vol. 44, pp. 1865-1869, 1998.
- [8.2.] A.S. Jaffe, L. Baduin, F.S. Apple, “Biomarkers in acute cardiac disease”, *J. Am. Coll. Cardiol.*, vol. 48, pp. 1-11, 2006.
- [8.3.] E.C. Lewandowski, “Update on cardiac biomarkers”, *Labmedicine*, vol. 37, pp. 597-605, 2006.
- [8.4.] <http://www.emcreg.org/publications/monographs/acep/2005/alb2.pdf>
- [8.5.] M.M. Mion, E. Novello, S. Altinier, S. Rocco, M. Zaninotto, M. Plebani, “Analytical and clinical performance of a fully automated cardiac multi-markers strategy based on protein biochip microarray technology”, *Clin. Biochem.*, vol. 40, pp. 1245-1251, 2007.
- [8.6.] L. Tang, K.A. Kang, “Preliminary study of fiber optic multi-cardiac-marker biosensing system for rapid coronary heart disease diagnosis and prognosis”, *Adv. Exp. Med. Biol.*, vol. 578, pp. 101-106, 2006.
- [8.7.] <http://www.nanogen.com/products/cardiacstatus>
- [8.8.] J. Wei, Y. Mu, D. Song, X. Fang, X. Liu, L. Bu, H. Zhang, G. Zhang, J. Ding, W. Wang, Q. Jin, G. Luo, “A novel sandwich immunosensing method for measuring cardiac troponin I in sera”, *Anal. Biochem.*, vol. 321, pp. 209-216, 2003
- [8.9.] J.D. McBride, M.A. Cooper, “A high sensitivity assay for the inflammatory marker C-reactive protein employing acoustic biosensing”, *J. Nanobiotechnology*, 6:5, 2008.
- [8.10.] R.E. Slovacek, W.F. Love, S.C. Furlong, “Application of a plastic evanescent-wave sensor to immunological measurements of CKMB”, *Sens. Actuat. B-Chem.*, vol. 29, pp. 67-71, 1995.
- [8.11.] J.-P. Chapelle, M. El Allaf, R. Larbuisson, R. Limet, M. Lamy, C. Heusghem, “The value of serum CK-MB and myoglobin measurements for assessing perioperative myocardial infarction after cardiac surgery”, *Scand. J. Clin. Lab. Inv.*, vol. 46, pp. 519-526, 1986.
- [8.12.] C. Gabay, I.N. Kushner, “Acute-phase proteins and other systemic responses to inflammation”, *New Engl. J. Med.*, vol. 340, pp. 448-454, 1999.
- [8.13.] N. Rifai, P.M. Ridker, “High-sensitivity C-reactive protein: a novel and promising marker of coronary heart disease”, *Clin. Chem.*, vol. 47, pp. 403-411, 2001.
- [8.14.] P.M. Ridker, “C-reactive protein: a simple test to help predict risk of heart attack and stroke”, *Circulation*, vol. 108, pp. e81-e85, 2003.
- [8.15.] P.J. Gaffney, “Breakdown products of fibrin and fibrinogen: molecular mechanisms and clinical implications”, *J. Clin. Pathol. Suppl. (R. Coll. Pathol.)*, vol. 14, pp. 10-17, 1980.
- [8.16.] H. Bounameaux, P. de Moerloose, A. Perrier, G. Rebe, “Plasma measurement of D-dimer as diagnostic aid in suspected venous thromboembolism: an overview”, *Thromb Haemost.*, vol. 71, pp. 1-6, 1994.
- [8.17.] A. Bayes-Genis, J. Mateo, M. Santaló, A. Oliver, J. Guindo, L. Badimon, A. Martínez-Rubio, J. Fontcuberta, R. S. Schwartz, A. Bayés de Luna, “D-dimer is an



early diagnostic marker of coronary ischemia in patients with chest pain”, *Am. Heart J.*, vol. 140, pp. 379-384, 2000.

[8.18.] A. Bayes-Genis, C.A. Conover, M.T. Overgaard, K.R. Bailey, M. Christiansen, D.R.Jr. Holmes, *et al.*, “Pregnancy-associated plasma protein A as a marker of acute coronary syndromes”, *N. Engl. J. Med.*, vol. 345, pp. 1022-1029, 2001.

[8.19.] C. Heeschen, S. Dimmeler, C.W. Hamm, S. Fichtlscherer, M.L. Simoons, A.M. Zeiher, “Pregnancy-associated plasma protein-A levels in patients with acute coronary syndromes: Comparison with markers of systemic inflammation, platelet activation, and myocardial necrosis”, *J. Am. Coll. Cardiol.*, 45, pp. 229, 2005.

[8.20.] S. Saliterman, “Fundamentals of BioMEMS and medical microdevices”, Wiley Interscience Press, pg.267, ISBN 081945977-1, 2006.

[8.21.] S. Kabir, “Immunoglobulin purification by affinity chromatography using protein A mimetic ligands prepared by combinatorial chemical synthesis”, *Immunol. Invest.*, vol.31, pp.263-278, 2002.

[8.22.] Q.-P. Qin, S. Wittfooth, K. Pettersson, “Measurement and clinical significance of circulating PAPP-A in ACS patients”, *Clin. Chim. Acta*, vol. 380, pp. 59-97, 2007.

[8.23.] Product datasheet: “Enzyme immunoassay for the quantitative measurement of human PAPP-A in serum”, ALPCO Diagnostics, <http://www.alpco.com/pdfs/38/38-PAPHU-E01.pdf>.



CHAPTER 9. Correlation of acoustic signal to biomolecules' properties



Microfluidic networks and wells in Agilent's Lab-on-a-Chip platform probed with 2100 Bioanalyzer
<http://www.chem.agilent.com/en-US/products/instruments/lab-on-a-chip>





Chapter 9. Correlation of acoustic signal to biomolecules' properties

9.1. Introduction

During the experiments that were carried out throughout the project in order to validate the functionality of μ F-on-SAW as multi-sample detection platform, two groups of biomolecular interactions were investigated: the biotinylated molecules with neutravidin, and the cardiac markers with their corresponding antibodies. Examining these biomolecules from a different perspective some interesting side-results emerged, which are irrelevant of the multiplexing and multisensing evaluation. These results correlate the acoustic signal to biomolecules' properties, and are discussed separately in this chapter, so as not to interfere with the main objective of the project. More specifically, the acoustic signal is qualitatively and quantitatively correlated to properties of the biomolecules, such as their molecular weight and viscoelastic nature. For this reason both the output acoustic signals, ΔPh and ΔA , were used in combination. SPR was also used to cross-check some of the results, especially for (independently) quantitating the bound mass of the molecules.

9.2. SPR and SAW for the quantification of the bound mass

In the analytical curves of chapter 7 and chapter 8 the acoustic signal was related to the bulk analyte concentration. However, in order to extract biomolecules' properties, the bound molecules are of interest, rather than the ones in the bulk solution. Therefore, it is initially needed to estimate the mass bound on the surface (surface concentration, or mass per area, m/A) by correlating it to the acoustic signal, i.e., calculate the proportionality constant, c , of eq.4.3. This constant is necessary to be defined because it will be used in the calculation of the viscoelastic properties, as well; and because it is directly related to the wave parameters ($\Delta\alpha/k_o$ and $\Delta v/v_o$) rather than the network analyzer quantities (see eq.4.3.) the former notation will be used for this purpose.

In fact, this procedure was partly done in sec.4.4.1. upon gold deposition in air. For the Q155-0.70 μ m PMMA configuration (the one used in all experiments) it comes that $\Delta v/v_o = 1.94 \times 10^{-8} \cdot \omega ph$, corresponding to the black triangles in Fig.4.8. (after rearranging the axes: $\Delta v/v_o$ vs. ωph , instead of $\Delta Ph/area$ vs. $\Delta m/area$). Therefore, using the above proportionality constant, a layer of BSA ($h \sim 3 \times 10^{-9}$ m, $\rho \sim 1050$ kg/m³) should give approximately $\Delta Ph \cong 6$ deg. On the contrary, a typical experiment using the standard flow cell (i.e., total sensing area) gave $\Delta Ph = 18.6 \pm 1.7$ deg, which is a large difference. When, however, the signal change of a BSA layer was measured *in air* (i.e., deposited in PBS and the dried mildly with nitrogen flow) the signal was $\Delta Ph = 7.0 \pm 1.2$ deg, i.e., very close to the expected value. This shows clearly that when working in *liquid* environment, it is incorrect to use the proportionality constant c calculated in *air*. That is why the constant c was calculated with the aid of SPR for calculations with liquid-based experiments: practically, m/A



was calculated via SPR and the equivalent ΔPh via acoustics. Once the ratio $\frac{\Delta Ph}{m/A}$ was defined (Tab.9.1.) ΔPh was transformed into $\Delta v/v_o$, and m/A into ωph , so as to eventually extract the constant c :

$$\Delta Ph = 2.88 \frac{\text{deg} \cdot \text{mm}^2}{\text{ng}} \frac{m}{A} \quad (\text{from Tab.9.1., } m/A \text{ in ng/mm}^2) \quad (\text{eq.9.1(a)})$$

$$\Rightarrow \frac{\Delta Ph}{1845 \cdot 57} = \frac{1}{1845 \cdot 57} 2.88 \frac{\text{deg} \cdot (10^{-3} \text{ m})^2}{10^{-12} \text{ kg}} \frac{m}{A} \quad (\text{changing notation, from } \Delta Ph \text{ to } \Delta v/v_o)$$

$$\Rightarrow \frac{\Delta v}{v_o} = \frac{1}{1845 \cdot 57} 2.88 \frac{\text{deg} \cdot (10^{-3} \text{ m})^2}{10^{-12} \text{ kg}} \frac{m}{A}$$

$$\Rightarrow \frac{\Delta v}{v_o} = 27.4 \frac{m}{A} \quad (\text{units in SI}).$$

$$\text{Since } \frac{\Delta v}{v_o} = c \cdot \omega ph = c \cdot \omega \frac{m}{A}, \text{ then } c\omega = 27.4 \text{ and } c = 2.8 \cdot 10^{-8} \frac{\text{m}^2 \text{s}}{\text{kg}} \quad (\text{eq.9.1(b)})$$

Tab.9.1. Proportionality between ΔPh (SAW) and m/A (SPR) for various loaded samples (molecules on Au and b-molecules on neutravidin).

Molecule	SAW ΔPh (deg)	SPR (μRIU)	SPR m/A^* (ng/mm ²)	$\frac{\Delta Ph}{m/A}^{**}$
PrA / Au	1.158	680	0.422	2.743
BSA / Au	3.142	1875	1.165	2.698
neu / Au	4.828	3165	1.966	2.456
IgG / Au	5.780	3710	2.304	2.508
b-PrG / neu	0.977	540	0.335	2.913
b-PrA / neu	1.323	677	0.420	3.147
b-BSA / neu	1.539	740	0.460	3.349
b-IgG / neu	2.965	1465	0.910	3.258
Average				2.88
St.Dev.				0.339

* For our SPR equipment the proportionality constant between SPR signal and surface coverage was defined by the manufacturer as: $1.61 \mu\text{RIU} = 1 \text{ pg/mm}^2$.

** The same proportionality constant derives if ΔPh (from SAW) is plotted against m/A (from SPR) (data not shown).

9.3. Correlation of acoustic signal to biomolecules' molecular weight

Observing Fig.7.3. qualitatively, it appears that there is a trend of increasing ΔPh as the molecules become “bigger”. “Bigger” refers to their molecular weight (MW), which increases from b-PrG to b-IgG. In an effort to quantify a possible relation, ΔPh (at surface saturation) was plotted against MW and interestingly, this plot appeared to be linear (Fig.9.1.). In order to verify this result, experiments with the



same molecules under the same conditions (buffer, batch, concentrations, etc.) were repeated using SPR; the trend remained linear. Fig.9.1. is a combined graph from data acquired with SAW and SPR under the same experimental conditions.

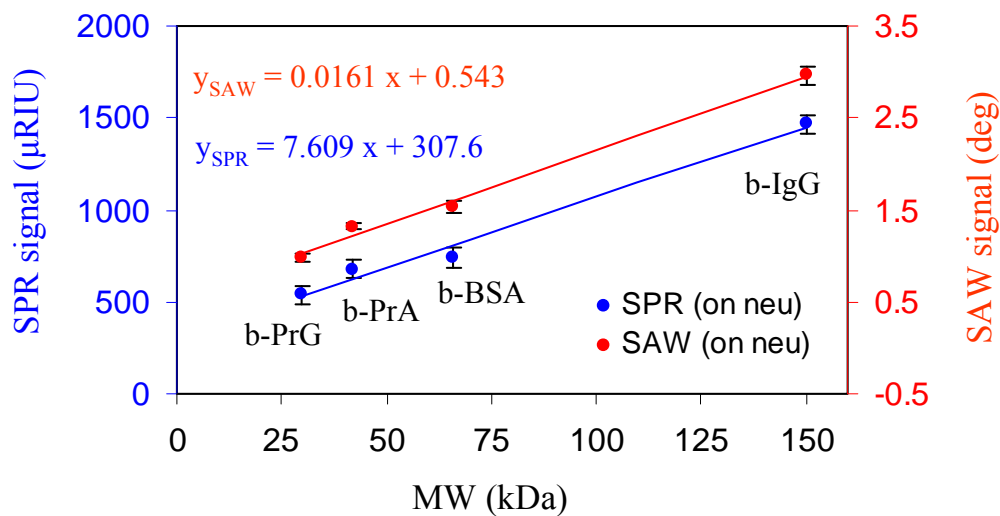


Fig.9.1. Linear relation between acoustic (SAW) and optical (SPR) signals with MW for the biotinylated molecules.

It could be argued that this is an expected trend, since ΔPh is proportional to adsorbed mass and the MW , essentially, represents mass. In order to check this assumption and verify whether this is a universal phenomenon, another set of experiments was carried out: the same molecules in their non-biotinylated form were left to adsorb on gold, without any neutravidin layer, in concentration 100 $\mu\text{g}/\text{mL}$; in this case neutravidin was used as well, because its MW is very close to the one of BSA. In addition, the non-biotinylated molecules were also left to adsorb on SPR gold-coated chip, so as to compare the results between the two techniques. The outcome is summarized in Fig.9.2.

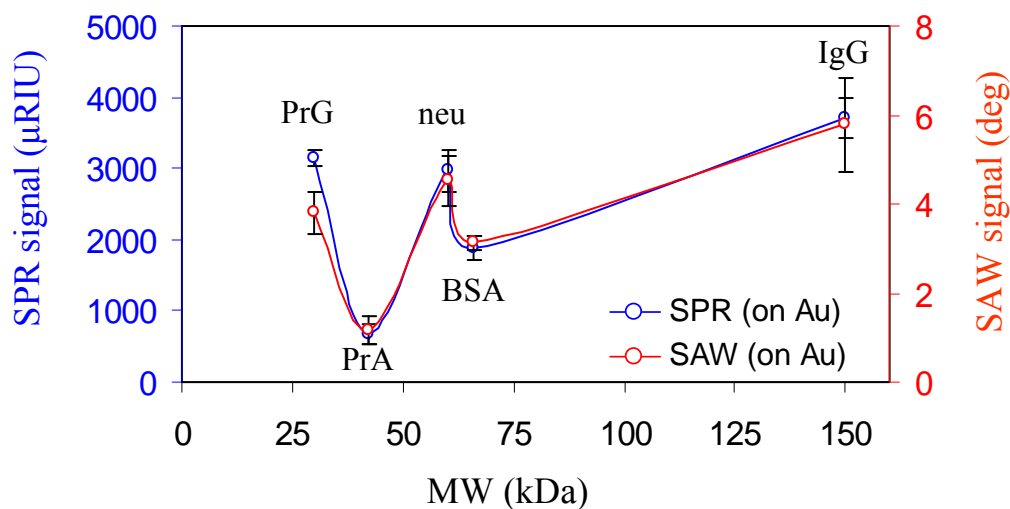


Fig.9.2. Acoustic (SAW) and optical (SPR) signal vs. MW for non-biotinylated molecules on gold.



Clearly, there is a remarkable non-linearity between the signal and the MW , unlike the case of biotinylated molecules. This lack of trend is evident for both SPR and SAW signals (both of which present the same non-trend with respect to MW). Indicative examples:

- comparing neutravidin and BSA, although $MW_{neu} \cong MW_{BSA}$, the relation of the acoustic signal is $\Delta Ph_{neu} \cong 1.5 \times \Delta Ph_{BSA}$ (same relation for SPR).
- PrA exhibits a very low signal, disproportional to its MW .
- even though $MW_{IgG} \cong 5 \times MW_{PrG}$ and $MW_{IgG} \cong 2 \times MW_{neu}$, all three molecules give almost the same signal, in both SAW and SPR.

What the above first imply is that the linearity between the biotinylated molecules MW and signal is not inferred from the Sauerbrey relation of signal vs. mass proportionality. If this was the case, the linearity should hold for the non-biotinylated molecules as well. Staying a bit more at Sauerbrey equation, though, the bound mass can be expressed as:

$$m = n \times MW \Rightarrow m = \frac{N \times MW}{N_A}, \text{ thereby } \Delta Ph = K \times N \times MW \quad (\text{eq.9.2.})$$

where n and N are the number of moles and molecules, and N_A is the Avogadro number; K is a constant in which the frequency, N_A and other constants related to the SAW device have been incorporated. Therefore, it is not just mass, but the product of number of molecules with MW that is proportional to the signal. Now, keeping in mind that between the two experimental sets (b-molecules on neu, and non-b-molecules on gold) the experimental conditions, buffer, pH , MW were all the same, the only way that ΔPh vs. MW is linear, is if N is invariable and incorporated in the constant K ; in other words, this linearity holds because the number of biotinylated molecules bound on neutravidin is the same for all four different b-molecules, which does not happen for the same molecules adsorbing on gold. This assumption is verified by actually measuring the number of molecules per area, N/A , for each examined case (based on SPR calculation of m/A). The results are summarized in Fig.9.3. It is clear that N/A varies from 4 to 6×10^9 molecules/ mm^2 for the biotinylated molecules on neutravidin, but from 6 to 18×10^9 molecules/ mm^2 for those adsorbed on bare gold.

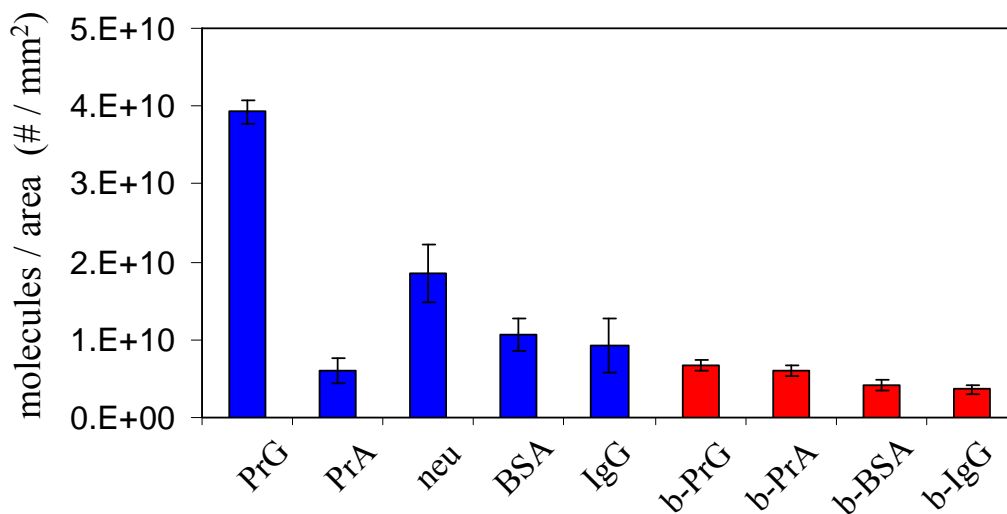


Fig.9.3. Number of molecules per area for all examined molecules.



The difference in the number of molecules per area (which apparently leads to the signal vs. MW linearity discrepancy) happens most likely due to the difference of the nature of the two interactions: one is a mere adsorption of biomolecules on the gold surface, whereas on the other hand, the interaction of biotinylated molecules with neutravidin is of specific nature. In support of this argument, the signal of the cardiac markers investigated in chapter 8 was also plotted vs. their MW (Fig.9.4.). The linearity holds for this case as well, enhancing the above argument, since antibody-antigen interactions are also of specific nature (like avidin-biotin). Moreover, the antibodies are monoclonal, which means that the antigen always binds in the same way, once the interaction is accomplished. Calculating the number of molecules per area (Fig.9.4., inset) we get that the deviation in N/A is even more “narrow” than the case of biotinylated molecules, and lies from 1.4 to 2.4×10^9 molecules/ mm^2 . (*Note: In the case of cardiac markers, neither SPR experiments, nor simple adsorption of the markers on gold surface was tried because the samples were valuable for the immunoassay detections and also limited in amount. However, the linearity is beyond dispute.*)

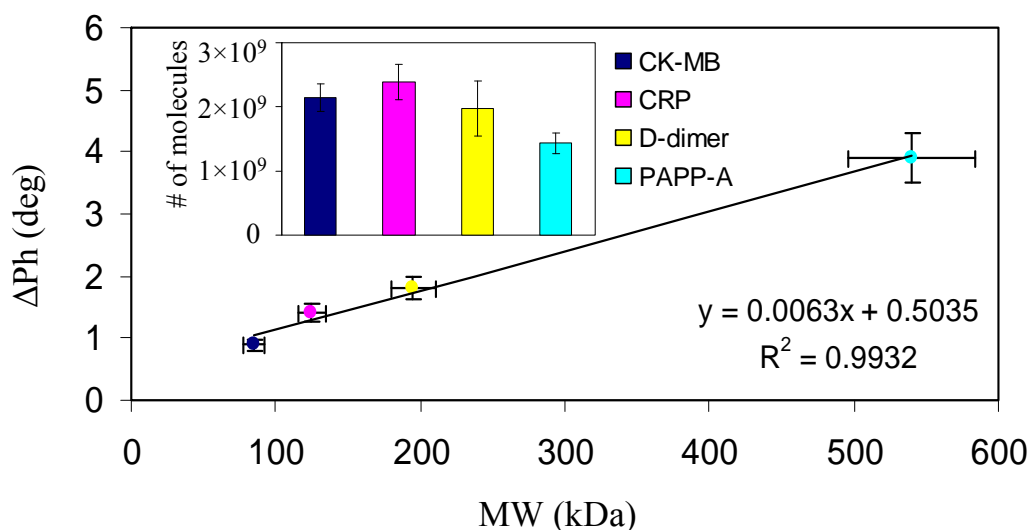


Fig.9.4. ΔPh vs. MW linearity for cardiac markers. Inset: number of molecules/ mm^2 .

Eventually, it appears that, even though the linearity between signal and MW seems not to follow a universal validity, it appears to hold for cases when (specific) interactions of the same nature are compared. Particularly in the case of biotinylated molecules, this finding can even lead to a practical impact: if a biomolecule of unknown MW is biotinylated and injected on a neutravidin-modified surface, its MW can be determined (considering Fig.9.1. as a calibration line) and compared with other methods (as long as it falls within the limits of calibration, e.g. here between 30 and 150 kDa, where the linearity has been proven to be valid).

9.4. Acoustic signal and viscoelastic nature of probed samples

Another observation during the analysis was the fact that the proteins directly adsorbed on gold gave a higher signal than their equivalent biotinylated ones bound on neutravidin. One would argue that this is expected since the b-molecule layer is



located further from the surface than the adsorbed molecules, which are located directly on the sensor surface. In an effort to test this assumption, PrG-IgG interaction was probed with respect to neutravidin-b-IgG. A reasonable assumption (expressed before as well) is that IgG and b-IgG have the same MW . Second, both of them are not adsorbed on the surface, but bound on two molecules which, more or less, have the same size, so, both IgG and b-IgG films are located at approximately the same distance from the surface. If the assumption of sensitivity decrease along the surface-normal direction is correct, these two interactions should give the same signal, within error. Well, this was clearly not the case since $\Delta Ph (PrG - IgG) : \Delta Ph (neu - b-IgG) = 5 : 3$.

Moreover, mass loading was investigated via successively depositing thin gold films, as it was discussed in sec.4.4.1. If sensitivity was reduced due to increasing distance from the sensor surface, the addition of the upper gold layers should give less signal than the lower layers, since the former are deposited at a higher distance from the sensor initial surface than the latter; however, this was clearly not observed in any case.

Therefore, it is not just the distance from the sensor surface that accounts for this observation. Instead, it is the “*nature*” of the underlying material that plays an important role. More specifically, the Au thin films are rigid mass layers, which move synchronously with the sensor surface (Fig.4.2.) and, thus, do not dissipate energy. On the contrary, a neutravidin film, unlike gold, dissipates energy (which is evident from the non-zero ΔA) due to its viscoelastic nature. Consequently, as the biotinylated molecules “sit” on this viscoelastic layer, the interaction with the acoustic wave is weaker than that of their equivalent non-biotinylated lying directly on the bottom of the sensor. This is in agreement with reports elsewhere [9.1.] that the addition of a layer on another layer of viscoelastic nature does not lead to linear combination of the two, and accounts for the reduced signal observed for the biotinylated molecules.

9.5. Viscoelastic properties of protein films

In order to define the complex shear modulus of PMMA viscoelastic films in air (sec.4.2.4. and sec.4.4.5.) eq.4.12. was used, which was under conditions analytically “split” into real (eq.4.14(a)) and imaginary (eq.4.14(b)) parts. The ratio $G2/G1$ was calculated much lower than 1 in all cases and it was concluded that the PMMA films exhibit elastic rather than viscous behavior. In this section, the elastic vs. viscous regime in a protein film is investigated, and its viscoelastic properties are quantified.

For simplicity reasons, the investigation initially took place in air. Towards this scope, a “dry” protein film was measured. More specifically, using the standard flow cell configuration, BSA (1 mg/mL) adsorbed on gold till saturation of the surface. The chip was then removed from the holder, rinsed, dried with mild nitrogen flow, and placed again on the holder. ΔA and ΔPh after drying were measured with respect to the unloaded sensor prior to the experiment: $\Delta Ph_{dry} = 7.0 \pm 1.2 \text{ deg}$ and $\Delta A_{dry} = 0.45 \pm 0.11 \text{ dB}$. Using these values in the above equations, as well as thickness $h = 3 \times 10^{-9} \text{ m}$, and $c = 1.94 \times 10^8 \text{ m}^2\text{s/kg}$, it was calculated that $G2/G1 = 4.02$ (the Q155-



0.7 μm device was used and measured *in air*, that is why this particular value for c was used, see sec.9.2.). This clearly shows that the behavior of the BSA protein film has a more viscous than elastic behavior, which is a reasonable result for a protein film to be a more “lossy” material, in contrast to the PMMA. Then, calculating $G1$ and $G2$, we get: $G1 = 5.57 \times 10^3$, $G2 = 1.23 \times 10^5 \text{ Pa}$.

The values for $G1$, $G2$, although reasonable, appear to be quite low. However, it should be kept in mind that the above calculations were done considering the protein film as a viscoelastic film *in air*. In reality, the protein film is overlaid by liquid and $G1$ and $G2$ are expected to take higher values, just like the actual acoustic signal was higher (for example, for the same type of experiments, $\Delta Ph_{wet} = 18.6 \pm 1.7 \text{ deg}$ and $\Delta A_{wet} = 0.64 \pm 0.10 \text{ dB}$).

Thus, considering the protein layer as a viscoelastic material in contact with liquid, eq.4.12. is no longer valid, and eq.4.13. should be used, instead. In that case, the values for ΔA and ΔPh (or $\Delta \alpha/k_o$ and $\Delta v/v_o$) should be measured with respect to the unloaded device, i.e., air. This is quite impractical, though, since the signal changes of interest due to the actual sample are measured right before and after the sample injection, i.e. when there is *already* liquid on the sensor. This issue can be solved in the following way: although it is not directly obvious from eq.4.13., setting h equal to zero, Z_{liq} reduces to Z_{visc} (eq.4.6.). Thus, subtracting Z_{visc} from Z_{liq} we get eq.9.3., which is the one eventually used for the calculations (*allowing the use of ΔA and ΔPh values of the actual samples, without worrying about the pre-loaded buffer/liquid*):

$$Z_{liq} = \sqrt{\rho_F G} \frac{\sqrt{j\omega\rho_L\eta_L} + \sqrt{\rho_F G} \cdot \tanh\left(j\omega h \sqrt{\frac{\rho_F}{G}}\right)}{\sqrt{\rho_F G} + \sqrt{j\omega\rho_L\eta_L} \cdot \tanh\left(j\omega h \sqrt{\frac{\rho_F}{G}}\right)} - \sqrt{j\omega\rho_L\eta_L} \quad (\text{eq.9.3.})$$

$$Z_{liq} = Z_F \frac{Z_L + Z_F \cdot \tanh\left(j\omega h \sqrt{\frac{\rho_F}{G}}\right)}{Z_F + Z_L \cdot \tanh\left(j\omega h \sqrt{\frac{\rho_F}{G}}\right)} - Z_L$$

Z_F and Z_L represent the acoustic impedance of a semi-infinite viscoelastic film and liquid, respectively. Plotting the real and imaginary parts of eq.9.3. and eq.4.13. in a common graph (Fig.9.6.) it clearly appears that the graphic representation of eq.9.3. (black line) is only shifted in the y-axis with respect to eq.4.13. (red line) by the values of ΔA_{buffer} and ΔPh_{buffer} . Thus, the two equations are equivalent and eq.9.3. can be “safely” used instead of eq.4.13.

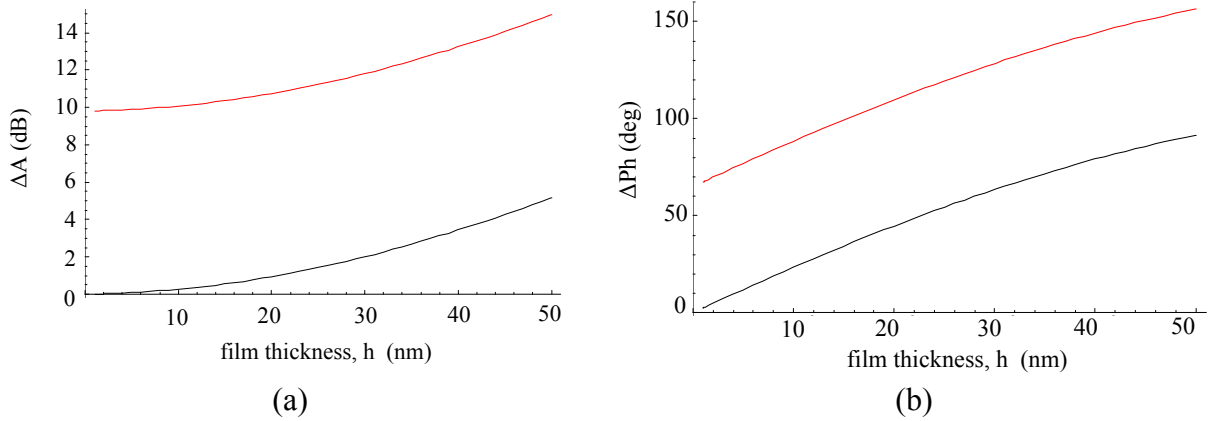


Fig.9.6. (a) Real part (ΔA) and (b) imaginary part (ΔPh) of the complex acoustic impedance for a viscoelastic film overlayed by liquid; red lines correspond to eq.4.13., black lines to eq.9.3.

After defining the formula to be used, the next step is to quantitatively extract the protein films' properties. At this point some assumptions are necessary. The reason is that there are only two known quantities (measured ΔA and ΔPh) whereas many more unknown ones: liquid density and viscosity, ρ_L and η_L , film thickness h , storage modulus $G1$ and viscosity η_F ($G2 = \omega\eta_F$, the film fluidity considered to obey to Newtonian behavior, where $G2 = \omega\eta$). Thus, it is firstly assumed that the buffer overlying the protein film is a Newtonian liquid, with parameters equal to those of water at 25°C: $\rho_L = 1000 \text{ kg/m}^3$ and $\eta_L = 0.001 \text{ Pa}\cdot\text{s}$; the film density was taken 1050 kg/m^3 , which is a reasonable value between the pure water and PMMA (1200 kg/m^3). The film thickness was measured independently with SPR. The value of c was taken to be $2.8 \times 10^{-8} \text{ m}^2\text{s/kg}$, as it was calculated in sec.9.2., via independent measurements of m/A (SPR) and ΔPh (SAW) for the Q155-0.70 μm μF -on-SAW setup. Finally, the film thickness of each protein layer was measured independently using SPR.

Under the above conditions, the unknown parameters were reduced to $G1$ and η_F , and the method towards their quantification is depicted in the 3D plots of Fig.9.7., designed with "Mathematica" software. Equation 9.3. is defined as a two-parameter function in the software; $G1$ and η_F are considered free parameters (plotted in x- and y-axes, respectively). Varying $G1$ and η_F within some range, the values for real and imaginary part of Z_{liq} are plotted on the z-axis against $G1$ and η_F (Fig.9.7(a) and Fig.9.7(b), respectively). When the z-axis values from these simulations coincide with the actual experimental values of both ΔA and ΔPh , then the ranges of $G1$ and η_F are the accepted ones. The limits in z-axis were set according to the experimental standard deviation; making the z-limits as narrow as possible, the x- and y-axes range becomes narrower. The values for all adsorbed protein layers on gold are summarized in Tab.9.2.; indicatively, for BSA:

$$2.5 \leq \Delta Ph \leq 3.5 \text{ deg and} \\ 0.08 \leq \Delta A \leq 0.15 \text{ dB}$$

and within these z-limits, a small "window" of values was determined for $G1$ and η_F :

$$1.2 \times 10^5 \leq G1 \leq 3 \times 10^5 \text{ Pa} \\ 1.5 \times 10^{-3} \leq \eta_F \leq 1.7 \times 10^{-3} \text{ Pa}\cdot\text{s}$$

or

$$1.45 \times 10^6 \leq G2 \leq 1.65 \times 10^6 \text{ Pa}$$

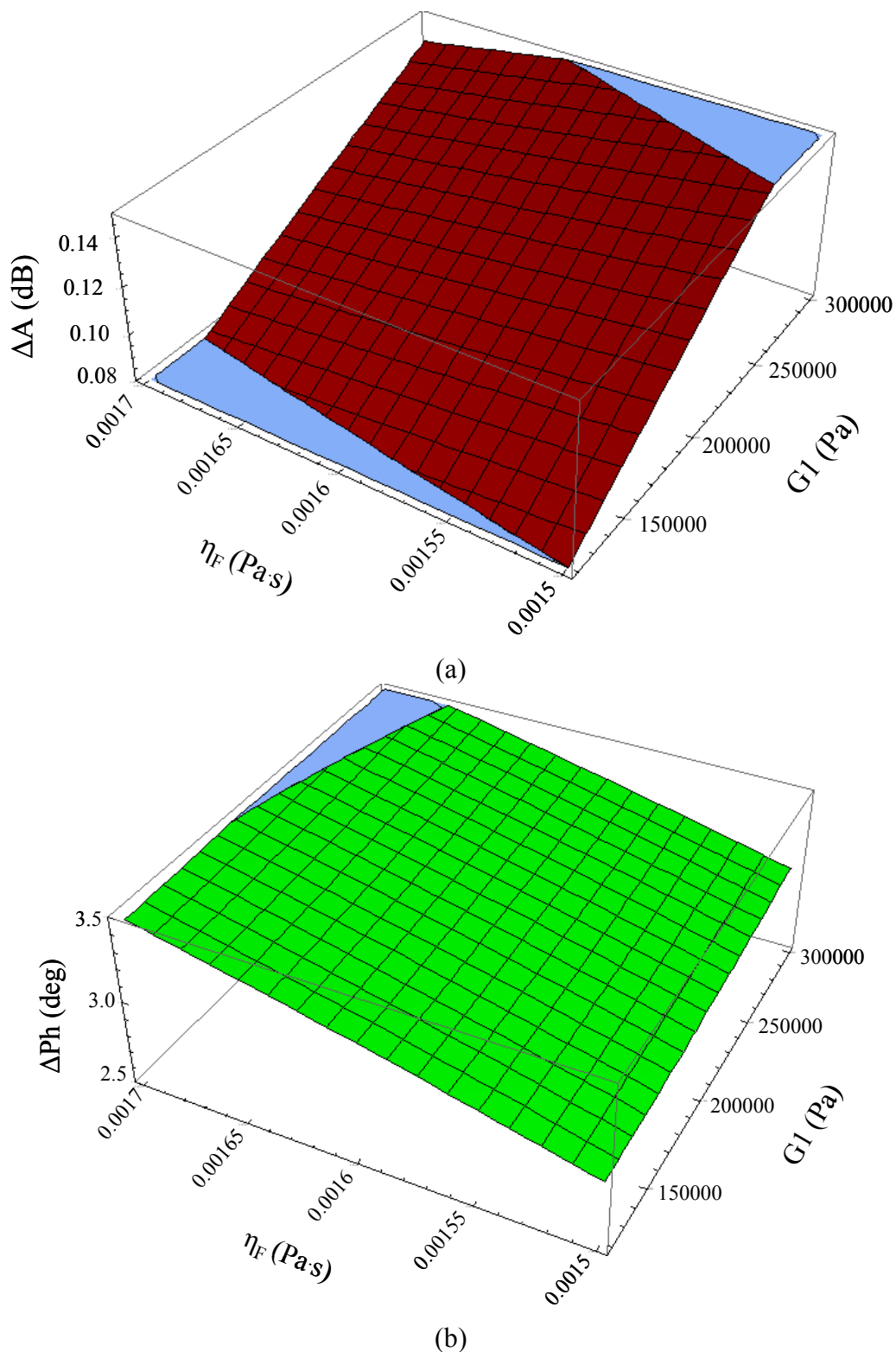


Fig.9.7. Determination of protein films' viscoelastic properties using Mathematica computer software. ΔA (a) and ΔPh (b) plotted against the same G_1 and η_F range.



Tab.9.2. Estimation of viscoelastic properties of biomolecules adsorbed on Au.

	PrG	PrA	BSA	neu	IgG
ΔPh limits (deg)	3.2 - 4.5	0.8 - 1.5	2.5 - 3.5	4.5 - 6	4.5 - 6.5
ΔA limits (dB)	0.05 - 0.10	0.02 - 0.06	0.08 - 0.15	0.10 - 0.16	0.20 - 0.30
G_1 range (Pa)	3×10^4 - 5×10^4	1×10^5 - 3.5×10^5	1.2×10^5 - 3×10^5	1×10^5 - 2×10^5	1.3×10^5 - 2.8×10^5
η_F range (cP)	1.2 - 1.5	1.5 - 2	1.5 - 1.7	1.5 - 2	1.5 - 1.7
G_2^* range (Pa)	1.15×10^6 - 1.14×10^6	1.45×10^6 - 1.95×10^6	1.45×10^6 - 1.65×10^6	1.5×10^6 - 1.9×10^6	1.45×10^6 - 1.65×10^6

* $G_2 = \omega \eta_F$

It is clear that both G_1 and G_2 are higher than those calculated in air (for BSA, beginning of this section), which is reasonable since that estimation was done using the equation for viscoelastic films in air. Moreover, from the above values it is evident that the “viscous” regime of the protein films is more dominant since in all cases, $G_2 > G_1$ ($G_2 \cong 10 \times G_1$). In addition, G_1 and G_2 values fall within the range that has been estimated by other groups [9.2.], [9.3.]. Finally, it appears that there is no significant deviation of G_1 and G_2 among the examined proteins. This implies that they exhibit a similar viscoelastic behavior (when probed by the particular sensor configuration), which is reasonable, since none of the proteins has any special structural feature or conformation (e.g. different shape, they are all globular) that could lead to remarkable variation of its viscoelastic nature [9.4.].

In the end, it must be noted that the above calculations were done only for the proteins directly adsorbed on gold, and not for the proteins specifically bound on the neutravidin layer, or for the biomarkers bound on the antibody layer. The reason is that, when two viscoelastic layers are present, the linear combination of their acoustic impedances, it is not correct. Non-linear combinations should be considered for the multi-layer configuration, and this exceeded the scope of this chapter, which was to demonstrate the capacity of SAW to quantitatively determinate the viscoelastic properties (complex shear modulus) of an adsorbed protein film.

9.6. Conclusions

This chapter was not related to multi-sensing, like the rest of the thesis, but it reported an overview of side-results that emerged from the various experimental parts during the μF -on-SAW evaluation. Three groups of biomolecules were examined in this chapter: (i) biotinylated molecules bound on neutravidin, (ii) non-biotinylated molecules adsorbed on gold, and (iii) cardiac markers bound on their homologous antibodies. More specifically, the acoustic signal was found to be linearly correlated to the MW of the probed molecules in the cases of specific binding - cases (i) and (iii) - whereas no trend was observed in the case of non-specific adsorption.



In addition, the viscoelastic nature of protein films was discussed. In a quantitative approach, the shear modulus of five protein films directly adsorbed on gold was calculated via proper mathematical expressions and simulations, and under reasonable physical assumptions. The real and imaginary parts of the shear modulus were found to be very close to numbers reported in literature, which proves that the SAW devices are competitive biophysical tools capable of performing such quantitative evaluation.

References

- [9.1.] H.L. Bandey, S.J. Martin, R.W. Cernosek, A.R. Hillman, "Modeling the responses of TSM resonators under various loading conditions", Sandia National Laboratories Report (SAND99-0631), Mar. 1999.
- [9.2.] M.V. Voinova, M. Rodahl, M. Jonson, B. Kasemo, "Viscoelastic acoustic response of layered polymer films at fluid-solid interfaces: continuum mechanics approach", *Phys. Scripta*, vol. 59, pp. 391-396, 1999.
- [9.3.] M. Weiss, W. Welsch, M.v.Schickfus, S. Hunklinger, "Viscoelastic behavior of antibody films on a Shear Horizontal Acoustic Surface Wave sensor", *Anal. Chem.*, vol. 70, pp. 2881-2887, 1998.
- [9.4.] A. Tsortos, G. Papadakis, K. Mitsakakis, K.A. Melzak, E. Gizeli, "Quantitative determination of size and shape of surface-bound DNA using an acoustic wave sensor", *Biophys. J.*, vol. 94, pp. 2706-2715, 2008.



Chapter 10. Epilogue



Glucose meter: the first biosensor





Chapter 10. Epilogue

10.1. Conclusions

The current work was based on a novel concept for developing a multi-sample analytical microsystem, by means of microfluidics integration with SAW devices. The motivation was the achievement of multiplicity by keeping the overall system as simple as possible, versatile and flexible. The novelty was in the means of achieving the multiplexity in biosensing: instead of using a number of M sensor elements, like traditionally done in multi-sensing in any classification of biosensors, the idea was to divide the single sensing area of one sensor element into N sub-areas. The compartmentalization was introduced via a properly designed parallel-channel microfluidic module, which facilitated the separation of fluids as well as the *in-situ* immobilization of biomolecules and independent hosting of N experiments on a single sensor. Thus, the two main components of the microsystem were the SAW biochip and the PDMS microfluidic module, constituting the “ μ F-on-SAW”.

The first stage of realization was the selection of the optimum SAW device configuration as the sensing platform of the μ F-on-SAW; substrate material, operating frequency and waveguide thickness were the parameters under investigation. For the performance comparison of the various configurations, a number of different types of samples were probed with the sensors: (i) **pure mass** loading, via gold thin film deposition; phase shift was proportional to the deposited mass per area, whereas the energy loss was negligible, (ii) **pure viscous** loading at low viscosities (in Newtonian region), via glycerol solutions of increasing concentrations; both amplitude and phase were proportional to the square root of density-viscosity product, (iii) high viscosity liquids deviating from the Newtonian behavior and falling into the **Maxwellian regime**; in this case amplitude and phase were saturated at high viscosities and the solutions exhibited a solid-like behavior. The components G_1 and G_2 of their complex shear modulus were also calculated, (iv) **viscoelastic films** (PMMA) of various thicknesses were characterized and their storage and loss moduli were determined. Among the examined configurations of this parametric study, a quartz-based 155-MHz device with 0.70 μm waveguide was considered to be the most suitable to be used as the sensor chip of the μ F-on-SAW microsystem.

The next stage was the development of the microfluidic module that was intended to induce the multiplicity to the SAW device. The design was based on geometrical and functional considerations imposed by the biosensor chip: (i) The piezoelectric nature of the sensor had to be taken into account and minimize the contact areas between the micromodule with the surface, without, on the other hand, endangering the hermeticity and stability of the sealing. (ii) Special design care was taken so as to avoid contact of the PDMS with the IDT sets which were located in close proximity with the sensing area, on either sides of it. (iii) Both the module and the sensor chip were intended to be re-usable, so the assembly of the microfluidic cell had to be made in a reversible way to ensure its re-usability and minimum wear.

The implemented fabrication method was soft lithography, based on rapid prototyping and replica molding. It was used due to the inexpensive materials



involved and the fast production procedure. The mold was made of SU8 by means of standard lithographic patterning procedures and was used over and over again, in a series of steps that did not even demand clean room facilities (replica molding), which was one of the advantages of the production method.

A series of evaluation steps followed in order to assess the functionality of the newly produced microsystem, and define its sensitivity and signal response. In addition, one major question that was vital for the new microsystem to pass the “yes or no” test was the agreement of results between the sub-areas, in other words, the reproducibility.

(i) A set of aqueous glycerol solutions was used in order to probe the response of the new setup to liquid loading, the basis of biosensing environment.

(ii) Protein adsorption was tested via neutravidin and PrG on gold.

(iii) Protein binding was checked via biotinylated BSA specific interaction with neutravidin, and IgG with PrG.

(iv) The multiplexity capacity was tested via the interaction of four different biotinylated molecules with neutravidin, in the four microchannels. The system was successful in detecting all four proteins and distinguishing between their *MW*.

(v) Finally, various concentrations of these proteins were measured so as to probe their interaction kinetics and affinities, as well as to investigate the detection limits of the system.

In all experiments, the sample injection was sequential among the microchannels, in order to avoid interference of signal between the different sub-areas. The evaluation of the acquired results led to the following conclusions for the μ F-on-SAW setup:

- The signal response from each sub-area was reduced by the ratio $A_{total}/A_{sub-area}$ with respect to the total area signal response (signal-to-surface proportionality)
- The sensitivity reproducibility was remarkable: up to 95% for aqueous solutions, up to 90% for protein adsorption and binding, which are very good levels, considering that μ F-on-SAW is open to environmental fluctuations and without temperature control unit.
- The signal was independent of the location of the sub-area, the series of injections (i.e. $4 \rightarrow 3 \rightarrow 2 \rightarrow 1$ or arbitrary) and the “history” of the setup (i.e., what had already happened in another microchannel).

In addition, the full capacity of the microsystem to detect 8 different interactions was explored ($N_{microchannels} \times M_{sensors} = 4 \times 2$) by pre-modifying the total sensing areas of the two sensor elements with neutravidin and PrG, and then applying the micromodule and injecting different samples in each compartment. A mixture of two proteins was used and the result was fully successful and opened the way for the implementation of the μ F-on-SAW in applications of clinical significance and diagnostics.

In an overall view of the above experiments with biomolecules, apart from the multi-sensing purpose, a number of side-project interesting results emerged: the phase shift of the acoustic signal was found to be proportional to the *MW* of the biotinylated molecules when they bound on a neutravidin layer, but *not* when they adsorbed on gold. This difference in trend was attributed to the different nature of interaction: specific, in the case of biotinylated molecules on neutravidin versus non-specific



adsorption on gold (the signal-to-*MW* linearity was also observed in case of biomarkers binding on their corresponding antibodies). Moreover, the viscoelastic properties of the protein films, i.e., the storage and loss moduli, were quantitatively determined both experimentally and theoretically, using proper mathematical expressions and computer software.

Ultimately, the μ F-on-SAW setup was used for multi-sensing of clinically relevant biomolecules, namely cardiac markers. Cardiac biomarkers were selected to be used as an application due to their increased value in healthcare, in particular for personalized diagnostics to assess the risk of incoming critical heart conditions, in intensive care units in pre- and post-operational cases, etc. In addition, the high number of available cardiac markers and their multiplexed role in early diagnosis of critical heart conditions makes them very suitable for multi-sample analytical tools, like the μ F-on-SAW. CK-MB, CRP, D-dimer and PAPP-A were the selected biomarkers, covering both standard and newly-emerged molecules in the field. None of them (but CRP) has been used on a SAW device detector, which was another novelty of the work.

During its application on cardiac markers, μ F-on-SAW was essentially used as a multi-immunoassay tool, probing the interaction of each biomarker with its corresponding PrG-immobilized antibody. Signal-concentration curves were derived and the lowest detectable concentration for each marker was defined. For all four the dynamic range of detection covered the concentration values of critical heart conditions; in the case of CRP and D-dimer, even down to the “border” of the healthy concentration levels. Indicatively, detection lower than 1 nM was achieved. Moreover, the kinetics of these molecules were investigated and their binding constants were defined.

Finally, the “highlight” of the μ F-on-SAW function came with the achievement of “capturing” one desired biomarker from a mixture of all four of them. After the ensurement of the proper control experiments (showing negligible interaction between a biomarker with its non-homologous antibodies) the mixture of all four markers was left to interact with each antibody, separately in each of the four microchannels. Not only was the proper biomarker “fished” by its corresponding antibody, but the signal from the antibody-*multi antigen* interaction was the same with that from the antibody-*single antigen* interaction, which was a very significant finding. It ensures the capability of μ F-on-SAW to operate with high selectivity under conditions of increased complexity (4-marker mixture). Thus, it can potentially be implemented with body fluids, such as blood and/or serum and be eventually brought closer to real-patient application.



10.2. Suggestions for future work

The experiments carried out during this PhD work are a complete set of steps followed for the proof-of-principle of a novel microsystem, as well as its application on biomolecules of clinical interest. However, there is plenty of room for further work on its development, which can be categorized into the following three levels:

1. Sensor chip level
2. Microfluidics level
3. Application level

Regarding the biochip itself, it would be desirable to increase its sensitivity so as to detect even lower analyte concentrations. In order to achieve this, higher operating frequencies can be used, but also new waveguide materials can be applied. It should also be considered if the biochip is intended to be re-usable or disposable. In the latter case, the selected material should have good waveguiding properties, and be compatible with bonding processes with the PDMS. Furthermore, new geometries and IDT designs can be explored towards the sensitivity improvement.

Another direction of biochip-oriented development lies in the pre-functionalization of the sub-areas with different receptors. This will potentially increase the functionality of μ F-on-SAW, and reduce the time and sample consumption. In fact, first attempts towards this scope have been successfully made, in cooperation with the Institute of Nanotechnology in Forschungszentrum Karlsruhe; Dip Pen Nanolithography was used to pattern a single SAW device with four different receptors in rectangular-shaped sub-areas, above which the microfluidic module was assembled and the specific interactions of the pre-functionalized receptors with their corresponding ligands were successfully probed.

On the fluidics level, a further development step involves the optimization of the “environment-to-chip” interface. In other words, it is necessary to develop an injection system that will allow serial change of fluids in an instant way, i.e., without time gaps. Such a system will: (i) eliminate sudden signal “jumps” during fluid change, (ii) reduce the danger of bubble formation along the tubes and, subsequently, the blocking of the microchannels with air bubbles.

Finally, on the application level, the natural continuation of the biomarkers’ experiments is to use real clinical samples from hospital patients. Applying all the necessary ethical conditions (patients’ consent and other EU regulations regarding the experiments on human samples) such an approach would establish the μ F-on-SAW to a greater extent as a multi-analyte microsystem for clinical diagnostics.



Publications and conferences

➤ Publications (directly related to my PhD work)

- K. Mitsakakis, A. Tsortos, J. Kondoh, E. Gizeli, “Parametric study of SH-SAW device response to various types of surface perturbations”, ***Sensors and Actuators B, Chemical***, vol. 138, pp. 408-416, 2009.
- K. Mitsakakis, A. Tserepi, E. Gizeli, “SAW device integrated with microfluidics for array-type biosensing”, ***Microelectronic Engineering***, vol. 86, pp. 1416-1418, 2009.
- K. Mitsakakis, A. Tserepi, E. Gizeli, “Integration of microfluidics with a Love wave sensor for the fabrication of a multi-sample analytical microdevice”, ***Journal of Microelectromechanical Systems***, vol. 17, no 4, pp.1010-1019, 2008.

Three more publications are under preparation, deriving from chapters 7, 8, and 9 of the thesis:

1. The operation of μ F-on-SAW with 4 different biotinylated proteins, the equilibrium and kinetics analysis, and the multiplexing of 2×8 interactions, described in chapter 7 (*targeting the “Analytical Chemistry” journal*).
2. The clinical application of μ F-on-SAW with cardiac markers described in chapter 8 (*targeting the “Lab Chip” journal*).
3. The correlation of acoustic signal with biomolecules’ properties, described in chapter 9 (*targeting the “Biosensors & Bioelectronics” journal*).

➤ Publications (not directly related to my PhD work)

- G. Papadakis, A. Tsortos, K. Mitsakakis, E. Gizeli, “Characterization of DNA-Hv1 histone interactions; discrimination of DNA size and shape”, ***FEBS Letters***, *accepted*.
- A. Tsortos/G. Papadakis, K. Mitsakakis, K.A. Melzak, E. Gizeli, “Quantitative determination of size and shape of surface-bound DNA using an acoustic wave sensor”, ***Biophysical Journal***, vol. 94, pp. 2706-2715, 2008.
(*Commentary*): HFSP Journal, vol. 2, no. 4, pp. 171-177, Aug. 2008.



➤ Conferences and presentations

- **Conference/Meeting “Highlights in Microtechnology”, July 2-4 2009, Neuchatel, Switzerland;** “Integrated SAW biosensors for multi-sample analysis” (oral)
K. Mitsakakis, E. Gizeli
- **34th International Conference on Micro- and Nano-Engineering, September 15-19 2008, Athens, Greece;** “SAW device integrated with microfluidics for array-type biosensing” (poster)
K. Mitsakakis, A. Tserepi, E. Gizeli
- **2008 IEEE International Frequency Control Symposium, May 19-21, Honolulu HI, USA;** “An integrated microfluidics-on-SAW (“ μ F-on-SAW”) setup for multi-sample sensing” (oral)
K. Mitsakakis, A. Tserepi, E. Gizeli
- **33rd International Conference on Micro- and Nano-Engineering, September 23-26 2007, Copenhagen, Denmark;** “Integration of microfluidics on Surface Acoustic Wave biosensors for multi-sensing purposes” (poster)
K. Mitsakakis, A. Tserepi, M.E. Vlahopoulou, E. Gizeli
- **2006 IEEE International Frequency Control Symposium, June 5-7 Miami FL, USA;** “Sensing the Shape of Biomolecules using Love Waves” (oral)
K. Mitsakakis, G. Papadakis, E. Gizeli